Universidad de Valladolid

Escuela de Doctorado Universidad de Valladolid

PROGRAMA DE DOCTORADO EN INVESTIGACIÓN EN CIENCIAS DE LA SALUD

TESIS DOCTORAL:

ADVANCED NANODEVICES BASED ON ELASTIN-LIKE RECOMBINAMERS AS SMART DRUG DELIVERY SYSTEMS FOR BIOMEDICAL APPLICATIONS

Presentada por Juan González Valdivieso para optar al grado de
Doctor por la Universidad de Valladolid

Dirigida por:

Dr. Francisco Javier Arias Vallejo

Dra. Alessandra Girotti

A mi familia

“No es el más fuerte ni el más inteligente
el que sobrevive, sino aquel que mejor
se adapta a los cambios”
Charles Darwin.

Agradecimientos

Aquí estamos, en la fase final. El objetivo que aparece y desaparece como un oasis en el desierto. Lo que parece muchos días imposible pero que al final acaba llegando. Y qué mejor manera de empezar una tesis que por los agradecimientos, que al fin y al cabo es lo primero que leemos todos cuando cogemos una.

En primer lugar, me gustaría agradecer a mis directores Javier y Alessandra la oportunidad que me dieron para hacer la tesis bajo su dirección, así como la confianza depositada en mí durante todo este tiempo. Muchas gracias por vuestra acogida, generosidad, tiempo invertido y ayuda. Han sido años llenos de consejos, paciencia, sugerencias y reuniones interminables en el despacho, pero también de risas y chistes. Mi dominio del sarcasmo y espíritu crítico no serían lo mismo sin vosotros.

También me gustaría agradecer a Carlos y Matilde su tiempo dedicado y consejos. A Merche, que tiene la gran capacidad de recibirte y despedirte con una gran sonrisa de oreja a oreja. Gracias por tu ayuda con los espectros de RMN, un auténtico jeroglífico para los biólogos. A Menchu, la guardiana del DSC, por su ayuda con su amplia experiencia del mundo "particular" y por su capacidad para arrancarte unas risas con sus ideas disparatadas de bromas y concursos navideños. A Isra, siempre dispuesto a echarte una mano (y la suya es muy grande) y a Luis, por la multitud de consejos prácticos que ha compartido conmigo.

I would like to thank Professor Stephen Pereira for hosting me in his research group, where I could take advantage of an incredible life experience. During my stay in London, Pilar was my guide. From the awkward British bureaucracy to my daily work and life in Hampstead. Absolutely THANK YOU PILAR. Andrés, who taught me not only how to work with pancreatic cells, but also amazing places only for authentic Londoners. I would also like to thank the other Pancrew colleagues for their warm welcome, help and advices about the pancreatic world: Alex (Mr Hola), Ismahan, Pete, Ponni, George, Khadra, Sonal, Navya and Diana. You all allowed me to feel myself as part of the group. Although it could be strange, spending lots of minutes waiting for the lift between the Upper Third

and Ninth floor allowed me to plan my intense days at Royal Free Hospital and think about my life. Out of the lab, all these Pancrew friends helped me to improve other interesting skills for a scientist: bowling, karaoke, dancing (at least a salsa and bachata attempt) and playing tennis. Thank you all and see you soon!

No es fácil describir en unas líneas todo lo que agradecer a los compañeros de poyata, con los que más horas he coincidido estos últimos años. A Filippo, mi gran amigo vividor italiano que da los mayores abrazos revitalizantes y tranquilizadores del mundo. Cuántas largas conversaciones hemos compartido riéndonos y charlando de nuestros planes futuros, siempre empezadas por un entusiasta "Is coming today?". ¡Nos vemos pronto amigo! A Sofía y Soraya, por la increíble cantidad de carcajadas, consejos y ayuda a partes iguales. Poca gente habrá disfrutado tanto durante estos años como nosotros. A Arturo, un libro abierto lleno de conocimiento con una respuesta siempre para todo. En el fondo creo que nos comunicábamos mentalmente en el silencio de nuestro despacho. A Doriana, nuestros momentos musicales en la sala de cultivos celulares quedarán para la posteridad. Ha sido un privilegio "enseñarte" los grandes clásicos de la música española cantados a capela. A Sergio, capaz de dejar todo por ayudarte en lo que sea. Llegarás muy lejos en todo lo que te propongas. A Ito y Tatjana, los Pimpinela de BIOFORGE, porque nunca ver discutir a dos personas provocó tantas risas. A Leander, seguramente el alemán con mayor dominio de los refranes españoles más allá de los Pirineos. A Mohammed, el hombre del desierto, por su alegría al saludarte "Hombreeeee!". A los M&M's (Miguel y Marcos) y Fernando, un trío disparatado que daría de sobra para un cómic superventas. A Reinal, compañero de fatigas del DTX y sus cálculos demoníacos. A las últimas incorporaciones, Sara, Diana, Irene y Julio, con quienes me he reído mucho gracias a vuestra inocencia del principiante predoctoral. Quiero agradecer también a Lubinda sus conversaciones sobre biomateriales y sus aplicaciones. Ha sido un placer haber coincidido con todos vosotros.

Muy especial tiene que ser el agradecimiento a la productora Rocío. Por nuestras charlas de purificaciones imposibles, fútbol (aún puedes hacerte seguidora del Pucela o la Real y dejar ese equipo al que animas…), baloncesto y cualquier tema que se nos pusiera por delante. A Sandra, por su ayuda con las purificaciones urgentes. A Ana y Leticia, aunque lleváis menos tiempo mostráis ganas y actitud a raudales. También a las chicas de

administración: Beatriz e Irene, siempre ayudando con la divertida burocracia. Quiero dar las gracias también a la gente con la que he coincidido estos años y ya no está en BIOFORGE: Lorena (con su risa inconfundible más allá del pasillo), Alicia, Dasha, Teresa, Leticia, Esther y especialmente a Elena, la enfermera productora que durante su estancia en el laboratorio fue fiel testigo de bromas y canciones irrepetibles.

Además, me gustaría agradecer la ayuda proporcionada por el personal del animalario, empezando por Ángel, y en especial a Raquel y Ainhoa, las "casi jefas" del animalario. Me habéis ayudado un montón todo este tiempo con los ratones, y siempre con una sonrisa. También quiero agradecer a Javier Gutiérrez su ayuda con las resonancias de los ratones y el confocal.

Pero también fuera del mundo bioforgiano hay mucha gente a quien agradecer su aportación a esta tesis. A mis amigos parisinos Rods y Leyre (Jaso si estás a tope de adrenalina en una montaña rusa), por los Skypes y quedadas patrocinadas por Guinness®. A Bea, Carmen, Cristian, David, Eva, Jorge y Natalia, por nuestras reuniones nocturnas en el Seamrog charlando de cualquier cosa. Al grupo de veterifrikis (Pati, Natalia, Davo, etc) porque cada ocasión en que nos hemos podido juntar por la geografía española a recordar viejos tiempos leoneses hemos compartido risas y confidencias. No me quiero olvidar tampoco de los padreisleños Suso y Estíbaliz, también embarcados en la aventura de la ciencia y con quienes di mis primeros pasos científicos en León. A Rafa, por las noches de tapas y picoteos para desconectar. A la pandilla de bios: Iris, Juanma, Dalia, con vosotros empezó todo. A los padeleros Carlos, Ceci, Diego y Jose, no sé si hemos conseguido jugar bien al pádel estos años, pero lo que nos hemos reído no está escrito. También me gustaría agradecer a la Doctora Itsaso García-Arcos, mi mentora en el International Mentoring Program de la Fundación IMFAHE, todos sus consejos para poder encaminar mi carrera investigadora. Además, al equipo TDJ, porque haber conseguido acabar esta tesis escuchando vuestras locuras es casi un milagro.

Durante mi experiencia estos últimos meses en el LAPCoV he podido conocer gente fantástica: David, Marta, Pilar, Yoli, Irene, Pili, Carla y muchos otros. Gracias a vosotros también he mejorado en otros aspectos de mi vida científica no tan explotados hasta entonces.

Un espacio aparte se merece Noa. Esta tesis no sería posible sin ti. La comprensión y el cariño que me has demostrado este tiempo no son de este mundo. Si ya es complicado estar con un doctorando, estarlo con un loco como yo tiene que ser de aúpa. Gastar nuestro tiempo libre en sumergirnos en conversaciones llenas de partículas, kinasas, genes, mutaciones, secuencias y PCRs, entre otras cosas, ha contribuido a desarrollar nuestra capacidad de escucharnos mutuamente hasta límites insospechados. Sé que no hemos podido disponer del tiempo como nos hubiera gustado, pero estar siempre unidos apoyándonos el uno al otro nos ha hecho aún más fuertes. Ahora empieza lo bueno.

Y por último, pero no por ello menos importante, a mi familia. A mi hermana María, por todo lo que me has tenido que soportar (sé que puedo llegar a ser muuuy pesado). No se paga con dinero tu aguante. Y por encima de todo, esta tesis tiene un agradecimiento especial a mis padres, Jesús y Carmen. Por vuestro esfuerzo y apoyo, por darme la libertad desde el minuto cero para que pudiera dedicarme a lo que más me gusta. Porque siempre tenéis una frase de ánimo y un brazo en el hombro, incluso en los momentos más complicados, que los ha habido. Por vuestra capacidad para ver y aguantar presentaciones y artículos en vuestro tan querido inglés, aun sin tener mucha idea de los elastin no sé qué, la Akt esa, etc. Habéis sido el impulso que me empujaba a ir siempre a por lo que me propusiera. También a mis abuelos y al resto de mi familia, porque siempre estáis atentos para preguntarme "¿Qué tal las investigaciones?" antes de saludarme.

GRACIAS, GRACIAS Y MÁS GRACIAS. ¡Qué afortunado soy de teneros a mi lado!

P.D.: Esta tesis no sólo puede medirse por la producción científica, sino porque también ha dado lugar a grandes frases que quedarán en mi memoria. He aquí algunos ejemplos:

- “Los papers son como los gnomos: todo el mundo ha oído hablar de ellos, pero nadie los ha visto ni tocado”: cuando charlas acerca de la capacidad escritora de artículos con Filippo, Sofía y Soraya.

- “El altruismo son los padres”: cuando Filippo te pregunta inocentemente un sábado por la mañana si has ido al laboratorio a lavar bacterias para Doriana.

Index

Index

Abstract/ Resumen

Abstract

Despite of the numerous advances in biomedicine, there are some issues to be resolved. One of these limitations is the low specificity of therapeutic agents with undesired side effects on healthy tissues. Thus, novel strategies for achieving an accurate action on targeted cells are needed. Over the years, advanced biomaterials have emerged as one of the most promising tools to increase therapeutic efficiency and biocompatibility, and possess the ability to mimic properties and features found in natural macromolecules in order to use in multiple biomedical applications, such as tissue engineering or drug delivery.

Among the novel biomaterials, we can find Elastin-Like Recombinamers (ELRs). ELRs are protein-based polymers composed by the repetition of VPGXG (Val-Pro-Gly-X-Gly) pentapeptide, where X can be any amino acid except proline. This pentapeptide can be found in the sequence of natural elastin protein, a major component of extracellular matrix (ECM) and confers some characteristic features to ELRs. Thus, ELR-based biomaterials show biocompatibility, biodegradability and stimuli-responsive behavior. Moreover, ELRs are defined by the Inverse Temperature Transition (ITT), a reversible phase transition above the so-called Transition temperature (Tt). When the Tt is reached, ELRs change from a disordered soluble state to self-assemble into well-defined structures, from the macro to the nanoscale, such as nanoparticles, micelles or vesicles. Due to the recombinant origin of ELRs, the Tt of these biopolymers can be modulated depending on the polarity of side chains of amino acid placed in the guest position. Thus, the molecular design allows us to obtain in the lab different ELRs with self-assembling ability in response to characteristic Tt and achieve smart devices for biomedical applications.

This Thesis describes novel ELR-based biomaterials as a promising approach for biomedical applications and their potential use as therapeutic tools for different diseases.

A novel strategy for DNA vaccination against a viral antigen was developed, thereby obtaining a fusion gene library with different properties and behaviour under physiological conditions, and several nanodevices derived from multiple ELR constructs

were tested. Natural antigens usually trigger low immunogenic responses, so novel strategies for modulated immunogenicity are needed in order to achieve safer vaccines. By taking advantage of genetic engineering techniques, ELR genes with different hydrophilic/hydrophobic nature were fused to the gene codifying for Gn glycoprotein from Rift Valley fever virus (RVFV). Eukaryotic cells were transfected with DNA constructs, cell viability was measured and protein expression was evaluated by immunocytochemistry and confocal microscopy. At light of results, gene constructs whose ELR block involved the presence of hydrophobic amino acid, as valine, improved the expression of Gn glycoprotein. Also, DNA vaccination was performed in an in vivo mouse model and immune response to viral antigen was studied. Results determined that the more hydrophobic constructs reduced viremia levels after RVFV challenge and were better inducers of cellular immunity, as judged by in vitro re-stimulation experiments. Thus, results highlighted the potential of ELR biomaterials for DNA vaccination strategies against Rift Valley fever virus infections and achieve higher yield productions of natural antigens.

The second chapter of this work is focused on the description of the design and development of novel ELR polymers based on an amphiphilic backbone with multiple bioactive sequences in order to selectively release a therapeutic peptide thereby modulating the cell growth. One of the most important problems of current medicine is the lack of selective agents which only affect targeted cells. Chemotherapeutic drugs are such an example, as this kind of agents tackles both tumor and healthy tissues. By means of genetic engineering techniques, two complex biopolymers were developed involving multiple blocks in order to achieve full control of the release of a therapeutic peptide in the cellular cytoplasm. Thus, internalization pathway, intracellular fate and spatiotemporal action were driven by the molecular complexity of ELR biopolymers. Physicochemical characterization demonstrated that these two biopolymers were able to self-assemble into nanoparticles with adequate size and surface charge for intracellular delivery of therapeutic peptides. The internalization pathway and intracellular activation were also determined. Finally, the cytotoxic effect of nanoparticles on cancer cells and non-cancer cells was compared and results showed an enhanced effect over cancer cells with minimum toxicity in non-cancer ones. Thus, results showed that a smart complexity

was successfully acquired to achieve the controlled delivery of a therapeutic peptide and avoid aberrant proliferation of targeted cells.

The following chapter describes the potential use of these self-assembling ELR-based nanoparticles carrying a peptide for the inhibition of Akt phosphorylation as therapeutic nanodevices against pancreatic cancer. By taking advantage of patient-derived cells, the developed nanoparticles were tested in a closer model to real disease and heterogenic tumor populations. First, the in vitro assays showed that developed nanocarriers possessed a time and dose-dependent effect not only in pancreatic cancer cells metabolism, but also in cell viability. Flow cytometry and confocal microscopy assays were performed in order to determine cell uptake and intracellular localization. At light of the results, ELR-based nanoparticles co-localized with lysosomes in the cellular cytoplasm. Synergic effect of developed nanodevices and light-derived therapy was also studied. Thus, combination of ELR nanoparticles and photosensitizer TPP2Sa appeared to have synergic effect and significantly affected pancreatic cancer cell metabolism. Furthermore, a mouse animal model was used in order to determine the pharmacokinetic profile and biodistribution of nanocarriers in vivo. At light of the results, ELR-based nanoparticles met the requirements for drug delivery systems.

Finally, Chapter 4 is focused on the development of novel hybrid nanodevices as advanced drug delivery systems with combined therapeutic approaches for colorectal cancer treatment. For this purpose, a dual hybrid ELR nanodevice was designed as a consequence of the combination of two previously described amphiphilic polymers: one forming highly monodisperse nanoparticles with encapsulated chemotherapeutic agent Docetaxel and another one consisting on smart nanoparticles carrying an Akt inhibitor previously described in Chapter 2. Thus, the resulting device was characterized and in vitro efficacy was tested on cancer and endothelial cells. Results from the in vitro assays showed that targeted nanohybrids selectively affect cancer cells by two different ways: Akt inhibitor triggered early apoptosis whereas DTX elicited both apoptosis and necrosis at longer times. A reliable colorectal cancer animal model close to real disease was produced in order to study the anti-tumor effect of systemically injected ELR nanohybrids. Magnetic Resonance Imaging showed that tumor-associated inflammation was decreased after intravenous administration of the ELR-based nanodevices. *Ex vivo*

analysis showed that dual-approach ELR nanohybrids significantly decreased the number of tumor polyps, whose size was also reduced. Moreover, histological analysis determined that those animals treated with ELR nanohybrids possessed improved tissue architecture and crypt morphology in the distal colon.

In summary, this Thesis explores new insights about nanodevices for biomedical applications involving multiple diseases. In this work, all the necessary steps needed for such aim are included, from gene design and cloning, bioproduction in a prokaryotic organism, purification, synthesis and physicochemical characterization to the assessment of both in vitro and in vivo behavior.

Resumen

A pesar de los numerosos avances en la biomedicina, aún hay algunos problemas sin resolver. Una de esas limitaciones es la baja especificidad de los agentes terapéuticos con efectos secundarios no deseados en tejidos sanos. Por eso, son necesarias nuevas estrategias para conseguir una acción efectiva en las células diana. A lo largo de los años, los biomateriales avanzados han emergido como una de las herramientas más prometedoras para incrementar la eficacia terapéutica y la biocompatibilidad, con la habilidad de imitar las propiedades y características de las macromoléculas naturales para su uso en aplicaciones biomédicas, como la ingeniería de tejidos o la dosificación de fármacos.

Entre los biomateriales novedosos, encontramos los recombinámeros tipo elastina (ELRs). Los ELR son polímeros proteicos compuestos por la repetición del pentapéptido VPGXG (Val-Pro-Gly-X-Gly), en el que X puede ser cualquier aminoácido excepto la prolina. Este pentapéptido puede encontrarse en la secuencia de la elastina natural, el principal componente de la matriz extracelular (ECM) y confiere algunas características típicas a los ELR. Así, los biomateriales basados en ELR presentan biocompatibilidad, biodegradabilidad y comportamiento en respuesta a estímulos. Además, los ELR se caracterizan por la transición inversa de temperatura (ITT), una transición de fase reversible por encima de la llamada temperatura de transición (Tt). Al alcanzar la Tt, los ELR pasan de un estado soluble desordenado a autoensamblar en estructuras definidas, en las escalas macro y nano, como nanopartículas, micelas o vesículas. Debido al origen recombinante de los ELR, la Tt de estos biopolímeros puede modularse en función de la polaridad de la cadena lateral del aminoácido situado en la posición X. De esta manera, podemos diseñar en el laboratorio distintos ELR con capacidad de autoensamblaje en respuesta a una Tt determinada y desarrollar dispositivos inteligentes para aplicaciones biomédicas.

Esta Tesis Doctoral describe nuevos biomateriales basados en ELR como una estrategia prometedora para aplicaciones biomédicas y su uso potencial como herramientas terapéuticas frente a múltiples enfermedades.

Se ha desarrollado una nueva estrategia para vacunas DNA frente a antígenos virales, obteniendo de esta manera un conjunto de genes fusión con diferentes propiedades y comportamiento en condiciones fisiológicas. Los antígenos naturales provocan habitualmente respuestas poco inmunogénicas, por lo que se necesitan nuevas estrategias capaces de modular su inmunogenicidad y obtener vacunas más seguras. Mediante técnicas de ingeniería genética, genes ELR de distinta naturaleza hidrofílica/hidrofóbica fueron fusionados al gen que codifica para la glicoproteína Gn del virus de la fiebre del Valle del Rift (RVFV). Células eucariotas fueron transfectadas con las construcciones DNA, se estudió la viabilidad celular y la expresión proteica fue evaluada mediante inmunocitoquímica y microscopía confocal. A la vista de los resultados, las construcciones génicas cuyo bloque ELR se basaba en un aminoácido hidrofóbico, como la valina, mejoraron la expresión de la glicoproteína Gn. Además, las vacuna DNA fueron probadas *in vivo* en un modelo de ratón donde ese estudió la respuesta inmune al antígeno viral. Los resultados determinaron que las construcciones más hidrofóbicas redujeron los niveles de viremia después del desafío con RVFV e indujeron mayor inmunidad celular, como demostraron los ensayos de re-estimulación *in vitro*. Así, los resultados pusieron de manifiesto el potencial de los biomateriales basados en ELR como estrategia de vacunación DNA contra infecciones provocadas por el virus de la fiebre del Valle del Rift y conseguir producciones a gran escala de antígenos naturales.

El segundo capítulo de este trabajo aborda el diseño y desarrollo de nuevos polímeros ELR basados en una estructura anfifílica con diferentes secuencias bioactivas para liberar de manera selectiva un péptido terapéutico y modular el crecimiento celular. Uno de los problemas más importantes de la medicina actual es la falta de selectividad de los fármacos para afectar únicamente a las células diana. La quimioterapia es un ejemplo de ello, ya que afecta tanto a los tumores como a tejidos sanos. Mediante técnicas de ingeniería genética, se han construido dos biopolímeros complejos incluyendo distintos bloques para conseguir el control total de la liberación de un péptido terapéutico en el citoplasma. De esta manera, la complejidad molecular de los biopolímeros ELR determina la internalización, comportamiento intracelular y la acción espaciotemporal. La caracterización fisicoquímica demostró que estos dos biopolímeros fueron capaces de autoensamblar formando nanopartículas de tamaño y carga superficial adecuados para la liberación de péptidos terapéuticos en el interior celular. También se estudiaron la ruta de

internalización y la activación intracelular. Finalmente, se comparó el efecto citotóxico de las nanopartículas en células cancerígenas y células sanas, y los resultados mostraron un mayor efecto sobre células cancerígenas con una toxicidad mínima en células sanas. En consecuencia, los resultados demostraron que esa complejidad es necesaria para conseguir una liberación controlada del péptido terapéutico y evitar de esta manera la proliferación descontrolada de las células diana.

En el siguiente capítulo, se describe el uso de nanopartículas ELR autoensamblables que transportan un péptido inhibidor de la fosforilación de Akt como nanodispositivos terapéuticos frente a cáncer de páncreas. Gracias al uso de células derivadas de pacientes, se ha podido probar las nanopartículas en un modelo muy parecido a la enfermedad y a la heterogeneidad intratumoral. En primer lugar, los ensayos *in vitro* determinaron que las nanopartículas tienen un efecto dependiente del tiempo y de la dosis tanto en el metabolismo como la viabilidad de las células tumorales pancreáticas. Mediante citometría de flujo y microscopía confocal se estudiaron la internalización y localización intracelular de las nanopartículas, que colocalizan con los lisosomas en el citoplasma. Además, se estudió el efecto de la combinación de las nanopartículas ELR y la terapia basada en la luz a través del fotosensibilizador TPP2Sa, que demostró un efecto sinérgico y afectó significativamente al metabolismo de las células tumorales pancreáticas. Se utilizó un modelo animal de ratón para estudiar el perfil farmacocinético y la biodistribución de las nanopartículas, cuyos resultados determinaron que las nanopartículas ELR cumplen los requisitos necesarios para la administración sistémica de dispositivos de liberación de fármacos.

Finalmente, el capítulo 4 aborda el desarrollo de nuevos nanodispositivos híbridos como sistemas avanzados de liberación de fármacos combinando diferentes estrategias terapéuticas frente a cáncer de colon. De esta manera, se diseñó un nanodispositivo ELR híbrido doble como resultado de la combinación de la combinación de dos polímeros anfifílicos descritos previamente: uno capaz de formar nanopartículas con el agente quimioterápico Docetaxel encapsulado en su interior y otro capaz de formar las nanopartículas que incluyen el inhibidor de Akt descrito en el capítulo 2. Así, el dispositivo resultante fue caracterizado y se probó su eficacia en células tumorales y endoteliales. Los resultados de los ensayos *in vitro* mostraron que los nanohíbridos

afectan selectivamente a las células tumorales mediante dos rutas diferentes: el inhibidor de Akt desencadena apoptosis a tiempos cortos mientras que el DTX provoca apoptosis y necrosis a tiempos más largos. Además, se estudió el efecto antitumoral de los nanodispositivos híbridos mediante su inyección sistémica en un modelo animal que imita de forma realista el cáncer de colon. Los resultados de resonancia magnética demostraron una disminución en la inflamación típica asociada a los tumores tras la administración intravenosa de los nanodispositivos basados en ELR. El análisis *ex vivo* indicó un descenso significativo en el número de pólipos tumorales, cuyo tamaño también fue reducido. Además, el análisis histológico determinó que los animales tratados con los nanohíbridos ELR presentaban una mejor arquitectura y morfología de las criptas intestinales en el colon.

En resumen, esta Tesis Doctoral explora nuevos conceptos de nanodispositivos para aplicaciones biomédicas frente a múltiples enfermedades. En este trabajo se incluyen todos los pasos necesarios para dicho propósito, desde el diseño y clonación de los genes, bioproducción en un organismo procariota, purificación, síntesis y caracterización fisicoquímica hasta la validación *in vitro* e *in vivo*.

Introduction

2. Introduction

2.1 Biomaterials

Although medicine started in the early human civilization, the most recent scientific research has promoted some disciplines derived from the acquired medical knowledge, such as biochemistry, biotechnology and immunology, among others, whose ensemble is also known as biomedicine. The relationship between biomedicine and biomedical research is referred to a kind of medicine closely associated with experimentation at the laboratory rather than the experience in a clinical environment. During the last years, the scientific research tries to develop novel biomedical devices in order to improve not only the diagnosis and the replacing of structural and biological functionality but also the treatment of multiple diseases. The growing interest in biomedicine and biomaterials science is mainly due to two factors: the great number of directly affected population and the increased lifetime. These challenges require an advance in materials engineering for suiting to emerging medical technologies the proper tailor-made biomaterial. According to the definitions of N.A Peppas and D.F. Williams, a biomaterial is "substance other than food or drugs contained in therapeutic or diagnostic systems that is in contact with tissue or biological fluids" and "a substance that has been engineered to take a form which, alone or as part of a complex system, is used to direct, by control of interactions with components of living systems, the course of any therapeutic or diagnostic procedure, in human or veterinary medicine" [1, 2]. Thus, biomaterials are designed for multiple purposes, such as tissue engineering [3], regenerative medicine [4], gene delivery [5], drug delivery [6], nanovaccines [7], *in vivo* imaging [8], early diagnosis [9], 3D bioprinting [10, 11], biosensors [12], cell harvesting [13], surface biofunctionalization [14]. Biomaterials are therefore those materials which are synthesized from a biological source or whose final aim consists on its interaction with the biological system in order to assist diagnosis, therapy or restore physiological functionality [15, 16]. Thus, biomaterials science studies their different applications in human health. There are different types of biomaterials: metals and alloys, composites, ceramic materials, synthetic polymersand natural biopolymers [17]. Bone plates, dental roots or implants are some of the applications for metallic biomaterials, whose main advantages are the strength, and ductility [18, 19]. Applications of composites-based biomaterials involves

joint implants and heart valves [20]. Although this type of biomaterials has interesting advantages as their compression ability and strength, they are difficult to make. Many different ceramic materials have been used over the years, such as zirconia, bioactive glasses, calcium phosphates and glass ceramics [21]. However, they show some disadvantages, as brittleness, difficult implantation and not easily controllable degradation [22]. Also, synthetic polymers have been widely used. Thus, many research groups have studied therapeutic approaches consisting on polystyrene, poly-l-lactic acid (PLLA), polyglycolic acid (PGA) and poly-dl-lactic-co-glycolic acid (PLGA) [23, 24]. Even though these materials can be developed with tailored architecture, they present poor cell interaction. Contrary, natural polymers were thought as promising choices due to their high biocompatibility and biological properties. Polysaccharide-based and protein-based biomaterials highlight among biopolymers-derived biomaterials. The first type involves β-glucans, chitosan, cellulose, and hyaluronic acid, among others, as natural origins. Contrary, protein-based polymers (PBP) are formed by different combinations of up to 20 amino acids, whose chemical properties and side chains determine the protein structure and function [25-27]. Such huge amount of combinations offers high versatility when designing protein-based biomaterials, and these wide combination possibilities together with recombinant DNA technology allow researchers to control over their sequence and structure [28]. Moreover, PBPs take advantage of the well-known sequence of natural proteins, such as elastin, silk's fibroin, collagen, keratin, fibrin, gelatin, resilin or bovine serum albumin [29].

2.2 Elastin

Among these proteins, elastin is of major interest, as it is one of the main components of extracellular matrix (ECM) the non-cellular portion of tissues and organs that offers both structural and biochemical support to cells. [16, 30]. Elastin is a hydrophobic insoluble network, secreted in the form of a soluble precursor: tropoelastin. Tropoelastin is a 60-72 kDa protein composed by alternating hydrophobic and hydrophilic domains, which are responsible for its elastic properties and elastin microfibrillar networks crosslinking respectively [31, 32]. The hydrophobic domains are mainly composed by non-polar amino acids such as valine, alanine, proline and glycine, whereas the cross-linking domains are formed by alanine and lysine-rich regions. The tropoelastin gene is highly expressed only during fetal and neonatal periods and disappears after 10 years. Thus, the

protein is characterized by extremely low turnover and high lifetime [33, 34]. Tropoelastin is synthesized by multiple cell types, such as smooth muscular cells [35], fibroblasts [36], chondrocytes [37] and endothelial cells [38]. The synthesis occurs inside the cell, where the elastin binding protein (EBP) chaperone binds, and is then secreted to the extracellular matrix [39].

Elastin shows remarkable mechanical properties as peculiar elasticity, resistance to fatigue, extreme durability and the ability to deform reversibility. This protein mainly provides mechanical properties, such as elasticity and resilience to most tissues, such as blood vessels, elastic ligaments, skin, bladder and lungs [40-42]. However, elastin's functions do not only consist on provided mechanical support, but also a bioactive molecule with cell-interacting domains which trigger multiple biochemical signals [43]. The origin of these abilities roots in its amino acid composition, based on repeated motifs as VPGG, VPGVG, APGVG and VGVAPG. Moreover, the conformational structure of elastin allows it to undergo high deformation and return to the original state without damages [44]. For all these reasons, elastin has been thought as an interesting inspiration for biomaterials.

2.3 Elastin-Like Recombinamers (ELRs)

Elastin-Like Polymers (ELPs) can be defined as polypeptides based on the repetition of certain sequences found in natural elastin, such as KGGVG, LGAGGAG, VPGG, GVGVP, IPGVG and VAPGVG [43, 45-55]. Among the wide variety of repeating possibilities, VPGVG (Valine-Proline-Glycine-Valine- Glycine) has been the most studied over the years. This sequence has been used as basis for the development of the majority of the so-called Elastin-Like Recombinamers (ELRs), recombinant ELPs synthesized by genetic engineering techniques [56]. Thus, the term ELR refers to proteinaceous molecules whose composition can be modified by recombinant DNA technology [57]. Indeed, ELRs are based on the repetition of pentapeptide VPGXG, where X can be any amino acid except proline as guest residue [58-60]. ELRs retain many of elastin's properties, such as biocompatibility, elastic and self-assembling behavior, although the most important feature of ELRs is their thermosensitive behavior. Prof. D. Urry demonstrated that elastin undergoes a reversible Inverse Temperature Transition (ITT) above the so-called Transition Temperature (Tt) [33, 61]. Elastin possesses hydrophobic

nature, as the structural domains are formed by the repetition of hydrophobic residues in patterns. Urry proposed that ELPs remain soluble and hydrophobically hydrated in aqueous solutions below the Tt. This hydration is characterised by the presence of ordered clathrate-like structures which surround non-polar residues of the polymer [62]. However, when the temperature is increased, clathrate structures around non-polar residues disappear and polypeptide chains fold in order to acquire a β-spiral disposition with the peptide bonds belonging to the polymer chain form a hydrophilic inner channel and the hydrophilic groups exposed to the outside [63]. Recombinant origin of ELRs allow us to design multiple polymers, depending on the amino acid chosen as guest residue at 4th position in the pentapeptide.

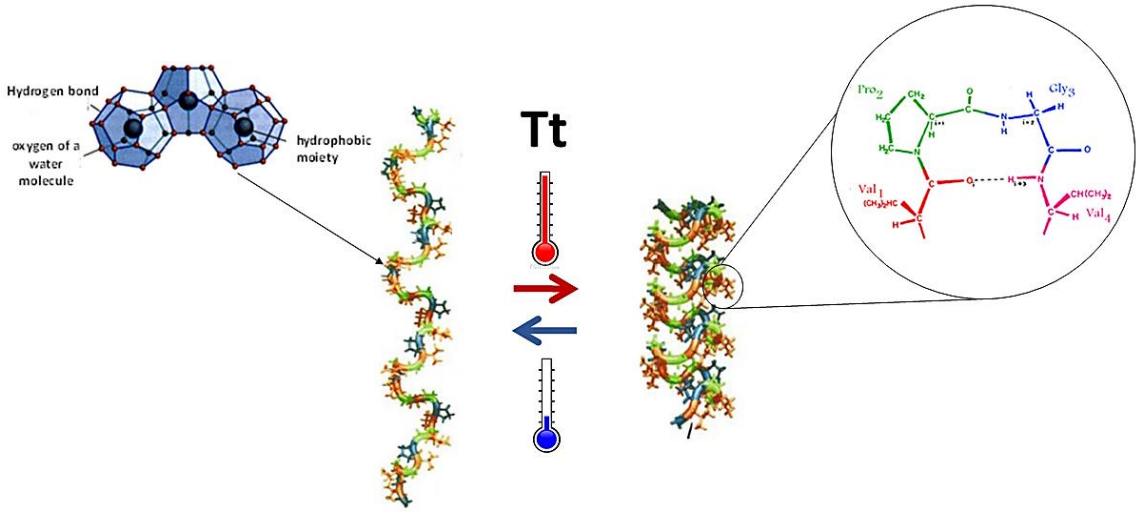

Figure 1. The thermal transition of Elastin-like Recombinamers from the extended state at low temperature to the folded state at high temperature. Clathrate structures surrounding the ELR chains and type II β turn in VPGVG pentapeptides are highlighted.

2.3.1 Tt modulation of ELRs

There are several factors that affect Tt of ELRs. First, we have inherent properties of the recombinamers, such as concentration, amino acid composition and length [64-66]. ELR concentration and Tt are inversely related, so when the concentration is increased the Tt diminishes [65]. This fact is explained by a cooperation phenomenon. Moreover, the polarity of the side chain belonging to the guest amino acid in ELR sequence is one of the main factors determining the Tt of an ELR [67, 68]. Thus, hydrophobic residues, such as valine or isoleucine, tend to decrease the Tt. Contrary, hydrophilic amino acids, namely glutamic or aspartic acid, increase it [66, 69]. The role of the different amino acids over

the Tt in a VPGXG monomer is depicted in Figure 2. Furthermore, the sequence length involves a cooperation phenomenon, where longer ELRs result in lower Tt [64, 65].

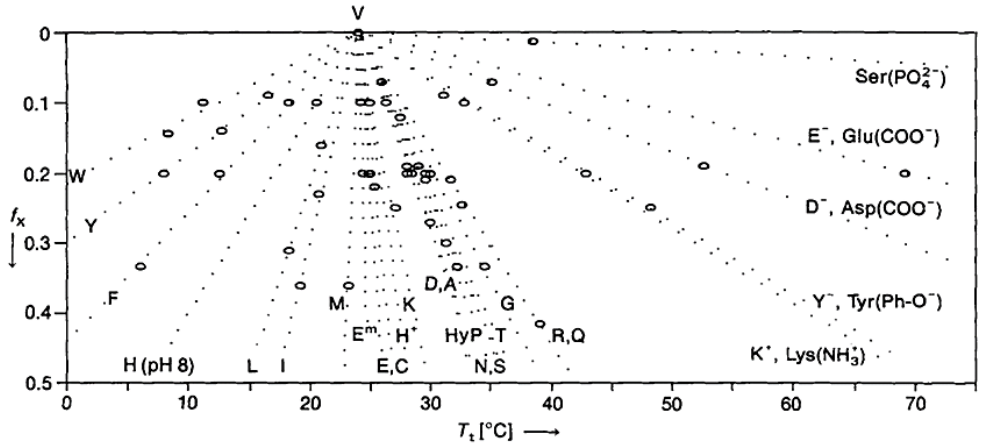

Figure 2. The effect of the amino acid composition at guest residue position on the Tt. f_x represents the mole fraction of pentamers containing the residue X. Reproduced from [61].

On the other hand, there are many other extrinsic factors that modulate Tt, such as pH or the presence of salts [14, 70]. As instance, pH provokes changes in Tt due to its effect in the hydrophobic/hydrophilic state of ELR [14]. This effect is noticed when the guest residue in ELR sequence is a polar residue whose side chain can modify its structure depending on the pH, such as lysine, histidine, tyrosine, arginine, aspartic acid and glutamic acid. When ionized, ELR chains become more hydrophilic and as a consequence, the Tt decreases [71].

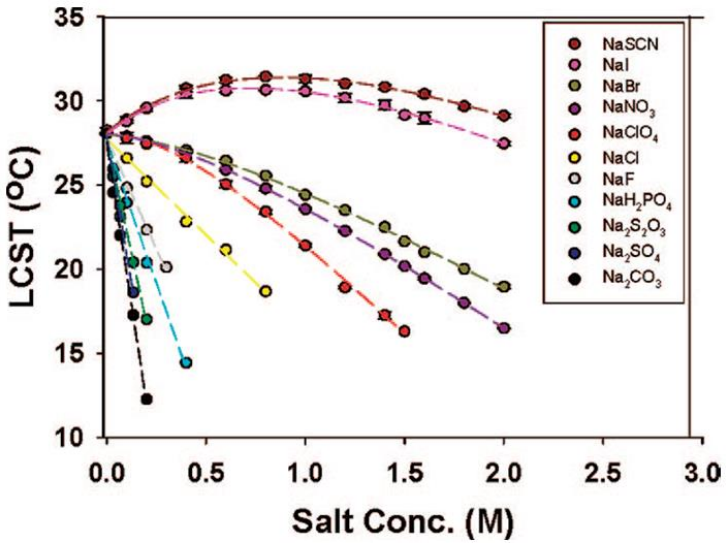

Figure 3. The effect of sodium salts concentration on the Tt of an ELR. Reproduced from [71].

The Tt has also been demonstrated to be affected by the presence of salts. As instance, salts decrease Tt due to the increased interaction between ELR chains and water [70]. Reguera *et al*. demonstrated that when NaCl is added, the polarity is increased in the medium and, as a consequence, there are higher differences in terms of polarity between the aqueous solution and the polymer [72]. Therefore, stronger clathrate structures are formed and surround the hydrophobic polypeptide chains. This effect has great importance, as NaCl is present in physiological conditions.

2.3.2 ELR biosynthesis

ELRs are designed through genetic engineering techniques. This recombinant approach offers us several advantages: from reduced production costs, environmental friendly production, higher yields and scaled bioproduction process to absolute control over the recombinamer sequence and properties [57, 73, 74]. As explained above, ELRs backbones synthetized in this work are based on VPGXG pentapeptide repetitions where the amino acids placed at guest position have been chosen depending on the desired characteristics of the polymer and its potential applications.

ELR polymers are built as multi-block genes formed by oligomerization of smaller monomeric genes through directional oligomerization [56, 75, 76]. Among oligomerization methods, the iterative-recursive directional ligation (RDL) approach allows us to sequentially concatenate monomeric genes in order to achieve multimeric fusion genes with fully controlled length and molecule architecture [57]. Moreover, restriction sites for non-palindromic enzymes are needed at both 5' and 3' gene ends. Once the monomer gene is cloned in a plasmid, this construct acts as donor/receptor in the following oligomerization steps. The ligation of monomers/multimers in order to achieve the definitive gene construct could need several RDL cycles. This cloning method has a main drawback: superfluous nucleotides included in the sequence. As an alternative, the seamless cloning method has been widely developed and applied to ELRs biosynthesis and involves the use of type IIS restriction enzymes as *Sap*I and *Ear*I [77]. Type IIS restriction enzymes are characterized for their ability to cleave the DNA sequence outside the recognition site, and as a consequence, the introduction of undesired nucleotides in the gene sequence is avoided. There are only two premises in this approach: First, one restriction site for *Sap*I has to be included at the 5' extreme of the ELR cloning

vector in order to allow vector linearization and gene step by step construction (Figure 4A). *Sap*I cuts infrequently respect to conventional restriction enzymes, because it has a seven-base-pair recognition sequence, therefore several gene of interest are "clonable" with *Sap*I. Secondly, the gene needs to be flanked by two *Ear*I recognition sites, which thereby facilitate the isolation of the gene inserts which can be cloned in previously linearized plasmids [78].

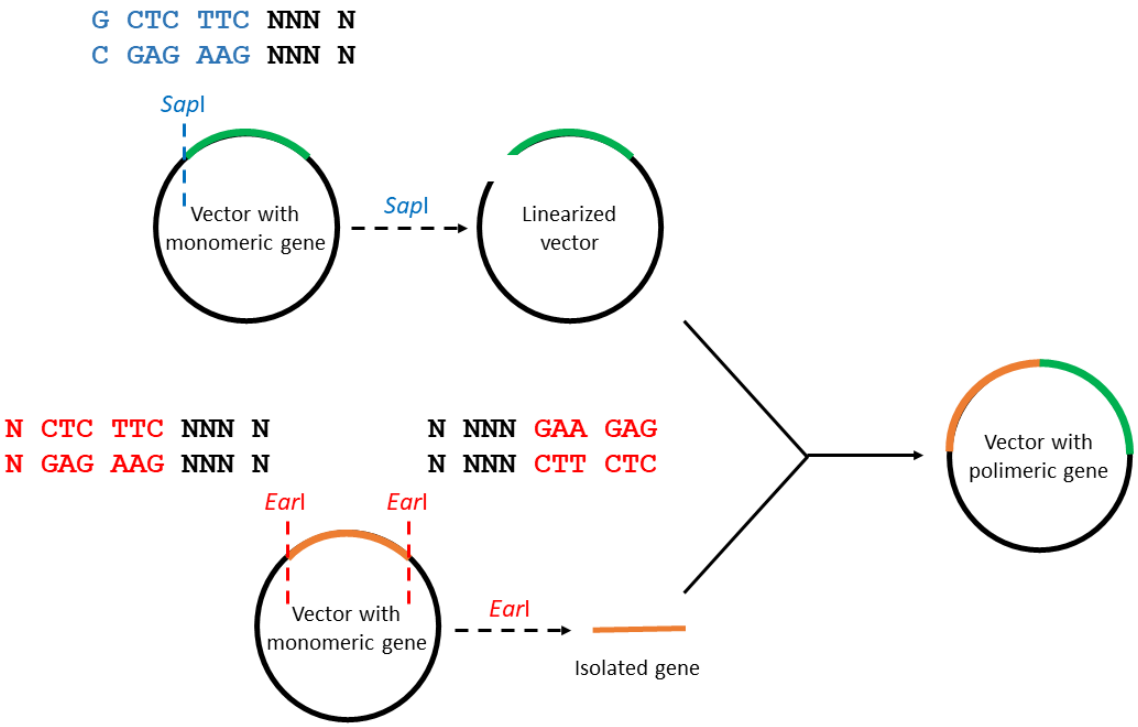

Figure 4. The RDL ligation method using *Ear*I and *Sap*I type IIS restriction enzymes. The plasmid containing the monomer gene can be linearized (when incubated with *Sap*I) or used for the isolation of the monomeric gene (when incubated with *Ear*I). Recognition and cutting sequences of *Ear*I and *Sap*I endonucleases are indicated. *Ear*I recognizes and cuts in all *Sap*I restriction sites but not *vice versa*. The asymmetrical extremities generated by *Sap*I have the same size and orientation than those generated by *Ear*I endonuclease, and therefore allow subsequent ligation steps.

The final cloning step involves the introduction of the gene of interest in an expression vector that possesses some characteristic components to optimize the recombinant polymer production, such as an inducible promoter, a low copy origin of replication and an antibiotic resistance gene. After the inclusion of the final construct in an expression vector, an heterologous expression host as the well-known *Escherichia coli* is used for expression and bioproduction of recombinant polymers [79, 80].

Once the ELR is bioproduced, purification process is needed in order to isolate the recombinant protein from the bacterial lysate. Even though there are different purification methods [81, 82], we can take advantage of the previously described ITT of ELRs. Therefore, ELR purification by several cooling-heating cycles (Inverse Transition Cycling) , consisting on centrifugation and solubilisation steps takes advantage of the ability of recombinamers to reversibly aggregate above their transition temperature and allow us to remove bacterial debris and endogenous proteins [83]. After this purification method we achieve pure recombinant polymers and, we can also proceed with endotoxin-removal treatments in order to obtain proper materials for *in vitro* and *in vivo* assays [84].

2.3.3 Self-assembled ELR-based structures for delivery purposes

Over the years, multiple ELRs have been designed in order to build delivery devices [85-90]. One interesting class of block polymers with especial relevance are the so-called amphiphilic block co-polymers, as they have affinities for two different environments. Due to their different chemical nature and behavior in solution, the two blocks show distinct interactions with their environment. Therefore, self-assembling ability of amphiphilic ELRs block co-polymers or ELR-based co-recombinamers is based on the fact that only one of these two forming blocks is able to self-assemble due to their different Tt and behavior under physiological conditions. In particular, amphiphilic block co-polymers have been explored as promising carriers due to their self-assembling ability into different structures, such as hydrogels, fibers, micelles and nanoparticles.

2.3.3.1 Hydrogels

Hydrogels are well-known scaffolds for biomedical applications with tissue engineering and drug delivery purposes in the last years [91, 92]. In particular, hydrogels have great interest due to their ability to be implanted in the site of interest and deliver therapeutic agents locally for prolonged periods of time. Hydrogels are promising candidates as drug reservoirs for controlled release of active compounds in time and space, especially in localized diseases where avoiding systemic exposure and lowering toxicity and secondary effects for the healthy tissues. As a consequence, lower amount of drug is needed as the compounds do not have to overcome hepatic and renal clearance. Also, the therapeutic

agent is preserved to body neutralization and the number of administrations is also reduced. Moreover, both mechanical properties and stimuli-responsive behavior deal with the properties of natural tissues [93, 94]. The extracellular matrix (ECM), whose major component is elastin, possesses characteristic properties, such as elasticity, stiffness, presence of signaling molecules, protease-sensitive sites and adhesion domains. Therefore, any material with potential use in tissue engineering needs many of these properties. Thus, ELRs, which are inspired in the natural protein elastin, are excellent candidates regarding to the development of artificial matrices as scaffolds for biomedical applications.

Moreover, the development of ELR-based hydrogels requires special attention to the cross-linking of such different ELRs molecules. Cross-linking methods can be based on chemical or physical approaches to achieve the desired mechanical properties. Genetic engineering techniques allow us to include cross-linking points along the ELR backbone. Physical cross-linking of ELRs can be obtained by several strategies, such as ionic interactions between opposite charged segments (as instance, cationic and anionic amino acids in the X position of the ELR sequence) [95]. ELRs are sensible to salts concentration, so the presence of ions could also trigger the formation of hydrogels [96]. Another way of physical cross-linking is achieved by the introduction of protein secondary structures forming dimerization domains, such as β-sheets formed by the repetition of GAGAGS hexapeptide from *Bombyx mori* silkworm [97, 98] or the coiled-coil leucine zipper motifs, which are capable to form dimers with other leucine zipper domains by both hydrophobic [99-101] and ionic interactions [102-104]. Contrary, chemical cross-linking mechanisms for ELRs-based hydrogels can involve chemical modifications, complementary reactive groups or enzymatically induced cross-linking [105, 106]. Thus, lysine-rich ELRs are the most widely used in the preparation of hydrogel networks due to the ability of the ε-amino group belonging to the side chains from lysines to form covalent bonds, which are useful for both crosslinking reactions between ELR chains and chemical modifications. Moreover, chemical crosslinking strategies present some important advantages. For instance, the covalent bonds are able to avoid hydrogel dilution and prevent the diffusion of the components from the implantation site.

By the design of ELRs compositions is possible modulating mechanical and self-assembly properties to adapt ELR-hydrogel to the final application. Moreover the recombinant nature of ELRs allow integrate in their sequence specific functionalities as bioactive domains to potentiate the hydrogel interaction with the tissues and, as a consequence, improve its integration [88, 107, 108], therapeutic action [109, 110], biodegradability [111-113], or biological triggers [114-116] within the host organism.

2.3.3.2 Fibers

ELRs can also form fibers with different diameters, when obtained by wet spinning or electrospinning [117, 118]. This technique consists on the application of a high voltage to a polymer solution in order to form fibers through a syringe [119, 120]. Furthermore, the electrospinning technique helps to develop tailor-made fiber scaffolds with tuneable porosity and orientation. Although the number of works involving ELR-based fibers is still limited, these materials have shown promising results in terms of cell viability and proliferation [90]. Thus, self-assembling fibers seem to have potential use for wound healing purposes and, in particular, dermal applications [121-123]. Moreover, bioactive sequences can be included. As instance, da Costa *et al*. have developed an ELR polymer fused to the antimicrobial peptide ABP-CM4 which not only showed high fibroblasts and keratinocytes cytocompatibility, but also notable antimicrobial effect against both Gram-positive and Gram-negative bacteria [124].

2.3.3.3 Micelles and nanoparticles

Taking advantage of both different nature of the components and the characteristic thermosensitivity of ELRs, it is possible to induce the formation of self-assembled nanoparticles. Thus, the hydrophobic component constitutes the inner core, whereas the corona is formed by the hydrophilic block. The hydrophobic core is responsible of the stability of the structure, whereas the hydrophilic corona takes part in the interaction with other molecules, cells, etc. One example of amphiphilic polymers is AB diblock polymer, with a considerable solubility difference between the two blocks [125, 126]. When the amphiphilic AB diblock is in a proper solvent for one block, an attractive and a repulsive force is generated thereby resulting in microphase separation and self-assembly of individual molecules into supramolecular structures [86]. Thus, self-assembly results in the formation of a spherical micelle consisting of a core formed by the insoluble block

and a hydrated corona composed of the soluble block, which shields the core from the solvent [126]. Self-assembling ability of amphiphilic ELRs block co-polymers is based on the fact that only one of these two forming blocks is able to self-assemble due to their different Tt and behavior under physiological conditions allow us to design amphiphilic constructs for drug encapsulation, especially of low solubility drugs, and gene or peptide delivery [127-130].

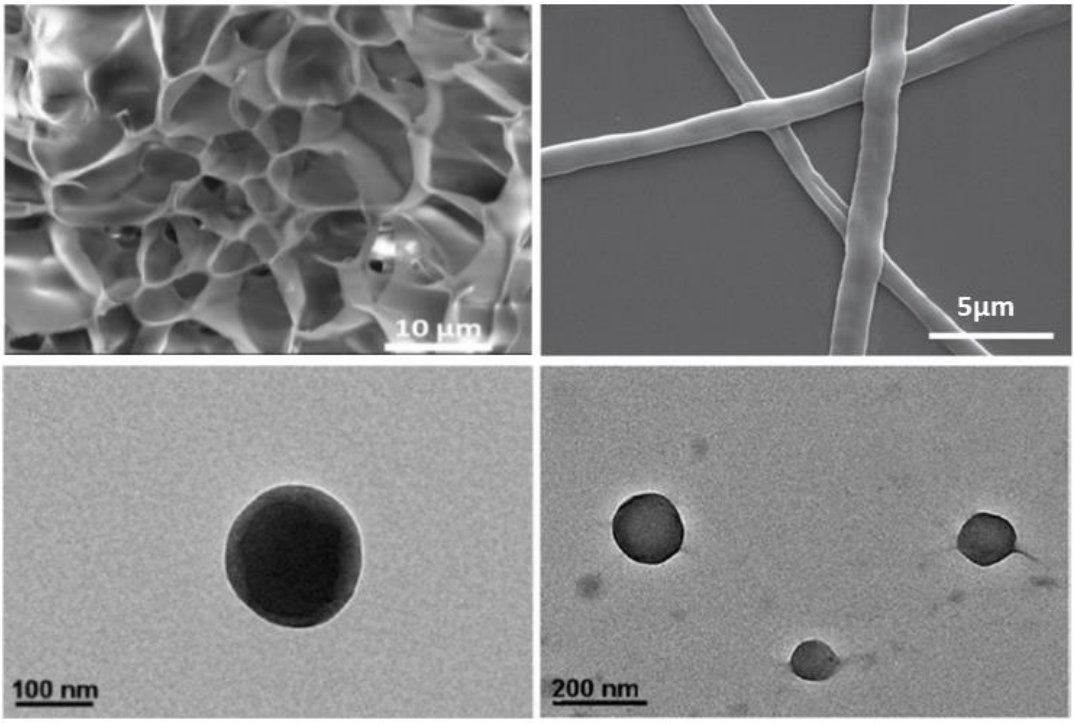

Figure 5. Amphiphilic ELR co-recombinamers can form different scaffolds due to their ability to self-assemble into multiple structures, such as porous hydrogels with an interconnected structure (Top left), stable fibers immersed in aqueous medium (Top right) and monodisperse micelles (Bottom left) or vesicles (Bottom right). Adapted from [92, 128, 131].

Depending on the length of the blocks, we can form other structures, such as cylindrical micelles, toroids, lamellar sheets or vesicles. Furthermore, other assemblies are based on tri-blocks [128, 132] and tetra-blocks [133] structures have been also studied for controlled delivery purposes. Thus, amphiphilic blocks polymers able to self-assemble into ordered structures have great interest in the development of new self-assembling devices for multiple applications in nanotechnology and biomedicine as therapeutic carriers in the nano and micro scale [86, 87, 126, 128].

The molecular weight of the ELR is directly related to the particle size [134]. Even though ELR-based nanoparticles usually show sizes in the range of 10 to 100 nm [135-137], microparticles have also been reported due to the temperature sensitivity and related agglomeration [138]. Several methods have been explored to stabilize ELR-based micelles, as the concentration of the ELR solution, which has a clear effect in the particle size [139], or the addition of surfactants, which can stabilize or destabilize the ELR particles [140]. Salt concentration is also critical, as stronger particles agglomeration can be achieved by the compensation of the charges of the hydrophilic blocks [135], and the pH affects the stability and size, depending on the chemical properties of the guest amino acid in the fourth position of the basic pentapeptide (VPGXG). Although the general shape of homogeneous micelles is round, it can be changed to cylindrical shapes by varying the architecture of the ELRs through the introduction of amphiphilic blocks of different sizes in the protein sequence [141]. Each ELR possesses one transition temperature, however, amphiphilic ELRs with different blocks long enough to develop their own intrinsic transition can show two temperature-induced transitions. Thus, the hydrophobic core is firstly rearranged and then, the second change is provoked by the collapse of the hydrophilic part, responsible for the coalescence, agglomeration and precipitation of the micelles [134]. The first change also corresponds with the exhibition of a cylindrical shape of the particles, the so-called critical micelle temperature (CMT). Moreover, reorganizations of the hydrophobic blocks have been demonstrated as the responsible mechanisms to change from micelles to vesicles. Here, vesicles could be obtained by increased length of the hydrophilic block or the addition of another hydrophilic block, thereby resulting in a triblock copolymer consisting on hydrophilic-hydrophobic-hydrophilic structure [128].

Therefore, ELRs with different transition temperatures can be developed for different medical devices, employed in multiple biomedical applications such as hydrogels for tissue engineering, surface biofunctionalization for coronary stents, tissue engineering or cell harvesting devices, and gene/vaccine/drug delivery systems [28, 73, 142-146].

2.4 Nanomedicine

As described above, ELRs are able to self-assemble and thereby form scaffolds with sizes at nano scale for biomedical applications. Nanomedicine combines nanotechnology,

biomedicine and pharmaceutical science. Thus, nanomedicine involves nanopharmaceutics, nanodevices for imaging purposes and theranostics. Although nanomedicine is relatively new, this research field evolves very fast and is becoming more and more used not only for biomedical applications, but also in many other fields of our dairy life. In particular, "nano" materials represent one of the most promising approaches for therapeutic purposes. According to the criteria from the Food and Drug Administration (FDA), nanodrugs are those products that range from 1 to 100 nm, and due to their small size and high surface area exhibit key differences compared to bulk materials or materials outside of this range that exhibit related dimension-dependent properties [147-149]. Thus, nanomedical devices include liposomes, dendrimers, polymer nanoparticles, micelles, nanocrystals, metals, other inorganic materials and proteins.

2.4.1 Interactions within the body

The options for the design and function of nanomaterials are hugely varied and the list of potential applications increases more and more, so current tendency points to tailor-made devices [150]. Nonetheless, it is important to notice that nanoparticle-based treatments are not miracle cures, as they still have challenges to overcome.

As instance, bioavailability is a typical challenge when developing a nanodevice [151, 152]. As the most important biological fluid, blood contains more than 3000 different proteins. Once injected in the bloodstream, nanoparticles interact with plasma proteins and, as a consequence, its surface is usually covered by various biomolecules (especially proteins) and the so-called corona is formed [153-155]. This adsorption of proteins not only alters the particle size, stability and surface properties [156, 157], but also affects its behavior and distribution within the body [158-160]. Even though the composition of the protein corona varies, it is well known that more abundant proteins first bind to nanoparticles surface and then the composition is changed during the circulation time [158]. Thus, non-specific interactions with serum proteins are one limiting factor in terms of circulation time. Opsonins are some of the corona-forming proteins and are recognized by reticuloendothelial systems (RES) and the mononuclear phagocyte system (MPS), leading to rapid blood clearance and high liver and spleen accumulation, so this could be an interesting strategy when needed target delivery to these organs [161-163]. On the

other hand, dysopsonins such as apolipoproteins and albumin, inhibit phagocytic uptake, increase blood circulation time [164-167]. Covering the nanoparticles surface with polymers such as polyethylene glycol (PEG) is the most used approach in order to develop long-circulating nanoparticles and therefore prevent rapid clearance, as pegylation reduces protein adsorption through hydrophilicity and steric repulsion effects thereby resulting in longer blood circulation time and lower accumulation in the liver [163, 168, 169]. Furthermore, it was demonstrated that increased density of PEG on the surface of gold nanoparticles can decrease the amount and change the types of the protein corona and reduce macrophage uptake *in vitro* [167].

Blood circulation time is directly related to the efficient extravasation of a nanoparticle. Thus, short blood circulation half-life may be sufficient for tissues with relatively large blood flow. Contrary, , longer circulation half-lives are necessary to progressively extravasate in poorly perfused tissues [170]. Moreover, nanoparticles biodistribution within the body is dramatically affected by their size. . Thus, nanoparticles smaller than 10 nm are cleared by renal filtration [163]. Contrary, it is well known that molecules bigger than 100 nm are accumulated in the liver, which is one of the most problematic side effects of current drugs [171]. Different sizes of nano-devices are proper for overcoming biological barriers and achieving their target. As instance, 11–30 nm size nanoparticles are suitable for liver and brain, whereas nanodevices with 31–80 nm diameter are appropriate for lungs, tumors and inflamed tissue [172]. Therefore, nanoparticles between 10 and 100 nm are preferred due to their accurate accumulation and effect in desired tissues and organs.

2.4.2 Nanoparticles entry into the cells

Once described the importance of nanotechnology in current and future medicine and the interactions involving nanodevices in the whole organism, it is essential to understand how nanoparticles enter into the cells in order to modulate different intracellular processes [173].

Cell membrane protects intracellular organelles from the environment. Also, cell membrane plays additional roles: regulates cell homeostasis, provides physical support and control the bidirectional flow of any molecule, from ions to nutrients [174]. The cell

membrane is composed by an amphiphilic phospholipid bilayer with incrusted receptors, channels and transporters. When a nanoparticle is developed, interaction between cell membrane and the nanocarrier has to be taken in consideration [175, 176]. Thus, depending on the physicochemical features of the nanoparticle, its entry occurs by different ways.

When a nanoparticle interacts with the cell membrane, it enters into the cell in a process called endocytosis. Depending on the cell type and the endocytic mechanism, we can classify endocytosis in five types: phagocytosis, clathrin-mediated endocytosis, caveolae-mediated endocytosis, clathrin/caveolae-independent endocytosis and micropinocytosis [177, 178].

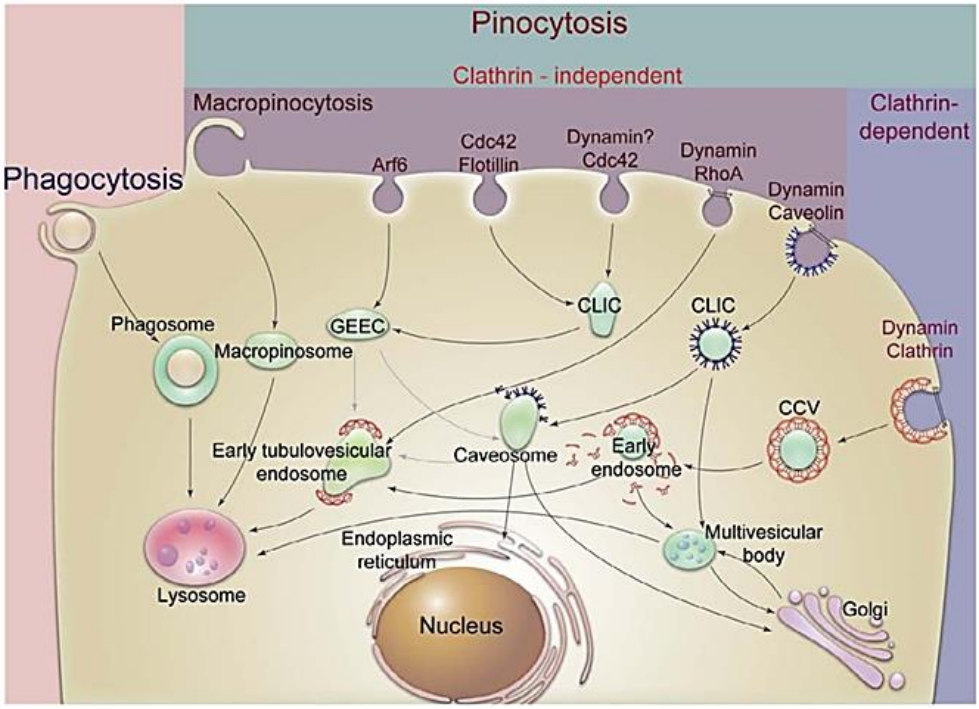

Figure 6. The different pathways for cell internalization. First, large particles can be taken up by phagocytosis, especially at monocytes, macrophages and dendritic cells. Contrary, fluid uptake occurs by macropinocytosis. The rest of particles are internalized via clathrin or caveolin-mediated endocytosis, which derive from the plasma membrane, and are released to early endosomes. CCV: clathrin coated vesicles; CLIC: clathrin-independent carriers; GEEC: GPI-anchored protein enriched early endosomal compartment; MVB: multivesicular body. Reproduced from [173].

2.4.2.1 Phagocytosis

Phagocytosis is realized by phagocytic cells, such as macrophages, dendritic cells and monocytes, whose main role consists on host defense [179]. Phagocytosis starts by opsonization of the nanoparticle at the blood torrent and consists on the binding of different proteins (opsonins, immunoglobulins, complement proteins) to the surface. Thus, when the nanoparticle reaches the cell membrane, the opsonins attached to the nanoparticle corona are recognized by specific receptors by ligand-receptor interactions. Then, a signaling pathway is triggered and the nanoparticle is engulfed into the phagosome. Even though there is no general law about which types of nanoparticles is more likely phagocytosed, it is said that nanodevices larger than 200 nm undergo this type of endocytosis [180].

2.4.2.2 Clathrin-mediated endocytosis

Clathrin-mediated endocytsosis is the most common mechanism for nutrients caption by cells and occurs in those areas rich in clathrin [181]. In fact, this mechanism is present in all mammalian cells. Cholesterol and iron entry into the cells via Low Density Lipoprotein (LDL) and transferrin receptors, respectively, are classical examples of clathrin-mediated endocytosis. Moreover, clathrin has been proposed as a stabilizator component of the membrane curvature [182]. This process consists on the formation of invaginations in the cell membrane. Furthermore, adaptor and accessory proteins, such as AP-2, AP-180, Eps15 or intersectin help in order to generate this membrane deformation [183, 184]. Thus, vesicles of between 100 and 150 nm size are invaginated and their content is released in lysosomes [185].

2.4.2.3 Caveolae-mediated endocytosis

Caveolae-mediated endocytosis is another type of endocytosis and has a key role in many cellular processes, such as regulation of lipids and fatty acids, or cell signaling. Also, this endocytic mechanism is absent in leukocytes and neurons, and contrary is enhanced in muscle, fibroblasts, adipocytes and endothelial cells. Caveolae are membrane areas rich in cholesterol, also known as lipid rafts, where caveolin protein is present [186]. Even though caveolin presence is critical for caveolae formation, other proteins are involved, such as SNAP and VAMP2 [187, 188]. Caveolae-mediated invaginations are formed by

caveolin dimers and have a size of 50-80 nm [189]. This mechanism has been involved in some diseases, such as cancer and diabetes, and is deeply studied as an entry route used by pathogen agents. Cholera toxin B is the typical example of caveolae-mediated endocytosis. Moreover, this route is slower than clathrin-mediated endocytosis and is preferred for specific delivery in cell nucleus [173].

2.4.2.4 Clathrin/caveolae-independent endocytosis

Clathrin and caveolae-independent endocytosis only occurs in special cases, when a specific composition without clathrin and caveolae is required [173]. This is the case of interleuking-2 and growth hormones [190, 191]. Also, folic acid is internalized by this mechanism [174]. Different effectors are present in clathrin/caveolae independent endocytosis, such as flotilin, Cdc42, Arf6 or RhoA, and it is proposed that these internalization pathways to require specific lipid composition, specially cholesterol, and are able to form 90 nm size vesicles [192, 193].

2.4.2.5 Macropinocytosis

Macropinocytosis is a different pathway, as it does not involve lipid rafts or proteins. In fact, this entry mechanism is formed by big vesicles, the so-called macropinosomes, of 0.2-10 µm after a rearrangement of the cytoskeleton, which is then fused to the cell membrane [194]. This mechanism is started by activation of tyrosine kinases receptors, which trigger a signaling pathway and changes in the cytoskeleton. Therefore, membrane is able to engulf nutrients-rich extracellular fluid [195]. Even though this mechanism is only used by cells in order to gulp extracellular fluid, it is present in other physiologic processes, as antigen presentation [196]. Moreover, some bacteria are able to provoke micropinocytosis in order to enter into host cells [197].

2.4.3 Nanoparticles features and their effect in cell internalization

It is well known that physicochemical features of nanoparticles have an important role in terms of determination of interactions with cells surface. Thus, nanoparticles entry into the cell can be affected by different factors, such as size, shape and surface charge. Moreover, different cell entry mechanism can be preferred depending on the cargo, so all

these parameters can be modulated in order to reach the best cell compartment for the delivery.

2.4.3.1 Size

The size of nanoparticles is directly related to the mechanism by which the entry into the cell is achieved [198, 199]. Larger particles (up to 10 µm) enter by phagocytosis, whereas particles smaller than 1 µm are endocytosed by non-phagocytosis mechanisms [179]. Moreover, clathrin-mediated endocytosis is the preferred pathway for nanoparticles of less than 200 nm [181]. Contrary, nanoparticles with a size between 200 and 500 nm are likely entered by caveolae-mediated endocytosis [186]. Very small nanoparticles, smaller than 25 nm, are internalized by clathrin/caveolae-independent endocytosis [173].

2.4.3.2 Shape

Moreover, nanoparticles shape is other factor affecting cellular uptake [199]. Thus, some studies have determined a comparison between rod-shaped and spherical nanoparticles. At light of the results, spherical nanocarriers seemed to be internalized faster than rod-shaped ones. Chitrani *et al*. concluded that membrane wrapping time is longer for rod-shaped compared to spherical nanoparticles [200]. Moreover, Qiu *et al*. pointed to the different number of available receptors depending on the shape, due to the increased surface area of rod-shaped nanoparticles [201]. Related to these results, Herd *et al*. demonstrated that spherical nanoparticles are likely endocytosed by clathrin-mediated mechanisms, whereas worm-shaped devices are internalized by micropinocytosis and phagocytosis, probably due to the fact that worm shape is too long for clathrin vesicles [202].

2.4.3.3 Surface charge

Surface charge is a critical parameter and plays an important role regarding nanoparticles internalization, due to the electrostatic interactions between nanoparticles surface and the cell membrane [199, 203]. Literature describe that charged nanoparticles show improved uptake when compared to nanoparticles with neutral surface charge [204] and furthermore anionic and neutral nanoparticles are only internalized by endocytic mechanisms. Although positive nanoparticles are thought to have stronger interactions with negatively charged cell membrane, cationic nanoparticles present some

disadvantages compared to anionic ones [205]. Thus, cationic nanoparticles generate holes and other disrupting processes in cell membrane, and as a consequence involved higher cytotoxicity [206]. Moreover, positively charge nanoparticles possess short circulation half-life in the blood torrent, as they suffer opsonisation and clearance [207, 208]. This is an important parameter, as the success of a drug delivery system is directly related to high circulation times and bioavailability.

2.4.4 Intracellular trafficking

Once internalized into the cells, intracellular trafficking determines the fate and therapeutic accuracy of nanoparticles [209]. After endocytosed, nanoparticles end up at a complex formed by endosomes, lysosomes Golgi apparatus and endoplasmic reticulum [210]. Endosomes are intracellular compartments produced by plasmatic membrane and can be sorted into three types: early endosomes, recycling endosomes and late endosomes (also known as multivesicular bodies or MVB) [211, 212]. The intracellular trafficking can be described as a journey composed by several steps. First, endocytic vesicles are fused to early endosomes [213]. The cargo from endocytic vesicles remains inside early endosomes, which mature until become late endosomes [214]. Also, a minor part of the cargo can be removed in the recycling endosomes, small vesicles that remove their cargo to the plasmatic membrane [215]. Then, late endosomes fuse with lysosomes, where multiple degradative enzymes act [212]. It is important to mention that internalized nanoparticles can escape from this pathway and be released into the cytoplasm [216]. Thus, escape mechanisms are used in nature by multiple viruses and pathogen agents and are becoming more studied in different biomedical fields [217]. Moreover, this approach could have potential applications for accurate delivery of therapeutic agents in order to modulate cell processes in the cytoplasm.

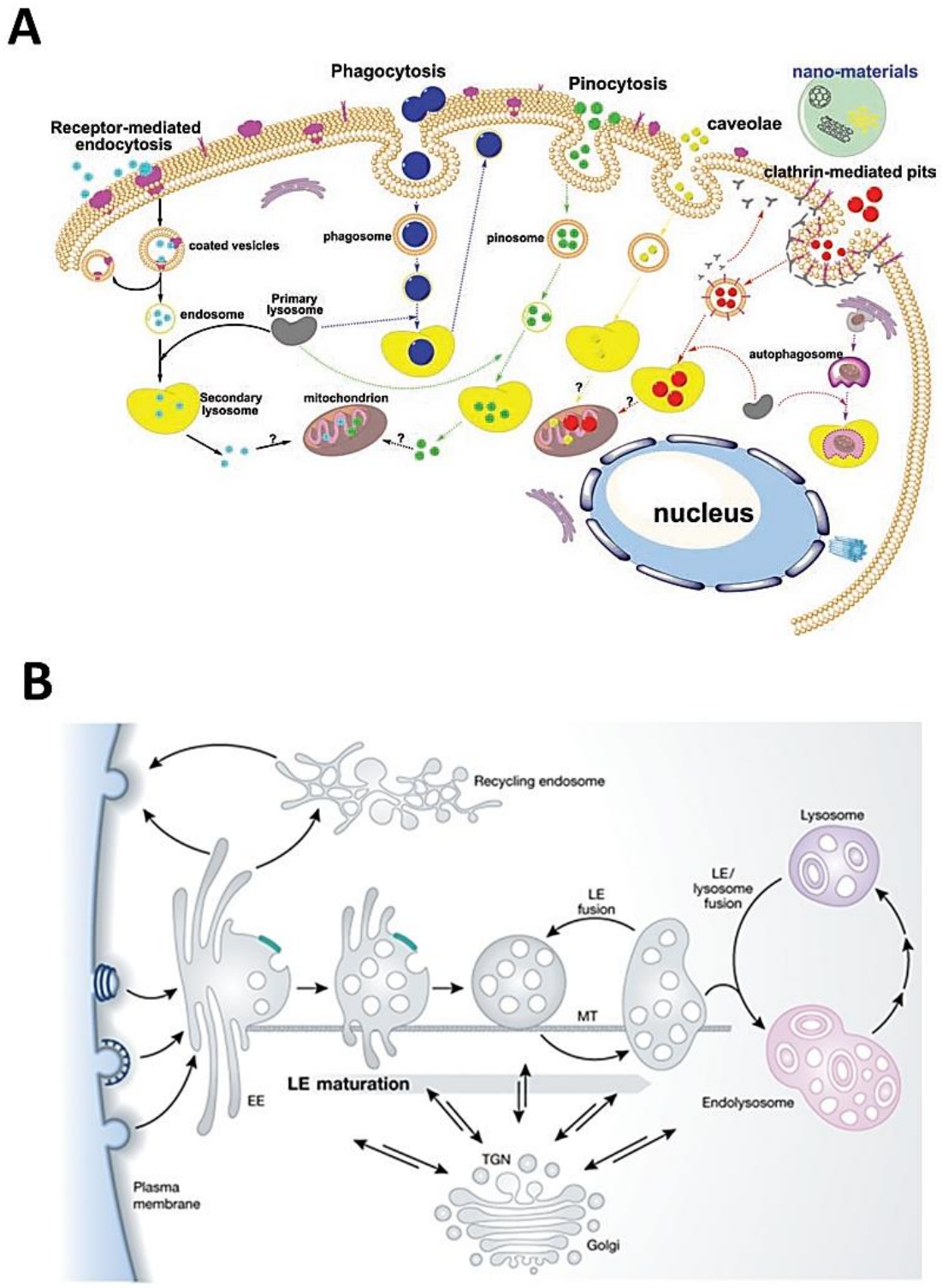

Figure 7. A: The intracellular trafficking for endocytosed nanoparticles. B: The endosome/lysosome system. The primary endocytic vesicles deliver their content and their membrane to EEs in the peripheral cytoplasm. The fusion of an endosome and a lysosome generates the endolysosome, a hybrid organelle in which active degradation takes place. Then, the endolysosome is converted to a classical dense lysosome, a major storage compartment for lysosomal degradative hydrolases. Adapted from [209, 212].

2.4.5 Applications of nanotechnology

2.4.5.1 Vaccines

The term vaccination is referred to the administration of dead or attenuated pathogens in order to mimic the immune response that would be induced by an active infection in the host [218]. One of the advantages of vaccination is the avoiding of the undesirable effects of disease. However, the natural infection with the pathogenic organism is the most potent and lasting immune response in a host, as all the antigens from the pathogen are present, inducing thereby both innate and adaptive immune responses [219]. In vaccination with live or attenuated pathogens all the antigens are present but these vaccines show virulence. Moreover, traditional vaccines based on live or attenuated pathogens possesses disadvantages in terms of storage or durability [220, 221].Therefore, the immune response induced by this strategy is less potent, as the organisms cannot replicate in the host, and multiple doses are needed [222].

DNA vaccines based on genetic sequences coding for antigens from the pathogen, especially surface proteins, were thought as an interesting approach with no side effects and able to produce large amounts of antigen by recombinant techniques.

2.4.5.1.1 DNA vaccines

Over the years, new approaches have been thought for mimicking the structure of pathogen organisms. Genetic engineering has been used for the development of nude plasmid DNA vaccines and recombinant proteins which could induce immune responses [223]. Thus, genetic sequence coding for epitopes are synthesized, inserted into vectors and then used for immunization. The principle of DNA vaccination consists on the injection of bacterial-derived plasmids coding for immunogenic peptides controlled by eukaryotic promoters [224]. Thus, host cells produced the foreign antigen, which is presented to the host immune system after post translational modifications. In this promising immunization approach, vaccines are easily designed and, as plasmids do not involve immune responses, are safe [225], as there is no manipulation of infective antigens and immune responses elicited against nucleic acid backbones are weak. Importantly, they are also easy and cheap to produce. On the other hand, immune responses are only developed against antigens coded in the developed plasmid, so we can

therefore easily differentiate vaccinated animals from infected ones [225]. Recombinant DNA technology also allows us to combine several antigens or targeting systems.

Furthermore, DNA vaccines are administered by intramuscular injections, so muscle cells are transfected and express the immunogenic protein [224]. Finally, as the antigen is produced by host cells, the immune response mimics that generated by natural infection presenting with both cellular and humoral responses [220]. This fact has great importance important when working with persistent infections, which are based on cell-mediated immunity. Innate responses are also stimulated, since plasmids contain molecular elements such as unmethylated CpG motifs that are not prevalent in mammal, avian and fish cells [226].

Although many studies are performed in small animal models, there are also examples of DNA vaccination in large animals [227, 228]. Another advantage of DNA vaccination is that it is generally well tolerated by the injected animals. Thus, most of the plasmids stay at the injection site for several weeks after an intramuscular administration [229-231]. Contrary, a minor amount of the plasmids is detected in the blood and other organs [232, 233].

DNA vaccination has been also exposed to criticisms, such as the risk of integration of the injected nucleic acid into the host genome. However, Faurez *et al.* demonstrated that the frequency of integration was lower than the frequency of spontaneous mutation [234]. Another typical criticism for DNA vaccination is their low efficacy, in terms of the large amounts of injected DNA needed to get a strong response in the host. Different strategies are being developed for producing better responses with reduced amounts of DNA. Thus, plasmids based on replicon from alphaviruses not only are able to produce more antigen but also trigger other innate mechanisms that may play a role in protection [235, 236]. This strategy has also shown promising results with PRV [237] and goatpox [238].

2.4.5.1.2 ELRs as vaccine delivery systems

Different materials consisting on stimuli-responsive polymers have been proposed as self-assembling nanodevices. ELRs are one of such biomaterials able to reversibly self-assemble under determined conditions. Moreover, ELRs can be bioproduced in an easily

scale up process, one interesting advantage regarding the manufacturing of vaccines. ELRs have been widely reported as absolute biocompatible biomaterials [239], which means that ELR-based vaccines would be innocuous for the host and any immune response would be due to the immunogenic component. The recombinant origin of ELRs allows us to modulate their features, such as size, morphology and biofunctional behavior, so ELRs could enhance low immunogenicity of some antigens.

Although there are many works describing ELRs as successful approaches for gene and drug delivery involving multiple diseases, there is only few works in which ELRs are thought as part of vaccines. Thus, the authors produced a fusion protein composed of an ELR and two major antigens from *M. tuberculosis*, ESAT-6 and Ag85B, in a plant [240]. In this work, the fusion protein did not show efficient release of the antigen and liposomal adjuvants were needed. However, the humoral immune response showed low intensity and short duration. Thus, the ELR helped the production of the fusion protein but did not improve the immunogenicity of the bacterial antigens. Garcia-Arevalo *et al*. also developed a fusion protein composed by an ELR block and an antigen from *M. tuberculosis*, Ag85 [136]. In this work, the authors studied if an amphiphilic ELR could be a suitable vaccine carrier for immunogenic peptide antigens. Above the transition temperature (15°C), the ELR backbone self-assembled into highly monodisperse nanoparticles of 60 nm diameter and enlarged the half-life of the bacterial antigen. On the other hand, the ELR carrier was innocuous. Furthermore, *in vivo* immune challenge showed a biphasic immune response in a mouse model, characterized by a first innate-immune phase with early secretion of cytokines and a subsequent adaptive-immune Th-2 response, which showed IL-5 production and upregulated IgM and IgG-mediated immune responses.

2.4.5.2 Cancer

Cancer has reached pandemic dimensions in the whole world. Cancer is a general term for a large group of diseases, whose causes, characteristics and occurrence can vary. All of them are characterized by the development of abnormal cells that divide uncontrollably and have the ability to infiltrate and destroy normal body tissue. Therefore, current therapeutic strategies against cancer are based on early diagnosis as well as personalized medicine. Although the administration of free chemotherapeutic drugs remains as the

gold standard for cancer treatment, this therapeutic strategy still presents inherent challenges. One of the most important problems of current medicine resides in the lack of specific treatments and poor drug accumulation in the tumors [241]. As a consequence, undesired side effects in healthy tissues occur, especially in the heart [242], bone marrow [243], gastrointestinal tract [244], and nervous system [245]. Cancer is characterized by aberrant cell proliferation compared to normal cell growth and novel branched vasculature. For all these reasons drug accumulation within the tumors is really poor. Although drug delivery approaches have been explored for diverse diseases, cancer is undoubtedly the main target of drug delivery research [170, 246]. According to NIH, there are 110 clinical trials involving nowadays the application of nanotechnology for cancer treatments [247]. The development of accurate drug delivery systems is a promising strategy in order to improve the selective action of unspecific drugs and, in fact, some of the most encapsulated drugs in novel nanodevices are clinical chemotherapeutic agents, as doxorubicin, paclitaxel and docetaxel [248-250]. This fact is due not only to the high incidence of the disease, but also because tumors present a characteristic physiology which is a huge challenge for biomedical research and demands therapeutic agents to have special features. Thus, nanotechnology has explored over the past several decades different approaches in order to achieve better encapsulation devices, such as liposomes, nanoparticles, micelles or dendrimers [251-254]. Furthermore, some of these promising nanodevices have been used in clinical trials. In fact, the chemotherapeutic drug doxorubicin, which is currently used for treatment of breast cancer among others, is administered with liposomal nature.

As most clinically used chemotherapeutic agents are highly hydrophobic, drug encapsulation inside nanocarriers allow us to achieve higher concentrations within tumor cells [250, 255, 256]. Furthermore, cancer cells are characterized by higher expression of multiple proteins, not only cytoplasmic proteins but also anchored receptors to cell membrane. These cancer markers have huge interest, as we can use different targets depending on the type of tumor and we can even differentiate primary tumors from distance metastasis [257]. Nanoparticles surface can therefore be decorated with molecules as targeting systems in order to specifically drive these devices to cancer cells and thereby avoid undesired effects in healthy cells. Thus, nanotechnology can take

advantage of cancer markers in order to develop advanced nanocarriers that allow us to achieve personalized biomedical therapeutics.

2.4.5.2.1 Enhanced permeability and retention (EPR) effect

As explained above, poor drug accumulation is one of the most important failures of current chemotherapeutic agents [258]. As a consequence, effective clinical therapies require higher drug concentrations and larger treatment times in order to reach real cytotoxic effect in cancer cells [259]. However, this approach provokes severe side effects in healthy tissues in patients, such as liver, kidneys, spleen or heart. Thus, Matsumura and Maeda proposed the Enhanced Permeability and Retention (EPR) effect in 1986 as a potential tool to be taken into account when designing therapeutic nanodevices for anti-cancer purposes [260]. This revolutionary discovery was based on the unique architecture of novel blood vessels formed within the tumors. Due to their fast growth, cancer cells have higher requirements of nutrients and oxygen [261]. In order to meet these demands, tumor neoangiogenesis is enhanced. However, these novel vasculature has abnormal architecture and form. Thus, novel blood vessels present multiple defects, such as poorly aligned endothelial cells with wide fenestrations, poor smooth muscle layer, wider lumen, lack of effective lymphatic drain system and multi-branch architecture [262]. All these factors, as well as high production of vascular permeability factors that stimulate extravasation, involve much more accumulation of macromolecules within the tumors compared to normal tissues [263, 264].

However, although EPR has been demonstrated to enhance nanoparticles accumulation inside the tumors, this fact is not enough for accurate activity of this kind of cancer therapeutics, so active targeting systems have a clear potential in order to achieve acceptable effectiveness [259]. Therefore, multiple molecules have been used for specifically drive nanocarriers to cancer cells, such as DNA aptamers, RNA aptamers, peptides, antibody fragments, etc.

2.4.5.2.2 ELRs for cancer

Due to their biocompatibility and thermoresponsive behavior, ELRs are an interesting choice for cancer treatment, as this is one biomedical application where prolonged local

drug exposure not only can significantly increase therapeutic efficacy but also avoid undesired toxicity in healthy tissues [107, 143].

Thus, several approaches have been explored over the years. Due to the fact that ELRs assembly can be induced by charge effects, ionic interactions between the ELR chain and the cargo can produce nanodevices. As an example, polyplexes formed by positively charged ELR and condensed negatively charged DNA trigger intracellular delivery of therapeutic gene delivery. Piña *et al*. demonstrated the significantly decreased toxicity of the ELR carrier, when compared to PEI, and the potential use of ELR-based polyplexes for gene delivery to cancer cells [265].

A second approach consists on conjugated chemotherapeutic drugs to ELRs. For example, conjugation of doxorubicin, through a pH-sensitive hydrazone bond, allowed the release of drug from the macromolecular carrier. Moreover, the length of the pH-labile drug linker the pH-sensitive allowed to modulate the release rate of the drug [266, 267]. Such pH-labile drug linker enabled the release of the drug in acidic endosomal compartments in the cell cytoplasm. These ELR–doxorubicin complexes exhibited long half-life, good blood circulation time and significant accumulation in subcutaneous tumors in mice [127].

Taking advantage of the tailored Tt of ELRs, other research approach has explored the difference between body temperature (37°C) and the characteristic tumor hyperthermia (42°C) [268]. This strategy allows polymers to increase intratumoral accumulation by leading the aggregation of systemically administered ELRs to the heated tumor [269, 270]. The reversible temperature-dependent self-assembling of ELRs also allows the rapid dissolution of ELR aggregates within the tumoral vasculature upon cessation of hyperthermia. As a consequence, the temperature-triggered self-assembling of ELRs provides enhanced tumor accumulation compared to soluble ELRs that have their Tt above this temperature range [271, 272].

2.5 References

[1] N.A. Peppas, R. Langer. New challenges in biomaterials. Science, 1994. 263 (5154):1715-1720.

[2] D.F. Williams. On the nature of biomaterials. Biomaterials, 2009. 30 (30):5897-5909.
[3] D.F. Williams. To engineer is to create: the link between engineering and regeneration. Trends Biotechnol, 2006. 24 (1):4-8.
[4] B.V. Slaughter, *et al.* Hydrogels in regenerative medicine. Advanced Materials, 2009. 21 (32-33):3307-3329.
[5] J.A. Wolff, D.B. Rozema. Breaking the bonds: non-viral vectors become chemically dynamic. Molecular Therapy, 2008. 16 (1):8-15.
[6] A.S. Hoffman. The origins and evolution of "controlled" drug delivery systems. Journal of Controlled Release, 2008. 132 (3):153-163.
[7] A.C. Rice-Ficht, *et al.* Polymeric particles in vaccine delivery. Curr Opin Microbiol, 2010. 13 (1):106-112.
[8] T. Jamieson, *et al.* Biological applications of quantum dots. Biomaterials, 2007. 28 (31):4717-4732.
[9] J. Pan, S.S. Feng. Targeting and imaging cancer cells by folate-decorated, quantum dots (QDs)- loaded nanoparticles of biodegradable polymers. Biomaterials, 2009. 30 (6):1176-1183.
[10] S.V. Murphy, A. Atala. 3D bioprinting of tissues and organs. Nat Biotechnol, 2014. 32 773.
[11] S. Salinas-Fernandez, *et al.* Genetically engineered elastin-like recombinamers with sequence-based molecular stabilization as advanced bioinks for 3D bioprinting. Applied Materials Today, 2020. 18
[12] Z.S. Wu, *et al.* A hairpin aptamer-based electrochemical biosensing platform for the sensitive detection of proteins. Biomaterials, 2009. 30 (15):2950-2955.
[13] M. Pierna, *et al.* Efficient cell and cell-sheet harvesting based on smart surfaces coated with a multifunctional and self-organizing elastin-like recombinamer. Biomacromolecules, 2013. 14 (6):1893-1903.
[14] J. Reguera, *et al.* Nanopore formation by self-assembly of the model genetically engineered elastin-like polymer [(VPGVG)2(VPGEG)(VPGVG)2]15. Journal of American Chemical Society, 2004. 126 (41):13212-13213.
[15] N. Huebsch, D.J. Mooney. Inspiration and application in the evolution of biomaterials. Nature, 2009. 462 (7272):426-432.
[16] J.M. Aamodt, D.W. Grainger. Extracellular matrix-based biomaterial scaffolds and the host response. Biomaterials, 2016. 86 68-82.
[17] M.P. Nikolova, M.S. Chavali. Recent advances in biomaterials for 3D scaffolds: A review. Bioact Mater, 2019. 4 271-292.
[18] M.P. Staiger, *et al.* Magnesium and its alloys as orthopedic biomaterials: a review. Biomaterials, 2006. 27 (9):1728-1734.
[19] G. Yang, *et al.* Bioactive calcium sulfate/magnesium phosphate cement for bone substitute applications. Materials Science & Engineering: C 2014. 35 70-76.
[20] R. Zhang, P.X. Ma. Porous poly(L-lactic acid)/apatite composites created by biomimetic process. J Biomed Mater Res, 1999. 45 (4):285-293.
[21] I. Denry, J.R. Kelly. Emerging ceramic-based materials for dentistry. J Dent Res, 2014. 93 (12):1235-1242.
[22] J.G. Hardy, J.Y. Lee, C.E. Schmidt. Biomimetic conducting polymer-based tissue scaffolds. Curr Opin Biotechnol, 2013. 24 (5):847-854.
[23] J. Hu, *et al.* Porous nanofibrous PLLA scaffolds for vascular tissue engineering. Biomaterials, 2010. 31 (31):7971-7977.
[24] Z. Pan, J. Ding. Poly(lactide-co-glycolide) porous scaffolds for tissue engineering and regenerative medicine. Interface Focus, 2012. 2 (3):366-377.
[25] L.S. Nair, C.T. Laurencin. Polymers as biomaterials for tissue engineering and controlled drug delivery. Adv Biochem Eng Biotechnol, 2006. 102 47-90.
[26] D. Chow, *et al.* Peptide-based biopolymers in biomedicine and biotechnology. Materials Science & Engineering Reports, 2008. 62 (4):125-155.

[27] A. Altunbas, D.J. Pochan. Peptide-based and polypeptide-based hydrogels for drug delivery and tissue engineering. Top Curr Chem, 2012. 310 135-167.
[28] A. Girotti*, et al.* Recombinant technology in the development of materials and systems for soft-tissue repair. Adv Healthc Mater, 2015. 4 (16):2423-2455.
[29] S.M. Choi*, et al.* Advances in protein-based materials: From origin to novel biomaterials. Adv Exp Med Biol, 2018. 1078 161-210.
[30] L. Debelle, A.J. Alix. The structures of elastins and their function. Biochimie, 1999. 81 (10):981-994.
[31] A.M. Tamburro, B. Bochicchio, A. Pepe. The dissection of human tropoelastin: from the molecular structure to the self-assembly to the elasticity mechanism. Pathol Biol (Paris), 2005. 53 (7):383-389.
[32] S.G. Wise, A.S. Weiss. Tropoelastin. International Journal of Biochemistry & Cell Biology, 2009. 41 (3):494-497.
[33] D.W. Urry. Entropic elastic processes in protein mechanisms. I. Elastic structure due to an inverse temperature transition and elasticity due to internal chain dynamics. J Protein Chem, 1988. 7 (1):1-34.
[34] M. Halm*, et al.* Visualizing tropoelastin in a long-term human elastic fibre cell culture model. Sci Rep, 2016. 6 20378.
[35] P.A. Jones, T. Scott-Burden, W. Gevers. Glycoprotein, elastin, and collagen secretion by rat smooth muscle cells. PNAS, 1979. 76 (1):353-357.
[36] G.C. Sephel, J.M. Davidson. Elastin production in human skin fibroblast cultures and its decline with age. J Invest Dermatol, 1986. 86 (3):279-285.
[37] K. Madsen*, et al.* Synthesis of proteoglycans, collagen, and elastin by cultures of rabbit auricular chondrocytes--relation to age of the donor. Dev Biol, 1983. 96 (1):63-73.
[38] R.P. Mecham*, et al.* Elastin production by cultured calf pulmonary artery endothelial cells. J Cell Physiol, 1983. 116 (3):282-288.
[39] A. Hinek, M. Rabinovitch. 67-kD elastin-binding protein is a protective "companion" of extracellular insoluble elastin and intracellular tropoelastin. J Cell Biol, 1994. 126 (2):563-574.
[40] J. Uitto. Biochemistry of the elastic fibers in normal connective tissues and its alterations in diseases. J Invest Dermatol, 1979. 72 (1):1-10.
[41] E.C. Davis. Stability of elastin in the developing mouse aorta: a quantitative radioautographic study. Histochemistry, 1993. 100 (1):17-26.
[42] S.M. Mithieux, A.S. Weiss. Elastin. Adv Protein Chem, 2005. 70 437-461.
[43] D.V. Bax*, et al.* Cell adhesion to tropoelastin is mediated via the C-terminal GRKRK motif and integrin alphaVbeta3. J Biol Chem, 2009. 284 (42):28616-28623.
[44] J. Rosenbloom, W.R. Abrams, R. Mecham. Extracellular matrix 4: the elastic fiber. Faseb Journal, 1993. 7 (13):1208-1218.
[45] D.W. Urry. Characterization of soluble peptides of elastin by physical techniques. Methods Enzymol, 1982. 82 Pt A 673-716.
[46] D.W. Urry*, et al.* Temperature-correlated force and structure development in elastomeric polypeptides: the Ile1 analog of the polypentapeptide of elastin. Biopolymers, 1986. 25 (10):1939-1953.
[47] V. Guantieri*, et al.* Conformational studies on polypeptide models of collagen. Poly(Gly-Pro-Val), poly(Gly-Pro-Met), poly(Gly-Val-Pro) and poly(Gly-Met-Pro). Int J Pept Protein Res, 1987. 29 (2):216-230.
[48] A.M. Tamburro*, et al.* Synthetic fragments and analogues of elastin. II. Conformational studies. Biopolymers, 1990. 29 (4-5):855-870.
[49] A.M. Tamburro*, et al.* Polypeptide models of elastin: CD and NMR studies on synthetic poly(X-Gly-Gly). Chirality, 1991. 3 (4):318-323.

[50] H. Reiersen, A.R. Clarke, A.R. Rees. Short elastin-like peptides exhibit the same temperature-induced structural transitions as elastin polymers: implications for protein engineering. J Mol Biol, 1998. 283 (1):255-264.
[51] N. Annabi, *et al.* Synthesis of highly porous crosslinked elastin hydrogels and their interaction with fibroblasts in vitro. Biomaterials, 2009. 30 (27):4550-4557.
[52] J.F. Almine, *et al.* Elastin-based materials. Chem Soc Rev, 2010. 39 (9):3371-3379.
[53] A. Bandiera, P. Sist, R. Urbani. Comparison of thermal behavior of two recombinantly expressed human elastin-like polypeptides for cell culture applications. Biomacromolecules, 2010. 11 (12):3256-3265.
[54] G. Ciofani, *et al.* Human recombinant elastin-like protein coatings for muscle cell proliferation and differentiation. Acta Biomater, 2013. 9 (2):5111-5121.
[55] F. Boccafoschi, *et al.* Human elastin polypeptides improve the biomechanical properties of three-dimensional matrices through the regulation of elastogenesis. Journal of Biomedical Materials Research Part A, 2015. 103 (3):1218-1230.
[56] A. Girotti, *et al.* Elastin-like recombinamers: biosynthetic strategies and biotechnological applications. Biotechnol J, 2011. 6 (10):1174-1186.
[57] J.C. Rodriguez-Cabello, *et al.* Synthesis of genetically engineered protein polymers (recombinamers) as an example of advanced self-assembled smart materials. Methods in Molecular Biology, 2012. 811 17-38.
[58] D.W. Urry. Molecular perspectives of vascular wall structure and disease: the elastic component. Perspect Biol Med, 1978. 21 (2):265-295.
[59] D.S. Hart, S.H. Gehrke. Thermally associating polypeptides designed for drug delivery produced by genetically engineered cells. J Pharm Sci, 2007. 96 (3):484-516.
[60] J.C. Rodriguez-Cabello, *et al.* Elastin-Like polymers: properties, synthesis and applications. Encyclopedia of Polymer Science and Technology: John Wiley &Sons; 2017. p. 1-36.
[61] D.W. Urry. Molecular Machines: How Motion and Other Functions of Living Organisms Can Result from Reversible Chemical Changes. Angewandte Chemie International Edition, 1993. 32 (6):819-841.
[62] J.C. Rodriguez-Cabello, *et al.* Biofunctional design of elastin-like polymers for advanced applications in nanobiotechnology. J Biomater Sci Polym Ed, 2007. 18 (3):269-286.
[63] C.M. Venkatachalam, D.W. Urry. Development of a linear helical conformation from its cyclic correlate. β-Spiral model of the elastin poly(pentapeptide) (VPGVG)n. Macromolecules, 1981. 14 (5):1225-1229.
[64] A. Girotti, *et al.* Influence of the Molecular Weight on the Inverse Temperature Transition of a Model Genetically Engineered Elastin-like pH-Responsive Polymer. Macromolecules, 2004. 37 (9):3396-3400.
[65] D.E. Meyer, A. Chilkoti. Quantification of the effects of chain length and concentration on the thermal behavior of elastin-like polypeptides. Biomacromolecules, 2004. 5 (3):846-851.
[66] A. Ribeiro, *et al.* Influence of the amino-acid sequence on the inverse temperature transition of elastin-like polymers. Biophys J, 2009. 97 (1):312-320.
[67] D.W. Urry, *et al.* Mechanochemical coupling in synthetic polypeptides by modulation of an inverse temperature transition. PNAS, 1988. 85 (10):3407-3411.
[68] B. Li, V. Daggett. The molecular basis of the temperature- and pH-induced conformational transitions in elastin-based peptides. Biopolymers, 2003. 68 (1):121-129.
[69] D.W. Urry, *et al.* Hydrophobicity scale for proteins based on inverse temperature transitions. Biopolymers, 1992. 32 (9):1243-1250.
[70] C.H. Luan, *et al.* Differential scanning calorimetry studies of NaCl effect on the inverse temperature transition of some elastin-based polytetra-, polypenta-, and polynonapeptides. Biopolymers, 1991. 31 (5):465-475.
[71] Y. Cho, *et al.* Effects of Hofmeister anions on the phase transition temperature of elastin-like polypeptides. Journal of Physical Chemistry B, 2008. 112 (44):13765-13771.

[72] J. Reguera, *et al.* Effect of NaCl on the exothermic and endothermic components of the inverse temperature transition of a model elastin-like polymer. Biomacromolecules, 2007. 8 (2):354-358.
[73] S.R. MacEwan, A. Chilkoti. Elastin-like polypeptides: biomedical applications of tunable biopolymers. Biopolymers, 2010. 94 (1):60-77.
[74] J.C. Rodriguez-Cabello, *et al.* Recombinamers: combining molecular complexity with diverse bioactivities for advanced biomedical and biotechnological applications. Advances in Biochemical Engineering Biotechnology, 2011. 125 145-179.
[75] J. Cappello, *et al.* Genetic engineering of structural protein polymers. Biotechnol Prog, 1990. 6 (3):198-202.
[76] D.T. McPherson, *et al.* Production and purification of a recombinant elastomeric polypeptide, G-(VPGVG)19-VPGV, from Escherichia coli. Biotechnol Prog, 1992. 8 (4):347-352.
[77] A.J. Bath, *et al.* Many type IIs restriction endonucleases interact with two recognition sites before cleaving DNA. J Biol Chem, 2002. 277 (6):4024-4033.
[78] N.L. Goeden-Wood, *et al.* Improved assembly of multimeric genes for the biosynthetic production of protein polymers. Biomacromolecules, 2002. 3 (4):874-879.
[79] S.L. Martin, B. Vrhovski, A.S. Weiss. Total synthesis and expression in Escherichia coli of a gene encoding human tropoelastin. Gene, 1995. 154 (2):159-166.
[80] G.L. Rosano, E.A. Ceccarelli. Recombinant protein expression in Escherichia coli: advances and challenges. Front Microbiol, 2014. 5 172.
[81] J.A. Asenjo, B.A. Andrews. Protein purification using chromatography: selection of type, modelling and optimization of operating conditions. Journal of Molecular Recognition, 2009. 22 (2):65-76.
[82] W. Hassouneh, T. Christensen, A. Chilkoti. Elastin-like polypeptides as a purification tag for recombinant proteins. Current Protocols in Protein Scice, 2010. Chapter 6 Unit 6.11.
[83] D.E. Meyer, A. Chilkoti. Purification of recombinant proteins by fusion with thermally-responsive polypeptides. Nat Biotechnol, 1999. 17 (11):1112-1115.
[84] R.E. Sallach, *et al.* Long-term biostability of self-assembling protein polymers in the absence of covalent crosslinking. Biomaterials, 2010. 31 (4):779-791.
[85] S. Pispas, *et al.* Effect of architecture on the micellization properties of block copolymers: A2B miktoarm stars vs AB diblocks. Macromolecules, 2000. 33 (5):1741-1746.
[86] S. Forster, T. Plantenberg. From self-organizing polymers to nanohybrid and biomaterials. Angewandte Chemie International Edition, 2002. 41 (5):689-714.
[87] M.R. Dreher, *et al.* Temperature triggered self-assembly of polypeptides into multivalent spherical micelles. Journal of American Chemical Society, 2008. 130 (2):687-694.
[88] S.M. Staubli, *et al.* Control of angiogenesis and host response by modulating the cell adhesion properties of an Elastin-Like Recombinamer-based hydrogel. Biomaterials, 2017. 135 30-41.
[89] H. Cabral, *et al.* Block copolymer micelles in nanomedicine applications. Chemical Reviews, 2018. 118 (14):6844-6892.
[90] I. Gonzalez de Torre, *et al.* Random and oriented electrospun fibers based on a multicomponent, in situ clickable elastin-like recombinamer system for dermal tissue engineering. Acta Biomater, 2018. 72 137-149.
[91] J. Kopecek. Hydrogel biomaterials: a smart future? Biomaterials, 2007. 28 (34):5185-5192.
[92] F. Cipriani, *et al.* Cartilage regeneration in preannealed silk elastin-like co-recombinamers injectable hydrogel embedded with mature chondrocytes in an ex vivo culture platform. Biomacromolecules, 2018. 19 (11):4333-4347.
[93] N.A. Peppas. Bioadhesive drug delivery systems. Fundamentals, novel applications and development, M. Dekker, . In: Mathiowitz E, Chickering DE, Lehr CM, editors. Journal of Controlled Release. 2000/07/08 ed. New York: M. Dekker, ; 2000. p. 135.
[94] A.S. Hoffman. Hydrogels for biomedical applications. Adv Drug Deliv Rev, 2002. 54 (1):3-12.

[95] T.C. Holmes, *et al.* Extensive neurite outgrowth and active synapse formation on self-assembling peptide scaffolds. PNAS, 2000. 97 (12):6728-6733.
[96] S. Zhang. Fabrication of novel biomaterials through molecular self-assembly. Nat Biotechnol, 2003. 21 (10):1171-1178.
[97] B. Panilaitis, *et al.* Macrophage responses to silk. Biomaterials, 2003. 24 (18):3079-3085.
[98] H. Fan, *et al.* Anterior cruciate ligament regeneration using mesenchymal stem cells and silk scaffold in large animal model. Biomaterials, 2009. 30 (28):4967-4977.
[99] P.B. Harbury, *et al.* A switch between two-, three-, and four-stranded coiled coils in GCN4 leucine zipper mutants. Science, 1993. 262 (5138):1401-1407.
[100] J. Moitra, *et al.* Leucine is the most stabilizing aliphatic amino acid in the d position of a dimeric leucine zipper coiled coil. Biochemistry, 1997. 36 (41):12567-12573.
[101] B. Tripet, *et al.* Effects of side-chain characteristics on stability and oligomerization state of a de novo-designed model coiled-coil: 20 amino acid substitutions in position "d". J Mol Biol, 2000. 300 (2):377-402.
[102] T. Alber. Structure of the leucine zipper. Curr Opin Genet Dev, 1992. 2 (2):205-210.
[103] D. Krylov, I. Mikhailenko, C. Vinson. A thermodynamic scale for leucine zipper stability and dimerization specificity: e and g interhelical interactions. Embo j, 1994. 13 (12):2849-2861.
[104] D. Krylov, J. Barchi, C. Vinson. Inter-helical interactions in the leucine zipper coiled coil dimer: pH and salt dependence of coupling energy between charged amino acids. J Mol Biol, 1998. 279 (4):959-972.
[105] G.D. Prestwich, *et al.* Controlled chemical modification of hyaluronic acid: synthesis, applications, and biodegradation of hydrazide derivatives. Journal of Controlled Release, 1998. 53 (1-3):93-103.
[106] D. Campoccia, *et al.* Semisynthetic resorbable materials from hyaluronan esterification. Biomaterials, 1998. 19 (23):2101-2127.
[107] S.R. MacEwan, A. Chilkoti. Applications of elastin-like polypeptides in drug delivery. Journal of Controlled Release, 2014. 190 314-330.
[108] J.C. Rodriguez-Cabello, *et al.* Elastin-like polypeptides in drug delivery. Adv Drug Deliv Rev, 2016. 97 85-100.
[109] M. Amiram, *et al.* A depot-forming glucagon-like peptide-1 fusion protein reduces blood glucose for five days with a single injection. Journal of Controlled Release, 2013. 172 (1):144-151.
[110] C.A. Gilroy, S. Roberts, A. Chilkoti. Fusion of fibroblast growth factor 21 to a thermally responsive biopolymer forms an injectable depot with sustained anti-diabetic action. Journal of Controlled Release, 2018. 277 154-164.
[111] A.J. Alix. A turning point in the knowledge of the structure-function-activity relations of elastin. J Soc Biol, 2001. 195 (2):181-193.
[112] A. Girotti, *et al.* Design and bioproduction of a recombinant multi(bio)functional elastin-like protein polymer containing cell adhesion sequences for tissue engineering purposes. Journal of Materials Science, 2004. 15 (4):479-484.
[113] T. Flora, *et al.* Use of proteolytic sequences with different cleavage kinetics as a way to generate hydrogels with preprogrammed cell-infiltration patterns imparted over their given 3D spatial structure. Biofabrication, 2019. 11 (3):035008.
[114] K. Ulbrich, J. Strohalm, J. Kopecek. Polymers containing enzymatically degradable bonds. VI. Hydrophilic gels cleavable by chymotrypsin. Biomaterials, 1982. 3 (3):150-154.
[115] T. Miyata, N. Asami, T. Uragami. A reversibly antigen-responsive hydrogel. Nature, 1999. 399 (6738):766-769.
[116] C. Wang, J. Kopecek, R.J. Stewart. Hybrid hydrogels cross-linked by genetically engineered coiled-coil block proteins. Biomacromolecules, 2001. 2 (3):912-920.
[117] A. Greiner, J.H. Wendorff. Electrospinning: a fascinating method for the preparation of ultrathin fibers. Angewandte Chemie International Edition, 2007. 46 (30):5670-5703.

[118] W. Qiu, *et al.* Wet-spinning of recombinant silk-elastin-like protein polymer fibers with high tensile strength and high deformability. Biomacromolecules, 2009. 10 (3):602-608.
[119] M. Li, *et al.* Electrospun protein fibers as matrices for tissue engineering. Biomaterials, 2005. 26 (30):5999-6008.
[120] D. Han, P.I. Gouma. Electrospun bioscaffolds that mimic the topology of extracellular matrix. Nanomedicine, 2006. 2 (1):37-41.
[121] D.B. Khadka, D.T. Haynie. Protein- and peptide-based electrospun nanofibers in medical biomaterials. Nanomedicine, 2012. 8 (8):1242-1262.
[122] R. Machado, *et al.* Electrospun silk-elastin-like fibre mats for tissue engineering applications. Biomedical Materials, 2013. 8 (6):065009.
[123] M. Putzu, *et al.* Elastin-like-recombinamers multilayered nanofibrous scaffolds for cardiovascular applications. Biofabrication, 2016. 8 (4):045009.
[124] A. da Costa, *et al.* Single step fabrication of antimicrobial fibre mats from a bioengineered protein-based polymer. Biomedical Materials, 2017. 12 (4):045011.
[125] G. Riess. Micellization of block copolymers. Progress in Polymer Science, 2003. 28 (7):1107-1170.
[126] J.I. Rodriguez Hernandez, *et al.* Toward 'smart' nano-objects by self-assembly of block copolymers in solution. Progress in Polymer Science, 2005. 30 (7):691-724.
[127] J.A. MacKay, *et al.* Self-assembling chimeric polypeptide-doxorubicin conjugate nanoparticles that abolish tumours after a single injection. Nat Mater, 2009. 8 (12):993-999.
[128] L. Martin, *et al.* Temperature-triggered self-assembly of elastin-like block co-recombinamers:the controlled formation of micelles and vesicles in an aqueous medium. Biomacromolecules, 2012. 13 (2):293-298.
[129] M.J. Pina, *et al.* Elastin-like recombinamers with acquired functionalities for gene-delivery applications. Journal of Biomedical Materials Research Part A, 2015. 103 (10):3166-3178.
[130] J. Gonzalez-Valdivieso, *et al.* Self-assembling ELR-based nanoparticles as smart drug-delivery systems modulating cellular growth via Akt. Biomacromolecules, 2019. 20 (5):1996-2007.
[131] A. Fernandez-Colino, *et al.* Combining catalyst-free click chemistry with coaxial electrospinning to obtain long-term, water-stable, bioactive Elastin-like fibers for tissue engineering applications. Macromol Biosci, 2018. 18 (11):e1800147.
[132] R.A. Register. Materials science: Continuity through dispersity. Nature, 2012. 483 (7388):167-168.
[133] L. Martin, *et al.* Rapid micropatterning by temperature-triggered reversible gelation of a recombinant smart elastin-like tetrablock-copolymer. Soft Matter, 2010. 6 (6):1121-1124.
[134] S.M. Janib, *et al.* A quantitative recipe for engineering protein polymer nanoparticles. Polym Chem, 2014. 5 (5):1614-1625.
[135] A. Ghoorchian, *et al.* Size and shape characterization of thermoreversible micelles of three-armed star elastin-like polypeptides. Journal of Physical Chemistry B, 2013. 117 (29):8865-8874.
[136] C. Garcia-Arevalo, *et al.* Immunomodulatory nanoparticles from elastin-like recombinamers: single-molecules for tuberculosis vaccine development. Mol Pharm, 2013. 10 (2):586-597.
[137] X.X. Xia, *et al.* Hydrophobic drug-triggered self-assembly of nanoparticles from silk-elastin-like protein polymers for drug delivery. Biomacromolecules, 2014. 15 (3):908-914.
[138] N.U. Patel, *et al.* Effect of processing temperature on the morphology and drug-release characteristics of elastin-like polypeptide-collagen composite coatings. Biomacromolecules, 2013. 14 (8):2891-2899.
[139] M.H. Misbah, *et al.* Evolution of amphiphilic elastin-like co-recombinamer morphologies from micelles to a lyotropic hydrogel. Polymer, 2015. 81 37-44.

[140] G. Pinedo-Martin, *et al.* Effect of surfactants on the self-assembly of a model elastin-like block corecombinamer: from micelles to an aqueous two-phase system. Langmuir, 2014. 30 (12):3432-3440.
[141] J.R. McDaniel, *et al.* Noncanonical self-assembly of highly asymmetric genetically encoded polypeptide amphiphiles into cylindrical micelles. Nano Lett, 2014. 14 (11):6590-6598.
[142] D.L. Nettles, A. Chilkoti, L.A. Setton. Applications of elastin-like polypeptides in tissue engineering. Adv Drug Deliv Rev, 2010. 62 (15):1479-1485.
[143] S.R. MacEwan, D.J. Callahan, A. Chilkoti. Stimulus-responsive macromolecules and nanoparticles for cancer drug delivery. Nanomedicine, 2010. 5 (5):793-806.
[144] M. Santos, *et al.* Genetically engineered elastin-based biomaterials for biomedical applications. Curr Med Chem, 2019. 26 (40):7117-7146.
[145] A. Ibanez-Fonseca, *et al.* Trends in the design and use of elastin-like recombinamers as biomaterials. Matrix Biology, 2019.
[146] J. Gonzalez-Valdivieso, *et al.* A DNA vaccine delivery platform based on elastin-like recombinamer nanosystems for Rift Valley fever virus. Mol Pharm, 2020. 17 (5):1608-1620.
[147] V. Sainz, *et al.* Regulatory aspects on nanomedicines. Biochem Biophys Res Commun, 2015. 468 (3):504-510.
[148] J. Wolfram, *et al.* Safety of nanoparticles in medicine. Curr Drug Targets, 2015. 16 (14):1671-1681.
[149] D. Bobo, *et al.* Nanoparticle-based medicines: A review of FDA-approved materials and clinical trials to date. Pharm Res, 2016. 33 (10):2373-2387.
[150] S. Tran, *et al.* Cancer nanomedicine: a review of recent success in drug delivery. Clin Transl Med, 2017. 6 (1):44.
[151] S.R. Saptarshi, A. Duschl, A.L. Lopata. Interaction of nanoparticles with proteins: relation to bio-reactivity of the nanoparticle. J Nanobiotechnology, 2013. 11 26.
[152] S.T. Yang, *et al.* Biosafety and bioapplication of nanomaterials by designing protein-nanoparticle interactions. Small, 2013. 9 (9-10):1635-1653.
[153] A.A. Shemetov, I. Nabiev, A. Sukhanova. Molecular interaction of proteins and peptides with nanoparticles. ACS Nano, 2012. 6 (6):4585-4602.
[154] S. Tenzer, *et al.* Rapid formation of plasma protein corona critically affects nanoparticle pathophysiology. Nat Nanotechnol, 2013. 8 (10):772-781.
[155] S. Ritz, *et al.* Protein corona of nanoparticles: distinct proteins regulate the cellular uptake. Biomacromolecules, 2015. 16 (4):1311-1321.
[156] D. Huhn, *et al.* Polymer-coated nanoparticles interacting with proteins and cells: focusing on the sign of the net charge. ACS Nano, 2013. 7 (4):3253-3263.
[157] L. Yang, L. Shang, G.U. Nienhaus. Mechanistic aspects of fluorescent gold nanocluster internalization by live HeLa cells. Nanoscale, 2013. 5 (4):1537-1543.
[158] P. Aggarwal, *et al.* Nanoparticle interaction with plasma proteins as it relates to particle biodistribution, biocompatibility and therapeutic efficacy. Adv Drug Deliv Rev, 2009. 61 (6):428-437.
[159] P.P. Karmali, D. Simberg. Interactions of nanoparticles with plasma proteins: implication on clearance and toxicity of drug delivery systems. Expert Opinion in Drug Delivery, 2011. 8 (3):343-357.
[160] M.P. Monopoli, *et al.* Biomolecular coronas provide the biological identity of nanosized materials. Nat Nanotechnol, 2012. 7 (12):779-786.
[161] P. Camner, *et al.* Experimental and calculated parameters on particle phagocytosis by alveolar macrophages. Journal of Applied Physiology, 2002. 92 (6):2608-2616.
[162] T.M. Goppert, R.H. Muller. Adsorption kinetics of plasma proteins on solid lipid nanoparticles for drug targeting. Int J Pharm, 2005. 302 (1-2):172-186.
[163] D.E. Owens, N.A. Peppas. Opsonization, biodistribution, and pharmacokinetics of polymeric nanoparticles. Int J Pharm, 2006. 307 (1):93-102.

[164] K. Ogawara, *et al.* Pre-coating with serum albumin reduces receptor-mediated hepatic disposition of polystyrene nanosphere: implications for rational design of nanoparticles. Journal of Controlled Release, 2004. 100 (3):451-455.
[165] K. Michaelis, *et al.* Covalent linkage of apolipoprotein e to albumin nanoparticles strongly enhances drug transport into the brain. Journal of Pharmacology and Experimental Therapeutics, 2006. 317 (3):1246-1253.
[166] J. Kreuter, *et al.* Covalent attachment of apolipoprotein A-I and apolipoprotein B-100 to albumin nanoparticles enables drug transport into the brain. Journal of Controlled Release, 2007. 118 (1):54-58.
[167] C.D. Walkey, *et al.* Nanoparticle size and surface chemistry determine serum protein adsorption and macrophage uptake. Journal of American Chemical Society, 2012. 134 (4):2139-2147.
[168] M.T. Peracchia, *et al.* Visualization of in vitro protein-rejecting properties of PEGylated stealth polycyanoacrylate nanoparticles. Biomaterials, 1999. 20 (14):1269-1275.
[169] R. Gref, *et al.* 'Stealth' corona-core nanoparticles surface modified by polyethylene glycol (PEG): influences of the corona (PEG chain length and surface density) and of the core composition on phagocytic uptake and plasma protein adsorption. Colloids and Surfaces B Biointerfaces, 2000. 18 (3-4):301-313.
[170] J. Shi, *et al.* Cancer nanomedicine: progress, challenges and opportunities. Nature Reviews Cancer, 2017. 17 (1):20-37.
[171] C. Oussoren, *et al.* Lymphatic uptake and biodistribution of liposomes after subcutaneous injection. II. Influence of liposomal size, lipid compostion and lipid dose. Biochim Biophys Acta, 1997. 1328 (2):261-272.
[172] J.S. Souris, *et al.* Surface charge-mediated rapid hepatobiliary excretion of mesoporous silica nanoparticles. Biomaterials, 2010. 31 (21):5564-5574.
[173] G. Sahay, D.Y. Alakhova, A.V. Kabanov. Endocytosis of nanomedicines. Journal of Controlled Release, 2010. 145 (3):182-195.
[174] G.J. Doherty, H.T. McMahon. Mechanisms of endocytosis. Annu Rev Biochem, 2009. 78 857-902.
[175] M.M. Stevens, J.H. George. Exploring and engineering the cell surface interface. Science, 2005. 310 (5751):1135-1138.
[176] S. Kumari, S. Mg, S. Mayor. Endocytosis unplugged: multiple ways to enter the cell. Cell Res, 2010. 20 (3):256-275.
[177] A.F. Adler, K.W. Leong. Emerging links between surface nanotechnology and endocytosis: impact on nonviral gene delivery. Nano Today, 2010. 5 (6):553-569.
[178] S. Behzadi, *et al.* Cellular uptake of nanoparticles: journey inside the cell. Chem Soc Rev, 2017. 46 (14):4218-4244.
[179] J.A. Swanson. Shaping cups into phagosomes and macropinosomes. Nature Reviews Molecular Cell Biology, 2008. 9 (8):639-649.
[180] A. Aderem, D.M. Underhill. Mechanisms of phagocytosis in macrophages. Annu Rev Immunol, 1999. 17 593-623.
[181] S.D. Conner, S.L. Schmid. Regulated portals of entry into the cell. Nature, 2003. 422 (6927):37-44.
[182] E. Ungewickell, D. Branton. Assembly units of clathrin coats. Nature, 1981. 289 (5796):420-422.
[183] C.M. Brown, N.O. Petersen. Free clathrin triskelions are required for the stability of clathrin-associated adaptor protein (AP-2) coated pit nucleation sites. Biochem Cell Biol, 1999. 77 (5):439-448.
[184] M. Ehrlich, *et al.* Endocytosis by random initiation and stabilization of clathrin-coated pits. Cell, 2004. 118 (5):591-605.

[185] A. Nan, *et al.* Cellular uptake and cytotoxicity of silica nanotubes. Nano Lett, 2008. 8 (8):2150-2154.
[186] L. Pelkmans, A. Helenius. Endocytosis via caveolae. Traffic, 2002. 3 (5):311-320.
[187] J.E. Schnitzer, J. Liu, P. Oh. Endothelial caveolae have the molecular transport machinery for vesicle budding, docking, and fusion including VAMP, NSF, SNAP, annexins, and GTPases. Journal of Biological Chemitry, 1995. 270 (24):14399-14404.
[188] I.R. Nabi. Cavin fever: regulating caveolae. Nat Cell Biol, 2009. 11 (7):789-791.
[189] K.G. Rothberg, *et al.* Caveolin, a protein component of caveolae membrane coats. Cell, 1992. 68 (4):673-682.
[190] M. Kirkham, *et al.* Ultrastructural identification of uncoated caveolin-independent early endocytic vehicles. J Cell Biol, 2005. 168 (3):465-476.
[191] E.M. Damm, *et al.* Clathrin- and caveolin-1-independent endocytosis: entry of simian virus 40 into cells devoid of caveolae. J Cell Biol, 2005. 168 (3):477-488.
[192] D. Volonte, *et al.* Flotillins/cavatellins are differentially expressed in cells and tissues and form a hetero-oligomeric complex with caveolins in vivo. Characterization and epitope-mapping of a novel flotillin-1 monoclonal antibody probe. Journal of Biological Chemistry, 1999. 274 (18):12702-12709.
[193] C. Le Roy, J.L. Wrana. Clathrin- and non-clathrin-mediated endocytic regulation of cell signalling. Nature Reviews Molecular Cell Biology, 2005. 6 (2):112-126.
[194] J.P. Lim, P.A. Gleeson. Macropinocytosis: an endocytic pathway for internalising large gulps. Immunol Cell Biol, 2011. 89 (8):836-843.
[195] J. Mercer, A. Helenius. Gulping rather than sipping: macropinocytosis as a way of virus entry. Curr Opin Microbiol, 2012. 15 (4):490-499.
[196] C.C. Norbury, *et al.* Class I MHC presentation of exogenous soluble antigen via macropinocytosis in bone marrow macrophages. Immunity, 1995. 3 (6):783-791.
[197] D.A. Kuhn, *et al.* Different endocytotic uptake mechanisms for nanoparticles in epithelial cells and macrophages. Beilstein J Nanotechnol, 2014. 5 1625-1636.
[198] L. Johannes, S. Mayor. Induced domain formation in endocytic invagination, lipid sorting, and scission. Cell, 2010. 142 (4):507-510.
[199] M. Zhu, *et al.* Physicochemical properties determine nanomaterial cellular uptake, transport, and fate. Acc Chem Res, 2013. 46 (3):622-631.
[200] B.D. Chithrani, A.A. Ghazani, W.C. Chan. Determining the size and shape dependence of gold nanoparticle uptake into mammalian cells. Nano Lett, 2006. 6 (4):662-668.
[201] Y. Qiu, *et al.* Surface chemistry and aspect ratio mediated cellular uptake of Au nanorods. Biomaterials, 2010. 31 (30):7606-7619.
[202] H. Herd, *et al.* Nanoparticle geometry and surface orientation influence mode of cellular uptake. ACS Nano, 2013. 7 (3):1961-1973.
[203] Y. Li, N. Gu. Thermodynamics of charged nanoparticle adsorption on charge-neutral membranes: a simulation study. Journal of Physical Chemistry B, 2010. 114 (8):2749-2754.
[204] J. Lin, *et al.* Penetration of lipid membranes by gold nanoparticles: insights into cellular uptake, cytotoxicity, and their relationship. ACS Nano, 2010. 4 (9):5421-5429.
[205] S. Nangia, R. Sureshkumar. Effects of nanoparticle charge and shape anisotropy on translocation through cell membranes. Langmuir, 2012. 28 (51):17666-17671.
[206] P.R. Leroueil, *et al.* Wide varieties of cationic nanoparticles induce defects in supported lipid bilayers. Nano Lett, 2008. 8 (2):420-424.
[207] M. Azhdarzadeh, *et al.* Nanotoxicology: advances and pitfalls in research methodology. Nanomedicine, 2015. 10 (18):2931-2952.
[208] S. Zanganeh, *et al.* Protein corona: Opportunities and challenges. International Journal of Biochemistry & Cell Biology, 2016. 75 143-147.
[209] F. Zhao, *et al.* Cellular uptake, intracellular trafficking, and cytotoxicity of nanomaterials. Small, 2011. 7 (10):1322-1337.

[210] M.S. Cartiera, *et al.* The uptake and intracellular fate of PLGA nanoparticles in epithelial cells. Biomaterials, 2009. 30 (14):2790-2798.
[211] M. Jovic, *et al.* The early endosome: a busy sorting station for proteins at the crossroads. Histol Histopathol, 2010. 25 (1):99-112.
[212] J. Huotari, A. Helenius. Endosome maturation. EMBO Journal, 2011. 30 (17):3481-3500.
[213] B.D. Grant, J.G. Donaldson. Pathways and mechanisms of endocytic recycling. Nature Reviews Molecular Cell Biology, 2009. 10 (9):597-608.
[214] M. Park, *et al.* Plasticity-induced growth of dendritic spines by exocytic trafficking from recycling endosomes. Neuron, 2006. 52 (5):817-830.
[215] M. Dominska, D.M. Dykxhoorn. Breaking down the barriers: siRNA delivery and endosome escape. J Cell Sci, 2010. 123 (Pt 8):1183-1189.
[216] J. Wang, *et al.* Silica nanoparticles induce autophagy dysfunction via lysosomal impairment and inhibition of autophagosome degradation in hepatocytes. Int J Nanomedicine, 2017. 12 809-825.
[217] M. Mahmoudi, *et al.* Cell "vision": complementary factor of protein corona in nanotoxicology. Nanoscale, 2012. 4 (17):5461-5468.
[218] A.M. Krieg. Toll-free vaccines? Nat Biotechnol, 2007. 25 (3):303-305.
[219] J.H. Wilson-Welder, *et al.* Vaccine adjuvants: current challenges and future approaches. J Pharm Sci, 2009. 98 (4):1278-1316.
[220] A. Pashine, N.M. Valiante, J.B. Ulmer. Targeting the innate immune response with improved vaccine adjuvants. Nat Med, 2005. 11 (4 Suppl):S63-68.
[221] L.J. Peek, C.R. Middaugh, C. Berkland. Nanotechnology in vaccine delivery. Adv Drug Deliv Rev, 2008. 60 (8):915-928.
[222] D.N. Nguyen, *et al.* Polymeric materials for gene delivery and DNA vaccination. Advanced Materials, 2009. 21 (8):847-867.
[223] A. Brun. Vaccines and vaccination for veterinary viral diseases: A general overview. Methods Mol Biol, 2016. 1349 1-24.
[224] J.B. Ulmer, *et al.* Heterologous protection against influenza by injection of DNA encoding a viral protein. Science, 1993. 259 (5102):1745-1749.
[225] J.T. van Oirschot. Present and future of veterinary viral vaccinology: a review. Vet Q, 2001. 23 (3):100-108.
[226] G. Mutwiri, *et al.* Biological activity of immunostimulatory CpG DNA motifs in domestic animals. Vet Immunol Immunopathol, 2003. 91 (2):89-103.
[227] S. van Drunen Littel-van den Hurk, S.L. Babiuk, L.A. Babiuk. Strategies for improved formulation and delivery of DNA vaccines to veterinary target species. Immunol Rev, 2004. 199 113-125.
[228] K. Dhama, *et al.* DNA vaccines and their applications in veterinary practice: current perspectives. Vet Res Commun, 2008. 32 (5):341-356.
[229] I. Capua, *et al.* Development of a DIVA (Differentiating Infected from Vaccinated Animals) strategy using a vaccine containing a heterologous neuraminidase for the control of avian influenza. Avian Pathology, 2003. 32 (1):47-55.
[230] A.A. Coelho-Castelo, *et al.* Tissue distribution of a plasmid DNA encoding Hsp65 gene is dependent on the dose administered through intramuscular delivery. Genet Vaccines Ther, 2006. 4 1.
[231] R. Gravier, *et al.* In vivo tissue distribution and kinetics of a pseudorabies virus plasmid DNA vaccine after intramuscular injection in swine. Vaccine, 2007. 25 (39-40):6930-6938.
[232] S. Manam, *et al.* Plasmid DNA vaccines: tissue distribution and effects of DNA sequence, adjuvants and delivery method on integration into host DNA. Intervirology, 2000. 43 (4-6):273-281.
[233] S.E. Parker, *et al.* Safety of a GM-CSF adjuvant-plasmid DNA malaria vaccine. Gene Ther, 2001. 8 (13):1011-1023.

[234] F. Faurez, *et al.* Biosafety of DNA vaccines: New generation of DNA vectors and current knowledge on the fate of plasmids after injection. Vaccine, 2010. 28 (23):3888-3895.
[235] T.W. Dubensky, Jr., *et al.* Sindbis virus DNA-based expression vectors: utility for in vitro and in vivo gene transfer. J Virol, 1996. 70 (1):508-519.
[236] W.W. Leitner, *et al.* Type I Interferons are essential for the efficacy of replicase-based DNA vaccines. Vaccine, 2006. 24 (24):5110-5118.
[237] D. Dory, *et al.* Prime-boost immunization using DNA vaccine and recombinant Orf virus protects pigs against Pseudorabies virus (Herpes suid 1). Vaccine, 2006. 24 (37-39):6256-6263.
[238] M. Zheng, *et al.* Immunogenicity and protective efficacy of Semliki forest virus replicon-based DNA vaccines encoding goatpox virus structural proteins. Virology, 2009. 391 (1):33-43.
[239] A. Ibanez-Fonseca, *et al.* Biocompatibility of two model elastin-like recombinamer-based hydrogels formed through physical or chemical cross-linking for various applications in tissue engineering and regenerative medicine. J Tissue Eng Regen Med, 2018. 12 (3):e1450-e1460.
[240] D.M. Floss, *et al.* Expression and immunogenicity of the mycobacterial Ag85B/ESAT-6 antigens produced in transgenic plants by elastin-like peptide fusion strategy. J Biomed Biotechnol, 2010. 2010 274346.
[241] M. Creixell, N.A. Peppas. Co-delivery of siRNA and therapeutic agents using nanocarriers to overcome cancer resistance. Nano Today, 2012. 7 (4):367-379.
[242] Y. Octavia, *et al.* Doxorubicin-induced cardiomyopathy: from molecular mechanisms to therapeutic strategies. J Mol Cell Cardiol, 2012. 52 (6):1213-1225.
[243] D. Daniel, J. Crawford. Myelotoxicity from chemotherapy. Semin Oncol, 2006. 33 (1):74-85.
[244] E.P. Mitchell. Gastrointestinal toxicity of chemotherapeutic agents. Semin Oncol, 2006. 33 (1):106-120.
[245] A. Grothey. Oxaliplatin-safety profile: neurotoxicity. Semin Oncol, 2003. 30 (4 Suppl 15):5-13.
[246] M.E. Davis, Z.G. Chen, D.M. Shin. Nanoparticle therapeutics: an emerging treatment modality for cancer. Nature Reviews Drug Discovery, 2008. 7 (9):771-782.
[247] www.clinicaltrials.gov.
[248] P.E. Saw, *et al.* Hyper-cell-permeable micelles as a drug delivery carrier for effective cancer therapy. Biomaterials, 2017. 123 118-126.
[249] W. Han, A. Chilkoti, G.P. Lopez. Self-assembled hybrid elastin-like polypeptide/silica nanoparticles enable triggered drug release. Nanoscale, 2017. 9 (18):6178-6186.
[250] V. Kushwah, *et al.* Co-delivery of docetaxel and gemcitabine using PEGylated self-assembled stealth nanoparticles for improved breast cancer therapy. Nanomedicine, 2018. 14 (5):1629-1641.
[251] L. Brannon-Peppas, J.O. Blanchette. Nanoparticle and targeted systems for cancer therapy. Adv Drug Deliv Rev, 2004. 56 (11):1649-1659.
[252] C. Minelli, S.B. Lowe, M.M. Stevens. Engineering nanocomposite materials for cancer therapy. Small, 2010. 6 (21):2336-2357.
[253] P.D. Howes, R. Chandrawati, M.M. Stevens. Bionanotechnology. Colloidal nanoparticles as advanced biological sensors. Science, 2014. 346 (6205):1247390.
[254] S.R. MacEwan, A. Chilkoti. From composition to cure: A systems engineering approach to anticancer drug carriers. Angewandte Chemie International Edition, 2017. 56 (24):6712-6733.
[255] K.M. Luginbuhl, *et al.* Recombinant synthesis of hybrid lipid-peptide polymer fusions that self-assemble and encapsulate hydrophobic drugs. Angewandte Chemie International Edition, 2017. 56 (45):13979-13984.
[256] P. Yousefpour, *et al.* Conjugate of Doxorubicin to albumin-binding peptide outperforms Aldoxorubicin. Small, 2019. 15 (12):e1804452.
[257] J.D. Byrne, T. Betancourt, L. Brannon-Peppas. Active targeting schemes for nanoparticle systems in cancer therapeutics. Adv Drug Deliv Rev, 2008. 60 (15):1615-1626.

[258] R.K. Jain, T. Stylianopoulos. Delivering nanomedicine to solid tumors. Nature Reviews Clinical Oncology, 2010. 7 (11):653-664.
[259] D.S. Spencer, A.S. Puranik, N.A. Peppas. Intelligent nanoparticles for advanced drug delivery in cancer treatment. Curr Opin Chem Eng, 2015. 7 84-92.
[260] Y. Matsumura, H. Maeda. A new concept for macromolecular therapeutics in cancer chemotherapy: mechanism of tumoritropic accumulation of proteins and the antitumor agent smancs. Cancer Res, 1986. 46 (12 Pt 1):6387-6392.
[261] H. Maeda. Toward a full understanding of the EPR effect in primary and metastatic tumors as well as issues related to its heterogeneity. Adv Drug Deliv Rev, 2015. 91 3-6.
[262] M. Kumar*, et al.* Novel polymeric nanoparticles for intracellular delivery of peptide Cargos: antitumor efficacy of the BCL-2 conversion peptide NuBCP-9. Cancer Res, 2014. 74 (12):3271-3281.
[263] R.K. Jain. Transport of molecules in the tumor interstitium: a review. Cancer Res, 1987. 47 (12):3039-3051.
[264] H. Maeda, G.Y. Bharate, J. Daruwalla. Polymeric drugs for efficient tumor-targeted drug delivery based on EPR-effect. European Journal of Pharmaceutics and Biopharmaceutics, 2009. 71 (3):409-419.
[265] M.J. Pina*, et al.* Biocompatible ELR-based polyplexes coated with MUC1 specific aptamers and targeted for breast cancer gene therapy. Mol Pharm, 2016. 13 (3):795-808.
[266] M.R. Dreher*, et al.* Evaluation of an elastin-like polypeptide-doxorubicin conjugate for cancer therapy. Journal of Controlled Release, 2003. 91 (1-2):31-43.
[267] D.Y. Furgeson, M.R. Dreher, A. Chilkoti. Structural optimization of a "smart" doxorubicin-polypeptide conjugate for thermally targeted delivery to solid tumors. Journal of Controlled Release, 2006. 110 (2):362-369.
[268] E. Jones*, et al.* Prospective thermal dosimetry: the key to hyperthermia's future. International Journal of Hyperthermia, 2006. 22 (3):247-253.
[269] W. Liu*, et al.* Tumor accumulation, degradation and pharmacokinetics of elastin-like polypeptides in nude mice. Journal of Controlled Release, 2006. 116 (2):170-178.
[270] J. Zhang*, et al.* The targeted behavior of thermally responsive nanohydrogel evaluated by NIR system in mouse model. Journal of Controlled Release, 2008. 131 (1):34-40.
[271] D.E. Meyer*, et al.* Targeting a genetically engineered elastin-like polypeptide to solid tumors by local hyperthermia. Cancer Res, 2001. 61 (4):1548-1554.
[272] M.R. Dreher*, et al.* Thermal cycling enhances the accumulation of a temperature-sensitive biopolymer in solid tumors. Cancer Res, 2007. 67 (9):4418-4424.

Materials

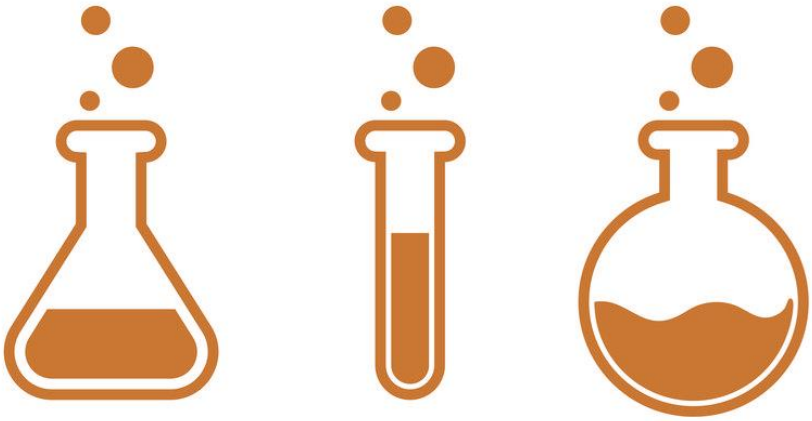

4. Materials

4.1 Reactives

4.1.1 Primers and genes

Primers for mutagenesis and DNA sequencing (Chapter 1 section) were acquired from Metabion. Genes codifying ELRs were available from BIOFORGE group library. Genes encoding for LAEL, Cathepsin D sensitive peptide, H5 peptide and Akt-in were acquired from NZYTECH (Portugal). The azide-modified DNA aptamer for specific binding to CD44 was purchased from Metabion (Germany).

4.1.2 Chemical reagents

Reactive	Brand
Acrylamide/Bis-acrylamide	Amresco
Agarose Seakem	Cambrex
Ammonium persulphate (APS)	Sigma-Aldrich
Ampicillin	Apollo Scientific
Anhydrous N,N Dimethylformamide (DMF)	Sigma-Aldrich
Bovine Serum Albumin (BSA)	Sigma-Aldrich
Bromophenol Blue	Sigma-Aldrich
Copper chloride (CuCl)	Acros Organic
Ethylenediamine tetraacetic acid (EDTA)	Sigma-Aldrich
EZ-Link Psoralen PEG_3 Biotin	ThermoFisher Scientific
Glycerol	Sigma-Aldrich
Glycine	Sigma-Aldrich
Kanamycin	Apollo Scientific
Magnesium chloride ($MgCl_2$)	Merck
NHS-Fluorescein (5/6-carboxyfluorescein succinimidyl ester)	Apollo Scientific
PEG-cyclooctine	Apollo Scientific

Phenylmethylsulfonyl fluoride (PMSF)	Apollo Scientific
PierceTM Unstained Protein MW Marker	ThermoFisher Scientific
Potassium acetate	Sigma-Aldrich
Qdot 800 streptavidin conjugate	Invitrogen
Simply Safe nucleic acid stain	Eurx
Sodium chloride (NaCl)	Sigma-Aldrich
Sodium dodecyl sulfate (SDS)	Sigma-Aldrich
Sodium hydroxide (NaOH)	Sigma-Aldrich
Tetracycline	Apollo Scientific
Tetramethylethylenediamine (TEMED)	Sigma-Aldrich
Tris(hydroxymethyl)aminomethane (Tris)	Sigma-Aldrich
1 Kb Plus DNA Ladder	Invitrogen
β-Mercaptoethanol	Sigma-Aldrich

4.1.3 *In vitro* assays reagents

Reactive	**Brand**
Amiloride	Sigma-Aldrich
Bradford reagent	Biorad/Sigma-Aldrich
Cell lysis RIPA buffer	Biorad/Sigma-Aldrich
Chloroquine	Sigma-Aldrich
COMPLETE protease inhibitor cocktail	Roche
Crystal Violet	Sigma-Aldrich
DePeX mounting medium	Serva
Diamidino-2-phenylindole dihydrochloride (DAPI)	Lonza
Dimethyl sulfoxide (DMSO)	Sigma-Aldrich
Docetaxel (DTX)	Apollo Scientific
Dulbecco's Phosphate Buffered Saline (DPBS)	Invitrogen
Filipin	Sigma-Aldrich
Lipofectamine LTX Plus Reagent	Invitrogen
LysoTracker Red DND-99	Life Technologies
Methanol	Sigma-Aldrich

Monodansylcadaverine	Sigma-Aldrich
Neutral Red reagent	Panreac Quimica
Paraformaldehyde (PFA)	Sigma-Aldrich
Pepstatin A	Apollo Scientific
PhosSTOP phosphatase inhibitor cocktail	Roche
Rhodamine	Sigma-Aldrich
Thiazolyl Blue Tetrazolium Bromide (MTT)	Sigma-Aldrich
TPP2Sa	Sigma-Aldrich
Triton X-100	Sigma-Aldrich
Trypsin-EDTA	Invitrogen
Turbofect Transfection Reagent	Fermentas

4.1.4 *In vivo* assays reagents

Reactive	**Brand**
Azoxymethane (AOM)	Sigma-Aldrich
Carboxy-methylcellulose (CMC)	Sigma-Aldrich
Dextrane sodium sulfate (DSS)	MP Biomedicals
Ethylenediamine tetraacetic acid (EDTA)	Sigma-Aldrich
Isoflurane	Esteve
Streptavidin-Phycoerithine (SAPE)	ThermoFisher Scientific

4.2 Biological materials

4.2.1 Bacteria strains

The *Escherichia coli* strains used in this work have the following genotypes:

- XL1-Blue (Stratagene): endA1 supE44 hsdR17 thi1 recA1 gyrA96 relA1 lac [F' proAB lacIq ZΔM15 Tn (Tetr)]s
- BLR (DE3) (Novagen): F- ompT hsdSB (rB- mB-) gal dcm Δ (srl-recA) 306: Tn10 (Tetr) (DE3)

4.2.2 Cells

The cells used for the *in vitro* assays are:

- **293T:** Human embryonic kidney cells (ATCC, CRL-3216)
- **Vero:** African green monkey kidney cells (ATCC, CCL-81)
- **BHK-21:** Syrian golden hamster kidney fibroblasts (ATCC, C-13)
- **RAW 264.7:** Murine macrophages (ATCC- TIB-71)
- **hMSCs:** Human adipose-derived mesenchymal stem cells (Invitrogen, R7788-115)
- **HFF1:** Human primary foreskin fibroblasts (ATCC, SCRC-1041)
- **HUVEC:** Human umbilical vein endothelial cells (Lonza Walker, cc-2517)
- **Caco-2:** Human epithelial colorectal adenocarcinoma cells (ATCC, HTB-37)
- **MCF-7:** Human breast adenocarcinoma cells (ECACC, 86012803)
- **MDA-MB-231:** Human breast adenocarcinoma cells (ATCC, HTB-26)
- **PANC-1:** Human pancreas carcinoma cells (ATCC, CRL-1469)
- **PDX354:** Patient-derived pancreatic cancer cells
- **PDX185:** Patient-derived pancreatic cancer cells

4.2.3 Animal models

BALB/c mice aged 6-8 and 14-16 weeks (Janvier Labs).

4.3 Culture media

4.3.1 Culture media for bacteria

The culture media used for bacteria growth and transformation are listed below:

- Luria Broth (LB) (Pronadisa): 25 g/L.
- LB-Agar: 25 g/L LB + 1.5% (p/v) Agar (Fluka).
- SOC I (Sigma-Aldrich).
- Terrific Broth based (TB) (Formedium): 55.85 g/L + 8 mL/L glycerol.
- TSS (Transformation and Storing Solution): LB with 10% (w/v) PEG Mw 3350, 5% (v/v) DMSO and 50mM MgCl2 (pH 6.5). Sterilized by filtration.

LB, LB-Agar and TB were sterilized on an autoclave (Selecta Autotester E-75) for 20 min at 120°C and 1 atmosphere.

4.3.2 Culture media for cells

- **293T, Vero and RAW 264.7** cells were grown Dulbecco's modified Eagle's medium (DMEM) (Invitrogen) supplemented with 10% FBS (Invitrogen), 2 mM glutamine (Invitrogen) and Penicillin/Streptomycin (100 U/mL/0.1 mg/mL) (Invitrogen).
- **BHK-21** cells were grown in Eagle's Minimum Essential Medium (EMEM) (Invitrogen) supplemented with 10% FBS and Penicillin/Streptomycin (100 U/mL/0.1 mg/mL).
- **hMSC** and **HFF-1** cells were grown in DMEM supplemented with 10% or 15% FBS, respectively, and Penicillin/Streptomycin (100 U/mL/0.1 mg/mL).
- **HUVEC** cells were grown in Medium 200 (Gibco) supplemented with 1% gentamicin/amphotericin (Gibco) and low serum growth supplement (LSGS) (Gibco).
- **Caco-2** and **MCF-7** cells were grown in Minimum Essential Medium (MEM) supplemented with 10% FBS, 2 mM glutamine, 1% Non-essential amino acids (NEAA) (Invitrogen) and Penicillin/Streptomycin (100 U/mL/0.1 mg/mL).
- **MDA-MB-231** cells were grown in L-15 medium (Gibco) supplemented with 10% FBS and Penicillin/Streptomycin (100 U/mL/0.1 mg/mL).
- **PANC-1** cells were grown in DMEM supplemented with 10% FBS and Penicillin/Streptomycin (100 U/mL/0.1 mg/mL).
- **PDX354 and PDX185** pancreatic cancer patients-derived cells were cultured in Roswell Park Memorial Institute (RPMI) medium supplemented with 10% FBS and Penicillin/Streptomycin (100 U/mL/0.1 mg/mL).

When required, cells were detached using a solution of 0.05% Trypsin-EDTA.

4.4 Buffers

- DNA loading buffer 5x: 30% (v/v) glycerol, 0.1% (w/v) SDS, 0.05% (w/v) bromophenol blue (BPB), 50mM Tris pH 8, 0.05 mM EDTA.
- PBS (pH 7.4): 10 mM Na_2HPO_4, 2mM KH_2PO_4, 137 mM NaCl, 2mM KCl.
- SDS-PAGE loading buffer 5x: 0.3 M Tris pH 6.5, 10% (w/v) SDS, 50% (v/v) glicerol, 25% (v/v) β-mercaptoethanol, 2% (v/v) bromophenol blue (BPB).

- SDS-PAGE running buffer (pH 8.3): 25 mM Tris-base pH 8.3, 192 mM glycine and 0.1% (w/v) SDS.
- TAE (pH 8): 40 mM Tris-acetate pH 8, 1mM EDTA.
- TBS washing buffer (pH 8): 20 mM Tris-base pH 8, 140 mM NaCl.
- TE sonication buffer (pH 8): 10 mM Tris-base pH 8, 1 mM EDTA. Prior to its use 1mM PMSF was added.

All solutions were prepared using ultrapure deionized water (Millipore).

4.5 Molecular biology materials

4.5.1 Restriction enzymes

- *Dpn*I
- *Ear*I (Eaml 104I)
- *Eco*RI
- *Hind*III
- *Sap*I (*Lgu*I)

All restriction enzymes were purchased from ThermoFisher Scientific.

4.5.2 Modification enzymes

- FastAP phosphatase (Fermentas)
- *Pfu* Turbo DNA Polymerase (Agilent)
- Shrimp alkaline phosphatase (SAP) (Fermentas)
- T4 DNA ligase (Fermentas)

4.5.3 Cloning and expression vectors

4.5.3.1 Cloning vectors

DNA fragments employed in this work were cloned in a modified version pDrive cloning vector (Qiagen) built in the Bioforge Research group, here referred as pD. Modifications done over the original cloning vector can be found in previous PhD Thesis from the group [1].

For gene synthesis carried out in Chapter 1, pCMV cloning vector was also used.

4.5.3.2 Expression vector

For the expression of the different recombinamers, p103K expression vector was employed. p103K was created from p10 expression vector in order to introduce 3 lysine residues in the amine terminal side of every polymer whose DNA is encoded in this plasmid. The p103K plasmid was created by PhD. Pierna [2]. p10 was designed by combination of two different expression plasmids: pET7 and pET9a (Novagen) to combine their advantages. pET7 is a modification of pET -25b(+) commercial plasmid produced by suppression of two Eam1104I recognition sites, and the insertion of two of them inside of the polylinker region in order to improve recombinamer clonation and expression. This reclaimed polylinker was inserted in pET9a polylinker, prior elimination of pET9a native polylinker. Such exchange was performed with the aim to obtain a better plasmid, since pET9a is characterized by Kanamycin resistance (more stable than pET7 ampicillin resistance) and by the lack of lac repressor (resulting in the increase of recombinamer yields). This exchange was carried out in the group by PhD. Pierna [2].

4.6 Antibodies

4.6.1 Primary antibodies

- Akt (Cell Signaling, #9272),
- Cleaved caspase-3 Asp175 (Cell Signaling, #9661)
- Glyceraldehyde 3-phosphate dehydrogenase (GAPDH) (Santa Cruz Biotechnology, sc-32233)
- NF-κB p65 (Cell Signaling, #4764),
- β-actin (Cell Signaling, #3700)
- ρ-Akt Ser473 (Cell Signaling, #9271)
- ρ-JNK (Cell Signaling, #9251)

4.6.2 Secondary antibodies

- Goat anti-mouse (Abcam, ab205719)
- Goat anti-mouse (Dako, P0447)
- Goat anti-mouse Alexa Fluor 488 (ThermoFisher Scientific, A21121)

- Goat anti-rabbit (Abcam, ab6721)
- Goat anti-rabbit (Dako, P0448)

4.7 Kits

4.7.1 Molecular biology

- EndoFree Plasmid Maxi Kit (Qiagen)
- PureLink Quick Gel Extraction Kit (Invitrogen)
- Quantum Prep Plasmid Miniprep Kit (Biorad)
- QuickChange Site-Directed Mutagenesis Kit (Stratagene)

4.7.2 *In vitro* assays

- Annexin V FITC Assay Kit (Invitrogen)
- LIVE/DEAD® Viability/Cytotoxicity Kit for mammalian cells (Invitrogen)
- Western-Ready ECL Substrate Kit (Biolegend)

4.7.3 *In vivo* assays

- Th1/Th2 Cytokine 11-Plex Mouse ProcartaPlex™ Panel Cytokine Detection Kit (ThermoFisher Scientific)

4.8 Histology

- Eosin (ThermoFisher Scientific)
- Ethanol absolute (Scharlau)
- Eukitt mounting medium (Sigma-Aldrich)
- Gill 3 Hematoxylin (ThermoFisher Scientific)
- Xylene (Scharlau)

References

[1] A. Ribeiro. Functionality development in systems based on elastin-like recombinamers: From nano-objects to macrogels. PhD Thesis, 2010.
[2] M. Pierna. New strategies to develop bioactive cell-harvesting systems based on elastin like recombinamers. . PhD Thesis, 2013.

Hypothesis & Objectives

3.1 Hypothesis

- It is hypothesized that ELRs will become suitable modulators of immunogenic response to viral antigens. By DNA recombinant techniques, the design of fusion genes involving ELR blocks with different composition and polarity, and immunogenic antigens can result in safe DNA nanovaccines capable of inducing a rapid and long-lasting immune response. Those fusion genes could be able to improve the immunogenicity of this viral antigen in eukaryotic systems and elicit an immune response in animals.

- It is well known the use of genetic engineering techniques and recombinant expression for the bioproduction of tailor-made Elastin-like Recombinamers (ELRs), which are able to self-assemble into different structures due to their thermosensitive behavior. Moreover, by taking advantage of a gene lego® approach, their sequence may be enriched with bioactive domains to obtain smart devices with potential biomedical applications. It is hypothesized that tailored amphiphilic ELR polymers including bioactive sequences are able to form nanosystems in order to selectively deliver therapeutic agents in the cellular cytoplasm, thereby modulating multiple cell processes. Thus, the molecular complexity of the bioactive sequences included in the nanoparticle triggers controlled cell internalization, intracellular fate and mechanism of action of the therapeutic agent.

3.2 Objectives

The main aim of this Thesis is the development of novel advanced nanodevices with potential biomedical applications against multiple diseases. For this purpose, different tailor-made Elastin-like Recombinamers (ELRs) with characteristic features as advanced biomaterials, such as thermosensitivity, biocompatibility, enzymatic modulation and cell-material interactions, will be designed and biosynthesized.

- First, this work aims to develop multiple ELR-Gn viral antigen constructs with different behavior under physiological conditions and test the most accurate strategy in terms of antigen expression and immunogenicity.

- The second objective is to design and bioproduce a novel amphiphilic ELR polymer including a small peptide inhibitor of Akt kinase and relevant bioactive sequences. Therefore, smart nanoparticles, whose conformational complexity allows us to modulate cancer cell growth in a controlled way, will be achieved.

- Third, a further goal aims to evaluate the therapeutic effect of thermoresponsive ELR nanoparticles carrying the Akt inhibitor in a patient-derived *in vitro* model close to real pancreatic cancer.

- Finally, this work aims to develop a novel dual therapeutic approach, by combining the encapsulation of antimitotic drug Docetaxel and Akt inhibitor within targeted nanodevices, and evaluate its anti-tumor accuracy for colorectal cancer treatment.

Results & Discussion

Chapter 1

A DNA vaccine delivery platform based on Elastin-like Recombinamer nanosystems for Rift Valley fever virus

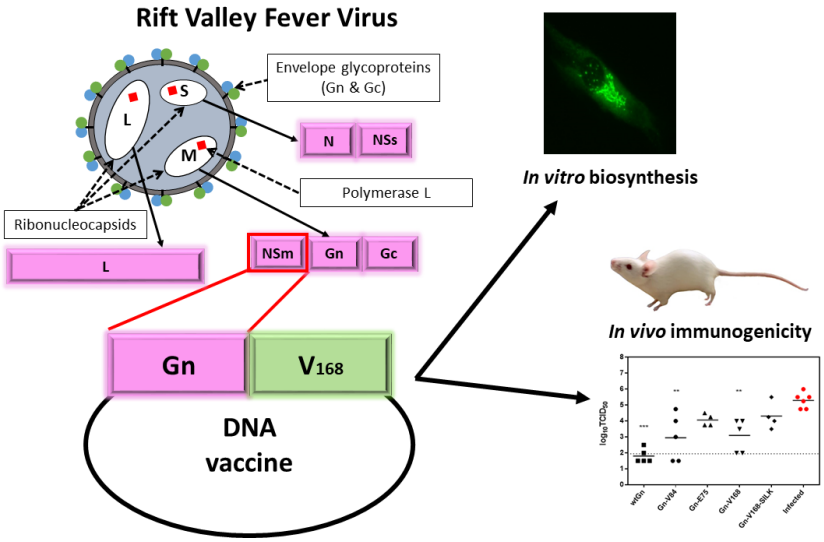

Part of the results of this chapter constitutes the article:

A DNA vaccine delivery platform based on elastin-like recombinamer nanosystems for Rift Valley fever virus. J. Gonzalez-Valdivieso, B. Borrego, A. Girotti, S. Moreno, A. Brun, J.F. Bermejo-Martin, F.J. Arias. *Molecular Pharmaceutics*. **2020**. 17(5): 1608-1620. DOI: 10.1021/acs.molpharmaceut.0c00054

Part of this work was performed at Instituto Nacional de Investigación y Tecnología Agraria y Alimentaria (INIA) in Madrid, in collaboration with Dr. Brun's group.

5.1.1. Introduction

Rift Valley fever virus (RVFV) is a negative strand RNA virus that belongs to the genus *Phlebovirus* (family *Phenuiviridae*, order *Bunyavirales*) and causes an important disease in wild and domesticated ruminants, resulting in high rates of morbidity, mortality and abortion, and is often transmitted to humans [1, 2]. This virus is transmitted by bite of many different mosquito species, as well as by direct contact with body fluids from viremic animals and inhalation of aerosols [3]. The disease caused by this pathogen, Rift Valley fever (RVF), is endemic in sub-Saharan Africa, Egypt and Saudi Arabia. In the sub-equatorial Africa outbreaks are cyclic and are linked to heavy rainfalls that allow the establishment of mosquito breeding areas [4]. More recently, the disease has occurred in different places, such as the Arabian Peninsula, Madagascar, Indian Ocean islands and Mayotte, which confirms that this disease has a wide potential to spread all over the world. In addition, the risk of virus introduction to disease-free areas such as Europe or America could be increased by phenomena associated with climate change as well as the rise in international trade of animals [5]. These facts together the wide host range of the virus and high vector competence of numerous mosquito species could facilitate the outbreaks of the disease with unpredictable consequences for public and animal health [6, 7].

The RVFV virus is composed by a tripartite genome (Figure 1), which comprises large (L), medium (M) and small (S) segments [8]. First, the L segment encodes a RNA-dependent RNA polymerase (RdRp), whose role involves transcription and replication of the viral genome. Secondly, the M segment encodes two structural glycoproteins (Gn and Gc) as well as the accessory proteins: a 13–14 kDa anti-apoptotic protein (NSm) and a 78 kDa protein [9]. Both Gn and Gc glycoproteins are responsible of host cell receptor binding and fusion, hence constituting the major structural antigens and main targets for neutralizing antibodies. Finally, the S segment encodes two different genes: the viral nucleoprotein N, which is associated with the viral RNA to form the nucleocapsid, and the non-structural protein NSs, which is associated with virulence [1, 10].

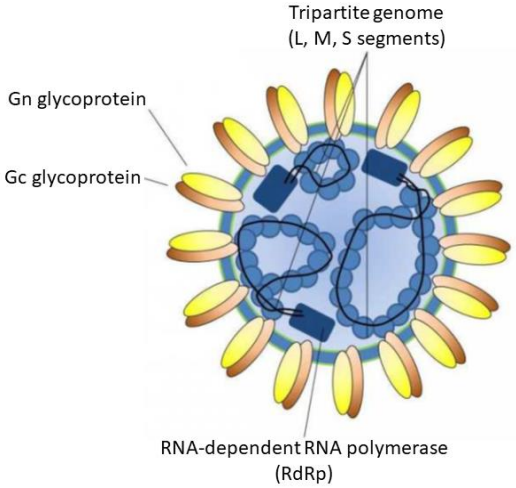

Figure 1. Structure of Rift Valley fever virus. The virus has a tripartite genome, with three different segments: L, M and S. The two glycoproteins (Gn and Gc) exposed at the surface and the RNA-dependent RNA polymerase (RdRp) are also depicted. Adapted from www.bunyavirus.org.

Vaccination is the only effective strategy for the control and prevention of this disease [11, 12]. Unfortunately, currently available vaccines are based on attenuated or inactivated virus that retain important disadvantages, such as low immunogenicity and adverse side effects resulting in teratogenicity and abortions, that preclude their use in non-endemic countries [13]. For this reason, the development of new generation RVF vaccines based on recombinant proteins, Virus-Like Particles (VLPs), recombinant viral vectors or DNA-based vaccines has been the subject of intense research activities in recent years aimed to achieve safer vaccines capable of inducing a rapid and long-lasting immune response with potential use for both human and veterinary purposes.

DNA vaccination is based on plasmids including genes codifying the interest protein under the control of an eukaryotic promoter, generally human cytomegalovirus (CMV) [14]. Thus, the foreign antigen is produced by the host cells and is presented to the host immune system [15]. DNA vaccination presents many other advantages: this strategy is able to induce both humoral and cellular response, therefore mimicking the replication of live pathogen [16]. Furthermore, the structure and post translational modifications of the antigen are maintained. Moreover, the genetic engineering techniques allow us to develop a wide library of antigens when designing vaccine combinations in order to modulate or improve the immune response induced in the host animal [17]. This approach has been used for the development of vaccines against diseases caused by

virus and bacteria, and therapeutic treatments for cancer, auto-immune diseases and allergies [18, 19].

Novel biomaterials have emerged as an useful tool for multiple biomedical applications [20]. Among the most promising biomaterials we find Elastin-like recombinamers (ELRs) [21-23], which are becoming increasingly important in different fields of biomedicine, as regenerative medicine or drug and gene delivery [24-26]. Moreover, recombinant DNA technology allows us to produce ELRs with absolute control over the sequence, and the capability of including different functionalities and bioactive sequences [27]. ELRs, due to their biological origin and properties, possess characteristic features that make them an interesting alternative for biomedical applications, such as biocompatibility, biodegradability and environmentally responsive behavior [28]. Garcia-Arevalo *et al*. developed ELR-based nanovaccines in order to present antigenic peptides from *M. tuberculosis* and achieve long half-life of the presented antigen in circulation. *In vivo* immune-challenge experiments demonstrated the induction of a biphasic response consisting on the early secretion of chemotactic cytokines, then followed by the induction of a Th-2 immune response [29].

One of the main disadvantages of therapeutic proteins resides in their short circulating half-lives, which means that frequent administration or high concentration to achieve effective levels are needed [30]. However, ELRs have been described as promising pharmacokinetic enhancers in order to prolonged half-life and stability of peptides as these new biomaterials are able to improve the pharmacokinetic profile and biodistribution of a peptide compared to the free molecule, resulting therefore in specific delivery of the therapeutic agent [20, 23].

5.1.2. Methods

5.1.2.1 Virus infections and titrations

The virulent South African RVFV strain 56/74 used in this study for mouse challenge studies has been described previously [31]. For titration of virus in post-challenge blood samples, serial ten-fold dilutions of blood-EDTA were mixed with freshly trypsinized Vero cells (duplicates) and seed on MW96 plates. Four days later, the cytopathic effect (cpe) was monitored and cells were fixed and stained with Crystal Violet stain. Titers

are expressed as the log10 of the highest dilution where 50% of the wells showed cpe. The attenuated RVFV-MP12 strain [32] was used for seroneutralization studies.

5.1.2.2 Site-targeted mutagenesis

The plasmid pCMV-NSmGn containing the RVFV-MP12 NSm/Gn sequence spanning nucleotides 21-2070 (GenBank accession number DQ380208) under transcriptional control of the human cytomegalovirus immediate early promoter (hCMVie) was mutated using QuickChange Site-Directed Mutagenesis Kit according to manufacturer's instructions. Briefly, the plasmid was incubated with two complementary oligonucleotides containing the desired mutation (Table 1), flanked by unmodified nucleotide sequence, and the reaction was performed by *Pfu* Turbo polymerase following manufacturer's instructions.

Table 1. Sequences of mutagenesis primers used for DNA mutagenesis.

Primer	Sequence (5'-3')	Tm
MutSappCMVFor	GCGTATTGGGCGCTATTCCGCTTCCTCGAC	78.5°C
MutSappCMVRev	GTCGAGGAAGCGGAATAGCGCCCAATACGC	78.5°C
MutCterGnFor	GCCCCTATTCCTCGTCATGTATGAAGAGCTAGGCGGCCG	80.18°C
MutCterGnRev	CGGCCGCCTAGCTCTTCATACATGACGAGGAATAGGGGC	80.18°C

Table 2. PCR parameters.

Segment	Cycles	Temperature	Time
1	1	95°C	30 seconds
2	12-18	95°C	30 seconds
		55°C	1 minute
		68°C	1 minute /kb of plasmid length

Table 3. PCR cycles depending on the type of mutation.

Type of mutation	Number of cycles
Point mutation	12
Multiple nucleotide insertion	18

Table 4. Mutations performed in DNA sequence of pCMVNSmGn. The first mutation consisted on the substitution c.1295C>A in Gn sequence for the removal of a *Sap*I restriction site. The second mutation involved the insertion c.2028_2029insGTATGAAGAGCTAGGC in Gn sequence for the insertion of a *Sap*I restriction site and STOP codon. Mutated nucleotides are depicted in red. Recognition site for *Sap*I enzyme is depicted in bold.

First mutation	DNA sequence (5'-3')
Original sequence	GCGTATTGGGC**GCTCTTC**CGCTTCCTCGCTC
Mutated sequence	GCGTATTGGGCGCTATTCCGCTTCCTCGCTC

Second mutation	DNA sequence (5'-3')
Original sequence	TATTCCTCGTCATTAGGCGGCCGCGG
Mutated sequence	TATTCCTCGTCATGTAT**GAAGAGC**TAGGCGGCCGCGG

After the amplification, the PCR products were incubated with restriction enzyme *Dpn*I, which is specific for methylated DNA and is used to select for mutation-containing synthesized DNA [33], for 1 hour at 37°C in order to digest parental plasmid DNA. Then, XL-1 Blue competent bacteria were transformed with PCR products, according to manufacturer's instructions (Section 2.6). Bacterial plasmid DNA of transformed clones was isolated and purified by using Endo Free Plasmid Maxi kit according to manufacturer's instructions. After DNA extraction, pure plasmids were incubated with restriction enzyme fast digest *Ear*I for 15 minutes at 37°C following manufacturer's instructions and visualized in agarose electrophoresis to check the purity of the plasmids. Results were corroborated by DNA sequencing performed in an external service, Cenyt Support System. For each sequencing (forward or reverse) 10 µL of a 100 ng/µL DNA solution were used with corresponding primers (Table 5).

Table 5. Sequences of primers used for DNA sequencing.

Primer	Sequence (5'-3')	Tm
CtGn For	TTATAGGGTGCTTAAGTGC	42°C
XhoI For	ATCCGGTACTCGAGGAAC	46°C
pCMV Rev	CCTGAACCTGAAACATAAAATG	46°C
Mid1Gn For	CGTGATGAAGACACACTGTC	45°C
Mid2Gn For	GCCTTTATGTGTAGGGTATG	44°C

5.1.2.3 Enzymatic DNA digestion with restriction enzymes

Controlled enzymatic digestion of the DNA was performed always following manufacturer's suggested conditions. Amount of enzyme used and time of incubation are enzyme and DNA-concentration dependent. These conditions vary depending on the type of digestion: analytical enzymatic digestions were performed 15 minutes at 37°C, while preparative digestions were performed always below start activity concentration overnight at 37°C.

5.1.2.4 DNA dephosphorylation

DNA dephosphorylation was a necessary step in order to avoid vector auto-ligation when the generated protruding ends were cohesive. After vector linearization the plasmid was dephosphorylated twice with two different phosphatases: SAP and FastAP. Dephosphorylating enzymes were used strictly following manufacturers' instructions and recommendations, as well as their subsequent inactivation.

5.1.2.5 DNA ligation

The ligation reaction among genes and vectors was performed with T4 ligase in a final volume of 10 µL in a molar ratio from 1:1 to 1:5 vector to insert proportion. T4 ligase was used under manufacturer's instructions.

5.1.2.6 Bacterial transformation

XL1-Blue Competent cells were transformed following supplier's protocols. Briefly, an aliquot of 50 µL of cells was transferred to a sterile round-bottom tube and kept in ice. The optimal amount of DNA was added and cells were incubated on ice for 30 minutes.

Right after, transformation was achieved via a heat shock of 45 seconds at 42° C. Immediately after the heat shock, cells were incubated on ice for 2 minutes, 450 µL of SOC I medium were added and then cells were incubated for an hour at 37°C with orbital shaking at 250 rpm. Aliquots of the transformation broth were plated on LB agar Petri dishes supplemented with the selective antibiotic to isolate transformed colonies and incubated at 37°C overnight.

5.1.2.7 DNA extraction and purification

Isolated colonies were selected and expanded by culturing them overnight in 5-10 mL of LB, supplemented with the appropriate antibiotic, in an orbital incubator at 37°C and 250 rpm. Plasmidic DNA extraction was carried out with NucleoSpin®Plasmid kit, strictly following manufacturer's instructions. This product is based on alkaline lysis for plasmid DNA isolation and extraction. Cleaning and elution buffer were pre-heated at 60˚C for increased buffer efficiency.

5.1.2.8 DNA gel electrophoresis

In order to analyze the purified DNA, DNA gel electrophoresis was used to separate the nucleic acid fragments after its controlled enzymatic digestion with endonucleases. Agarose gels were prepared by weighting in an Erlenmeyer the necessary amount of agarose and the corresponding volume of TAE 1x according to gel concentration and size following manufacturer's instructions. Agarose was heated in the microwave until complete dissolution and Erlenmeyer was weighted again. Mass loss due to water evaporation was restituted with ultrapure water, reestablishing the initial weight. Subsequently, agarose was poured into and horizontal tray with a comb. Gel was let to cool down to room temperature prior to its insertion in the electrophoresis chamber. Special care was taken to ensure that the TAE 1x buffer volume is sufficient to cover the gel. Samples were prepared by adding 0.2 DNA-volumes of a 5x DNA loading buffer. In order to estimate sample's migration in the agarose gel, BPB tracking dye was added to the 5x DNA loading buffer. Analytical gels (those performed to analyze DNA fragments after controlled enzymatic digestion) and preparative agarose gels (those performed for isolation of DNA bands of interest for their subsequent extraction) were run with different applied voltages: for analytical gels 7-9 V/cm were used, while for preparative 2-7 V/cm were used. Lower voltages ensure slower DNA migration and

higher band resolution, necessary to facilitate the isolation and extraction of the DNA bands of interest.

5.1.2.9 DNA extraction from agarose gel electrophoresis

DNA fragments of interest were sliced from the agarose gel electrophoresis and purified from agarose gel electrophoresis using the PureLink®Quick Gel Extraction Kit following manufacturer's instructions.

5.1.2.10 Final plasmid synthesis

The elastin-like recombinamers (ELRs) used in this chapter were obtained as described elsewhere [22]. The final fusion genes with a fully controlled composition and chain length were constructed by sequential introduction of the monomer gene segments in a stepwise manner using the recursive directional ligation method (RDL). Briefly, pCMVNSmGn plasmid was linearized by digestion with the restriction enzyme *Sap*I overnight at 37°C and corroborated by visualization in 1% agarose electrophoresis. The cloning of the linearized plasmid and corresponding ELR insert was performed by incubating with T4 DNA ligase for 1 hour at 22°C and then transformed into competent bacteria XL-1 Blue as described in sections 2.5 and 2.6, respectively**.** Plasmid DNA was isolated and purified by using Endo Free Plasmid Maxi kit according to manufacturer's instructions. After DNA extraction, pure recombinant plasmids were analyzed by digestion with restriction enzyme Fast digest *Hind*III for 15 minutes at 37°C following manufacturer's instructions and visualized in agarose electrophoresis. The gene sequence of every cloning step was verified by DNA sequencing. Endotoxin levels of the final gene constructs were determined using the Endosafe-PTSTM test (Charles River).

5.1.2.11 Cell culture

293T human embryonic kidney cells, African green monkey Vero cells and RAW 264.7 murine macrophages were maintained in a humid atmosphere of 5% CO2 and 37°C in Dulbecco's modified Eagle's medium (DMEM) supplemented with 10% FBS, 2 mM glutamine, 100 U/mL penicillin and 0.1 mg/mL streptomycin. BHK-21 (C-13) hamster kidney fibroblasts were cultured in EMEM Eagle's Minimum Essential Medium supplemented with 10% FBS, 100 U/mL penicillin and 0.1 mg/mL streptomycin at 5%

CO_2 and 37°C. When required, cells were collected using a solution of 0.05% Trypsin-EDTA.

5.1.2.12 Cell transfection

293T cells were seeded (2 x 10^4 cells per cm^2) and allowed to growth overnight. Then, transfection reagents Lipofectamine and Turbofect were prepared according to manufacturer's instructions for 20 minutes at room temperature. Transfection reagent/DNA mixture was added to cells. Cell medium was replaced by fresh medium after 24 hours and transgene expression was analyzed after 24 hours. A commercial plasmid provided by the manufacturer was used as control plasmid, referred as positive control, in order to determine the cytotoxicity inherent to the transfection process.

5.1.2.13 Cell viability

293T cells were transfected with plasmids as described above, and cytotoxic effect of the constructs was determined after 24 hours. Thus, LIVE/DEAD Viability/Cytoxicity Assay Kit was used according to the manufacturer's instructions. Briefly, a stock solution of the LIVE/DEAD reagents (1 µM calcein AM and 2 µM EthD-1 in 10 mL of DPBS) was prepared and 100 µL were distributed in each well. After incubation for 20 minutes in the dark, the fluorescence intensity emission was measured at 525 and 645 nm after excitation at 485 and 525 nm (SpectraMax M5e Molecular Devices microplate reader). Additionally, photographic images of cultures were taken using a Nikon eclipse Ti-SR (Japan) fluorescence microscope. Three independent experiments, each in triplicate, were performed.

5.1.2.14 Gn expression immunodetection

293T cells were seeded (2.5 x 10^4 cells per well) and allowed to growth overnight in complete medium. After 24 hours, cells were transfected as described in section 2.12. 24 hours later, cells were washed with PBS 1X, fixed with PFA 4% and permeabilized with Triton X-100 0.1%. After washing with PBS 1X, cells were blocked by FBS 2% and incubated with RVFV-immunized mouse serum for 1 hour. Then, cells were washed with PBS 1X and incubated with Alexa Fluor 488-labeled secondary antibody and fluorescence intensity was measured by SpectraMax M5e Molecular Devices microplate reader. Three independent experiments, each in triplicate, were performed.

5.1.2.15 Confocal microscopy

293T cells were transfected with plasmids as explained above. After 24 hours, cells were washed with PBS 1X, fixed with PFA 4% and permeabilized with Triton X-100 0.1%. After washing with PBS 1X, cells were blocked by FBS 2% and incubated with RVFV-immunized mouse serum for 1 hour. Cells were then washed with PBS 1X three times and incubated with Alexa Fluor 488-labeled secondary antibody for 1 hour. Cells were washed with PBS 1X and cellular nuclei were stained with DAPI for 5 minutes. Finally, cells were washed with PBS 1X. Confocal images were taken using a Leica TCS SP5 confocal microscope at Institute of Molecular Biology and Genetics (IBGM, Valladolid). Representative images were analyzed. Additionally, z-stack composed by six images with a z-focal difference of 0.4 μm was performed.

5.1.2.16 Fluorescent labeling of DNA constructs

Plasmid DNA was biotinylated with EZ-Link Psoralen-PEG3-Biotin according to manufacturer's instructions. Briefly, EZ-LinkPsoralen-PEG3-Biotin was dissolved in DMF and mixed with plasmid DNA. Then, the reaction was irradiated with a 15W UV lamp at 365 nm for 10 minutes on ice. To remove non-reacted biotin, biotinylated DNA was precipitated with 0.2M potassium acetate and 70% ethanol. After centrifugation, the DNA pellet was washed with 70% ethanol and allowed to dry. The biotinylated DNA was dissolved in sterile PBS.

The conjugation of Qdot800 with biotinylated DNA was prepared immediately prior to use. Briefly, quantum dots were dissolved at 20 nM in Secondary Incubation Buffer. Specifically, Qdot800 Streptavidin Conjugate were added to biotinylated DNA and incubated for 15 minutes at room temperature. We used a plasmid DNA: quantum dot molar ratio 2:1 which permitted all the quantum dots to be complexed with the plasmid DNA.

5.1.2.17 *In vivo* biodistribution

All animal experiments were conducted in accordance with the institutional guidelines for the care and use of experimental animals of the University of Valladolid (Spain) in accordance with Directive 2010/63/EU (Resolution Number 2010/2/23) under the supervision of the Animal Research and Welfare Committee.

BALB/c mice aged 14-16 weeks were injected intravenously via the tail vein with (2.5 mg/kg mouse) of Qdot-labeled DNA. Animals were anaesthetized with isoflurane in oxygen (4% for induction and 1.5% for maintenance) and transferred immediately to the IVIS imaging system with continuous anaesthesia during measurement. An untreated mouse was always measured at the same time as control. Animals were scanned for fluorescence by the IVIS *In Vivo* Imaging System (Perkin Elmer, Waltham, MA). Excitation and emission wavelengths were 470 and 800 nm, respectively. Fluorescence of animals was plotted by subtracting background from an untreated mouse.

5.1.2.18 Immunization and challenge of mice

Groups of 12-16 weeks old BALB/c mice (n=5; n=4 for Gn-E75 group) were inoculated through the intramuscular route with 100 µg of endofree plasmid in saline with two doses at 2 weeks intervals. An additional booster plasmid dose was supplied 12 weeks later. Two weeks after the second boost and four weeks after the third dose, animals were bled from the submandibular vein plexus. Sera post-vaccination were heat-inactivated at 56ºC for 30 minutes and kept at -20ºC until used. Four weeks after the last DNA dose, mice were challenged intraperitoneally (i.p) with 10^3 pfu of the RVFV isolate 56/74. Three days later animals were euthanized, total EDTA-blood samples were collected and kept at -80º until use.

Mice were housed in a BSL-3 containment area with food and water supplied ad libitum. All experimental procedures were handled in accordance with EU guidelines from the 2010/63 EU Directive for animal experimentation, and protocols approved by INIA´s Committees for Biosafety and Ethics of Animal Experiments (permit codes CEEA 2012/014 and CBS 2012/017).

5.1.2.19 *In vivo* humoral immune responses

The presence of serum neutralizing antibodies was analyzed by plaque reduction neutralization assay. Briefly, a fixed amount of virus (100 pfu of the MP12 strain of RVFV) was incubated for 30 minutes at 37ºC with three-fold serum dilutions or with medium only. The mixture was then added onto Vero cells grown in 6-well plates. After 1 hour of adsorption, the inoculum was removed, cells were washed and a semi-

solid medium containing 1% Carboxy-methylcellulose (CMC) was added. Monolayers were fixed and stained 3-5 days post infection. Cell lysis plaques were counted and the percentage of infectivity reduction for each serum dilution was calculated and expressed as $PRNT_{80}$. i.e, the dilution of serum (log10) rendering a reduction of infectivity of 80%.

5.1.2.20 *In vivo* cellular immune response assays

Spleen cells were obtained from grinded mouse spleens. Red blood cells were lysed by adding 0.16M NH_4Cl, washed with DMEM, and resuspended in DMEM supplemented with 10% FBS, 20 mM HEPES, 0.05 mM β-mercaptoethanol. For *in vitro* re-stimulation of lymphocytes, we followed two approaches: firstly, the spleen cells (10^6 cells/mL) were incubated with 5 µg/mL of either a RVFV-Gn specific H2-K^d Class-I major histocompatibility complex (MHC) peptide (SYAHHRTLL), or medium alone with no stimulus. Secondly, 10^5 cultured cells from the murine macrophage cell line RAW 264.7 were infected in 96-well plates with RVFV 56/74 at a multiplicity of infection of 2. As a negative control, uninfected RAW 264.7 cells were used. 24 hours later, $5x10^5$ spleen cells were added to each well and the co-cultures were incubated four additional days. Supernatants were harvested and frozen at -80ºC until used.

5.1.2.21 Cytokine quantification by Luminex

Measurement of cytokine release by splenocytes was performed using a cytokine detection kit (Th1/Th2 Cytokine 11-Plex Mouse ProcartaPlex™ Panel). Briefly, the supernatants from re-stimulated cells (see above) were diluted 1:2 in medium and incubated with paramagnetic-fluorescent beads coated with 11 different anti-mouse cytokine antibodies. Biotin-labeled antibody was incubated and a streptavidin-phycoerithine (SAPE) was used as detector of the immune complexes. Fluorescence was read using the MagPix xMAP 50 apparatus (Merck). Cytokine concentrations were estimated by interpolation of a curve fit generated by serially diluted cytokine standards using specific software (xPonent).

5.1.2.22 Statistical analysis

Data are reported as mean ± SD (n = 3). For the Gn glycoprotein *in vitro* expression, statistical analysis involved a variance analysis in combination with a subsequent

analysis using the Bonferroni method. A p value of less than 0.05 was considered to be statistically significant. *p < 0.01, **p < 0.001

For the neutralization assays, statistical analysis involved a variance analysis in combination with a subsequent analysis using the Bonferroni method. A p value of less than 0.05 was considered to be statistically significant. *p < 0.05, **p < 0.01, ***p < 0.001, ****p < 0.0001

When immune response was determined, Anova non-parametric Kruskall-Wallis test were performed. A p value of less than 0.05 was considered to be statistically significant. *p<0,5, **p<0.01

Data were handled using the SPSS Statistics software version 20 (IBM).

5.1.3. Results and Discussion

5.1.3.1 Plasmid design

ELR biomaterials have been proposed for multiple biomedical applications, such as drug delivery or tissue engineering [23, 28]. García-Arévalo *et al*. developed immunomodulatory nanocarriers as tuberculosis vaccines. These nanovaccines consisted on an amphiphilic ELR backbone decorated with the major membrane protein sequence from *Mycobacterium tuberculosis* [29]. Therefore, we hypothesized that ELR could be an accurate approach in order to improve viral Gn glycoprotein expression in eukaryotic cells and/or to enhance its immunogenicity in mice. The RVFV glycoprotein Gn carries determinants for both neutralizing antibody induction and cell-mediated immune responses [4, 34, 35] so it is often the antigen of choice in different vaccine formulations including subunit or DNA vaccines [36, 37]. In this work, we designed six chimeric Gn-ELR fusion genes consisting on Gn and ELR blocks of different nature (Figure 2). The structure of the six Gn-ELR genes is depicted in Figures 5-11. Due to the hydrophilic nature of Gn glycoprotein, three different fusion genes (Gn-A80, Gn-I80 and Gn-V84) based on hydrophobic residues, whose sequences were $(VPGAG)_{80}$, $(VGIPG)_{80}$ and $(VPGVG)_{84}$ respectively, were synthesized. Moreover, previous works from the group demonstrated the ability of these hydrophobic ELR-based blocks to self-assemble at physiologic temperature [29, 38, 39] and thereby form aggregates when

fused to hydrophilic Gn glycoprotein. Thus, amphiphilic structures could be built as a first approach. The second strategy consisted on one fusion gene (Gn-E75), based on hydrophilic glutamic acid, whose sequence was $[(VPGVG)_2(VPGEG)(VPGVG)_2]_{15}$. This construct could stay soluble without aggregation ability, due to the fact that glutamic acid-based block is not able to self-assemble in a physiological environment [40, 41]. Thus, we could compare the viral glycoprotein expression and immunogenicity between amphiphilic aggregates and soluble Gn-E75 construct. Moreover, we developed a new construct with two valine-rich blocks (Gn-V168), whose sequence was $(VPGVG)_{168}$, as third approach. Thus, the reinforced polymeric component could allow an easier aggregation under physiological conditions, as Tt is directly increased by ELRs chain length [38, 42].

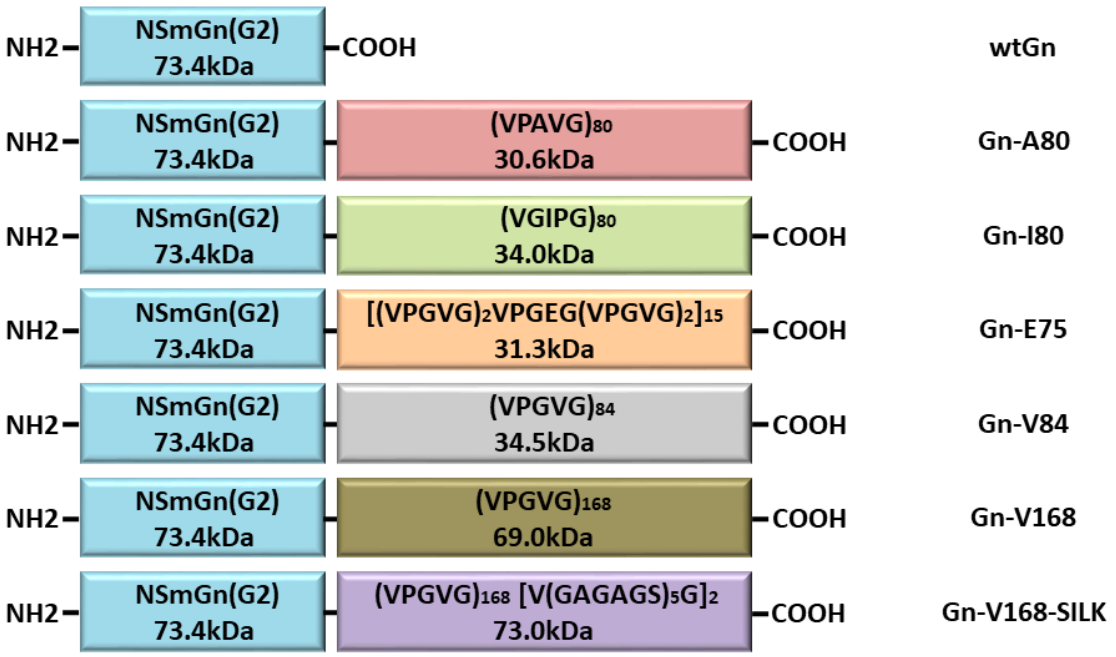

Figure 2. Design, composition and molecular weight of the developed fusion proteins. The ELR blocks include their amino acid composition. Non-scaled scheme.

Finally, the fourth strategy consisted on $[V(GAGAGS)_5G]_2$ sequence from silk fibroin produced by silkworm, which was added to Gn-V168 construct in order to improve the aggregation stability (Figure 2). The silk fibroin produced by silkworm is characterized by its self-assembling in irreversibly way into a highly stable amphiphilic β-sheet secondary structure [43, 44].

5.1.3.2 Site-targeted mutagenesis

Site-targeted mutagenesis was performed in order to build the different constructs previously described. For this reason, a pCMV plasmid containing the gene codifying for glycoprotein Gn, kindly provided by Dr. Alejandro Brun, was mutated in order to allow us to clone the genes codifying for different ELRs constructs. This process was done in two steps (Figure 3).

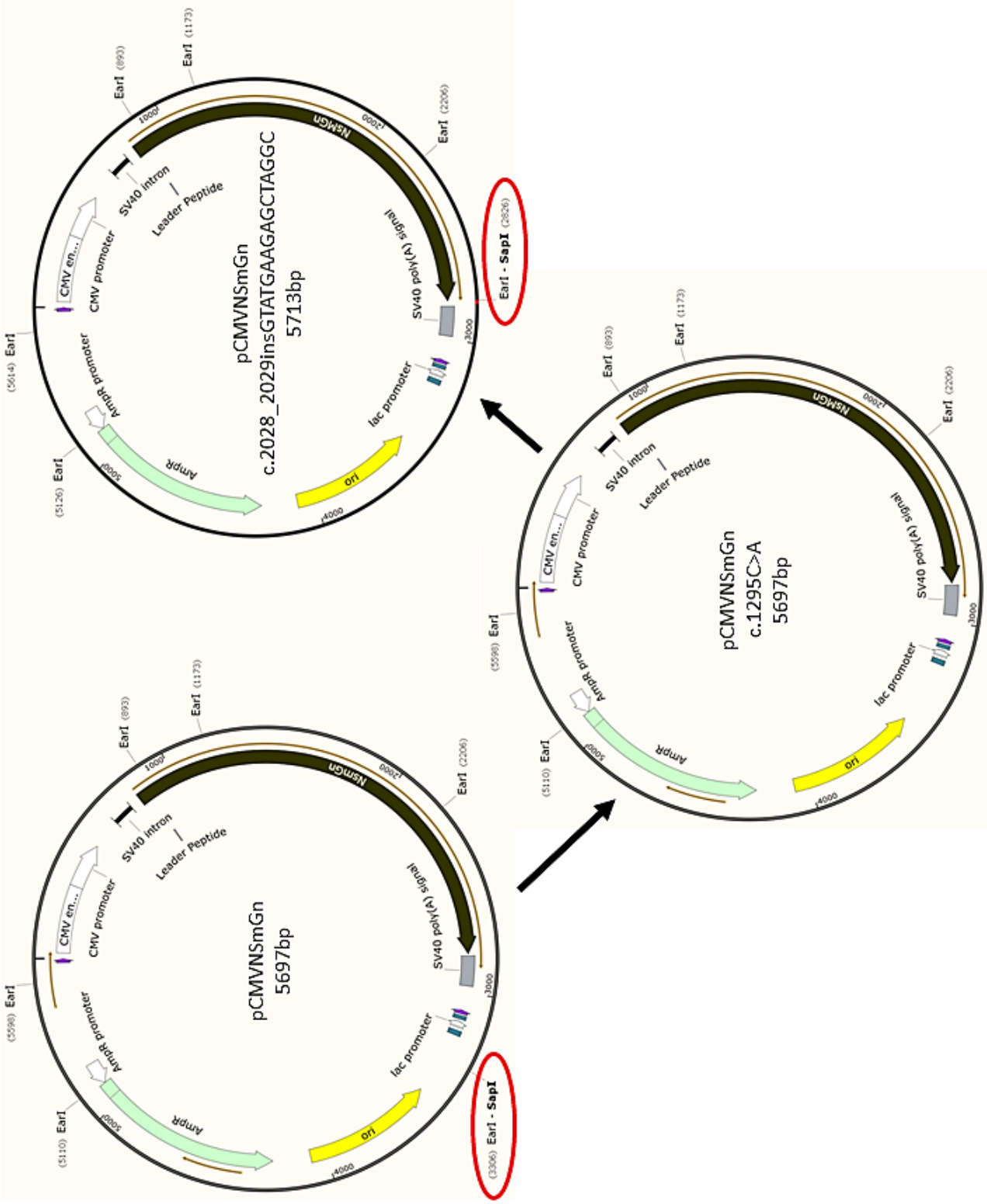

Figure 3. Composition of original and mutated plasmids. The recognition sites for restriction enzymes (*Ear*I and *Sap*I) and other features are indicated in the map.

First, endogenous *Sap*I recognition site (5'-GCTCTTC-3') was removed by the substitution of a cytosine for an adenine at position 3306 in the plasmid sequence (Table

4, Figures 3 and 4). Two different mutagenesis primers were specifically synthesized and used for this site-directed mutagenesis (Table 1). Pure plasmidic DNA was incubated with restriction enzyme *Ear*I and visualized in agarose electrophoresis to check the success of the mutagenesis (Figure 4). The theoretical fragments for the original plasmid (pCMV-NSmGn) were 280 bp, 488 bp, 992 bp, 1033 bp, 1100 bp and 1804 bp. On the other hand, the theoretical fragments for the mutated plasmid were 280 bp, 488 bp, 992 bp, 1033 bp, 2904 bp. Due to the mutation c.1295C>A, an *Ear*I/*Sap*I recognition site was removed from position 3306 (Figure 3) and, as a consequence, the fragments of 1100 and 1804 bp were fused in one fragment of 2904 bp length. Results were corroborated by automatic DNA sequencing.

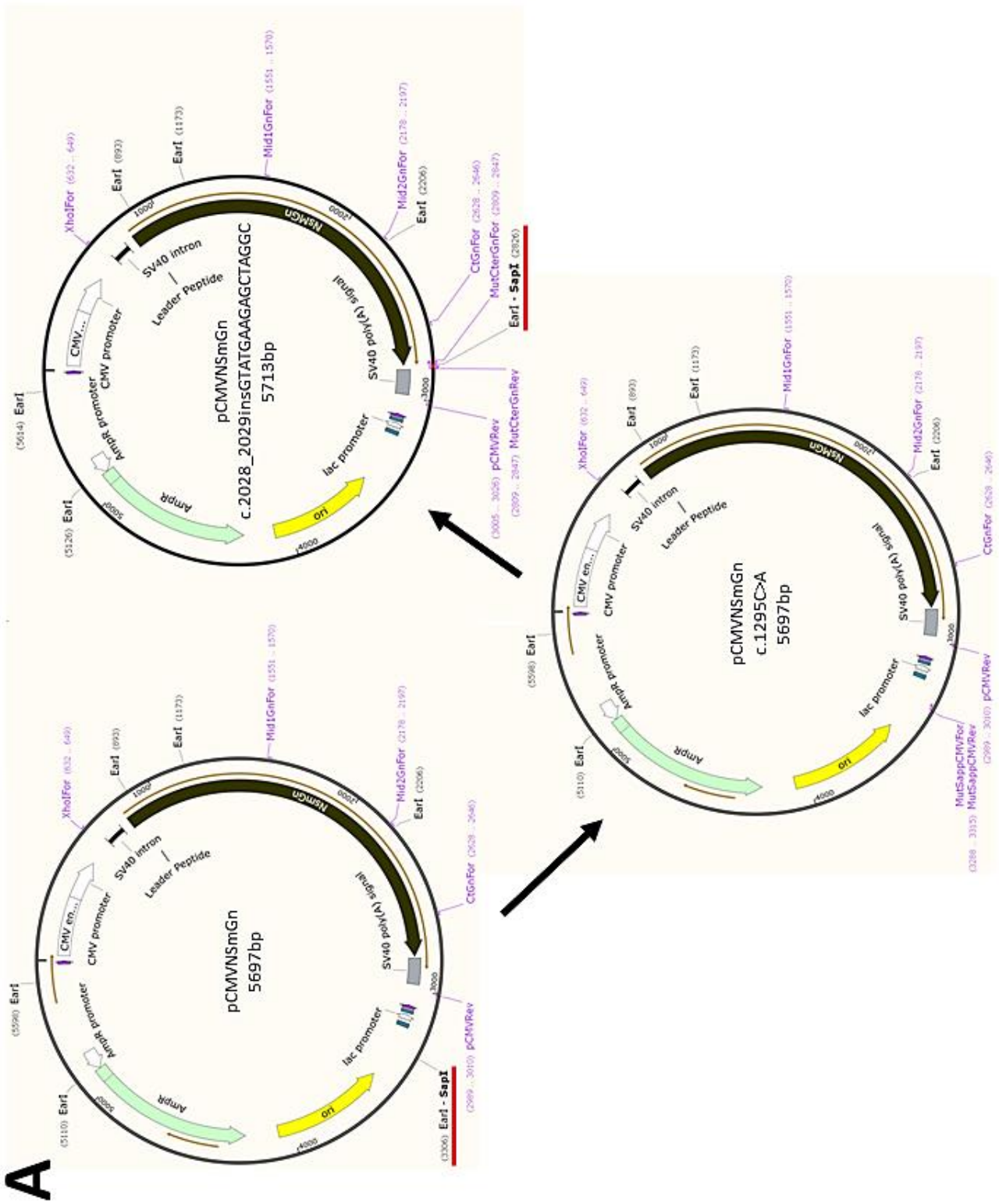
A
pCMVNSmGn
5697bp
pCMVNSmGn
c.2028_2029insGTATGAAGAGCTAGGC
5713bp
pCMVNSmGn
c.1295C>A
5697bp
NSmGn
SV40 intron
Leader Peptide
CMV promoter
AmpR promoter
AmpR
lac promoter
ori
SV40 poly(A) signal
XhoIFor
EarI
MidGnFor
MidGnFor
CtGnFor
MutCterGnFor
EarI - SapI
pCMVRev
MutCterGnRev
MutSappCMVFor
MutSappCMVRev

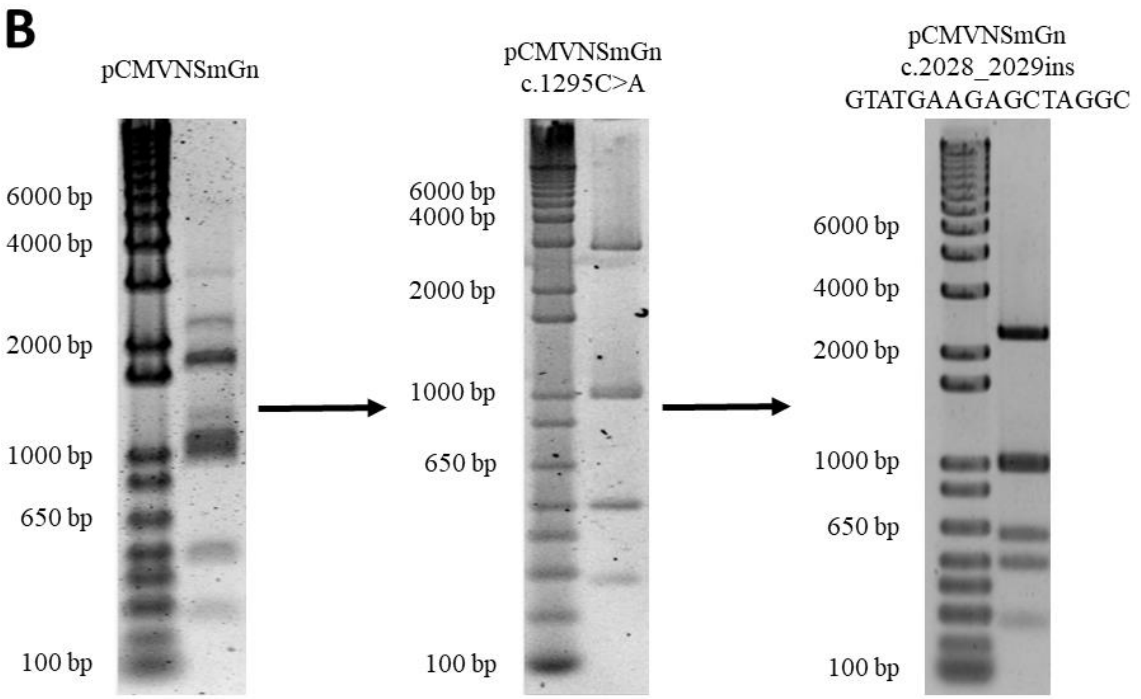

Figure 4. A: Composition of original and mutated plasmids. The construct contained the Gn glycoprotein gene (Brown color) and Ampicillin resistance gene (Light green color). The recognition sites for restriction enzymes (*Ear*I and *Sap*I) and other features are indicated in the map. The binding site for primers used in DNA mutagenesis and sequencing are indicated. B: Digestion of original and mutated plasmids with restriction enzyme *Ear*I visualized by agarose electrophoresis. Left: The theoretical fragments for the original plasmid were: 280 bp, 488 bp, 992 bp, 1033 bp, 1100 bp and 1804 bp. Middle: The theoretical fragments for the intermediate plasmid were: 280 bp, 488 bp, 992 bp, 1033 bp, 2904 bp. Due to the mutation c.1295C>A, an *Ear*I/*Sap*I recognition site was removed. As a consequence, the fragments of 1100 and 1804 bp were fused in one fragment of 2904 bp length. Right: The theoretical fragments for the final plasmid were: 280 bp, 488 bp, 620 bp, 992 bp, 1033 bp and 2300 bp. Due to the mutation c.2028_2029insGTATGAAGAGCTAGGC, an EarI/SapI recognition site was created. As a consequence, the fragment of 2904 bp length was split in two fragments of 620 and 2300 bp, respectively.

Once the deletion of the endogenous *Sap*I recognition site was performed and checked (Figure 4), a second site-directed mutagenesis was performed in order to introduce a new *Sap*I recognition site (5'-GAAGAGC-3') after Gn glycoprotein codifying gene. Thus, genes codifying for different ELRs could be introduced next to the viral glycoprotein Gn gene and achieve the final fusion genes (Figures 5-11). For this purpose, two mutagenesis primers were specifically synthesized (Table 1). This second mutation consisted on the insertion of the 16 nucleotides "GTATGAAGAGCTAGGC" at position 2826 in the plasmid sequence. As described above, the introduction of this new *Sap*I recognition site was corroborated by *Ear*I digestion (Figure 4) and DNA sequencing. The theoretical fragments for the final plasmid were: 280 bp, 488 bp, 620

bp, 992 bp, 1033 bp and 2300 bp. Due to the mutation c.2028_2029insGTATGAAGAGCTAGGC, an *Ear*I/*Sap*I recognition site was created at position 2826. As a consequence, the fragment of 2904 bp length was split in two fragments of 620 and 2300 bp, respectively. Thus, after the second mutation, the pCMVNSmGn plasmid was already prepared for introducing ELR genes from a gene library in order to develop different constructs which could improve the expression of viral glycoprotein Gn in eukaryotic systems.

5.1.3.3 Construct synthesis

Sequential introduction of the repetitive polypeptide-coding gene segments to form fusion genes with a fully controlled composition and chain length was carried out using the RDL (recursive directional ligation) technique, as described in the general introduction and section 2.10.

The gene sequences encoding for the ELR blocks A80, I80, E75, V84 and SILK blocks were available in the laboratory from previous studies and had been constructed through the same procedure of DNA concatenation involving sequential rounds of RDL of the monomeric DNA sequences.

Once the pCMVNSmGn construct was prepared after site-directed mutagenesis, the plasmid was digested with *Sap*I. The genes codifying A80, I80, E75 and V84 ELRs blocks were cloned in pCMVNSmGn in order to obtain pCMVNSmGnA80, pCMVNSmGnI80, pCMVNSmGnE75 and pCMVNSmGnV84 constructs (Figures 6-9).

In order to obtain the pCMVNSmGnV168 construction, pCMVNSmGnV84 was digested with *Sap*I. A ligation reaction was performed between V84 block and pCMVNSmGnV84 construction, and the products of such reaction were transformed into *E. coli* as previously described in section 2.6. Several colonies were selected for restriction mapping analysis of their plasmid content by using the enzyme *Hind*III (Figure 10). Among the colonies rendering the expected bands, positive colonies were further verified by DNA sequencing and selected for following steps of the process.

The next step involved the digestion of pCMVNSmGnV168 construct with *Sap*I. Then, a ligation reaction between SILK block and pCMVNSmGnV168 was performed and the products of such reaction were transformed into *E. coli* as previously described in section 2.6. Several colonies were selected for restriction mapping analysis of their plasmid content by using the enzyme *Hind*III (Figure 11). Among the colonies rendering the expected bands, positive colonies were further verified by sequencing and selected for following steps of the concatenation process. Thus, the final constructions were achieved (Figures 6-11).

As shown in Figures 5-11, all the constructs showed fragments of the expected length. These results confirmed the accurate synthesis of the constructs. Furthermore, the sequences were corroborated by DNA sequencing. The constructs were isolated and purified by means of an endotoxin-free kit in order to obtain pure plasmid suitable for following *in vivo* assays. Endotoxin levels were measured and were lower than 0.25 EU/mg in all cases.

According to Figures 5-11, *Hind*III digestion hypothetically resulted in 3 DNA fragments of 13 and 4525 bp length, respectively. The third fragment size varied depending on the length of the ELR gene introduced. Thus, this fragment theoretically sized 1075 bp, 2275 bp, 2275 bp, 2235 bp, 2200 bp, 3595 bp and 3787 bp for wtGn, Gn-A80, Gn-I80, Gn-V84, Gn-E75, Gn-V168 and Gn-V168-SILK construct, respectively. As shown in Figures 5-11, all the constructs showed fragments of the expected length. These results confirmed the accurate synthesis of the constructs.

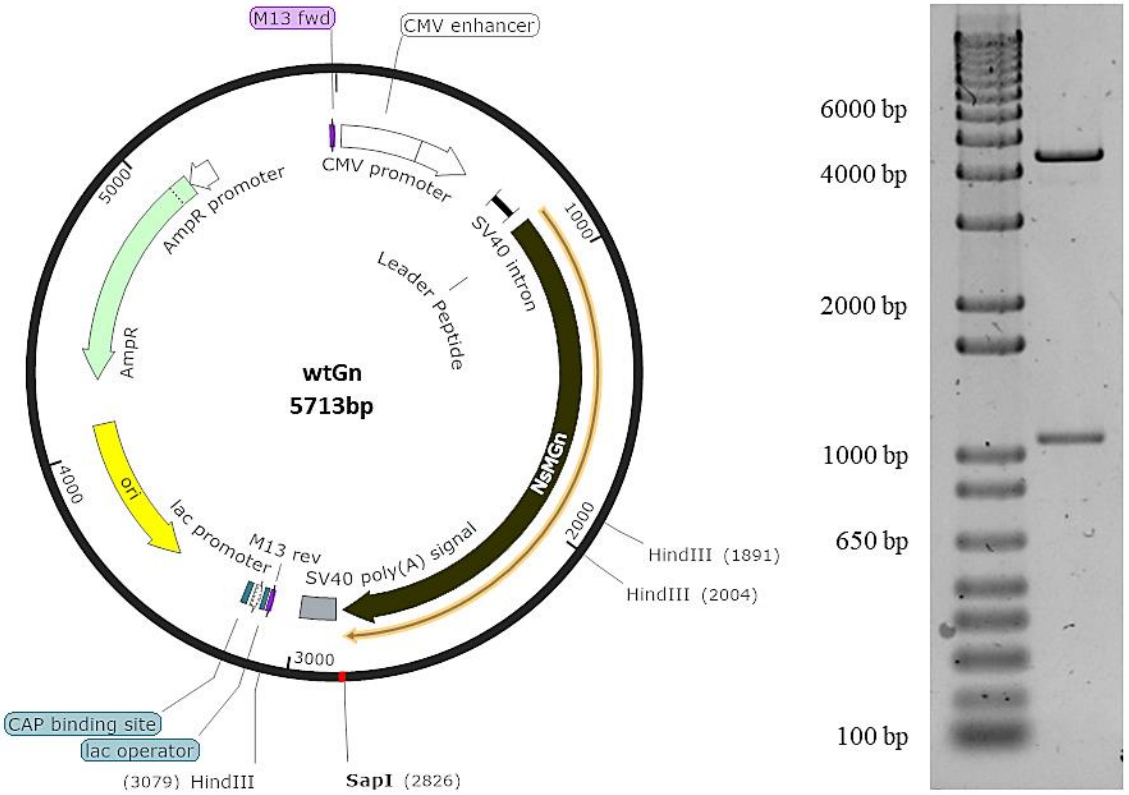

Figure 5. Composition of pCMVNSmGn plasmid. Since this point, the doubly mutated plasmid pCMVNSmGn is named wtGn in order to facilitate the reading. Left: The construct contained the Gn glycoprotein gene (Brown color) and Ampicillin resistance gene (Light green color). The recognition sites for restriction enzymes (*Hind*III and *Sap*I) and other features are indicated in the map. The plasmid was transformed into XL-1 Blue strain for its endotoxin-free purification. Then, eukaryotic cells were transfected and mice were immunized with the plasmid. Right: Digestion of Double mutant plasmid with restriction enzyme *Hind*III visualized by agarose electrophoresis. The theoretical fragments were: 13 bp, 1075 bp and 4525 bp.

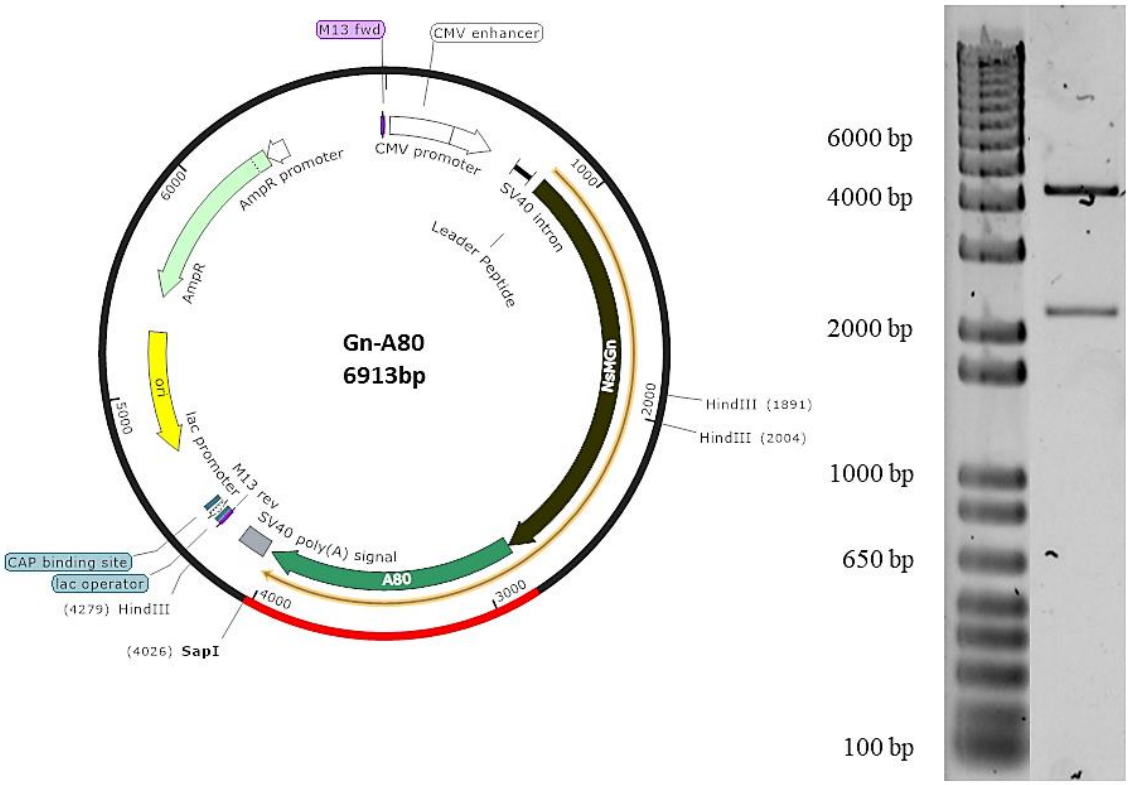

Figure 6. Composition of A80 plasmid. Left: The construct contained the Gn glycoprotein gene (Brown color), alanine-rich ELR block (Dark green color) and Ampicillin resistance gene (Light green color). The recognition sites for restriction enzymes (*Hind*III and *Sap*I) and other features are indicated in the map. The plasmid was transformed into XL-1 Blue strain for its endotoxin-free purification. Then, eukaryotic cells were transfected and mice were immunized with the plasmid. Right: Digestion of Double mutant plasmid with restriction enzyme *Hind*III visualized by agarose electrophoresis. The theoretical fragments were: 13 bp, 2275 bp and 4525 bp.

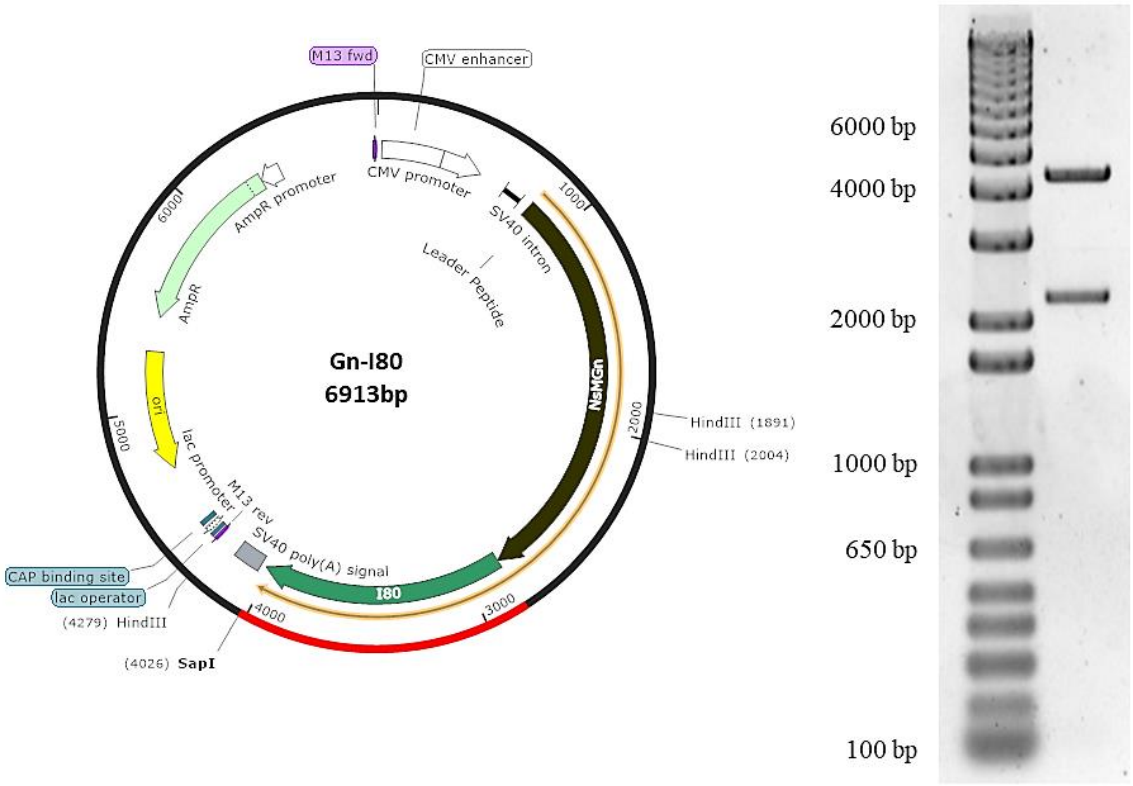

Figure 7. Composition of I80 plasmid. Left: The construct contained the Gn glycoprotein gene (Brown color), ELR block containing isoleucine (Dark green color) and Ampicillin resistance gene (Light green color). The recognition sites for restriction enzymes (*Hind*III and *Sap*I) and other features are indicated in the map. The plasmid was transformed into XL-1 Blue strain for its endotoxin-free purification. Then, eukaryotic cells were transfected and mice were immunized with the plasmid. Right: Digestion of Double mutant plasmid with restriction enzyme *Hind*III visualized by agarose electrophoresis. The theoretical fragments were: 13 bp, 2275 bp and 4525 bp.

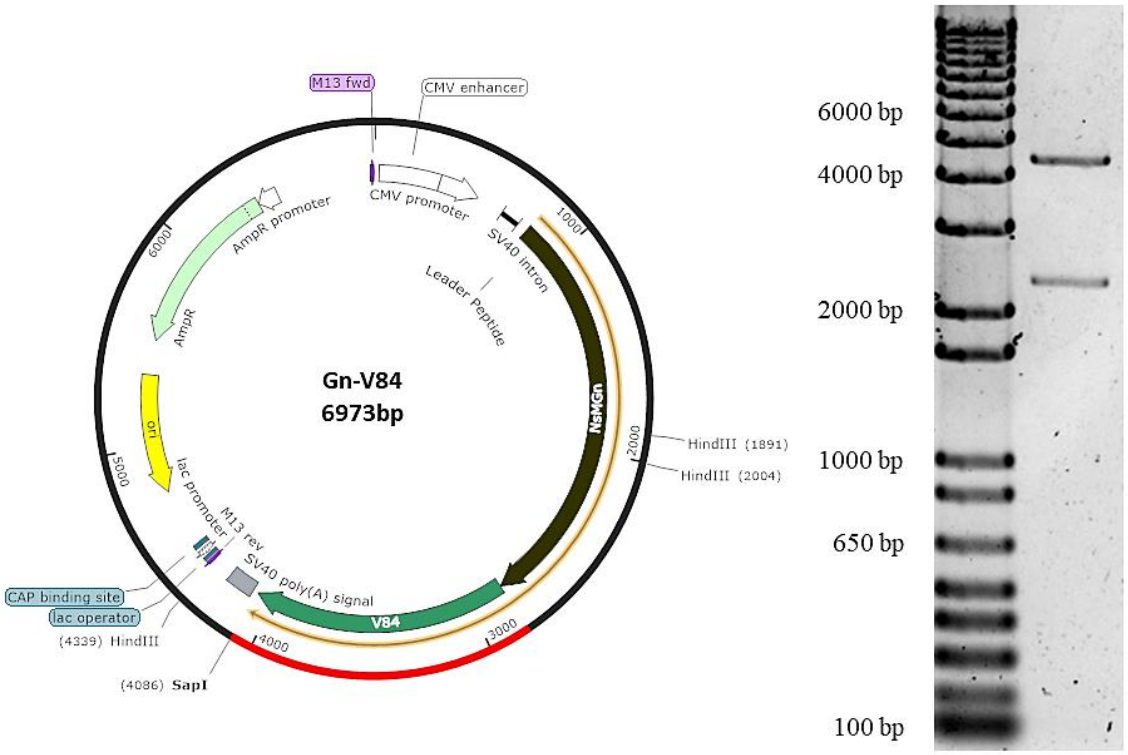

Figure 8. Composition of V84 plasmid. Left: The construct contained the Gn glycoprotein gene (Brown color), valine-containing ELR block (Dark green color) and Ampicillin resistance gene (Light green color). The recognition sites for restriction enzymes (*Hind*III and *Sap*I) and other features are indicated in the map. The plasmid was transformed into XL-1 Blue strain for its endotoxin-free purification. Then, eukaryotic cells were transfected and mice were immunized with the plasmid. Right: Digestion of Double mutant plasmid with restriction enzyme *Hind*III visualized by agarose electrophoresis. The theoretical fragments were: 13 bp, 2335 bp and 4525 bp.

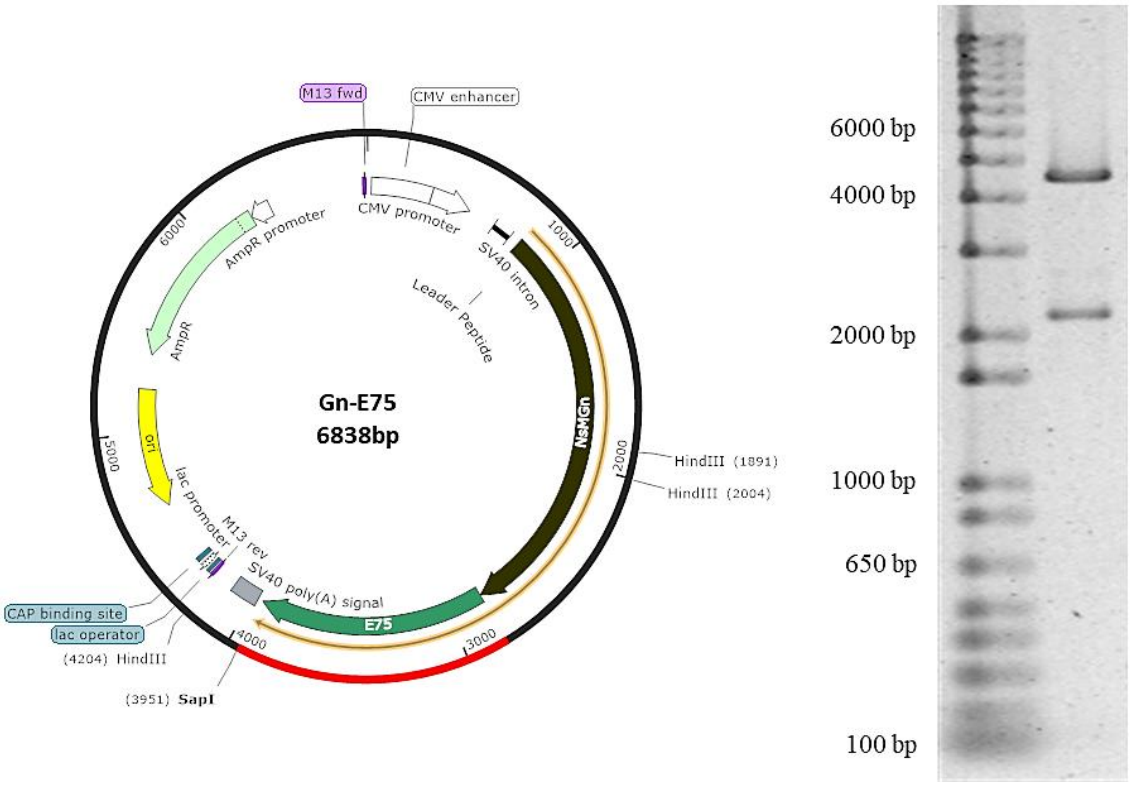

Figure 9. Composition of E75 plasmid. Left: The construct contained the Gn glycoprotein gene (Brown color), ELR block containing glutamic acid (Dark green color) and Ampicillin resistance gene (Light green color). The recognition sites for restriction enzymes (*Hind*III and *Sap*I) and other features are indicated in the map. The plasmid was transformed into XL-1 Blue strain for its endotoxin-free purification. Then, eukaryotic cells were transfected and mice were immunized with the plasmid. Right: Digestion of Double mutant plasmid with restriction enzyme *Hind*III visualized by agarose electrophoresis. The theoretical fragments were: 13 bp, 2200 bp and 4525 bp.

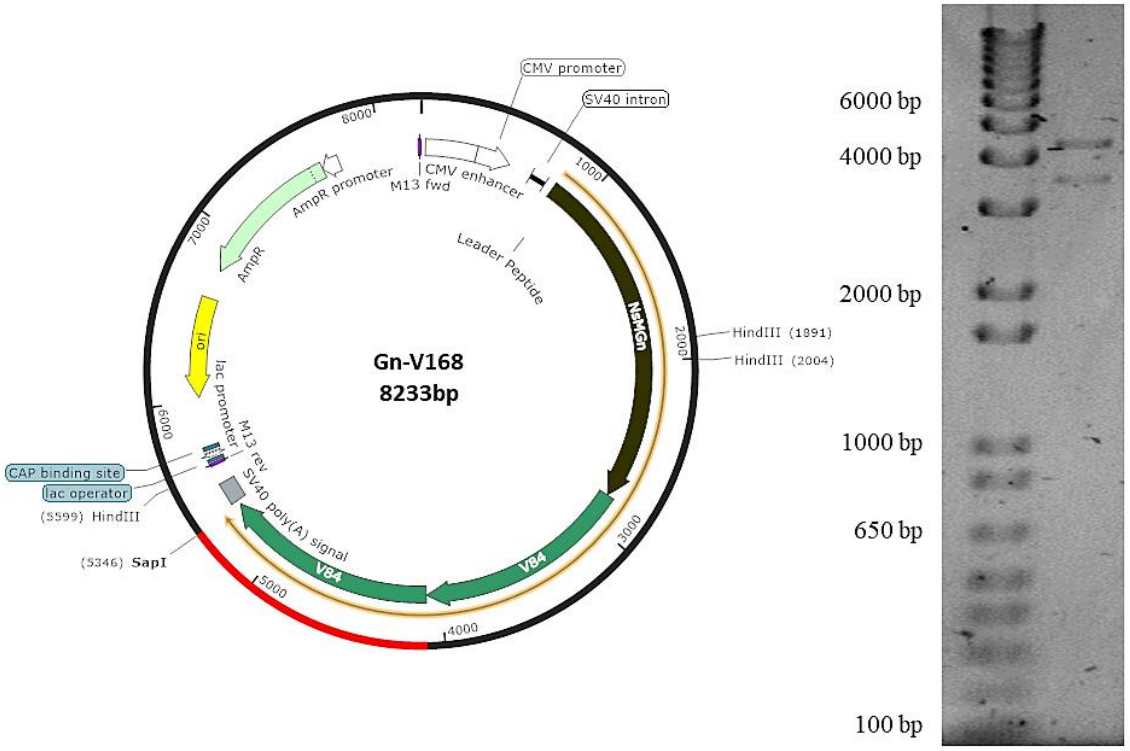

Figure 10. Composition of V168 plasmid. Left: The construct contained the Gn glycoprotein gene (Brown color), ELR block containing valine (Dark green color) and Ampicillin resistance gene (Light green color). The recognition sites for restriction enzymes (*Hind*III and *Sap*I) and other features are indicated in the map. The plasmid was transformed into XL-1 Blue strain for its endotoxin-free purification. Then, eukaryotic cells were transfected and mice were immunized with the plasmid. Right: Digestion of Double mutant plasmid with restriction enzyme *Hind*III visualized by agarose electrophoresis. The theoretical fragments were: 13 bp, 3595 bp and 4525 bp.

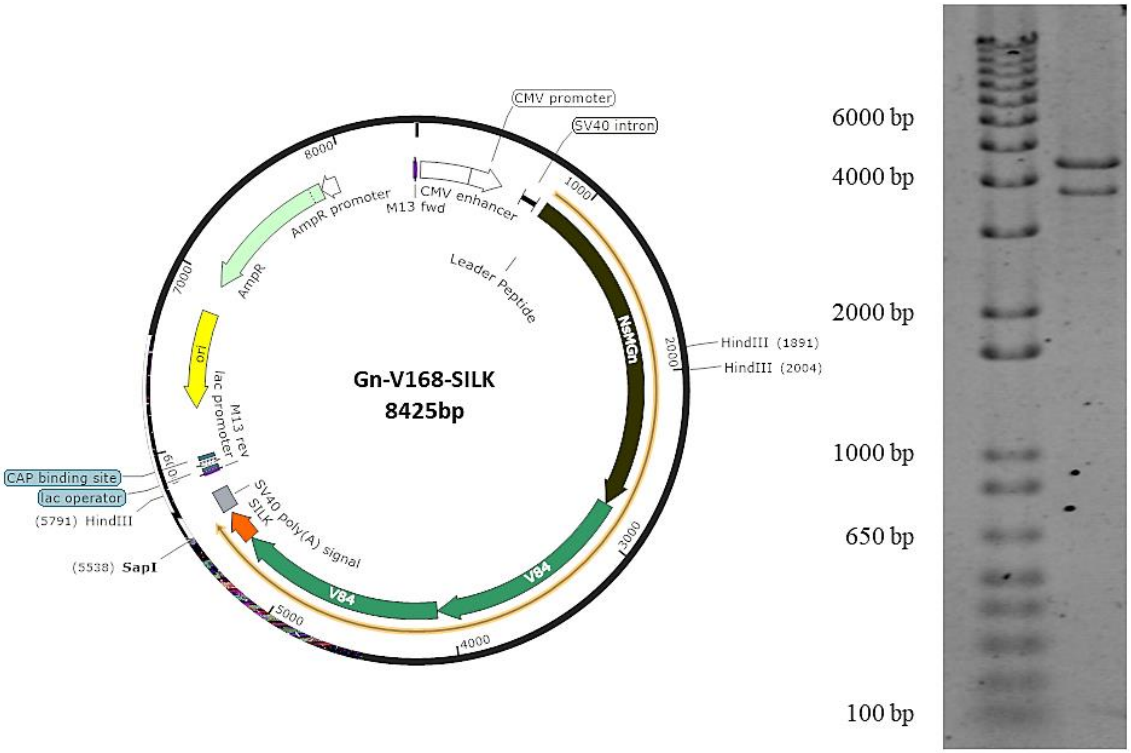

Figure 11. Composition of V168 SILK plasmid. Left: The construct contained the Gn glycoprotein gene (Brown color), ELR block containing valine (Dark green color), SILK sequence and Ampicillin resistance gene (Light green color). The recognition sites for restriction enzymes (*Hind*III and *Sap*I) and other features are indicated in the map. The plasmid was transformed into XL-1 Blue strain for its endotoxin-free purification. Then, eukaryotic cells were transfected and mice were immunized with the plasmid. Right: Digestion of Double mutant plasmid with restriction enzyme *Hind*III visualized by agarose electrophoresis. The theoretical fragments were: 13 bp, 3787 bp and 4525 bp.

5.1.3.4 Effect of transfected plasmids in cell viability

The main objective of this chapter was to obtain recombinant constructs able to improve the expression level of viral glycoprotein Gn in eukaryotic cells. Therefore, these plasmid constructs should be completely innocuous upon cell uptake. Cell viability was determined after transfection of the plasmid constructs in order to assess the suitability of the plasmid constructs (Figures 12 and 13). In order to transfect 293T cells, either Lipofectamine or Turbofect transfection systems were used, as both are some of the most standard transfection systems.

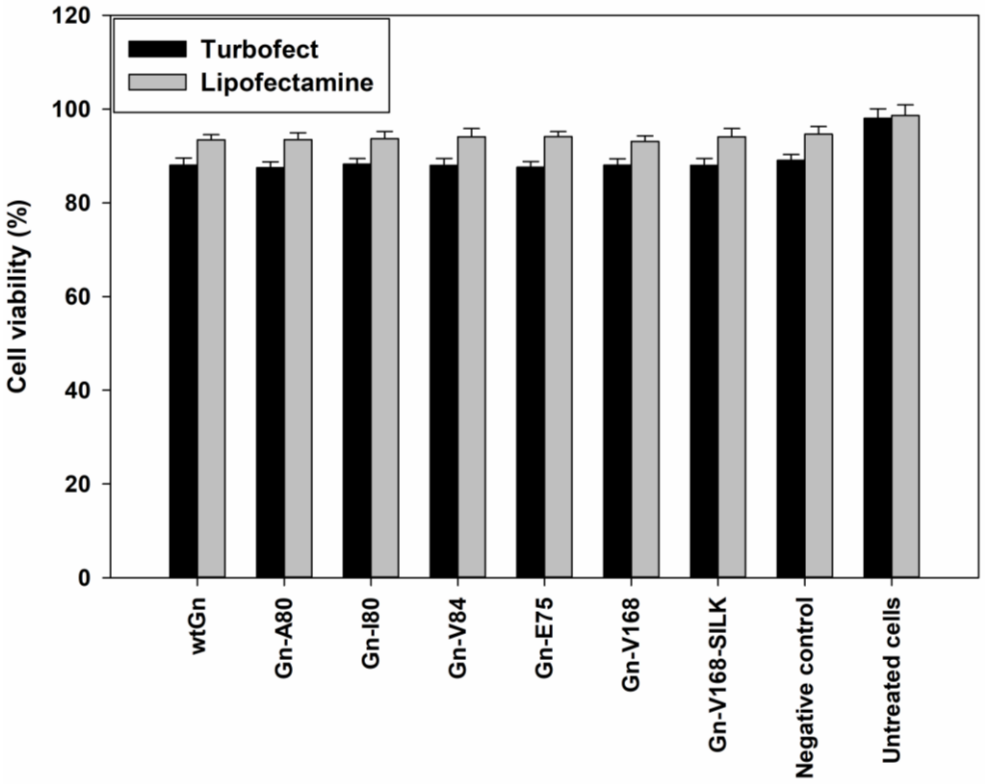

Figure 12. Cell viability of 293T human embryonic kidney cells after transfection of DNA constructs with Lipofectamine or Turbofect. Cells were transfected with corresponding DNA construct and viability was measured 24 hours later using the LIVE/DEAD assay kit. Negative control is referred to cells transfected with Lipofectamine or Turbofect without DNA. n = 3 independent experiments, mean ± SD.

Transfected cells with different fusion genes showed similar viability levels to positive control. At light of this result, we could conclude that the slightly effect on cell viability was due to the transfection procedure and none of the different gene constructs seemed to significantly affect cell viability. Thus, these results highlighted that the developed plasmid constructs were safe, one of the requirements when working with DNA vaccines. Moreover, cell viability was higher in Lipofectamine treated cells compared to Turbofect ones (Figures 12 and 13). For this reason, we used Lipofectamine as transfection reagent in the following experiments.

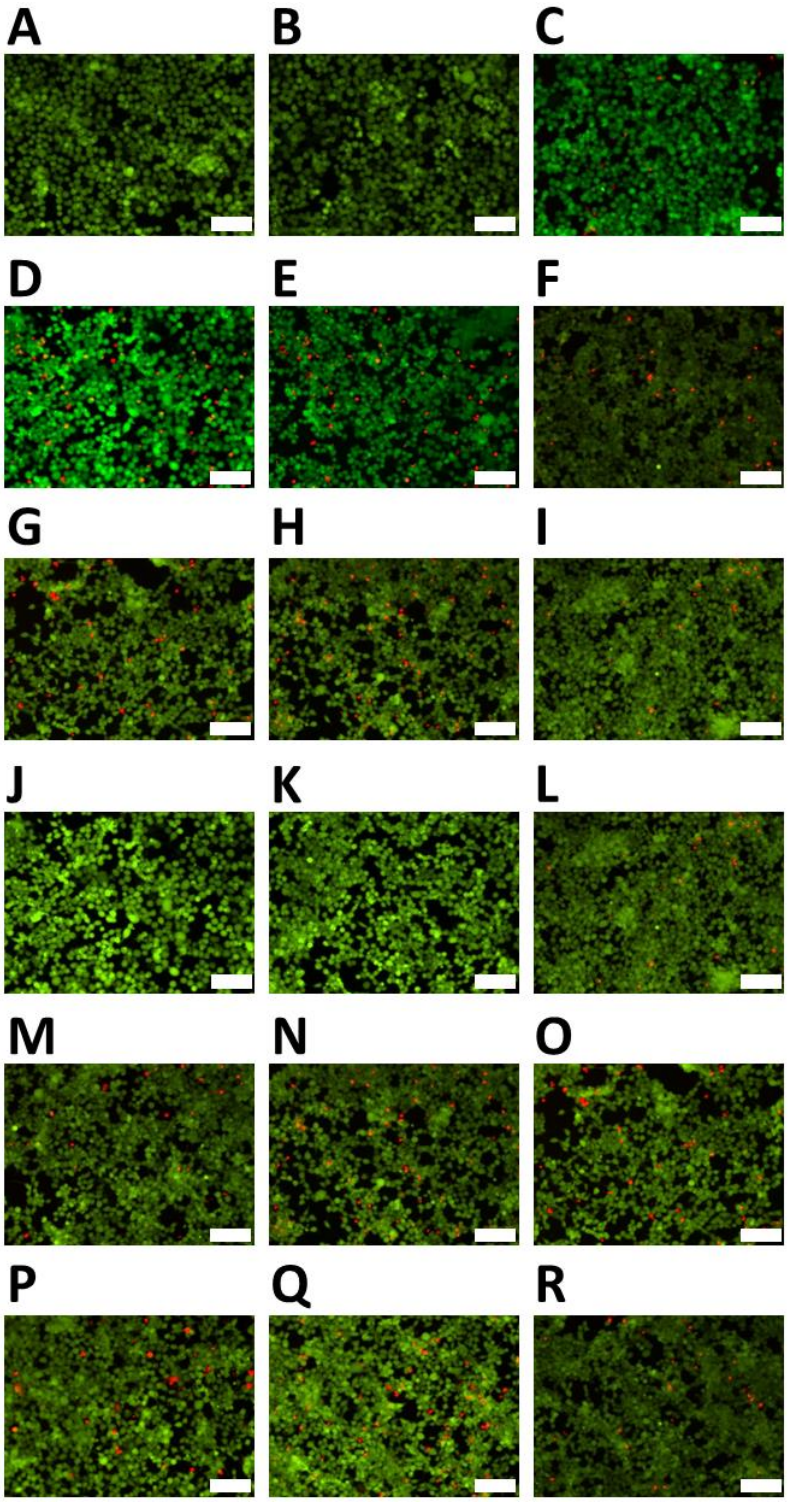

Figure 13. Representative fluorescence microscopy images of 293T human embryonic kidney cells after transfection of DNA constructs with (A-I) Lipofectamine or (J-R) Turbofect. Cells were transfected and viability was measured 24 hours later using the LIVE/DEAD assay kit. A and J: untreated cells; B and K: control plasmid; C and L: wtGn; D and M: Gn-A80; E and N: Gn-I80; F and O: Gn-V84; G and P: Gn-E75; H and Q: Gn-V168; I and R: Gn-V168-SILK. Scale bars: 100 µm.

5.1.3.5 Analysis of Gn glycoprotein *in vitro* expression

Once the gene constructs were shown innocuous, the expression of Gn glycoprotein in eukaryotic cells was determined in order to compare the production levels of the fused genes with respect to the expression of the non-fused Gn viral antigen (Figure 14). For this purpose, 293T cells were transfected as explained above and Gn glycoprotein expression was measured by immunocytochemistry. Hyperimmune serum from RVFV-infected mice was used as primary antibody. The wtGn plasmid containing the gene codifying for RVFV Gn glycoprotein was used as positive control. As shown in Figure 14, both Gn-A80 and Gn-I80 constructs not only did not improve the expression of the viral glycoprotein, but also the expression level was even lower than that of the positive control. However, either Gn-E75 or Gn-V84 constructs significantly increased the expression of RVFV Gn glycoprotein (40% and 29%, respectively). Interestingly, Gn-V84 improved Gn expression, contrary to the results shown by the other amphiphilic constructs Gn-A80 and Gn-I80. The enhanced expression of Gn glycoprotein comprised in the Gn-E75 construct correlated to the fact that the viral antigen was soluble instead of assembled in amphiphilic aggregates. Moreover, both the Gn-V168 and Gn-V168-SILK construct, containing two blocks of Valine and gene codifying for worm silk, showed similar Gn glycoprotein expression levels than the positive control. Even though the viral glycoprotein expression level in transfected cells with the Gn-V168 construct was higher than the level shown by cells transfected with positive control, this difference was not statistically significant.

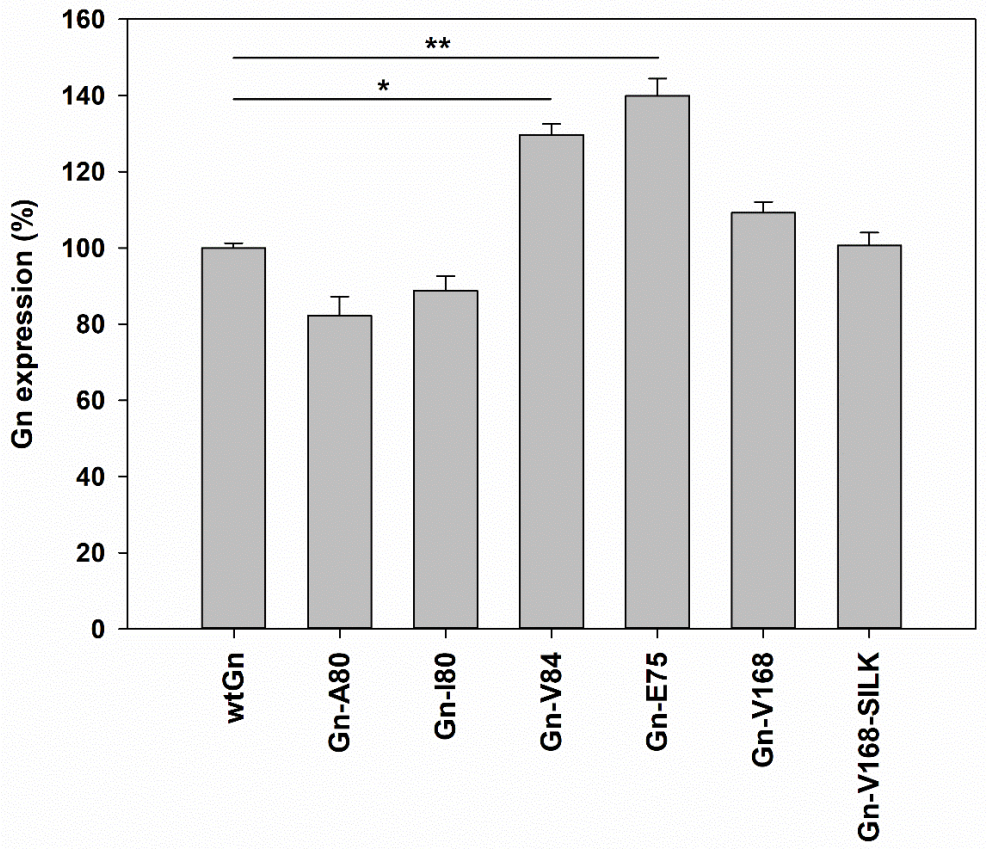

Figure 14. Expression level of Gn glycoprotein in 293T human embryonic kidney cells. Cells were transfected with Lipofectamine and the indicated DNA construct. After 24 hours, cells were fixed, permeabilized and blocked. After incubation with RVFV-immunized mouse serum and secondary antibody, fluorescence intensity was measured in a microplate reader. n = 3 independent experiments, mean ± SD. Statistical analysis involved an analysis of variance (Anova) test in combination with subsequent Bonferroni method. *$p < 0.01$ **$p < 0.001$

These results, in which longer constructs did not improve Gn expression, could be due to the fact that large proteins are more difficult to be translated and processed in eukaryotic cells [45, 46]. Furthermore, an excessive hydrophobicity of these constructs could difficult their translation in eukaryotic cells [47, 48]. Thus, we could conclude that the expression of Gn glycoprotein was not improved by constructs with hydrophobic ELR blocks, as Isoleucine and Alanine. Contrary, less hydrophobic Gn-V84 and hydrophilic Gn-E75 constructs significantly improved the antigen expression in 293T cells. Thus, we could conclude that our constructs would be a promising approach in order to produce huge amounts of antigens *in vitro.* This system could be used as an accurate strategy to improve the production of natural antigens needed for vaccines involving a scaled up process and reduced productions costs. As a consequence of these results, Gn-E75, Gn-V84, Gn-V168 and Gn-V168-SILK encoding

plasmid constructs were chosen for the *in vivo* assays in order to determine their ability to induce anti-Gn immune responses in mice.

Furthermore, confocal microscopy images were taken in order to determine cellular localization of translated fusion proteins after cell transfection with gene constructs. As shown in Figures 15 and 16, fusion proteins composed by ELRs and viral Gn glycoprotein showed cytoplasmic localization in all cases. This result suggested that the presence of ELR blocks did not change the perinuclear localization of the fusion proteins, regardless of its amino acid composition. Indeed, there were no differences in cellular localization between those constructs that improved Gn expression and those provoking lower expression levels.

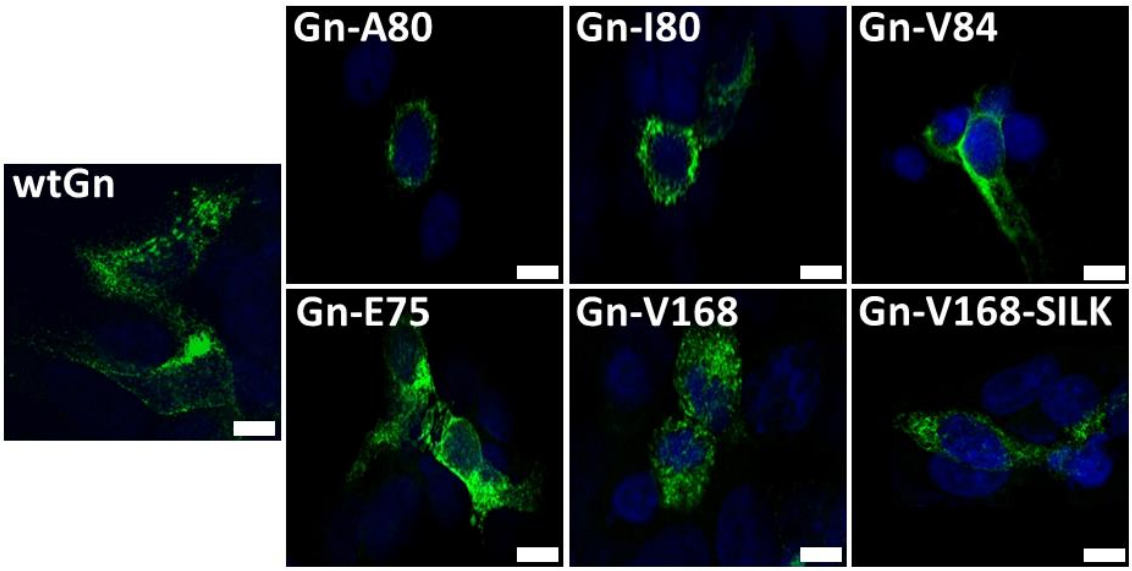

Figure 15. Confocal microscopy images of 293T human embryonic kidney cells after transfection with Lipofectamine and the corresponding DNA construct. After 24 hours, cells were fixed with PFA 4%, permeabilized with Triton X-100 0.1% and blocked by FBS 2%. After incubation with RVFV-immunized mouse serum, confocal pictures were taken. Representative pictures are depicted. Scale bars: 5 µm.

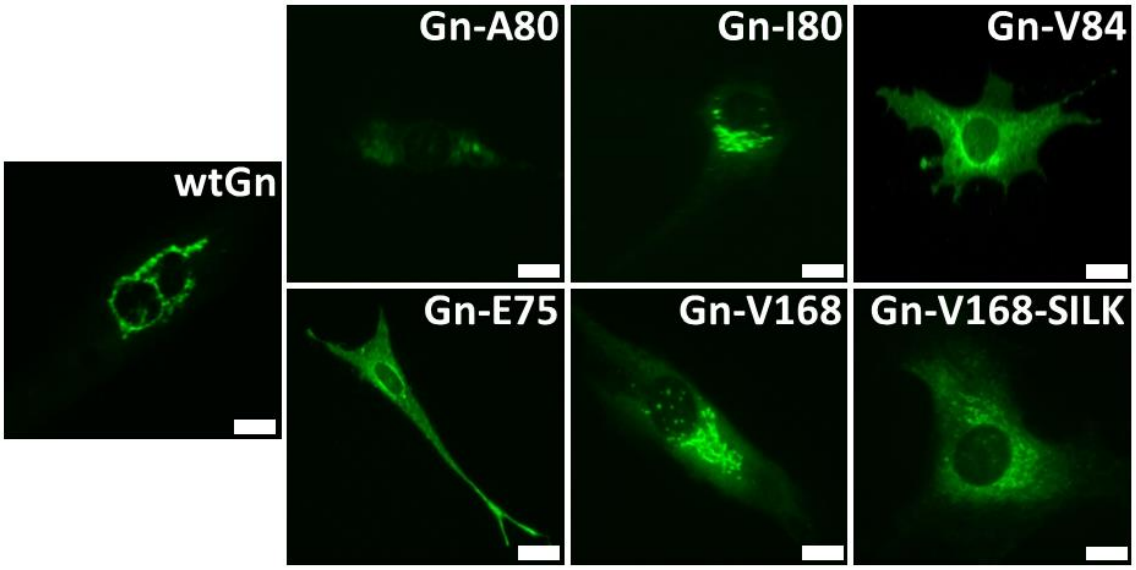

Figure 16. Confocal microscopy images of BHK-21 (C-13) hamster kidney fibroblasts after transfection with Lipofectamine and the corresponding DNA construct. After 24 hours, cells were fixed with PFA 4%, permeabilized with Triton X-100 0.1% and blocked FBS 2%. After incubation with RVFV-immunized mouse serum and secondary antibody, confocal pictures were taken. Representative pictures are depicted. Scale bars: 5 µm.

Based on the thermosensitive ability of ELRs, hydrophobic/hydrophilic nature of the chosen amino acid as guest residue within the pentapeptide sequence determines different Tt, above which self-assembling into ordered structures is achieved [40]. Thus, Urry determined that glutamic acid-containing blocks assembled above 70°C [41]. Contrary, ELRs based on hydrophobic residues, such as alanine, isoleucine and valine have been demonstrated to form aggregates-like structures [29, 38, 49]. As expected, fusion constructs involving ELR blocks composed by hydrophobic amino acids (Gn-A80, Gn-I80, Gn-V84, Gn-V168 and Gn-V168-SILK) seemed to show an aggregation-like appearance (Figures 15-17). These microscopic aggregates could be due to amphiphilic structures, as a consequence of the hydrophilic nature of RVFV Gn glycoprotein. Thus, when the hydrophobic component was increased, aggregates were observed. Contrary, cells transfected with Gn-E75 construct showed higher viral glycoprotein expression in the whole cytoplasm without aggregation appearance (Figures 15, 16 and 18). This could be due to the fact that glutamic acid remains soluble and is not able to self-assemble in an ordered structure under physiologic conditions [40, 41]. Due to the ionization of the glutamic acid side chains, the ELR polymer become less hydrophobic and the Tt shifts to higher temperatures. In fact, glutamic

acid-containing blocks self-assemble above 70°C, which means that Gn-E75 is not able to self-assemble under physiologic conditions [40, 41].

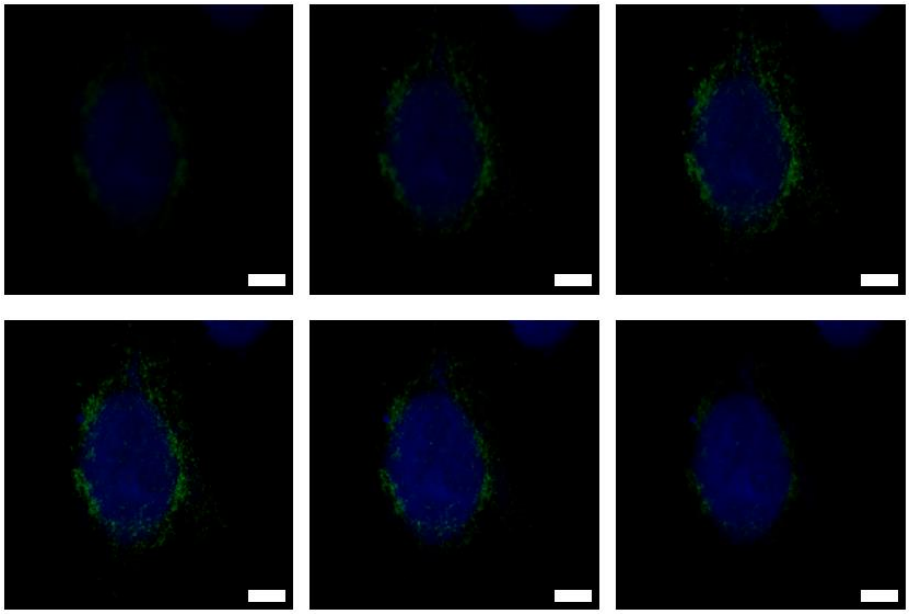

Figure 17. Z-stack confocal microscopy images of 293T human embryonic kidney cells after transfection of Gn-V168 construct. Cells were transfected with Lipofectamine and the Gn-V168 construct. After 24 hours, cells were fixed with PFA 4%, permeabilized with Triton X-100 0.1% and blocked by FBS 2%. After incubation with RVFV-immunized mouse serum, confocal pictures of different focal planes were analyzed. The z-focal difference between images is 0.4 µm. Scale bars: 2 µm.

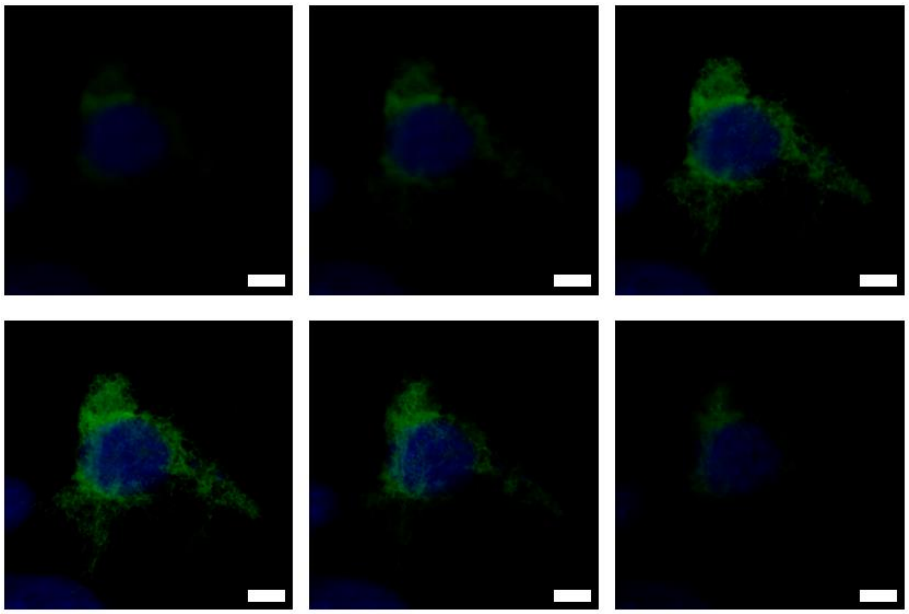

Figure 18. Z-stack confocal microscopy images of 293T human embryonic kidney cells after transfection of Gn-E75 construct. Cells were transfected with Lipofectamine and the Gn-E75

construct. After 24 hours, cells were fixed with PFA 4%, permeabilized with Triton X-100 0.1% and blocked by FBS 2%. After incubation with RVFV-immunized mouse serum, confocal pictures of different focal planes were analyzed. The z-focal difference between images is 0.4 µm. Scale bars: 2 µm.

5.1.3.6 *In vivo* plasmid biodistribution

Once showed cell viability was not affected by cell transfection with gene constructs, the plasmid biodistribution was analyzed *in vivo* in mice (Figure 19). Regarding Gn expression results (Figure 14), both Gn-E75 and Gn-V84 seemed to be enhancers of viral glycoprotein expression. For this reason, we selected Gn-E75 plasmid for determining the constructs biodistribution. Briefly, plasmids were labeled with Quantum Dots throughout a Biotin/Streptavidin reaction, as described above. Quantum dots-labeled Gn-E75 plasmid was injected intravenously into BALB/c mice and the biodistribution was monitored using the IVIS *In Vivo* Imaging System after subtracting background from an untreated mouse.

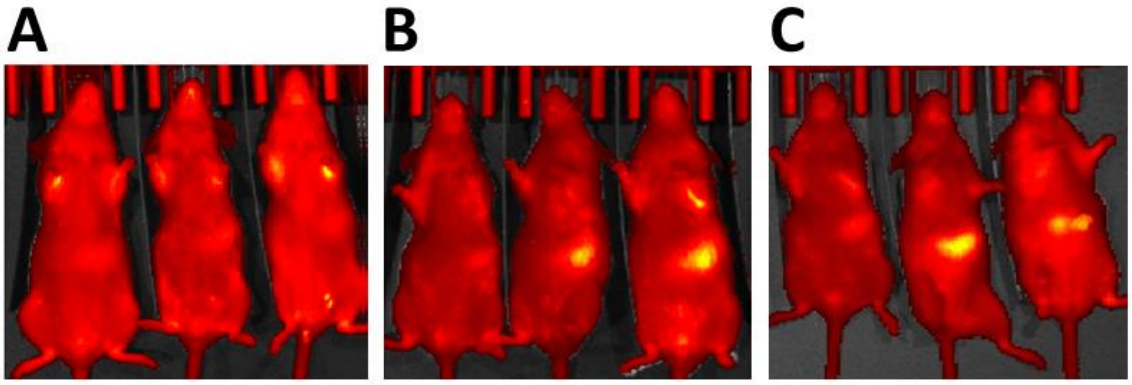

Figure 19. *In vivo* imaging of the biodistribution of QD-labeled Gn-E75 DNA construct after intravenous administration into anaesthetized BALB/c mice. Animals were transferred immediately to the IVIS imaging system with continuous anaesthesia during measurement. Untreated animal (Left) was measured as control. The images were obtained at 15 min (A), 1 hour (B) and 24 hours (C) post injection (p.i.).

As shown in Figure 19B-C, Gn-E75 construct accumulated in the spleen after 1 and 24 hours post injection. At earlier time point, 15 min, there was no signal in the body probably because the construct was still circulating systemically (Figure 19A). The spleen is an immune organ, whose functions involve antigen clearance, B and T cell maturation, and storage of monocytes, macrophages and lymphocytes [50]. Indeed, injected nanodevices are strained and therefore uptaken by macrophages or splenocytes in the spleen [51]. Thus, the presence of intravenously administered Gn-E75 plasmid in

the spleen, which is a major reservoir of Antigen-Presenting Cells (APC), could mean that the ELR-Gn construct was recognized by immune system and could thereby induce the expression of the antigen and later presentation. Furthermore, there was no lung accumulation, which is important due to lung capillaries are some of the smallest blood vessels in the whole body and accumulation occurs when aggregates are formed [52].

5.1.3.7 Neutralizing antibody responses and efficacy elicited upon plasmid immunization in mice

Once the expression of viral Gn antigen fused to different ELR blocks was determined *in vitro* (Figure 14), we studied the immune response in an *in vivo* mouse model of DNA vaccination strategy. Thus, the development of a neutralizing antibody response was analyzed after two or three plasmid intramuscular doses. Neutralizing antibodies play an important role within the immune system, as their function consists on the defense of host cells from antigens by neutralizing their biological effect [53]. Therefore, the action of these antibodies differs from binding antibodies, which target antigens in order to notice white blood cells to destroy the infectious agent [54]. The scheme of performed immunization is depicted in Figure 20A.

As shown in Figure 20, two plasmid doses were insufficient to achieve a robust and consistent neutralizing antibody response, with only few animals within each group developing detectable but low titers of antibodies (Figure 20B-C, empty symbols). However, higher and statistically significant neutralizing responses were detected in 100% of the animals in the group receiving the plasmid expressing wtGn. After a third DNA boost, neutralizing titers were clearly enhanced in all groups (Figure 20, full symbols) although a few animals remained negative in some groups (Gn-E75, Gn-V168-SILK and Gn-V168). No clear differences were observed in the group immunized with the Gn-V168-SILK construct and, surprisingly, the sera from wtGn group animals collected after the third plasmid dose showed a decrease in their neutralization titers. In fact, after three doses, wtGn animals showed similar neutralization titers compared to Gn-V84 group, which clearly improved the results obtained with only two doses. This could be due to the fact that expression levels of the viral antigen, when combined with ELR constructs, could have longer half-life compared to wild type antigen. Despite these single differences, statistical analysis did not reveal significant differences among

mean values of neutralizing antibody titers obtained after 3 doses of the different DNA constructs assayed.

Three days after the last DNA booster dose, mice were subjected to virus challenge with a lethal dose of the virulent RVFV strain 56/74. A naïve (mock-immunized) group of mice was included as a control. At day 3 p.i., when viremia is known to reach a peak in infected animals, blood samples were collected and viral loads were analyzed. Results are shown in Figure 20C. All groups showed a clear reduction in viremia levels compared to the infected control group (mean value = 5.29 ± 0.48). This decrease was around one log unit lower for the groups immunized with either Gn-E75 or Gn-V168-SILK constructs (mean values of 4.06 ± 0.37 and 4.31 ± 0.85, respectively; differences not statistically significant). In contrast, groups receiving Gn-V84 or Gn-V168 plasmids showed reductions of 2 log units (mean values of 2.95 ± 1.46 and 3.1 ± 1.02, respectively; $p < 0.001$), and 40% of the animals rendering viral loads at or below the detection limit of the assay. As expected from the higher neutralizing titers reached during immunization, the group of mice immunized with the wtGn expressing construct showed lower or undetectable viremia levels (mean value = 1.80 ± 0.45; $p<0.0001$).

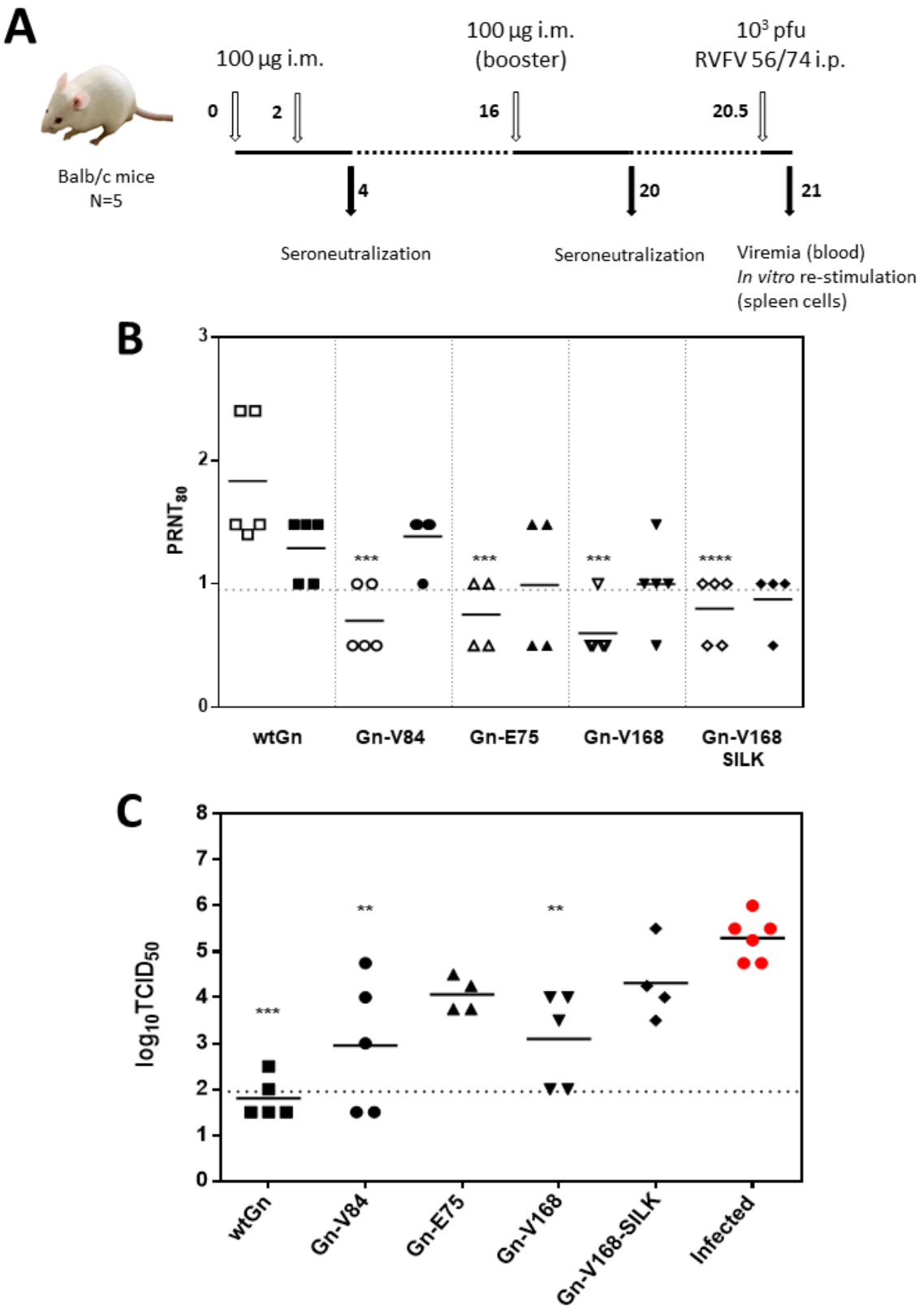

Figure 20. A: Scheme of the immunization and challenge of mice. Groups of n=5 BALB/c mice were intramuscularly immunized twice with each plasmid construct (n=4 for Gn-E75 group) with an additional boost 12 weeks later (open arrows). Mice were challenged intraperitoneally with 10^3 pfu of virulent RVFV 56/74 (one mouse belonging to the Gn-V168-SILK group died before the last boost). Blood samples were collected to monitor immune responses and viremia (closed arrows).

Numbers indicate weeks after the starting of the experiment. B: Neutralizing antibodies after immunization. Titers of serum neutralizing antibodies after two (empty symbols) or three immunizations (closed symbols). Each symbol corresponds to a single mouse. Titers correspond to the mean dilutions of serum that reduce the number of plaques by 80% in a plaque reduction neutralization test (PRNT). Serum dilutions are expressed as $\log_{10}$. Horizontal dotted line depicts the sensitivity of the assay. Negative values were given an arbitrary value of 0.5 log. One way Anova with Bonferroni multiple comparisons was used for testing the statistical significance. *p* values are shown with respect to wtGn group (***p<0.001 ****p<0.0001). C: Viremia after challenge of immunized mice. 3 days after viral challenge the mice were euthanized and diluted blood samples tested on Vero cells for the presence of infectious virus. Each symbol corresponds to a single mouse. Group meanings are shown. Titers correspond to the mean dilutions of blood causing 50% of cytopathic effect *in vitro* in a tissue culture infectivity dose (TCID) assay. Horizontal dotted line depicts the sensitivity of the assay. Negative values were given an arbitrary value of 1.5 log. One way Anova with Bonferroni multiple comparisons was used for testing the statistical significance. *p* values are shown with respect to infected (mock vaccinated) group (**p<0.01 ***p<0.001). This experiment was performed at Instituto Nacional de Investigación y Tecnología Agraria y Alimentaria (INIA) in Madrid.

These results suggest that, even though variability between individual mice within the groups was high, the best responses in terms of reduction of viral load were achieved by immunization with Gn-V84 and Gn-V168 constructs, without apparent correlation with the levels of Gn protein expression in cultured transfected cells (Figure 14). Thus, it is possible to assume that the quantity of Gn expression *in vitro* did not correlate with the neutralization levels nor efficacy *in vivo* and that the immunogenicity of the constructs may be conditioned by other factors. Among these, the level of aggregation could benefit the magnitude and duration of the immune responses in terms of neutralization suggested by the data from immunization with the more hydrophobic Gn-V84 or Gn-V168 constructs.

5.1.3.8 Cellular immunity in mice upon viral challenge

In order to gain more insight in the type of immune responses elicited by the different constructs, the induction of cellular immunity was assessed by *in vitro* re-stimulation of spleen cells obtained upon virus challenge. The measurement of the Th1/Th2 cytokine balance is a good indicative of the extent of antigen-specific cellular immune responses. A luminex-based assay was performed using supernatants of spleen cells collected after stimulation with either a class-I restricted Gn peptide described previously [55] or with virus infected RAW 264.7 cells (Figure 22). This cell line retains characteristics of an antigen presenting cell (APC). Upon isolation the viability of the spleen cells used for re-stimulation ranged between 80-95% (data not shown). The re-stimulation with the

Gn peptide increased the secretion of IFN gamma, in agreement with the Class-I MHC restricted nature of the peptide. IFN gamma levels were increased in wtGn, Gn-V84, Gn-V168 and Gn-V168-SILK groups, but not in non-vaccinated mice (mock) and Gn-E75 groups, although these differences did not reach statistical significance. Compared to mock treated cells, the stimulation of wt-Gn spleen cells showed significantly increased expression of IL12p70 and TNF. In turn, Gn-V168 induced a higher expression of IL1β and IL12p70, when compared to mock treated cells (Figure 21A). Interestingly, both wt-Gn and Gn-V168 groups secreted significantly higher levels of IL-6 than the mock group, and Gn-V168 had also increased levels of IL-4, IL-5 and IL-13, indicating a strong Th2 polarization (Figure 21B). Therefore, a more balanced T-cell response was promoted by V168 construct.

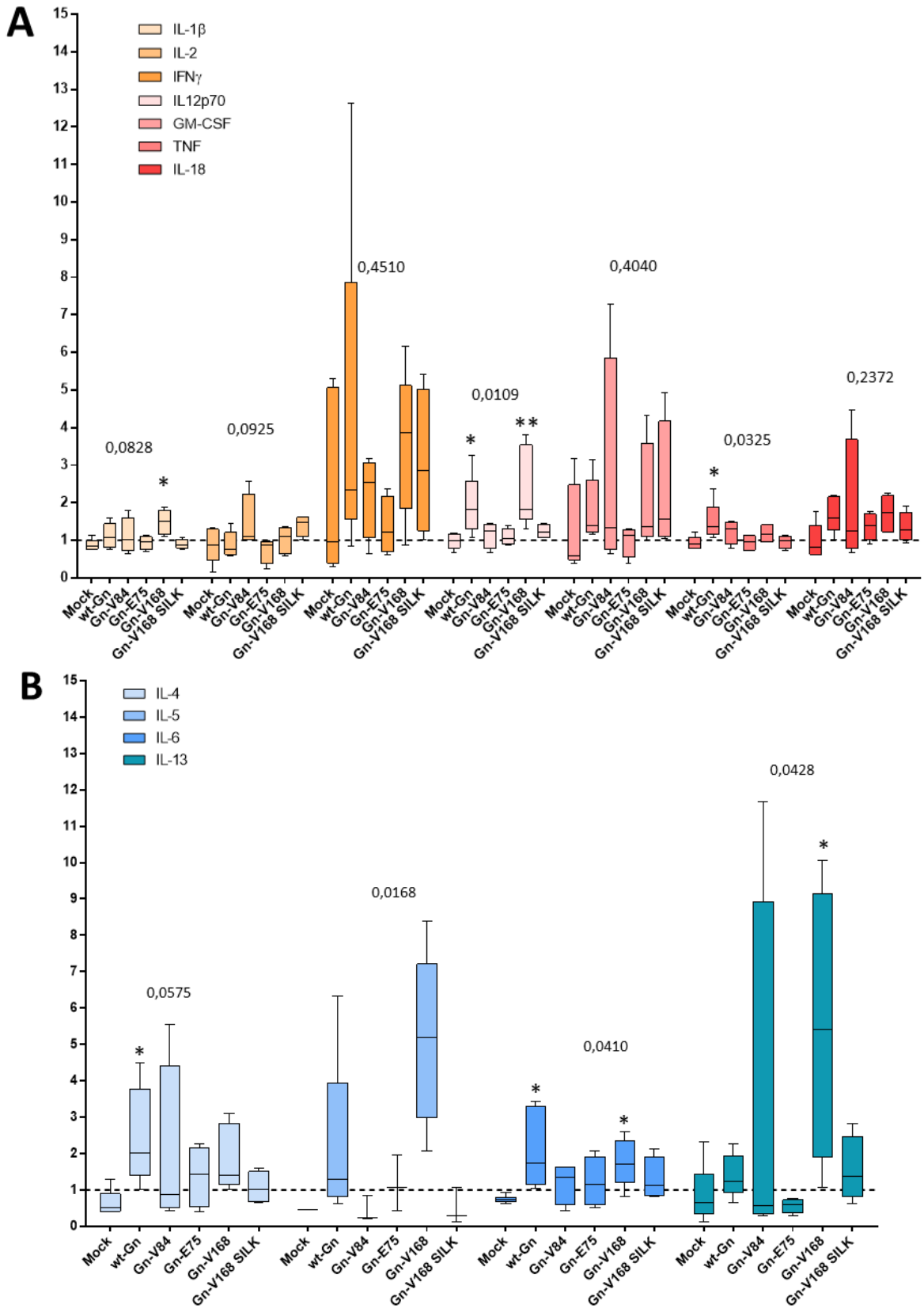

Figure 21. Th1 (A) or Th2 (B) cytokines secreted by cultured spleen cells upon stimulation with a Gn peptide. The values on the Y axis correspond to the stimulation index (ratio specific peptide/ medium). Each box represents the interquartile rank defined by the median value (horizontal line)

for the indicated groups of immunized and 3-day infected mice. Mock group refers to the non-immunized and infected mice. Values above 1 (horizontal dotted line) indicate a positive stimulation. Numbers above bars indicate p values (Anova, non-parametric Kruskall-Wallis test). Asterisks indicate the level of significance with respect to the mock immunized group. *$p<0.05$, **$p<0.01$. IL-5 index values were not determined for the mock group due to the low sensitivity of the assay. Only three values were obtained for Gn-V84, Gn-E75 and Gn-V168-SILK. This experiment was performed at Instituto Nacional de Investigación y Tecnología Agraria y Alimentaria (INIA) in Madrid.

In contrast, the cytokine secretion elicited by infected RAW 264.7 cells was predominantly IFN gamma and IL-12, perhaps as a consequence of the activation of naive CD4 cells (Figure 22). The Gn-V168 and wt-Gn constructs induced the strongest bias towards Th2 responses in which IL-13 was more prominently secreted. These data indicate that, among the ELR plasmid constructs, Gn-V168 induced stronger levels of cell-mediated soluble effectors, perhaps contributing more efficiently to the protective phenotype observed after viral challenge. Although more experiments are needed to explain these differences, it is possible to speculate that the more particulated nature of the antigen expressed by Gn-V168 (Figures 15F, 16F and 18) favors other forms of immune presentation, such as autophagy of intact antigens, that enhances the MHC-class-II processing pathway.

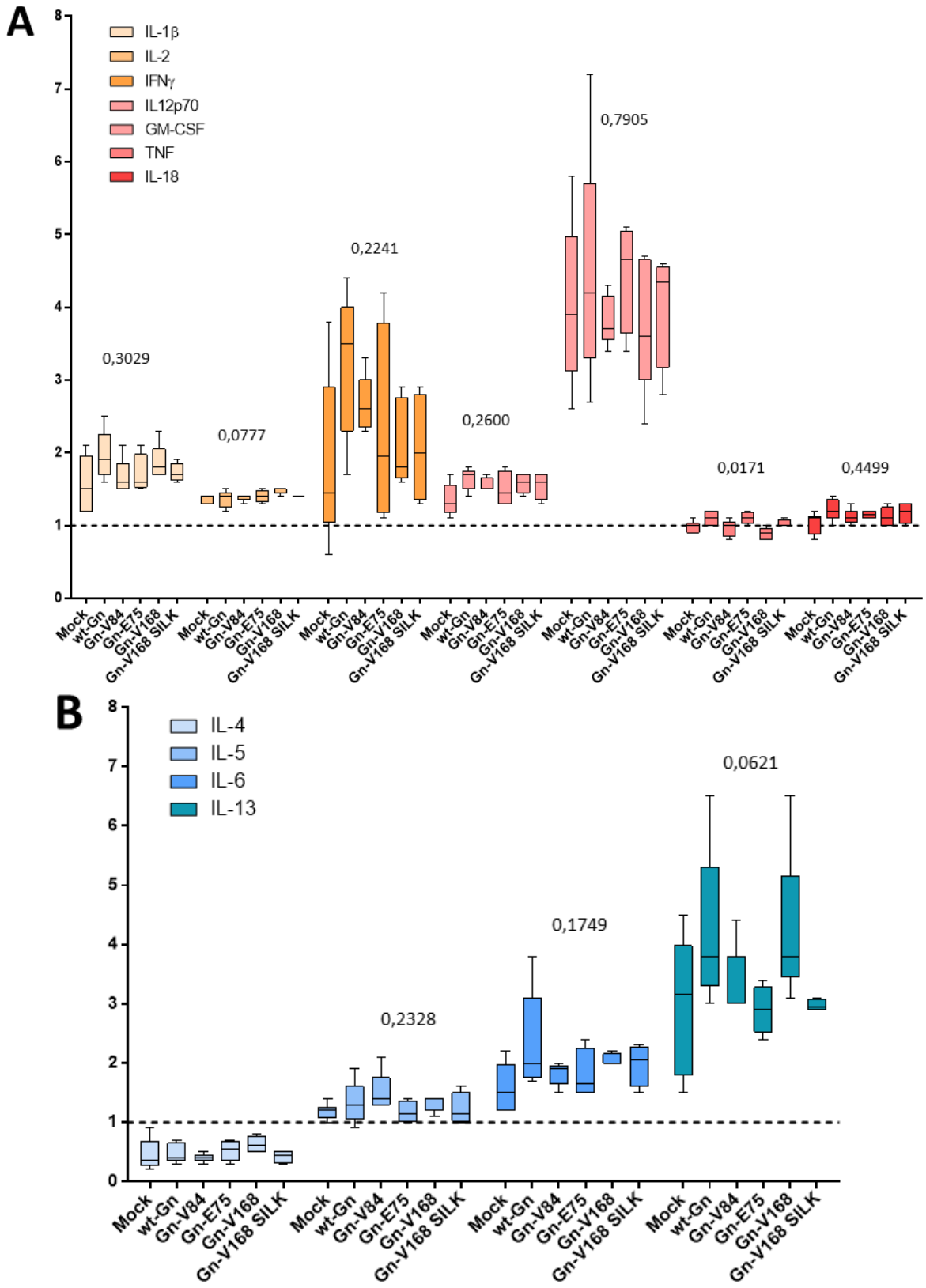

Figure 22. Th1 (A) or Th2 (B) cytokines secreted by cultured spleen cells upon stimulation with infected RAW 264.7 cells. The values on the Y axis correspond to the stimulation index (ratio infected cells/non-infected cells). Each box represent the interquartile rank defined by the median value (horizontal line) for the indicated groups of immunized and 3-day infected mice. Mock group

refers to the non-immunized and infected mice. Values above 1 (horizontal dotted line) indicate a positive stimulation. Numbers above bars indicate p values (Anova non-parametric Kruskall-Wallis test). This experiment was performed at Instituto Nacional de Investigación y Tecnología Agraria y Alimentaria (INIA) in Madrid.

5.1.4. Final remarks

In this chapter, we have developed novel ELR-based devices in order to test their immunogenicity and vaccine potential against Rift Valley fever virus by DNA vaccination strategies. First, viability in eukaryotic cells was not affected after transfection with genetic plasmids, which showed that our constructs are safe, one of the most important requirements for DNA vaccination. Moreover, two different constructs, Gn-E75 (with an ELR block based on glutamic acid) and Gn-V84 (whose ELR block contained valine), enhanced the viral glycoprotein expression. Therefore, this system could be a promising approach in order to achieve high yield productions of natural antigens, which could have great importance when huge amounts of vaccines are needed in pandemic situations. *In vivo* immune-challenge experiments in a mouse animal model determined the immunogenicity and efficacy after challenge of the construct Gn-V168. Thus, these constructs are highly suitable for further studies. Peptide antigens are not enough immunogenic to initiate adaptive immune responses, so adjuvants are responsible of the long-term efficacy of vaccines [56]. Furthermore, biomaterials have become an encouraging tool for vaccine development, due to their ability to isolate and produce pure proteins and peptide antigens safer than traditional vaccines [57-59]. Thus, ELRs possess most of features from an ideal adjuvant factor, such as biodegradability, stability, low cost, easy manufacture, minimal adverse effects and wide applicability [60, 61]. For all these reasons, ELRs could be promising tools in order to act as accurate adjuvants and improve immunogenic responses triggered by nude antigens.

This study is the first work in which ELR-based biomaterials are used for the development of vaccines against RFVF. Biomaterials constitute a promising strategy for gene and drug delivery purposes and, for instance, ELR polyplexes could be an interesting approach for the development of accurate carriers of viral antigens in order to improve immunogenicity in eukaryotic systems. Nonetheless, further studies are needed to study these constructs in other *in vivo* models resembling the disease.

Therefore, based on our findings, we can conclude that this novel approach could be a promising strategy for modulating the immunogenicity of different antigens from multiple infectious diseases in the future.

5.1.5. References

[1] J.T. Paweska. Rift Valley fever. Revue Scientifique et Technique, 2015. 34 (2):375-389.
[2] B. Borrego*, et al.* Lethal mutagenesis of Rift Valley fever virus induced by Favipiravir. Antimicrob Agents Chemother, 2019. 63 (8):
[3] K.J. Linthicum, S.C. Britch, A. Anyamba. Rift Valley fever: An emerging mosquito-borne disease. Annu Rev Entomol, 2016. 61 395-415.
[4] M. Pepin*, et al.* Rift Valley fever virus(Bunyaviridae: Phlebovirus): an update on pathogenesis, molecular epidemiology, vectors, diagnostics and prevention. Vet Res, 2010. 41 (6):61.
[5] H. Boshra*, et al.* Rift valley fever: recent insights into pathogenesis and prevention. J Virol, 2011. 85 (13):6098-6105.
[6] V. Chevalier. Relevance of Rift Valley fever to public health in the European Union. Clinical Microbiology and Infection, 2013. 19 (8):705-708.
[7] M. Brustolin*, et al.* Rift Valley fever virus and European mosquitoes: vector competence of Culex pipiens and Stegomyia albopicta (= Aedes albopictus). Med Vet Entomol, 2017. 31 (4):365-372.
[8] M. Bouloy, F. Weber. Molecular biology of Rift Valley fever virus. Open Virol J, 2010. 4 8-14.
[9] F. Kreher*, et al.* The Rift Valley fever accessory proteins NSm and P78/NSm-GN are distinct determinants of virus propagation in vertebrate and invertebrate hosts. Emerg Microbes Infect, 2014. 3 (10):e71.
[10] S.R. Gerrard, S.T. Nichol. Synthesis, proteolytic processing and complex formation of N-terminally nested precursor proteins of the Rift Valley fever virus glycoproteins. Virology, 2007. 357 (2):124-133.
[11] B. Borrego*, et al.* Potential application of silver nanoparticles to control the infectivity of Rift Valley fever virus in vitro and in vivo. Nanomedicine, 2016. 12 (5):1185-1192.
[12] G. Lorenzo*, et al.* Efficacy of different DNA and MVA prime-boost vaccination regimens against a Rift Valley fever virus (RVFV) challenge in sheep 12 weeks following vaccination. Vet Res, 2018. 49 (1):21-32.
[13] B. Faburay*, et al.* Current status of Rift Valley fever vaccine development. Vaccines (Basel), 2017. 5 (3):
[14] J.B. Ulmer*, et al.* Heterologous protection against influenza by injection of DNA encoding a viral protein. Science, 1993. 259 (5102):1745-1749.
[15] J.J. Donnelly, B. Wahren, M.A. Liu. DNA vaccines: progress and challenges. Journal of Immunology, 2005. 175 (2):633-639.
[16] M.A. Kutzler, D.B. Weiner. DNA vaccines: ready for prime time? Nature Reviews Genetics, 2008. 9 (10):776-788.
[17] A. Brun. Vaccines and vaccination for veterinary viral diseases: A general overview. Methods in Molecular Biology, 2016. 1349 1-24.
[18] M. Bouloy, R. Flick. Reverse genetics technology for Rift Valley fever virus: current and future applications for the development of therapeutics and vaccines. Antiviral Res, 2009. 84 (2):101-118.
[19] F. Dal Pozzo, E. Thiry. Antiviral chemotherapy in veterinary medicine: current applications and perspectives. Revue Scientifique et Technique, 2014. 33 (3):791-801.

[20] M. Goldberg, R. Langer, X. Jia. Nanostructured materials for applications in drug delivery and tissue engineering. J Biomater Sci Polym Ed, 2007. 18 (3):241-268.
[21] A. Girotti, *et al.* Elastin-like recombinamers: biosynthetic strategies and biotechnological applications. Biotechnol J, 2011. 6 (10):1174-1186.
[22] J.C. Rodriguez-Cabello, *et al.* Synthesis of genetically engineered protein polymers (recombinamers) as an example of advanced self-assembled smart materials. Methods in Molecular Biology, 2012. 811 17-38.
[23] S.R. MacEwan, A. Chilkoti. Applications of elastin-like polypeptides in drug delivery. Jounal of Controlled Release, 2014. 190 314-330.
[24] J.C. Rodriguez-Cabello, *et al.* Elastin-like polypeptides in drug delivery. Adv Drug Deliv Rev, 2016. 97 85-100.
[25] M.J. Pina, *et al.* Biocompatible ELR-based polyplexes coated with MUC1 specific aptamers and targeted for breast cancer gene therapy. Mol Pharm, 2016. 13 (3):795-808.
[26] J. Gonzalez-Valdivieso, *et al.* Self-assembling ELR-based nanoparticles as smart drug-delivery systems modulating cellular growth via Akt. Biomacromolecules, 2019. 20 (5):1996-2007.
[27] M.J. Pina, *et al.* Elastin-like recombinamers with acquired functionalities for gene-delivery applications. Journal of Biomedical Materials Research Part A, 2015. 103 (10):3166-3178.
[28] M. Santos, *et al.* Genetically Engineered Elastin-based Biomaterials for Biomedical Applications. Curr Med Chem, 2018. 26 (40):7117-7146.
[29] C. Garcia-Arevalo, *et al.* Immunomodulatory nanoparticles from elastin-like recombinamers: single-molecules for tuberculosis vaccine development. Mol Pharm, 2013. 10 (2):586-597.
[30] D.S. Pisal, M.P. Kosloski, S.V. Balu-Iyer. Delivery of therapeutic proteins. Journal of Pharmaceutical Sciences, 2010. 99 (6):2557-2575.
[31] G. Lorenzo, *et al.* Protection against Rift Valley fever virus infection in mice upon administration of interferon-inducing RNA transcripts from the FMDV genome. Antiviral Res, 2014. 109 64-67.
[32] H. Caplen, C.J. Peters, D.H. Bishop. Mutagen-directed attenuation of Rift Valley fever virus as a method for vaccine development. Journal of General Virology, 1985. 66 (Pt 10) 2271-2277.
[33] M. Nelson, M. McClelland. Use of DNA methyltransferase/endonuclease enzyme combinations for megabase mapping of chromosomes. Methods Enzymol, 1992. 216 279-303.
[34] J. Dalrymple, *et al.* Mapping protective determinants of Rift Valley fever virus using recombinant vaccinia viruses. In: Brown F.L., Chanock R.M., Ginsberg H.S., R.A. L, editors. Vaccines 89. New York: Cold Spring Harbor Laboratory 1989. p. 371-375.
[35] S.R. Gerrard, S.T. Nichol. Characterization of the Golgi retention motif of Rift Valley fever virus G(N) glycoprotein. J Virol, 2002. 76 (23):12200-12210.
[36] N. Bhardwaj, M.T. Heise, T.M. Ross. Vaccination with DNA plasmids expressing Gn coupled to C3d or alphavirus replicons expressing gn protects mice against Rift Valley fever virus. PLoS Negl Trop Dis, 2010. 4 (6):e725.
[37] J. Kortekaas, *et al.* Efficacy of three candidate Rift Valley fever vaccines in sheep. Vaccine, 2012. 30 (23):3423-3429.
[38] A. Ribeiro, *et al.* Influence of the amino-acid sequence on the inverse temperature transition of elastin-like polymers. Biophys J, 2009. 97 (1):312-320.
[39] C. Garcia-Arevalo. Elastin-like recombinamers for advanced biomedical applications: tissue engineering, gene delivery and nanovaccines PhD Thesis, 2012.
[40] D.W. Urry. Entropic elastic processes in protein mechanisms. I. Elastic structure due to an inverse temperature transition and elasticity due to internal chain dynamics. J Protein Chem, 1988. 7 (1):1-34.

[41] D.W. Urry. Molecular machines: How motion and other functions of living organisms can result from reversible chemical changes. Angewandte Chemie International Edition, 1993. 32 (6):819-841.
[42] A. Girotti*, et al.* Influence of the Molecular Weight on the inverse temperature transition of a model genetically engineered Elastin-like pH-responsive polymer. Macromolecules, 2004. 37 (9):3396-3400.
[43] Y. Takahashi, M. Gehoh, K. Yuzuriha. Structure refinement and diffuse streak scattering of silk (Bombyx mori). Int J Biol Macromol, 1999. 24 (2-3):127-138.
[44] T. Asakura*, et al.* Heterogeneous structure of silk fibers from Bombyx mori resolved by 13C solid-state NMR spectroscopy. J Am Chem Soc, 2002. 124 (30):8794-8795.
[45] F. Buttgereit, M.D. Brand. A hierarchy of ATP-consuming processes in mammalian cells. Biochem J, 1995. 312 (Pt 1) 163-167.
[46] M.H. Pontes, A. Sevostyanova, E.A. Groisman. When too much ATP is bad for protein synthesis. J Mol Biol, 2015. 427 (16):2586-2594.
[47] S. Xiao, J. Shiloach, M.J. Betenbaugh. Engineering cells to improve protein expression. Curr Opin Struct Biol, 2014. 26 32-38.
[48] L. Thoring*, et al.* High-yield production of "difficult-to-express" proteins in a continuous exchange cell-free system based on CHO cell lysates. Sci Rep, 2017. 7 (1):11710.
[49] L. Martin*, et al.* Temperature-triggered self-assembly of elastin-like block co-recombinamers:the controlled formation of micelles and vesicles in an aqueous medium. Biomacromolecules, 2012. 13 (2):293-298.
[50] B.S. Steiniger. Human spleen microanatomy: why mice do not suffice. Immunology, 2015. 145 (3):334-346.
[51] N. Bertrand, J.C. Leroux. The journey of a drug-carrier in the body: an anatomo-physiological perspective. Journal of Controlled Release, 2012. 161 (2):152-163.
[52] M. Ogris*, et al.* PEGylated DNA/transferrin-PEI complexes: reduced interaction with blood components, extended circulation in blood and potential for systemic gene delivery. Gene Ther, 1999. 6 (4):595-605.
[53] J.R. Mascola, B.F. Haynes. HIV-1 neutralizing antibodies: understanding nature's pathways. Immunol Rev, 2013. 254 (1):225-244.
[54] M. Recher*, et al.* Deliberate removal of T cell help improves virus-neutralizing antibody production. Nat Immunol, 2004. 5 (9):934-942.
[55] E. Lopez-Gil*, et al.* A single immunization with MVA expressing GnGc glycoproteins promotes epitope-specific CD8+-T cell activation and protects immune-competent mice against a lethal RVFV infection. PLoS Negl Trop Dis, 2013. 7 (7):e2309.
[56] S.T. Reddy, M.A. Swartz, J.A. Hubbell. Targeting dendritic cells with biomaterials: developing the next generation of vaccines. Trends Immunol, 2006. 27 (12):573-579.
[57] K.S. Jones. Biomaterials as vaccine adjuvants. Biotechnol Prog, 2008. 24 (4):807-814.
[58] J.A. Hubbell, S.N. Thomas, M.A. Swartz. Materials engineering for immunomodulation. Nature, 2009. 462 (7272):449-460.
[59] O.A. Ali*, et al.* Infection-mimicking materials to program dendritic cells in situ. Nat Mater, 2009. 8 (2):151-158.
[60] M. Singh, D.T. O'Hagan. Recent advances in vaccine adjuvants. Pharm Res, 2002. 19 (6):715-728.
[61] V. Apostolopoulos. Methods of delivery to antigen-presenting cells: development of new and improved vaccines. Mol Pharm, 2007. 4 (1):1-3.

Chapter 2

Self-assembling ELR-based nanoparticles as smart drug-delivery systems modulating cellular growth via Akt

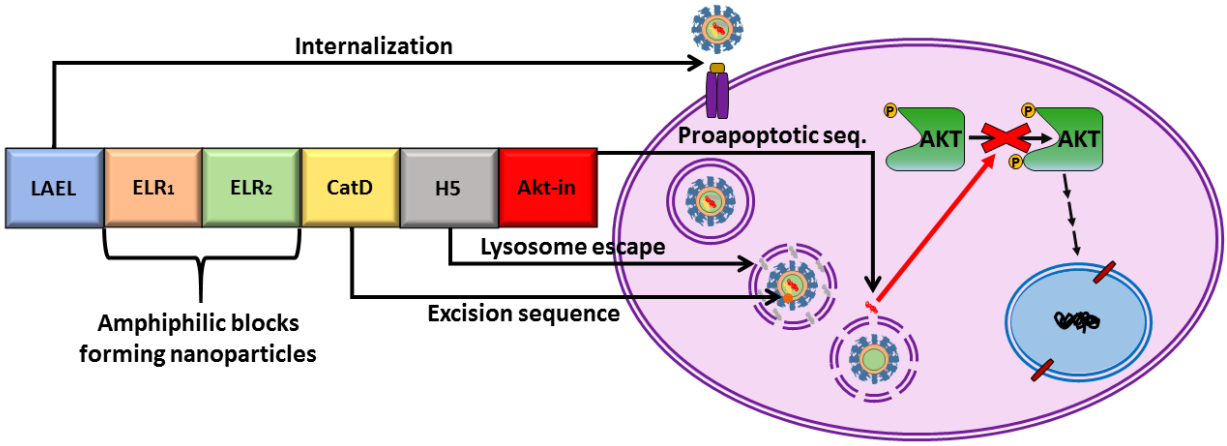

Part of the results of this chapter constitutes the article:

Self-assembling ELR-based nanoparticles as smart drug-delivery systems modulating cellular growth via Akt. J. Gonzalez-Valdivieso, A. Girotti, R. Munoz, J.C. Rodriguez Cabello, F.J. Arias. *Biomacromolecules*. **2019**. 20(5): 1996-2007. DOI: 10.1021/acs.biomac.9b00206.

5.2.1. Introduction

One of the limitations of modern medicine is the lack of efficient drug carriers. Such carriers should accomplish their main function, namely release of a drug in a targeted tissue, so as to achieve two benefits: an increase in drug efficacy and a reduction in possible adverse side effects [1]. The development of a good carrier for a specific drug is of particular importance as, in some cases, the therapeutic dose of a drug is so high that it cannot be used without causing severe damage to other organs [2]. One of the most recent therapeutic approaches is based on smart advanced biomaterials [3, 4], as they are able to overcome the limitations and improve the action of therapeutic agents [5, 6]. Multifunctional carriers have been proposed to overcome these deficiencies [7]. Although significant progress has been made in the field of synthetic devices with improved polymerization efficiency and lower polydispersities, genetically engineered polymers provide us the control to build advanced delivery carriers with acquired functionalities [8].

Advanced drug delivery systems enable to control the release of drugs in a specific cell or tissue, so smart bioresponsive biomaterials able to self-assemble and act under certain stimuli emerge as promising approaches for the achievement of reduced doses of the drugs and limited side effects.

Due to the poor tumor accumulation of standard drugs used in chemotherapy, carriers have become an interesting approach for drug-delivery purposes [9]. Nanoparticle-based delivery can reduce side effects by redistributing drug accumulation away from critical organs, such as the kidney or liver, thus allowing the administration of larger doses than is possible with free drugs [10]. As tumors have an aberrant vascular endothelium and enhanced vascular permeability, 10–100 nm sized nanoparticles accumulate in tumors because of the enhanced permeability and retention effect (EPR) [11]. This effect arises due to the fact that tumors have no functional lymphatic vessels, thus resulting in inefficient drainage from tumor tissue [12, 13]. As such, nanoparticles are able to enter into the interstitial space but are not efficiently removed [14], thus being retained in the tumor tissue.

The choice of the specific target in drug delivery makes the difference between whether healthy tissues are affected or not [15]. Cancer is one of the potential applications of drug delivery systems as it is one of the most common diseases worldwide. In this regard, cancer markers, such as overexpressed receptors and cytoplasmic proteins, are the most widely used targeting systems due to their higher expression in cancerous cells when compared to non-cancerous cells [12, 16]. Consequently, novel strategies that target overexpressed proteins could be of interest when determining how to stop uncontrolled cell proliferation, which is markedly faster in cancerous cells. Of these proteins, Akt stands out due to its important activity in controlling multiple signaling pathways and processes in cells [17]. Akt is a protein kinase that plays a central role in the regulation of multiple cellular processes, enhancing cellular proliferation, metabolism and motility and inhibiting apoptosis [17]. It has three differentiated functional regions, namely the N-terminal pleckstrin homology domain (PH), the central catalytic domain and, finally, the C-terminal hydrophobic region [18]. In response to growth factors, Akt is activated by products of phosphatidyl inositol triphosphate generated by PI3K. These lipid products bind to the PH domain of Akt, thereby inducing a conformational change and allowing PDK1 to phosphorylate threonine 308. Phosphorylation of serine 473 and membrane anchoring are also required after threonine 308 phosphorylation for final activation of Akt kinase [19]. There are three different isoforms (Akt1, Akt2 and Akt3) in mammalian cells. Akt1 is the most abundant isoform and is overexpressed in multiple types of cancer, such as colon, pancreatic, breast, ovarian and lung neoplastic diseases [20]. In light of this, Hiromura *et al*. have developed a small peptide (Akt-in) that accurately prevents phosphatidyl inositol species from binding to the pleckstrin homology domain (PH) of Akt by causing conformational changes, thereby inhibiting membrane translocation and Akt activation. This inhibitor prevents Akt kinase activity and, consequently, a biological response downstream. Moreover, Akt-in inhibits both *in vitro* proliferation and anti-apoptosis action as well as *in vivo* tumor progression [21].

The objectives of this study were to synthesize and characterize a smart stimulus-responsive therapeutic system that can be modulated for application in different cells. Only recombinant technology allows us to create multi-functional block copolymers that can self-assembly into versatile nanoparticles (NPs) carrying the peptidic inhibitor

of Akt, in a targeted and protected manner, and are specifically released in the intracellular environment. In light of the above, we have developed ELR nanoparticles carrying the peptidic inhibitor of protein kinase Akt (Akt-in). Moreover, we have determined *in vitro* the therapeutic window in which tumor cells are affected and normal ones not, and have studied their internalization pathway and intracellular trafficking.

5.2.2. Methods

5.2.2.1 Plasmid synthesis

The elastin-like recombinamers (ELR) used in this chapter were obtained as described elsewhere [22]. The protocols for DNA agarose electrophoresis, plasmid purification, DNA digestion, DNA purification and DNA ligation reaction are described in Chapter 1 sections 2.3-2.9. The final fusion genes with a fully controlled composition and chain length were constructed by sequential introduction of the monomer gene segments in a stepwise manner using the recursive directional ligation method (RDL). The DNA sequence of every cloning step was corroborated by DNA sequencing.

The DNA fragments employed were cloned in a modified version of pDrive cloning vector (Qiagen). The creation of such modified version was described in previous PhD Thesis of Bioforge Research Group [23] and is referred in the present work as pD.

For the expression of the different recombinamers, p103K expression vector was employed. p10 was designed by combination of two different expression plasmids: pET7 and pET9a (Novagen Ca.No.69431-3) to combine the advantages provided by both. pET7 is a modification of pET -25b(+) commercial plasmid produced by suppression of two Eam1104I recognition sites, and the insertion of two of them inside of the polylinker region in order to improve recombinamer clonation and expression. This reclaimed polylinker was inserted in pET9a (Novagen Ca.No.69431-3) polylinker, prior elimination of pET9a native polylinker. Such exchange was performed with the motivation of obtaining an even better plasmid, since pET9a is characterized by Kanamycin resistance (more stable than pET7 ampicillin resistance) and by the lack of lac repressor, resulting in the increase of recombinamer yields). This exchange was carried out in the group by PhD M. Pierna [24]. p103K was created from p10 with the

aim of introduce 3 lysine residues in the amine terminal side of every polymer whose DNA is encoded in this plasmid. The p103K plasmid was created by PhD. M. Pierna [24].

5.2.2.2 Expression strain transformation

BLR(DE3) expression strain was used for the bioproduction of the ELRs presented in this work. Preparation of competent cells of the *Escherichia coli* BLR(DE3) expression strains was performed as previously described [25]. Briefly, BLR cells were cultured in LB supplemented with tetracycline (12.5 μg/mL) up to an optical density (measured at 600 nm) of 0.2-0.5. Cells were pelleted by centrifugation at 3000g 4° C for 10 minutes. Supernatant was discarded and cells were resuspended in TSS medium using 10% of the initial LB medium volume. Resulting cell suspension was divided in 250 μL aliquots in sterile tubes, frozen in liquid nitrogen and stored at -82° C. Bacterial transformation was done as described by Chung [26]: a 250 μL BLR aliquot was thawed in ice and 100-400 pg of DNA were added, gently mixed for uniform DNA dispersion. The mixture was incubated for 30 minutes in ice. An equal volume of LB was added and cells were incubated at 37°C with 250 rpm orbital shaking for one hour. Aliquots of cell suspension were then plated on an LB agar plates supplemented with the corresponding antibiotic and incubated overnight at 37°C.

5.2.2.3 Best colony screening

Isolated transformed BLR colonies were randomly selected for ELR expression screening. Selected colonies were cultured in 5-10 mL of TB supplemented with kanamycin (30 μg/mL), at 37°C and 250 rpm orbital shacking overnight, letting them to express the ELR. Next day, best producing colony was selected by analyzing the total protein fraction. Briefly, 1 mL of bacterial culture was placed into a tube, pelleted and washed in 1 mL of distilled water. Bacteria were then pelleted and resuspended in 100 μL of distilled water. 20 μL from resulting suspension were placed in a new tube and 5 μL of 5x protein loading buffer were added. Samples were boiled at 100° C for 5 minutes for bacterial degradation and protein denaturation, facilitating SDS binding to protein and subsequently centrifuged at 16800 g for 5 minutes in a microfuge. For assessing the purity and the apparent molecular weight, Sodium Dodecyl Sulfate Polyacrylamide Gel Electrophoresis (SDS-PAGE) were performed. Protein staining was

carried out by negative $CuCl_2$ staining. $CuCl_2$ in presence of SDS stains all electrophoresis gel, except were proteins are present, therefore $CuCl_2$ is a negative staining. Briefly, $CuCl_2$ staining was done by directly immersing the electrophoresis gel into a 0.3 M $CuCl_2$ solution for 20 minutes in agitation. SDS-PAGE were done in order to separate proteins according to their electrophoretic mobility [27]. SDS-PAGE separates proteins depending on their molecular weight and based on their differential rates of migration through the gel, under the influence of a constant applied electrical field. Such migration is characterized by:

$$V = qE/f$$

where V is the migration velocity, q is the effective protein charge, E the electric field and f the friction coefficient of the protein in the gel. In order to separate proteins according to their native molecular weight, avoiding artifacts as result of protein-protein interactions, protein denaturation is necessary. SDS is an anionic detergent that denatures proteins breaking down secondary as well as tertiary structures. In addition, SDS provides proteins with a uniform negative charge, proportional to the number of amino acids, and thus to the molecular weight. As the reference, protein marker PierceTM Unstained Protein MW Marker was used. After centrifugation, sample's aliquots were placed in SDS-PAGE wells. SDS-PAGE was held at constant 25 mA of current immersed in SDS-PAGE running buffer. Electrophoresis were performed using a miniVE vertical electrophoresis system (Hoefer, Amersham Pharmacia Biotech).

5.2.2.4 ELR bioproduction

A bacterial inoculum prepared from the best producing colony was cultured in 30 mL of LB supplemented with glucose (1%) and kanamycin in a 500 mL Erlenmeyer for 5 hours and subsequently divided in to two equal volumes to inoculate 2 Erlenmeyer, each of them containing 0.5 L of LB supplemented with glucose (1%) and kanamycin (30 μg/mL). This culture was let to grow for another 3 hours at 37º C with 250 rpm orbital shaking, to be used as the inoculum for the bioreactor. Bioreactor (15 L) was filled with TB medium and sterilized by autoclaving. Once cooled down, TB was supplemented with 112 mL of glycerol and antibiotic, and the inoculum was added. Bacteria culture was incubated overnight under controlled conditions of temperature (37˚C), pH (maintained at 7.5) and constant supply of oxygen by incrementing the

stirring velocity (up to a limit of 500 rpm). After overnight bacterial culture, the biomass was calculated by OD600, and once the absorbance remains stable, cells were collected by centrifugation (5856 g, 10 minutes, 4° C) and supernatant was discarded. Bacteria were washed four times with TBS and pelleted by centrifugation (5856 g, 10 minutes, 4° C) until supernatant results clear of broth residuals. Bacteria were then resuspended in 0.1 L of TE buffer per liter of culture medium and PMSF protease inhibitor was added to a final concentration of 10 µg/mL. Bacteria were then lysed by pressure disruption at 1200-1500 bar (Model TS 0.75 KW Constant System) and lysate was kept in ice bath. Subsequently lysate was centrifuged at 4º C for 1 hour at 15300 g. Pellet was discarded while ELR was purified from the supernatant.

5.2.2.5 ELR purification

The purification process was based on repeated cycles of hot and cold centrifugations. The overall process is named as Inverse Transition Cycling (ITC). The purification of the recombinamer started with the processing of the obtained supernatant, taking advantage of the smart nature of the elastin-like moieties and especially of the inverse temperature transition (ITT). Supernatant was heated at 40° C in order to precipitate the recombinamer. In order to facilitate the precipitation of the ELR, its Tt was lowered by means of addition of NaCl until reached a final concentration of 1 M. Precipitated recombinamer was then pelleted by centrifugation at 7943 g for 10 minutes at 40° C. Supernatant was discarded and pellet was resuspended in 4° C ultrapure water type I (pH 7.4). After resuspension, soluble recombinamer was centrifuged at 15300 g for 20 minutes at 4° C. Pellet containing insoluble bacterial residues was discarded and supernatant underwent the next hot purification cycle. Purification progress was monitored by SDS-PAGE, and cold-hot cycles were repeated until a single protein band, corresponding to the designed ELR, was found. After the last purification cycle, the resuspended recombinamer was dialyzed against cold ultrapure water type I. Due to the envisaged biomedical applications of the recombinamers, pH adjustment to 7.4 was performed. Finally, the ELR solution was filtered with a 0.22 µm size pore filter for its sterilization (PES Thermo Scientific™ Nalgene™ Rapid- Flow™), frozen, lyophilized and stored at -20 °C. The lyophilization process was carried out in a LABCONCO lyophilizator, operating at a vacuum of 0.02 Torr, with the collector at -50° C. Freeze

dried product was then subjected to analysis and purity control by SDS-PAGE, as described in section 2.3.

To obtain endotoxin-free products suitable for *in vitro* and *in vivo* assays, ELRs undergone a secondary treatment with sterile sodium hydroxide (NaOH) 0.4 N and sodium chloride (NaCl) 2 M [28]. The protein was precipitated from solution at 25ºC and resuspended after centrifugation at 8500g for 20 min at 25 ºC, in cold sterile PBS at approximately 50 mg per 20 mL. This treatment was repeated three times. After the third treatment, the protein solution was adjusted to pH 7.4.

In order to determine the endotoxin levels, the resulting solutions were dialyzed on cold ultrapure deionized water, with four water changes, and sterilized through 0.2 µm filtration. The suspensions were then lyophilized and stored at -20ºC. The lyophilized ELRs were resuspended at serial dilutions in sterile molecular grade water from 1 mg/mL and protein endotoxin content was assessed using the QCL-1000 Chromogenic LAL Endpoint Assay ® (Lonza, Basel, Switzerland).

5.2.2.6 Matrix Assisted Laser Desorption/Ionization Time Of Flight (MALDI-TOF)

MALDI is a soft ionization technique used in mass spectrometry and allows the analysis of biomolecules which tend to be fragile and fragment when ionized by more conventional ionization methods. MALDI-TOF mass spectrum was used to confirm the exact molecular weight of ELRs. Experiments were performed by Laboratory of Instrumental Technics from University of Valladolid using a Bruker Autoflex using ultrapure water as solvent to adsorb the sample into the matrix at 1 mg/mL. MALDI is a three-step process: first absorption of sample in a matrix, desorption triggered by a UV laser and ionization of the desorbed molecules. The spectrometer used is the TOF (time-of-flight) due to its large mass range. With this method, ionized molecules flight through a magnetic field describing longer/shorter pathway depending on their mass and their ionization charge.

5.2.2.7 Proton Nuclear Magnetic Resonance (^{1}H-NMR)

The solvation of materials in deuterated solvents permits the observation of the ^{1}H nuclei of the sample. The analysis of the magnetization decay of ^{1}H permits the

compositional analysis of the samples. Indeed, as the ^{1}H nuclei decay at different times depending on their surrounding neighbors, analysis of the intensities related to each type of proton permits to assess the composition of the solved material. Proton nuclear magnetic resonance (^{1}H-NMR) was performed performed by Laboratory of Instrumental Technics from University of Valladolidin deuterated DMSO or D_2O, when indicated, using an Agilent 400 NMR spectrometer with 256 accumulated scans. Sample preparation was done by dissolving ELRs at 2mg/mL in deuterated DMSO or D2O and poured into a NMR tube (Sigma Aldrich). Spectra were analyzed using MestReNova v 9.0.1.

5.2.2.8 Amino acid analysis

Amino-acid analysis was performed by Laboratory of Instrumental Technics from University of Valladolidusing a WATERS600 HPLC gradient system with a WATERS2487 UV detector in order to assert the composition of the produced ELRs. Amino acid analysis was performed. First, ELR were hydrolyzed with 6M HCl, 1% phenol during 2.5 hours at 155˚C, and subsequently dried. Resulting powder was resuspended in 20 mM HCl and diluted 1/10 for separation by High Performance Liquid Chromatography (HPLC). Quantification was done by comparison with standard patrons.

5.2.2.9 Differential Scanning Calorimetry (DSC)

Differential scanning calorimetry is a thermoanalytical technique, where sample and reference are subjected to the same temperature program and the amount of heat needed to fulfill such program is monitored and compared to that of the reference. The basic principle that underlies this technique is that when a substance undergoes any physical transformation, more/less heat is be necessary to maintain the same temperature program than that of the reference. DSC experiments were performed using a Mettler Toledo 822e with liquid-nitrogen cooler using 40 µL aluminum pans for sample holding. Both temperature and enthalpy were calibrated against an indium standard. Solutions were prepared by dissolving the ELRs in PBS (pH 7.4) at 50 mg/mL. A 20 µL aliquot of each solution and its corresponding PBS reference were subjected to an initial isothermal stage (5 min at 0°C to stabilize the temperature and state of the samples), followed by heating from 0 to 60°C at 5°C/min with constant flow of N_2 to avoid water

condensation at 5 L/min. The enthalpy values for endothermic processes were taken as negative and exothermic values as positive.

5.2.2.10 Particle size and ζ-potential

Dynamic Light Scattering (DLS) is a technique for measuring sub-micron particle sizes that measures variation in scattered intensity with time at a fixed scattering angle (typically 90º). The disperse particles or macromolecules suspended in a liquid medium undergo Brownian motion (random motion of the particles) which causes fluctuations of local concentration of the particles, resulting in local inhomogeneity of the refractive index. This in turn results in fluctuations of intensity of the scattered light that can be used to determine their diffusion

The diffusion of the molecules is essentially controlled by the following factors:

- Temperature: the higher the temperature the faster the molecules will move.
- Viscosity of the Solvent: the more viscous the solvent the slower the molecules move.
- The size of the molecules: the bigger the molecules, the slower they move.

If the temperature and solvent are constant and known, the variation in the intensity of the scattered light is directly related to the "size" of the molecule. By measuring the time scale of light intensity fluctuations, DLS can provide information regarding the average size, size distribution, and polydispersity of molecules and particles in solution.

The particle size and ζ-potential of the polymers were determined by dynamic light scattering (DLS) using a Zetasizer Nano ZS (Malvern Instruments Ltd., UK) at a temperature of 37°C. Solutions of both ELRs were prepared by dissolving the ELRs in PBS (pH 7.4) or ultrapure water type I (pH 7.4), when indicated, at 1 mg/mL. The solutions were stored at 4°C overnight to allow complete dissolution of the recombinamers and filtered using a 0.45 µm PVDF syringe filter. The samples were then incubated for 30 minutes at 37°C to allow supramolecular assembly to occur and then introduced into polystyrene cuvettes and stabilized for 2 min at the desired temperature. Scattering light intensity measurements are normalized against toluene (I0). The size distribution (Hydrodynamic radius; Rh) and the polydispersity index

(PDI) were monitored at a scattering angle of 90 by the cumulant method and CONTIN analysis. The Z-average diameter (mean size particle and PDI) could be also fully automatically measured by photon correlation spectroscopy into a Zetasizer nano (Malvern instruments, Malvern, UK). Determinations were carried out at 37ºC by performing 10 readings.

For BSA interaction experiments, ELRs were incubated in 5% BSA PBS for 1, 2 or 3 hours at 37°C after overnight dissolution at 1 mg/mL and then filtered, introduced into polystyrene cuvettes and stabilized for 2 min at the desired temperature. Autocorrelation functions were used to obtain the size distribution and polydispersity index. Z-average mean (nm) and ζ-potential (mV) were used for data analysis. Three different samples were analyzed by performing 10 readings.

5.2.2.11 Transmission Electron Microscopy (TEM)

Solutions were prepared by dissolving the ELRs in ultrapure water type I and kept at 4 °C overnight to allow complete dissolution of the polymers. The sample was incubated for 30 minutes at 37°C to allow supramolecular assembly to occur, placed on a carbon-coated copper grid and stained with uranyl acetate solution (1.0 wt %) to enhance the contrast of the nanoparticles on a carbon-coated copper grid, followed by solvent evaporation. Samples were observed at the "Advanced Microscopy Unit" from the University of Valladolid using a JEM-2200 electron microscope operating at 200 kV. TEM captures were analyzed with the ImageJ software.

5.2.2.12 Surface tension by pendant drop technique

The critical micellar concentration (CMC) of the different ELR solutions in both PBS and ultrapure water type I was determined from surface tension measurements derived from a drop-shape analysis using the pendant drop technique [29]. The changes in the shape of the resulting drop at the air/water interface upon increasing the ELR concentration previously stabilized at 37°C for 15 min from a blank solution to 20 μM were monitored using the SCA 20 software of a Data Physics OCA20 instrument, which scaled the profile of the drop hanging from a straight precision dosing needle. The drops (4 μL at 0.5 μL/s) were infused using a 500 μL Gastight Hamilton syringe. The pendant drop image formed at the tip of needle was captured digitally and then analyzed by the

SCA 20 software (Dataphysics, 2003). Three drops were analyzed per condition and the CMC was determined from the point of slope change after plotting the change in surface tension values versus log(concentration) of the ELRs.

5.2.2.13 Fluorescent ELR labeling

ELR polymers were covalently modified with NHS-Fluorescein by conjugation to free amines. NHS-Fluorescein was dissolved in DMF at 10 mg/mL. Three equivalents of NHS-fluorescein were added to ELR polymers dissolved in DMF and incubated at 4°C for 2 hours. Finally, the polymer was dialyzed against ultrapure water type I in order to discard solvent and non-conjugated NHS-fluorescein and freeze-dried prior to storage.

5.2.2.14 Cell culture

MCF-7 and Caco-2 cells were maintained in MEM supplemented with 10% FBS, 2 mM glutamine, 1% NEAA, 100 U/mL penicillin and 0.1 mg/mL streptomycin at 5% CO_2 and 37°C. MDA-MB-231 cells were cultured in L-15 medium supplemented with 10% FBS, 100 U/mL penicillin and 0.1 mg/mL streptomycin at 0% CO_2 and 37°C. hMSC and HFF-1 cells were cultured in DMEM supplemented with 100 U/mL penicillin, 0.1 mg/mL streptomycin and 10% or 15% FBS, respectively, at 10% CO_2 and 37°C. HUVEC cells were grown in Medium 200 supplemented with 1% gentamicin/amphotericin and LSGS at 5% CO_2 and 37°C. When required, cells were detached using a solution of 0.05% Trypsin-EDTA. Cells were seeded onto 96-well plates at a quantity of 2×10^4 cells per cm^2 for tumor cells and 1×10^4 cells per cm^2 for primary cells, in order to maintain similar confluence levels for all the cell lines overnight prior to the treatment.

5.2.2.15 Confocal microscopy

MDA-MB-231 cells were seeded and, 24 hours after, treated with fluorescein-conjugated ELRs at 0.5 mg/mL for 90 minutes. Then, cells were washed with PBS 1x, fixed with PFA 4% and permeabilized with Triton 0.1%. Finally, cell nuclei were stained with DAPI. Images were taken with a Leica TCS SP8 X confocal microscope at Institute of Molecular Biology and Genetics (IBGM, Valladolid).

5.2.2.16 Flow cytometry

MDA-MB-231 cells (5x105 cells in 6-well plates) were incubated with complete medium containing fluorescein-labeled nanoparticles at 0.5 mg/mL for 90 minutes. Cells were washed with PBS, harvested and resuspended in PBS. Flow cytometry analysis was performed to assess the fluorescein internalized in cells with a Gallios flow cytometer (Beckman Coulter) at Institute of Molecular Biology and Genetics (IBGM, Valladolid).

5.2.2.17 Cell viability

MCF-7, MDA-MB-231, Caco-2, hMSC, HFF-1 and HUVEC were treated with ELRs at three different concentrations (0.25, 0.5 and 1 mg/mL) for different times (30, 60, 90 and 120 min). Live and dead staining (LIVE/DEAD Viability/Cytoxicity Assay Kit, Invitrogen) was used according to the manufacturer's instructions, as described in Chapter 1 section 2.13.

5.2.2.18 Cell proliferation

HFF-1, hMSC and HUVEC cells were seeded in 96-well plates. After 24 hours' incubation, cells were treated with ELRs at two different concentrations (1 mg/mL and 0.5 mg/mL) for 72 hours. Confluence percentages were determined each 4 hours by Cytosmart OMNI software (Cytosmart, Netherlands). Two independent experiments, each in quadruplicate, were performed.

5.2.2.19 Western Blot

Caco-2 and MDA-MB-231 cells were incubated with complete medium containing nanoparticles at 0.5 mg/mL for 2 hours. Cells were lysed and protein concentrations measured using Bradford's reagent following manufacturer's instructions. Thus, 50 µg of protein was separated using standard SDS-PAGE and transferred to PVDF membranes. Blocking was performed with 5% defatted dry milk in PBS (pH 7.4) for 1 h at room temperature. Primary Akt, ρ-Akt and Glyceraldehyde 3-phosphate dehydrogenase (GAPDH) antibodies were used in PBS with 0.5% defatted dry milk and 0.1% Tween-20 at 1:1000 and 1:2000, respectively, according to the manufacturer's instructions. After extensive washing, secondary HRP-linked antibodies were used at a

1:10,000 dilution. Specific proteins were visualized using the ECL chemoluminiscent substrate.

5.2.2.20 Apoptosis/Necrosis assay

Caco-2 and MDA-MB-231 cells were incubated with complete medium containing nanoparticles at 0.5 mg/mL for 2 hours. FITC-conjugated annexin V and propidium iodide staining (Annexin V FITC Assay Kit, Cayman Chemical) was used according to the manufacturer's instructions and the fluorescence intensity emission was measured (SpectraMax M5e Molecular Devices microplate reader) at 535 and 595 nm after excitation at 488 and 560 nm, respectively. Three independent experiments, each in triplicate, were performed.

5.2.2.21 Assessment of internalization pathway

Caco-2 and MDA-MB-231 cells were pre-treated with 25 μM chloroquine, 1 μg/mL filipin, 5 μg/mL amiloride, and 100 μM monodansylcadaverine in minimal medium for 30 min. After treatment with inhibitor, the medium was replaced with a fresh one containing 0.5 mg/mL polymer for 2 hours. Finally, the cell viability assay was carried out as described above. Three independent experiments, each in triplicate, were performed.

5.2.2.22 Assessment of intracellular trafficking

Caco-2 and MDA-MB-231 cells were pre-incubated with 100 μM Pepstatin A at 37°C in each cell culture in complete medium for 16 hours. After Pepstatin A treatment, the medium was replaced with a fresh one containing 0.5 mg/mL polymer for 2 hours. The cell viability was then determined as described above. Three independent experiments, each in triplicate, were performed.

5.2.2.23 Statistical analysis

Data are reported as mean ± SD (n = 3). Statistical analysis involved a variance analysis in combination with a subsequent analysis using the Bonferroni method. A p value of less than 0.05 was considered to be statistically significant. *$p < 0.05$, **$p < 0.01$, ***$p < 0.001$. Data were handled using the SPSS Statistics software version 20 (IBM).

5.2.3. Results and Discussion

5.2.3.1 ELR design

ELRs are able to self-assemble into different structures depending on their composition, with amphiphilic ELR-based diblocks forming vesicles or micelles above their transition temperature [30]. The genetic design of ELRs allows us to control their characteristic Tt below the physiological temperature of 37°C, thus resulting in coacervate formation. One disadvantage of therapeutic molecules, such as drugs or peptides, is their short circulating half-lives, thus meaning that frequent administration of high concentrations is required to obtain therapeutic level [31]. Therapeutic agents have to pass through several biological barriers to reach the tumor tissue and ensure an effective dose. Furthermore, systemic administration results in high toxicity, especially for healthy tissues [32, 33]. ELR-based carriers play an interesting role as regards overcoming all these limitations as they are able to extend the circulating half-life of therapeutic peptides or drugs and also improve their targeting and pharmacokinetics.

We designed two different polymers, control and Akt-in, both based on an amphiphilic backbone consisting on a hydrophilic block formed by glutamic acid and a hydrophobic block formed by isoleucine (Table 1 and Figure 1). The glutamic acid block is based on the monomer $[(VPGVG)_2\text{-}(VPGEG)\text{-}(VPGVG)_2]_{10}$, whereas the isoleucine block is based on $[VGIPG]_{60}$. This amphiphilic ELR construct has been shown to self-assemble into highly monodisperse and stable nanoparticles with a size of 55 nm [30]. We also included a small sequence containing three lysine residues, to which different molecules can be attached by covalent binding, at the amino terminus. According to the literature, we expected that our polymers would enter the cell via endosomes and continue to lysosomes [34], therefore we included an LAEL sequence, a small peptide that undergoes a structural change from random coil to a-helix after acidification of the pH in the endosome/lysosome (pH 5) and triggers destabilization and permeabilization of the vesicle membrane, thereby allowing endosomal escape, in both polymers [35]. The control ELR construct was designed with an amphiphilic backbone containing the three lysine residues and the LAEL sequence. This construct was used in order to clarify any effect of the ELR modules. Moreover, the LAEL sequence was included in the control polymer in order to study possible cytotoxicity due to internalization of the nanoparticles and their escape from endosomes/lysosomes. Furthermore, we added

different bioactive blocks to the functional polymer. For example, cathepsin D (CatD) is a lysosomal aspartyl endopeptidase [36] that is overexpressed in cancer cells compared to normal cells and is thought to promote tumor invasion and growth. As such, we included a cathepsin D-sensitive sequence in order to allow its enzymatic action and Akt inhibitor to reach the cytoplasm. In order to allow the Akt inhibitor to escape from the endosome/lysosome, we added the H5 codifying sequence, a histidine-rich peptide which undergoes a conformational change from a β-structure to a disordered structure at acidic pH [37] as a result of protonation of the imidazole ring in histidine, and provides lysosomal membrane permeation. Finally, we included the sequence codifying the peptide Akt-in, a small peptide of fifteen amino acids which acts as an inhibitor of protein kinase Akt. Indeed, this inhibitor prevents Ser473-phosphorylation, which is a key step, upon binding to Akt protein [21] before being active in the cellular cytoplasm and playing a key role in multiple signaling pathways [19]. In light of the above, our hypothesis for the mechanism of action is that, once CatD has digested the Cathepsin D-sensitive sequence, the H5 peptide and inhibitor will be released into the cellular cytoplasm and will be able to bind to Akt protein and block it.

The amino acid sequences for both control and Akt-in ELR constructs (Table 1) are, respectively:

MGKKKPV-LAELLAELLAEL-$[(VPGVG)_2(VPGEG)(VPGVG)_2]_{10}$-$[VGIPG_{60}$-V and MGKKKPV-LAELLAELLAEL-$[(VPGVG)_2(VPGEG)(VPGVG)_2]_{10}$-$[VGIPG]_{60}$-VQEYVYD-LFHAIAHFHIHGGWHGLIHGWY-AVTDHPDRLWAWERF-V.

Table 1. Composition of polymers. Amino acid sequence of ELR polymers.

	3K	LAEL	E_{50}	I_{60}	CatD	H5	Akt-in
Control	MGKK KPV	$(LAEL)_3$	$[(VPGVG)_2$ (VPGEG) $(VPGVG)_2]_{10}$	$[VGIPG]_{60}$	---	---	---
Akt-in	MGKK KPV	$(LAEL)_3$	$[(VPGVG)_2$ (VPGEG) $(VPGVG)_2]_{10}$	$[VGIPG]_{60}$	VQEYVYD	LFHAIA HFHIHG GWHGLI HGWY	AVTDH PDRLW AWERF

Figure 1. Composition of polymers. The different blocks forming ELR-based polymers. Non-scaled scheme.

5.2.3.2 ELR synthesis and bioproduction

Sequential introduction of the repetitive polypeptide-coding gene segments to form fusion genes with a fully controlled composition and chain length was carried out using the RDL (recursive directional ligation) technique, as described in the general introduction and section 2.1.

The gene sequences encoding for LAEL, CatD, H5 and $E_{50}I_{60}$, as well as the cloning vectors pD and p103K were provided by BIOFORGE Research Group gene library. The gene sequence encoding for Akt-in was purchased from NZYTECH and cloned in pD vector.

In order to obtain the final gene construct, a step-by-step strategy based RDL and seamless cloning was performed. This strategy is based on the controlled and sequential inclusion of coding genes to form the final recombinamer as a fusion polymer. The consecutive cloning steps can be summarized as following:

- Preparation of the acceptor vector (plasmid) digested with *Sap*I type IIS endonucleases that allows the direction and seamless cloning, whose 5'-ends of DNA are dephosphorylated to prevent the self-ligation events. This product is purified by agarose gel extraction.
- Isolation of the coding insert obtained after *Ear*I digestion and agarose gel purification. The single strand DNA ends generated are complementary to those generated by *Sap*I endonucleases and allow a directional and seamless cloning.
- Seamless cloning of plasmid and insert in a ligation reaction.
- Transformation of competent bacteria (*E. coli* strain) with the cloning mixture.

- Isolation of clones containing the expected gene recombination product. The selection of the potential positives clones is carried out through plasmid isolation and its analytic restriction analysis followed by DNA sequencing.

With the first cloning it was obtained the plasmid pDLAELE$_{50}$I$_{60}$, where the LAEL insert was cloned in the pDE$_{50}$I$_{60}$ plasmid (Figure 2). Potential positive colonies were selected for plasmid restriction mapping analysis by using the enzyme *Eco*RI (Figure 2C). Colonies rendering the expected bands were further verified by DNA sequencing and the correct ones, selected for following steps. Once achieved the correct gene sequence encoding for pDLAELE$_{50}$I$_{60}$, the plasmid DNA was digested with *Ear*I. The digestion sample was loaded into an agarose gel and the target DNA band was purified for the following step, namely the isolation of the LAELE$_{50}$I$_{60}$ gene block insert and subsequent subcloning into p103K expression vector and characterized by the presence of 3 lysine residues at the amino extreme (Figure 3). The product of such ligation reactions was transformed in *E. coli* expression strain BLR(DE3), as previously described in section 2.2, and several colonies were analyzed by restriction mapping and ulterior DNA sequencing.

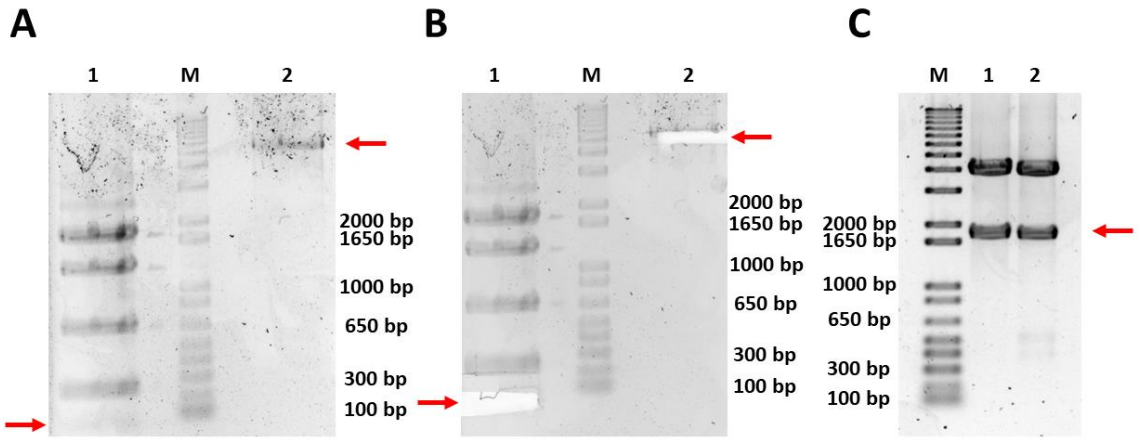

Figure 2: DNA electrophoresis for the isolation of the LAEL gene and pDE$_{50}$I$_{60}$ construction. Gels A and B: Preparative agarose gels. Lane 1: pDLAEL digested with *Ear*I before (A) and after (B) cutting the DNA band of interest. Lane M: DNA marker. Lane 2: pDE$_{50}$I$_{60}$ digested with *Sap*I before (A) and after (B) cutting the DNA band of interest. Gel C: Analytic agarose gel of *Eco*RI diagnostic digestion. Lane M: DNA marker. Lanes 1 and 2: restriction analysis with *Eco*RI of the plasmid content of two different colonies transfected with the cloning product of LAEL + pDE$_{50}$I$_{60}$ in order to obtain the pDLAELE$_{50}$I$_{60}$ construction. Red arrows indicate the DNA band in which the gene fragment of interest is included.

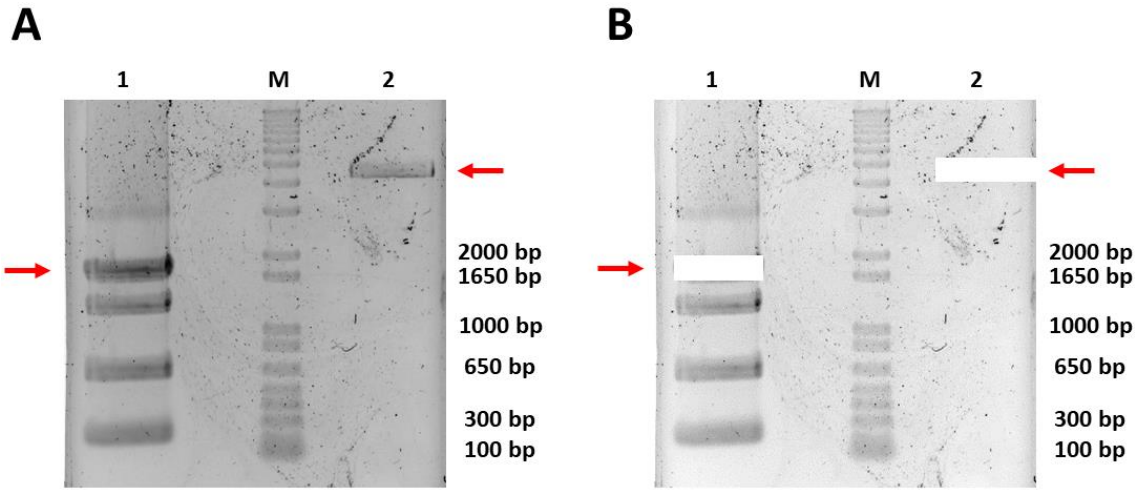

Figure 3: DNA electrophoresis for the isolation of the $LAELE_{50}I_{60}$ gene and p10NK expression vector. Gels A and B: Preparative agarose gels. Lane 1: $pDLAELE_{50}I_{60}$ digested with *Ear*I before (A) and after (B) cutting the DNA band of interest. Lane M: DNA marker. Lane 2: p10NK digested with *Sap*I before (A) and after (B) cutting the DNA band of interest. Red arrows indicate the DNA band of interest.

The following cloning step consisted on the preparation of the plasmid by digestion of pDAkt-in with *Sap*I and its enzymatic dephosphorilation using SAP (Shrink Alkaline Phosphatase) and FASTAP phosphatases (Figure 4A). Two consecutive dephosphorilation of the linearized plasmid are necessary to obtain the required product without damage the complementary ends. The resulting product was purified. Subsequently the insert, CatD gene, was isolated with *Ear*I digestion and preparative agarose extraction (Figure 4B). In the next step, the CatD block was cloned in the pDH5and the potential positive *E. coli*. colonies were analyzed by *Eco*RI restriction mapping and DNA sequencing as describe before. In the following step the gene of CatDH5 obtained in the previous cloning was isolated by digestion with *Ear*I (Figure 4C). In order to obtain pDCatDH5Akt-in, a ligation reaction was performed between CatD block and pDH5Akt-in construction, and the products of such reaction were transformed into *E. coli*. Several colonies were selected for restriction mapping analysis of their plasmid content by using the enzyme *Eco*RI, as described above.

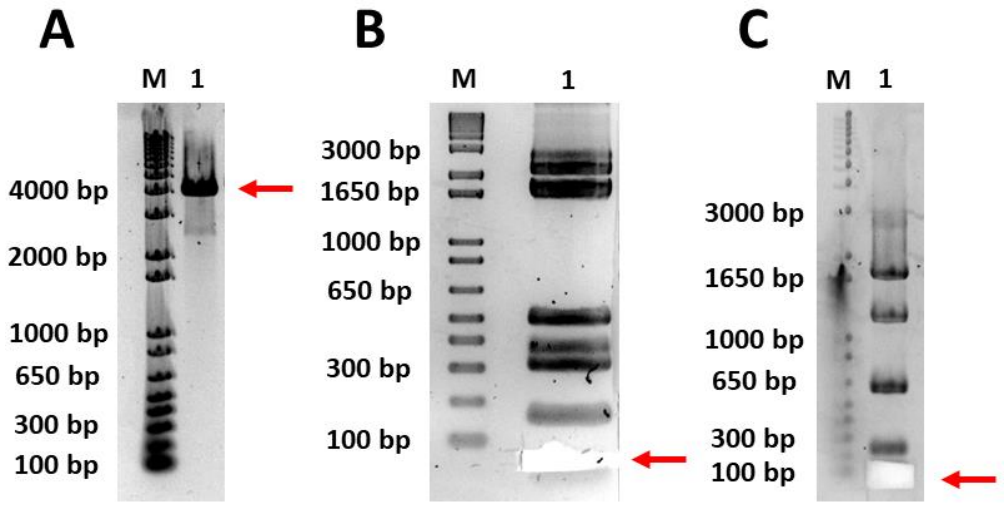

Figure 4: DNA electrophoresis for the isolation of the pDAkt-in construction, CatD and CatDH5 genes. Gel A: Preparative agarose gel. Lane M: DNA marker. Lane 1: pDAkt-in digested with *Ear*I before cutting the DNA band of interest. Gel B: Preparative agarose gel. Lane M: DNA marker. Lane 1: pUC57CatD digested with *Ear*I after cutting the DNA band of interest. Gel C: Preparative agarose gel. Lane M: DNA marker. Lane 1: pDCatDH5 digested with *Ear*I after cutting the DNA band of interest. Red arrows indicate the DNA band in which the gene fragment of interest is included.

In the next cloning step, the pDCatDH5Akt-in plasmid (Figure 5A-B) and $LAELE_{50}I_{60}$ insert (Figure 5A-B) were achieved as previously described. Then, a reaction ligation was performed between $LAELE_{50}I_{60}$ block and pDCatDH5Akt-in, and the potential positive clones plasmid analyzed by *Eco*RI restriction mapping (Figure 5C) and sequence analysis. Therefore, the final construct $pDLAELE_{50}I_{60}$CatDH5Akt-in was achieved.

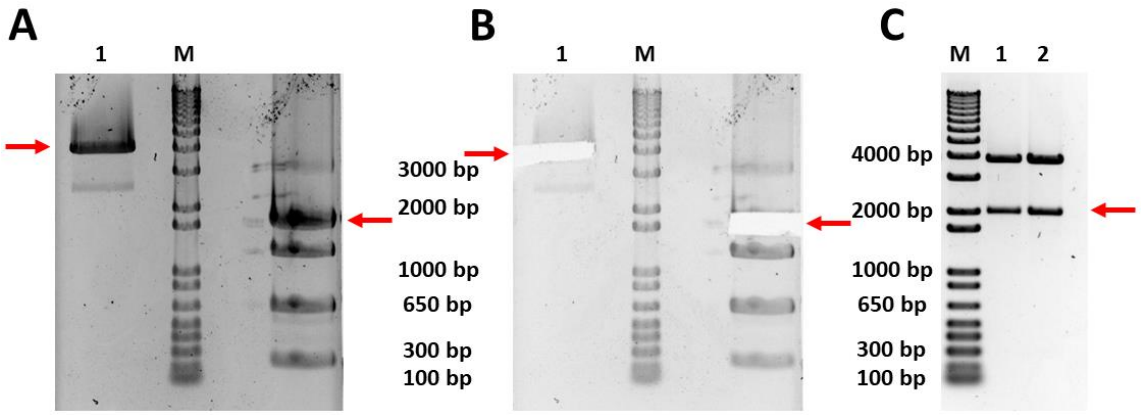

Figure 5: DNA electrophoresis for the isolation of pDCatDH5Akt-in construction and $LAELE_{50}I_{60}$ gene. Gels A and B: Preparative agarose gels.: Lane 1: pDCatDH5Akt-in digested with *Sap*I before (A) and after (B) cutting the DNA band of interest. Lane M: DNA marker. Lane 2: $pDLAELE_{50}I_{60}$

digested with *Ear*I before (A) and after (B) cutting the DNA band of interest. Gel C: Analytic agarose gel of *Eco*RI diagnostic digestion. Lane M: DNA marker. Lanes 1 and 2: restriction analysis with *Eco*RI of the plasmid content of two different colonies transfected with the product of the ligation reaction of $LAELE_{50}I_{60}$ + pDCatDH5Akt-in in order to obtain the $pDLAELE_{50}I_{60}$CatDH5Akt-in construction. Red arrows indicate the DNA band of interest.

Once achieved the final gene sequence encoding for $pDLAELE_{50}I_{60}$CatDH5Akt-in, the plasmid DNA of one colony containing the desired DNA was digested with *Ear*I. The digestion sample was loaded into an agarose gel and the target DNA band was purified for the following step, namely the isolation of the $LAELE_{50}I_{60}$CatDH5Akt-in block and subsequent subcloning into the p103K expression vector. The product of such cloning was transformed in *E. coli* expression strain BLR(DE3), as previously described in section 2.2, and several colonies were analyzed by restriction mapping and ulterior DNA sequencing.

The intrinsic variability among colonies of the same bacterial strain together with the particular repetitive character of this kind of recombinamers could lead to distinct expression patterns among the transformed colonies. These variations were controlled by comparison in an expression screening of eight BLR(DE3) clones (Figures 6-7). The screening assays showed good production uniformity within all the BLR(DE3) transformants. The encountered difference between the theoretical and experimental Molecular Weights can be properly explained by the previously reported reduced electrophoretic mobility of ELR [38]. For large scale recombinamer expression (section 2.4) the selected bacterial colonies were cultured until achieved the stationary phase, assumed as the cessation of cell growth when a constant absorbance value estimated at 600 nm was reached.

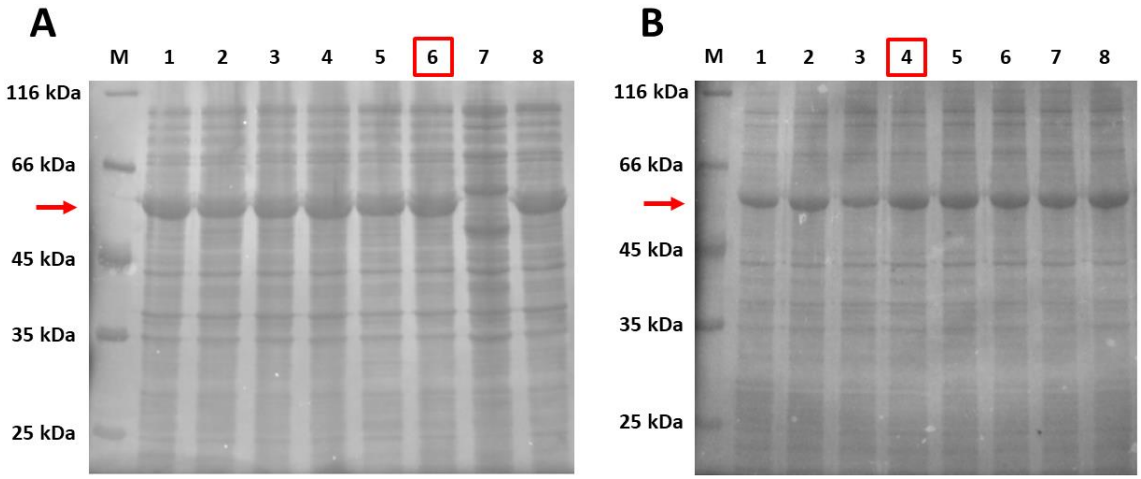

Figure 6: Total protein fractions analysis of p10LAELE$_{50}$I$_{60}$ (A) and p10LAELE$_{50}$I$_{60}$CatDH5Akt-in (B) expression colonies. 12.5% SDS-PAGE stained with copper. Lane M: Protein marker. Lanes 1-8: total protein fraction of 8 expression colonies transformed with p10LAELE$_{50}$I$_{60}$ (Left panel) or p10LAELE$_{50}$I$_{60}$CatDH5Akt-in (Right panel). Red boxes indicate the selected expression colony. Red arrows indicate the position of the protein band that corresponds to the corresponding recombinamer.

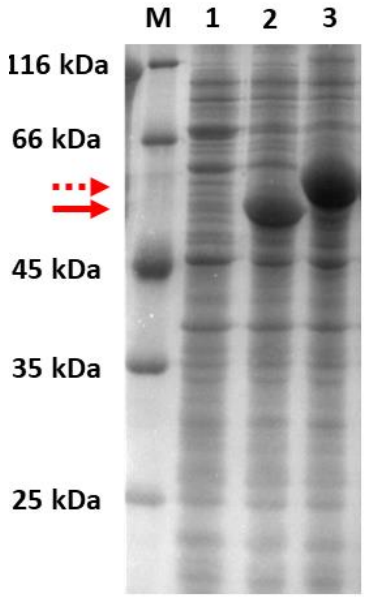

Figure 7: Total protein fractions analysis of the selected expression colonies. 12.5% SDS-PAGE stained with copper. Lane M: Protein marker. Lane 1: total protein fraction of expression colonies transformed with p103K. Lane 2 and 3: total protein fraction of selected expression colonies transformed with p103KLAELE$_{50}$I$_{60}$ (2) or p103KLAELE$_{50}$I$_{60}$CatDH5Akt-in (3). Red arrows indicate the position of the protein band that corresponds to the corresponding recombinamer (Continuous arrow: p103KLAELE$_{50}$I$_{60}$; Dashed arrow: p103KLAELE$_{50}$I$_{60}$CatDH5Akt-in).

The ELR purification protocol was based on the ITT (section 2.5) and consisted in three sequentially rounds of inverse transition cycling that rendered highly pure and

monodisperse polymers (Figure 8). The electrophoretic pattern showed an excellent level of purity for all the ELRs produced and purified where contaminant proteins from *E. coli* were not detected. The polymers were obtained in a yield of approximately 50 mg/L of bacterial culture. Their molecular weights were confirmed by SDS-PAGE and MALDI-TOF, (Figures 8-10). MALDI-TOF is a suitable technique to assess the exact molecular weight of high-molecular weight materials. Experimental and theoretical results were in good agreement. Thus, MALDI-TOF allowed to affirm that the experimental molecular weight was in great concordance with the theoretical one.

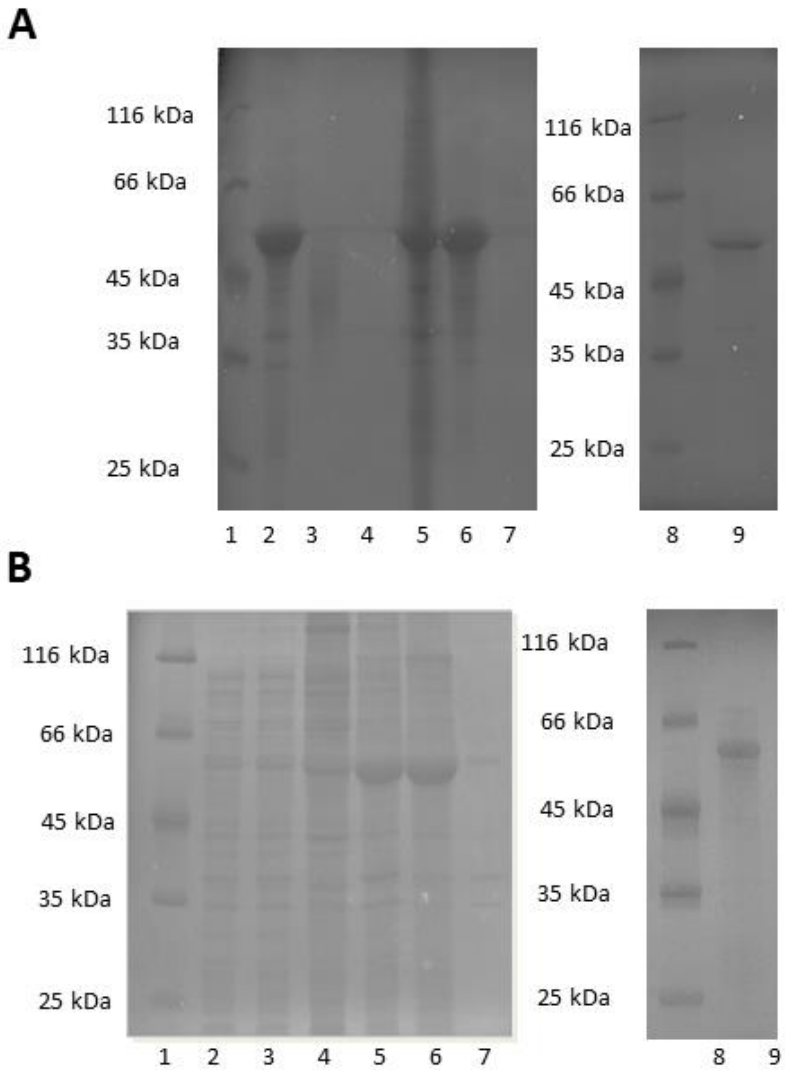

Figure 8. Characterization of ELR polymers. The expression vectors containing the selected ELR genes were transformed into *Escherichia coli* BLR(DE3) strain for production. The ELR was then bioproduced in *Escherichia coli* in a 15-L bioreactor and purified by several cooling and heating purification cycles (Inverse Transition Cycling) following centrifugation, thereby taking advantage of the ability of these recombinamers to aggregate above their transition temperature. Finally, the

polymer was dialyzed against ultrapure water type I and sterilized by filtration (0.22 µm filters). Gel A: SDS-PAGE of purification fractions of control polymer. 1: protein marker; 2: cold supernatant; 3: cold pellet; 4: hot supernatant; 5: hot pellet; 6: cold supernatant; 7: cold pellet; 8: protein marker; 9: pure lyophilized polymer. Gel B: SDS-PAGE of purification fractions of Akt-in polymer. 1: protein marker; 2: production sample; 3: production sample; 4: cold pellet; 5: cold supernatant; 6: hot pellet; 7: hot supernatant; 8: protein marker; 9: pure lyophilized polymer.

Moreover, the purity of the products was corroborated through the analysis of amino acid composition by high performance liquid chromatography (HPLC) and nuclear magnetic resonance (NMR) (Figures 9 and 10). The number of total amino acids found in both ELR as well as the determined number of each type was very similar to the theoretical values, ensuring their purity and correct amino acid composition. Differences among values were attributed to the experimental error associated with the technique. Regarding the NMR spectra, calculation of the integral values from the different protons present in the structure was performed and correct amino acid composition could be assessed by comparing them to the experimental values. Differences among experimental values are attributed to the experimental error of the technique.

A

			Experimental		Theoretical
	AA	Mr patron	% masa	count	count
D	ASP+ASN	133,11	0,00	0,00	
E	GLU +GLN	147,13	3,60	14,13	13
N		132,12	0,00	0,00	
S	SER	105,09	0,00	0,00	
Q		146,15	0,00	0,00	
H	HIS	151,9	0,00	0,00	
G	GLY	75,07	28,27	219,97	220
T	THR	119,12	0,00	0,00	
R	ARG	174,2	0,00	0,00	
A	ALA	89,1	0,80	5,17	3
Y	TYR	181,19	0,00	0,00	
C	CYS	240	0,00	0,00	
V	VAL	117,15	29,60	145,53	150
M	MET	149,21	0,00	0,00	
W	TRP	204,33	0,00	0,00	
F	PHE	165,19	0,00	0,00	
I	ILE	131,18	14,07	61,75	60
L	LEU	131,18	1,57	6,90	6
K	LYS	146,65	0,71	2,90	3
P	PRO	115,13	21,38	108,43	110
			100,00	564,77	565

B

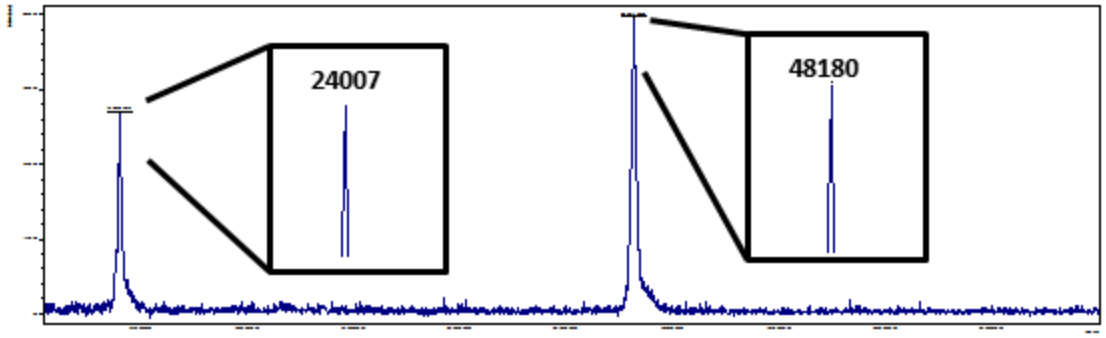

Figure 9. Characterization of control polymer. A: The amino acid composition was verified by high performance liquid chromatography (HPLC). B: The molecular weight of the recombinamer was determined by mass spectrometry (MALDI-TOF/MS). MALDI-TOF spectrum represents non-quantitative intensity (a.u.) against m/z (mass divided by net charge of the molecule) of the ELR. Either the mono charged either the doubly charged recombinamers were detected. The theoretical molecular weight was 48250 Da.

A

			Experimental		Theoretical
	AA	Mr patron	% masa	count	count
D	ASP	133,11	2,04	3,24	3
E	GLU + GLN	147,13	3,92	15,35	16
N	ASN	132,12	0,00	0,00	
S	SER	105,09	0,00	0,00	
Q		146,15	0,00	0,00	
H	HIS	151,9	0,80	5,39	6
G	GLY	75,07	28,21	253,28	252
T	THR	119,12	0,74	1,25	1
R	ARG	174,2	1,31	2,11	2
A	ALA	89,1	2,11	6,17	7
Y	TYR	181,19	1,23	3,63	3
C	CYS	240	0,00	0,00	
V	VAL	117,15	26,41	152,72	157
M	MET	149,21	0,39		
W	TRP	204,33	0,75	3,53	4
F	PHE	165,19	0,93	3,84	3
I	ILE	131,18	11,24	65,12	63
L	LEU	131,18	2,71	10,23	9
K	LYS	146,65	0,63	2,97	3
P	PRO	115,13	16,59	110,47	111
			100,00	639,3	640

B

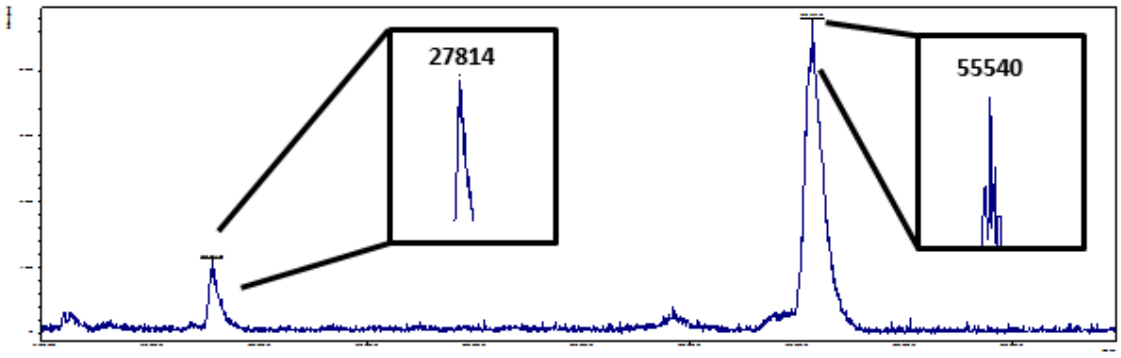

Figure 10. Characterization of Akt-in polymer. A: The amino acid composition was verified by high performance liquid chromatography (HPLC). B: The molecular weight of the recombinamer was determined by mass spectrometry (MALDI-TOF/MS). MALDI-TOF spectrum represents non-quantitative intensity (a.u.) against m/z (mass divided by net charge of the molecule) of the ELR. Either the mono charged either the doubly charged recombinamers were detected. The theoretical molecular weight was 55330 Da.

5.2.3.3 Physical characterization

ELRs are characterized by a thermosensitive behavior that can be useful for performing controlled drug delivery, thus meaning that the self-assembling ability of ELRs makes them an interesting alternative for the development of biomedical devices. Consequently, the availability of ELR-based delivery systems with a Tt below the physiological temperature is extremely important for our purposes due to the fact that nanoparticles would be formed in the human body [39].

Table 2. Characterization of ELR polymers. The experimental molecular weights were determined by MALDI-TOF/MS. Transition temperatures (Tt) for polymers dissolved in PBS buffer (pH 7.4) were measured by differential scanning calorimetry (DSC).

Polymer	Predicted Molecular Weight (Da)	Experimental Molecular Weight (Da)	Tt (°C)	Endotoxin level (EU/mg)
Control ELR	48250	48180	15.15	0.27
Akt-in ELR	55330	55540	14.58	0.25

The thermal behavior of both ELRs was measured by DSC in PBS. DSC is a thermoanalitical technique to assess the thermoresponsive smart properties of the ELRs. As shown from Table 2, both polymers were found to behave as self-assembling smart systems with a Tt of approximately 15°C, which corresponds to the transition of the hydrophobic block forming the nanoparticle core. These transition temperatures are very similar to those previously exhibited by amphiphilic blocks containing isoleucine and able to self-assemble into nanoparticles [30]. Interestingly, there are few differences between the Tt of both polymers despite their different composition, thus meaning that the bioactive sequences added to the polymer carrying the Akt inhibitor do not affect their transition temperature (Figure 11). This means that they could be used for biomedical applications because, at body temperature of 37°C, both ELR-based polymers self-assemble as required. Once the Tt of both polymers had been determined, nanoparticle formation had to be checked because the addition of bioactive sequences could affect self-assembly of the polymers.

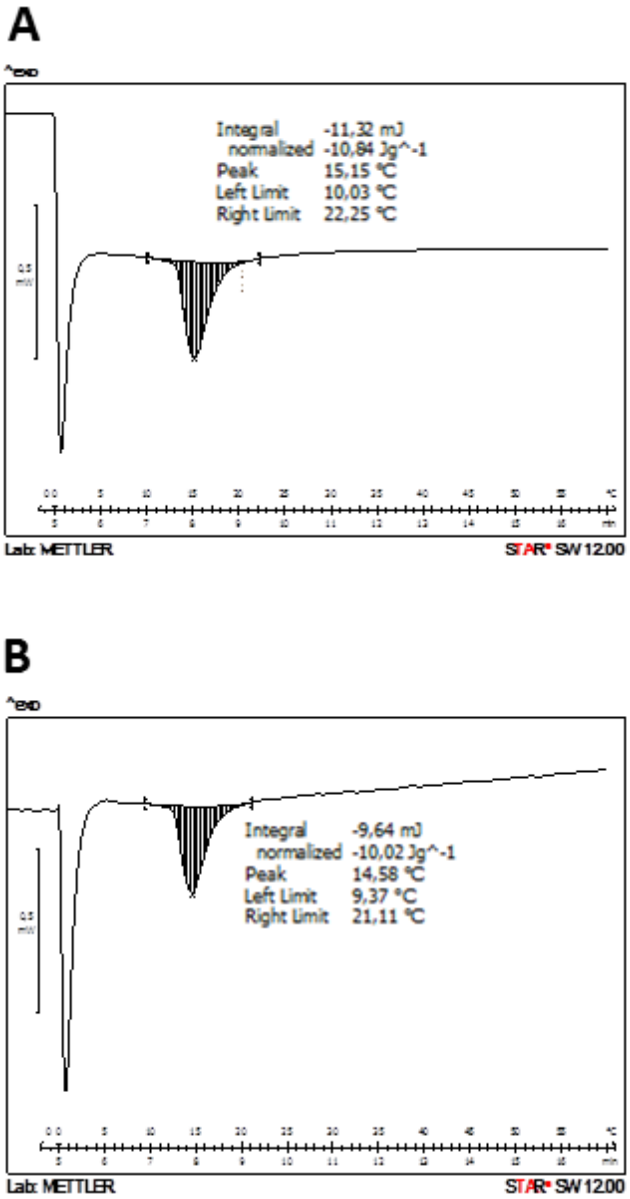

Figure 11. Characterization of ELR polymers. Determination of transition temperature (Tt) by differential scanning calorimetry (DSC) in PBS (pH 7.4). A: Control polymer. B: Akt-in polymer.

The nanotechnological approach to cancer therapy takes advantage of the multiple abnormalities inherent to tumor vasculature, such as hypervascularization, aberrant vascular architecture, enhanced production of vascular permeability factors, and the lack of lymphatic drainage [11-13]. Thus, nanocarriers can selectively extravasate into tumor tissues due to their abnormal vascular nature and are subsequently not efficiently removed, thus remaining retained therein [40]. The ideal size for a nanoparticle depends on several factors. First of all, for significant extravasation from fenestrations in the tumor vasculature, nanocarriers need to be smaller than 400 nm [14]. Secondly,

particles bigger than 200 nm are likely to be sensitive to macrophages and undergo opsonization [41]. As such, in order to avoid specific capture by the liver, they should be less than 100 nm in size [42] but larger than 10 nm to avoid filtration by the kidneys [43]. For all these reasons, nanoparticles with a size of 10-100 nm are preferred because of the enhanced permeability and retention effect (EPR) [14]. The EPR effect relies on the fact that tumors show abnormal vasculature, which means that nano-size drugs are accumulated in the tumors and show differential accumulation and therefore higher concentrations when compared to the plasma or other organs with proper vasculature.

Molecular self-assembly describes the spontaneous association of molecules under equilibrium conditions into well-defined stable aggregates joined by noncovalent bonds. Amphiphilic ELR polymers were shown to self-assemble into highly monodisperse nanoparticles and micelles [30, 44]. Different techniques can be utilized for the characterization of block copolymer self-assembly. Thus, interfacial tension measurements and scattering methods are useful techniques in order to determine the Critical Micelle Concentration (CMC) and the microstructure of aggregates with typical nano and micro sizes [45, 46]. Both, the CMC and light scattering analysis were investigated for the characterization of the developed ELRs.

Table 3. Characterization of ELR nanoparticles. Size and polydispersity index (PdI) of self-assembled polymers dissolved in PBS measured by dynamic light scattering (DLS). Surface charge of self-assembled polymers dissolved in ultrapure water type I measured by dynamic light scattering (DLS). The CMC of self-assembled polymers dissolved in PBS was calculated from the surface tension using the pendant drop technique. Mean ± SD.

Nanoparticle	**Size (nm)**	**PdI**	**ζ-potential (mV)**	**CMC**	
				mg/mL	µM
Control NPs	65.60 ± 3.73	0.087	-27.8 ± 1.5	0.25	4.49
Akt-in NPs	72.46 ± 3.52	0.079	-26.2 ± 1.2	0.21	4.21

The autocorrelation functions obtained from DLS at a scattering angle of 90° were analyzed using the CONTIN algorithm [47]. In this work, both polymers exhibited an ability to form nanoparticles, with an average size of 66 nm for the control polymer and 72 nm in the case of the Akt-in ELR, with low PDIs in both cases (Table 3 and Figure

12). This difference in size between the two nanoparticles is statistically relevant and bigger than for previous nanoparticles (55 nm) under the same conditions [30]. As these previous nanocarriers consisted only of the amphiphilic ELR backbone, this difference with respect to our new nanoparticles is mainly due to the additional functional peptides. To a lesser extent, the presence of the three bioactive sequences also results in a slight increase in the size of the Akt-in nanoparticles (72 nm). We can therefore conclude that both nanoparticles (control and those carrying the Akt inhibitor) meet all the size requirements for reaching the tumor in a controlled manner, as explained above. Furthermore, both control and Akt-in nanoparticles showed the same size when incubated with BSA (Table 4). The nanoparticles were stable in size and polydispersity in the presence of BSA, indicating that nanoparticles would remain stable in systemic circulation and are not affected by plasmatic proteins, such as albumin.

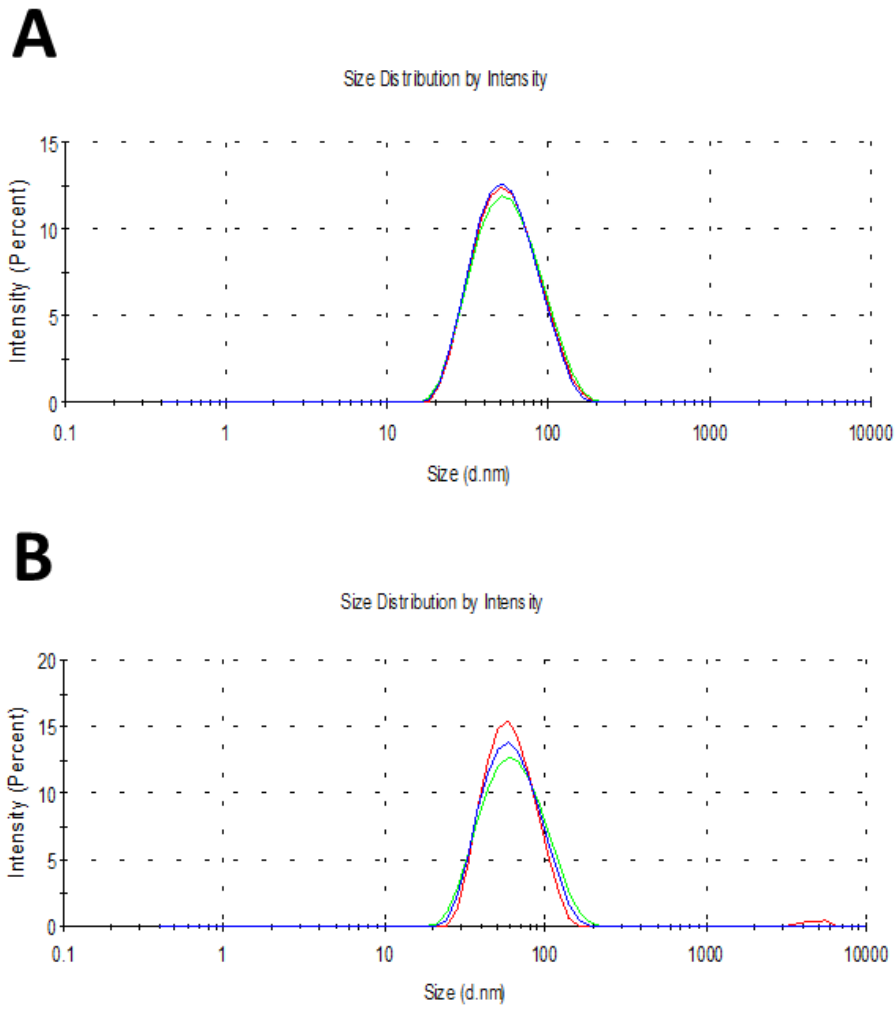

Figure 12. Characterization of ELR nanoparticles. Determination of size by dynamic light scattering in PBS buffer (pH 7.4) at 37°C at 0.5 mg/mL. A: Control polymer. B: Akt-in polymer.

Table 4. Characterization of ELR nanoparticles. Size and polydispersity index of self-assembled polymers incubated with 5% BSA at 37°C measured by dynamic light scattering (DLS). Mean ± SD.

Nanoparticle	Time (h)	Size (nm)	PdI
Control NPs	0	65.60 ± 3.73	0.087
	1	65.85 ± 3.23	0.070
	2	67.01 ± 2.78	0.134
	3	66.78 ± 2.46	0.127
Akt-in NPs	0	72.46 ± 3.52	0.079
	1	73.20 ± 2.88	0.141
	2	72.08 ± 3.02	0.116
	3	71.71 ± 3.38	0.102

The critical micellar concentration (CMC) was also studied in order to determine the concentration above which ELRs self-assemble into nanoparticles (Figure 13). The pendant drop technique allowed us to study the ability of amphyphilic block copolymers to self-assemble from the measurement of the surface tension variation (based on the drop size distribution), at the liquid interface, as a function of the copolymer concentration. The changes in the shape of the drops (4 µL at 0.5 µL/sg), at the air/water interface, when increasing the ELR concentration were monitored. The presence of increasing concentrations of block copolymers in solution can reduce the liquid interfacial tension due to their interfacial activity by a leveling off indicative of saturation of the interface [48].

The CMC is the inverse of the equilibrium constant for micelle formation and is determined as the intersection of two linearly extrapolated lines. The first line is extrapolated over the linear region where the surface tension is changing with concentration whereas the second line is extrapolated over the region where the surface tension is nearly constant with changing concentration. The pendant drop method showed that both polymers have their CMC in PBS buffer between 0.21 mg/mL (4.21 µM) for nanoparticles carrying the Akt inhibitor and 0.25 mg/mL (4.49 µM) for control nanoparticles, as shown in Figure 13. This difference again highlights the fact that the presence of bioactive sequences does not affect the association and self-assembling ability of ELR-based nanoparticles.

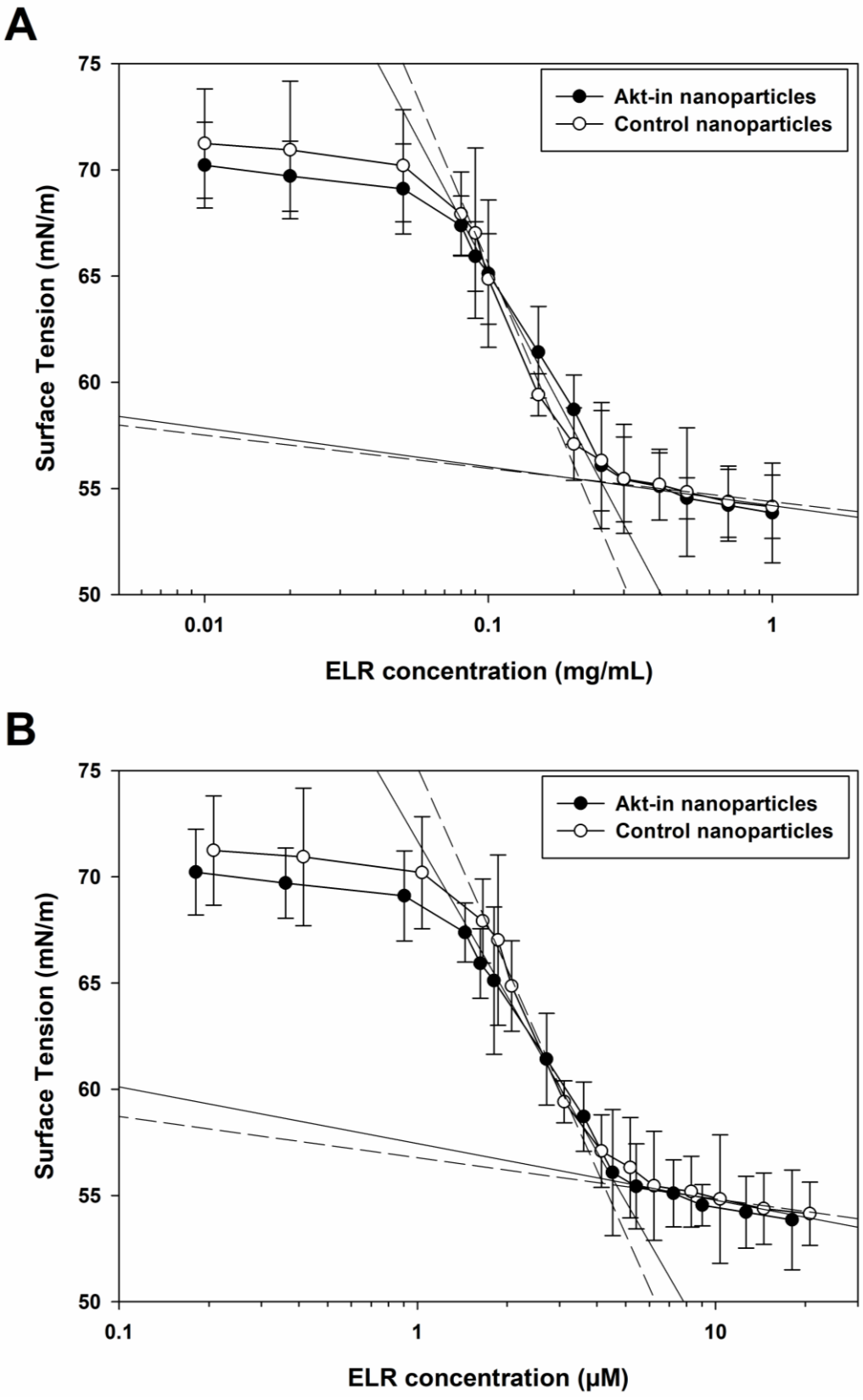

Figure 13. Characterization of ELR nanoparticles. Determination of critical micellar concentration (CMC) using the pendant drop method in PBS buffer (pH 7.4).

The size and morphology were corroborated by TEM and fluorescence microscopy images (Figure 14).

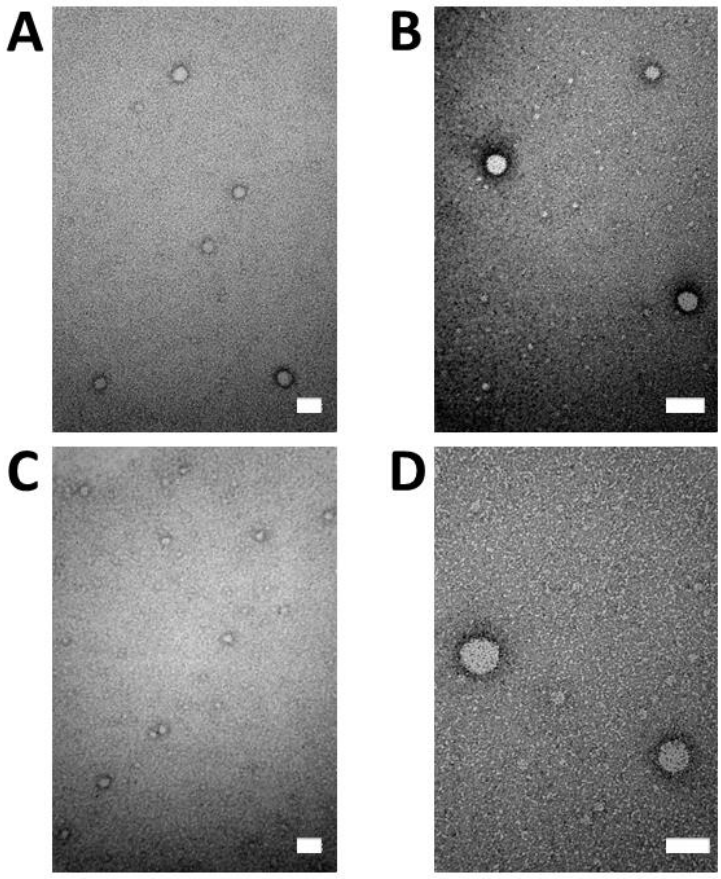

Figure 14. Characterization of ELR nanoparticles. TEM images of self-assembled nanoparticles stained with 1% uranyl acetate. A and B: Control nanoparticles. C and D: Akt-in nanoparticles. Scale bars: 100 nm.

The surface charge of nanoparticles is of marked importance as regards the electrostatic interactions between nanoparticles and the cellular membrane and evaluating nanoparticle stability. Due to the negative component of the cellular membrane, cationic particles are typically preferred in order to nonspecifically enter into cells by generating holes and inducing local disorders in the membrane [49], while anionic particles strongly influence membrane structures [50]. However, anionic and neutral nanoparticles are thought to enter cells via endocytic pathways. Moreover, positively charged nanoparticles result in membrane depolarization, which reduces the viability of normal cells, thus having a stronger disruptive ability on the lipid bilayer of the cellular membrane [51]. Furthermore, neutral and negatively charged nanoparticles are able to

enter into the lymphatic system better than cationic carriers, which are more likely to form aggregates with interacting proteins, whereas neutral and anionic particles are thought to avoid renal clearance more efficiently [52].

Self-assembling of amphiphilic di-block copolymers result in the formation of aggregates composed by a core formed by the insoluble block, which is shielded from the solvent by a hydrated corona formed by the more soluble block. The γ-carboxylic groups from the glutamic acid residues (pKa 4.1) displayed on the hydrated corona of the nanoparticles should be on the deprotonated state at pH 7.4. In order to confirm this point, the ζ-potential determination based on the electrophoretic mobility of the isoleucine-containing block was carried out. The ζ-potential, which determines the surface charge of the nanoparticles, was found to be clearly negative (-27 mV) due to the presence of glutamic acid residues at the nanoparticle surface (Table 3 and Figure 15). Despite the presence of three lysine residues in the corona, the ζ-potential was not altered when compared to previous nanoparticles containing the same amphiphilic backbone reported by García-Arévalo *et al.* [30]. Thus, these three lysine residues would not affect the nonspecific internalization of nanoparticles by electrostatic interactions with the cellular membrane. Moreover, the bioactive sequences of nanoparticles carrying the Akt inhibitor did not alter the ζ-potential compared to control nanoparticles containing the ELR amphiphilic backbone, thus suggesting that bioactive domains are located at the nanoparticle core.

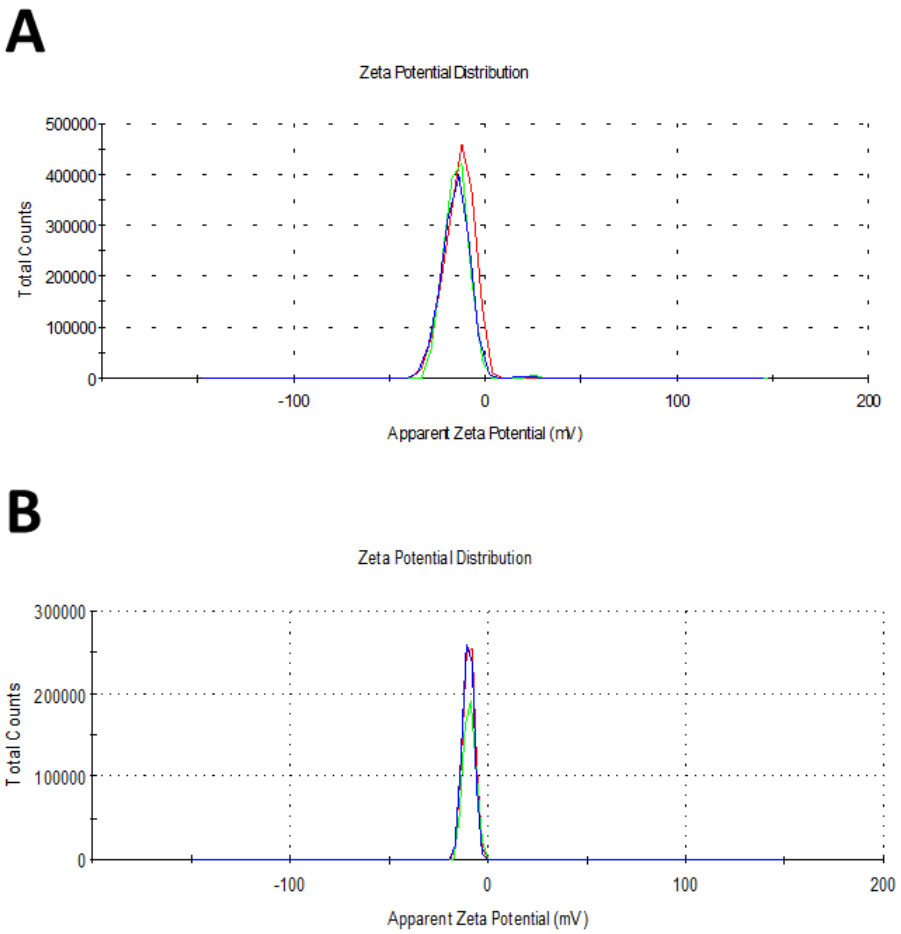

Figure 15. Characterization of ELR nanoparticles. Determination of ζ-potential measured by dynamic light scattering in ultrapure water type I at 37°C at 1 mg/mL. A: Control polymer. B: Akt-in polymer.

5.2.3.4 Cell uptake

As explained above, the nanoparticles' surface charge is one of the most important properties with regard to the cellular uptake. Flow cytometry analysis determined that both control and Akt-in nanoparticles were internalized in the same rate (Figure 16) as both flow cytometry profiles overlapped (blue and orange profiles). Thus, the slightly different size and ζ-potential did not affect the cellular uptake of ELR-based nanoparticles.

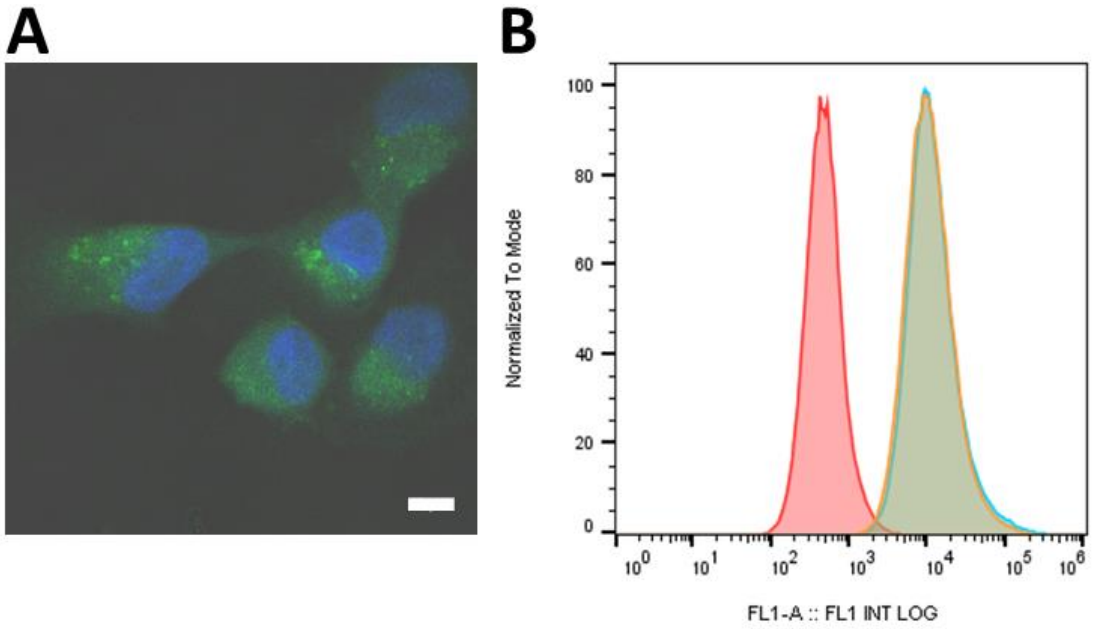

Figure 16. Cellular uptake of ELR nanoparticles. A: Confocal microscopy images of MDA-MB-231 cells incubated with self-assembled fluorescein-labeled control nanoparticles. Cell nuclei were stained with DAPI. Scale bar: 2 µm. B: Flow cytometry analysis of MDA-MB-231 cells incubated with fluorescein-labeled nanoparticles. The cell count was plotted as a function of FL1, which corresponded to the FITC channel for cells containing fluorescent nanoparticles (horizontal axis) against the number of events detected (vertical axis). Negative control untreated cells are plotted in red whereas cells treated with control and Akt-in nanoparticles are shown in blue and orange, respectively.

5.2.3.5 Effect of nanoparticles on cell viability

The main objective of this chapter was to develop a novel smart drug delivery system in order to achieve an accurate release of an Akt inhibitor, which was designed to trigger apoptosis-mediated death of cancerous cells. Thus, based on different expression levels of Akt protein between cancerous and normal cells, the ELR- based nanoparticles were expected to show enhanced effect on cell viability of cancerous cells, compared to normal ones. Once the nanoparticles had been physically characterized, their biological effect on three human cancer cell lines (Caco-2 epithelial colon carcinoma, and two breast cancer lines: MCF-7 and MDA-MB-231) and three normal human primary cell lines (HFF-1 fibroblasts, hMSCs (mesenchymal stem cells) and HUVEC endothelial cells) was examined. Human cancer cell lines were used for this purpose because of their higher expression of Akt protein than normal human cell lines. Furthermore, cancer cells are known to show higher internalization rates due to their faster metabolic state. We used three different concentrations of nanoparticles ranging from the critical

micellar concentration (CMC) of 0.25 mg/mL to 1 mg/mL. As shown in the Figures 17 and 19, the viability of cells exposed to three different concentrations of both types of particles was studied at increasing incubation times. First of all, we determined the cytotoxic effect of control nanoparticles (Figure 17). Although this type of nanoparticle did not carry any bioactive sequence, internalization could affect cellular viability by destabilizing the membrane. Incubation with control nanoparticles did not significantly affect the viability of any of the six cell lines studied. Indeed, the results showed no difference between either the three different concentrations studied or between the different time points (from 30 to 120 min). Thus, we can conclude that, under the experimental conditions used, the control system does not cause a decrease in the viability of either cancerous or non-cancerous cells. This lack of effect could happen either because control nanoparticles are not internalized, contrary to picture 16A, or because they do not affect cell viability. As both types of nanoparticles have the same surface components, we expected the same internalization rates (as demonstrated by flow cytometry in Figure 16B), thus meaning that we can conclude that control nanoparticles do not compromise cell viability as no detectable effect was observed.

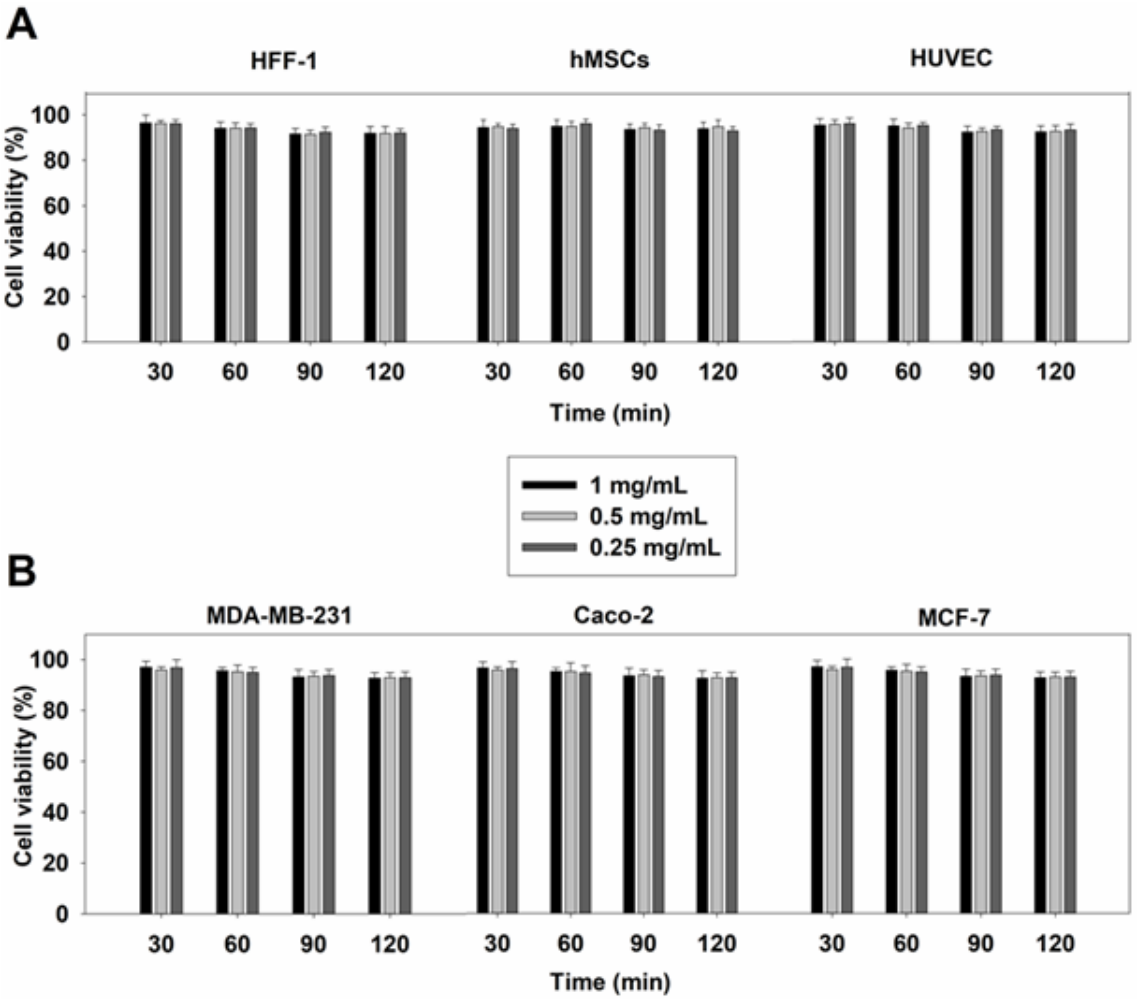

Figure 17. Percentage viability for HFF-1, hMSCs and HUVEC (panel A) and MDA-MB-231, Caco-2 and MCF-7 (panel B) with respect to untreated cells. Cells were incubated with control nanoparticles at three concentrations and times and viability was measured using the LIVE/DEAD kit Assay. n = 3 independent experiments, mean ± SD.

Akt-in nanoparticles also showed no effect on the viability of non-cancerous human cells at lower concentrations (Figures 18 and 19). Thus, endothelial cells, mesenchymal cells and fibroblasts were only slightly affected when incubated for 120 minutes with nanoparticles at the highest concentration (1 mg/mL), with cell viability decreasing to 71%, 83% and 77%, respectively. Furthermore, there were no significant differences between non-cancerous cells treated with 0.25 and 0.5 mg/mL nanoparticles carrying the Akt inhibitor at any time. Of the three normal cell lines used, HUVEC cells were the most affected. In light of the above, we have provided evidence that the effect of nanoparticles on cell viability is both time- and concentration-dependent. Indeed, there were no significant differences between the viability of normal cells with a concentration of 0.25 and 0.5 mg/mL at any time point.

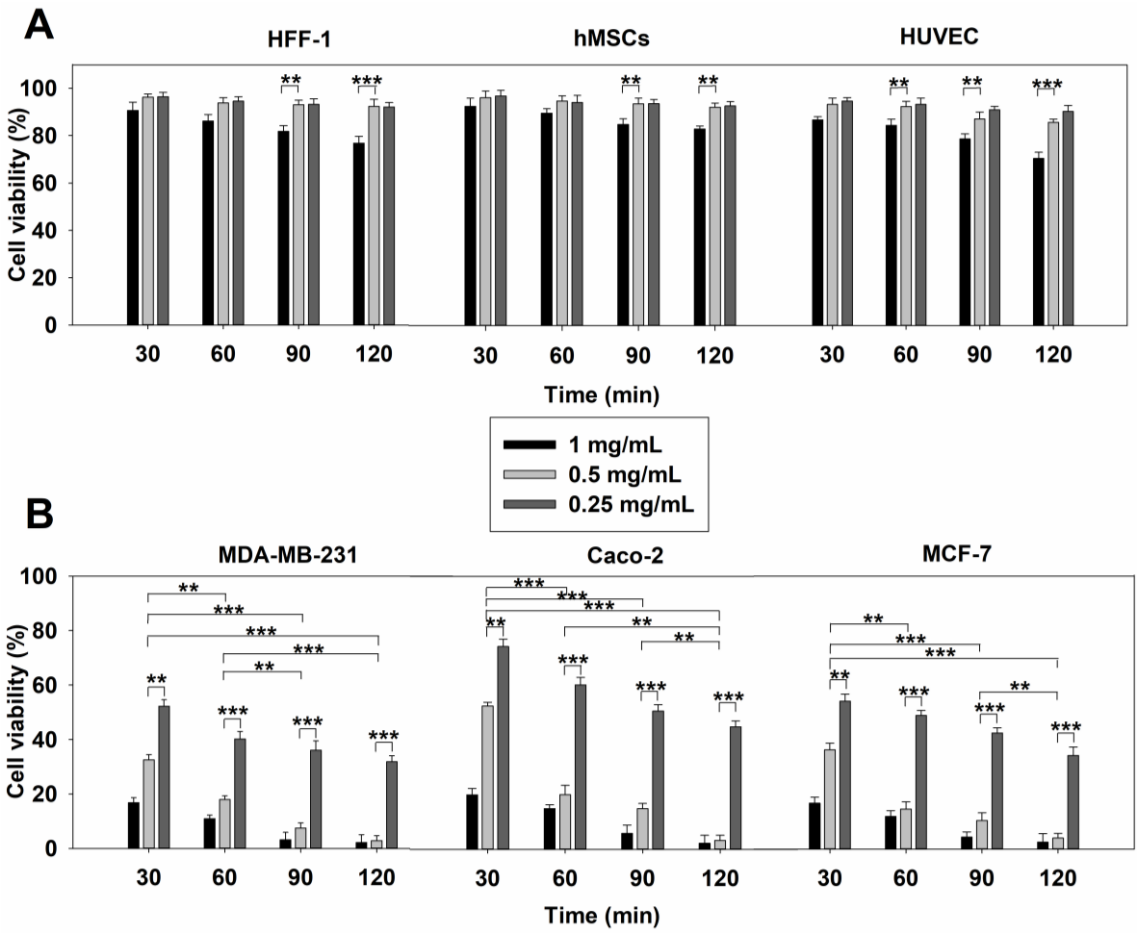

Figure 18. Percentage viability for HFF-1, hMSCs and HUVEC (panel A) and MDA-MB-231, Caco-2 and MCF-7 (panel B) with respect to untreated cells. Cells were incubated with Akt-in nanoparticles at three concentrations and times and viability was measured using the LIVE/DEAD assay kit. n = 3 independent experiments, mean ± SD. **p < 0.01 ***p < 0.001

In contrast, when cancer cell lines were incubated with nanoparticles carrying the detachable Akt inhibitor, cell viability was strongly affected (Figures 18 and 19). Thus, the viability of cancer cells decreased to less than 20% and 40% after incubation with 0.5 and 1 mg/mL for only 30 minutes, respectively, thus indicating the rapid internalization of these Akt-in NPs. After incubation for 120 minutes, the minimal dose tested, which also corresponds to the CMC of the nanoparticles (Table 3), resulted in the death of 55-65% of cancerous cells (Figure 18B). Similarly, when the nanoparticle concentration was increased to 0.5 and 1 mg/mL, the effect on cancer cells was markedly higher (cell viability of 4% and 8% respectively). Thus, an increase in the concentration of Akt-in nanoparticles results in a marked reduction in cell survival. This result suggests that this concentration is the minimal dose able to affect 50% cell viability. These findings also show that, of the three cancer cell lines studied, Caco-2

cells are more resistant to treatment with nanoparticles. These differences could be due to the fact that these cell lines have different internalization rates. Interestingly, the 0.5 mg/mL concentration strongly affected the viability of cancer cells without affecting normal cells, therefore this intermediate concentration was used for subsequent experiments because it seemed to be the largest therapeutic window in which significant differences in the viability of normal cells when compared to cancerous cells were observed. This is of particular importance as it could allow control by modulating the concentration. The enhanced action of nanoparticles on cancer cell lines when compared to normal cell lines could also be due to the fact that cancer cells are better able to internalize nanoparticles, as demonstrated by Villanueva *et al*. [53].

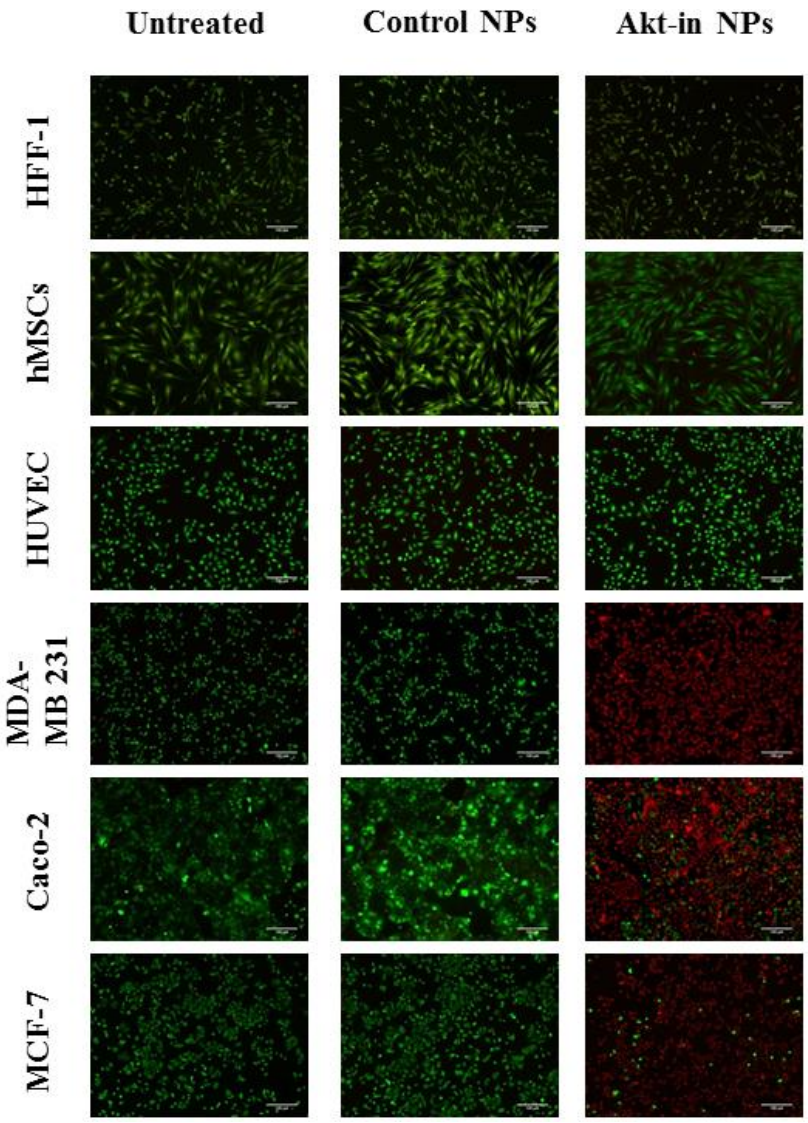

Figure 19. Representative fluorescence microscopy images for HFF-1, hMSCs, HUVEC, MDA-MB-231, Caco-2 and MCF-7 cells after incubation with control nanoparticles or Akt-in

nanoparticles. Cells were incubated with Akt-in nanoparticles 0.5 mg/mL for 120 minutes and viability was measured using the LIVE/DEAD assay kit. Scale bars: 100 µm.

As HUVEC cells seemed to be slightly affected by Akt-in nanoparticles at higher concentrations (Figures 18 and 19) and vascular cells are the most exposed healthy cells due to their contact with nanoparticles during systemic administration [54], cell proliferation was analyzed in order to determine the effect of our novel biomaterial when non-cancerous cells, including HUVEC, were incubated with smart ELR nanoparticles (Figure 20). Thus, human fibroblasts (HFF-1), mesenchymal stem cells (hMSCs) and endothelial cells (HUVEC) were treated with ELR nanoparticles at 1 mg/mL and 0.5 mg/mL for 72 hours. First of all, control nanoparticles did not affect cellular proliferation of any of the three non-cancerous cell lines, compared to untreated cells. Interestingly, when HFF-1, hMSCs and HUVEC cell lines were incubated with Akt-in nanoparticles, a slight effect was observed at early time points but, after the first 24 hours, non-cancerous cells were able to proliferate in the same rate than untreated cells. These results could mean that most of cells surviving to treatment with Akt-in nanoparticles normally proliferated.

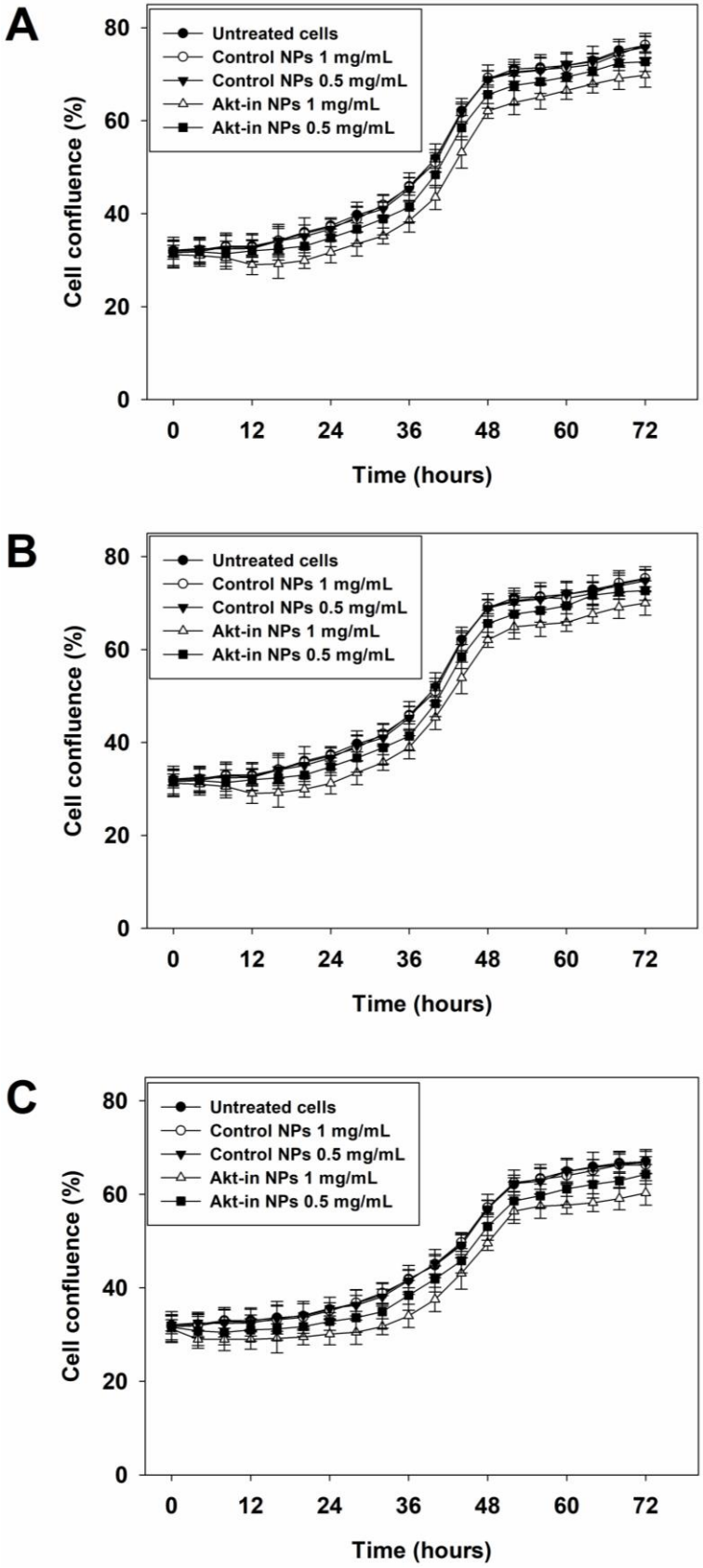

Figure 20. Cellular proliferation of non-cancerous cell lines HFF-1 (A), hMSCs (B) and HUVEC (C). Cells were incubated with ELR-based nanoparticles at two different concentrations (1 mg/mL and 0.5 mg/mL) for 72 hours. n = 2 (6 wells per condition) independent experiments, mean ± SD.

5.2.3.6 Inhibition of Akt phosphorylation

Akt kinase is activated in response to multiple stimuli, such as growth factors, by phosphatidyl inositol triphosphate products generated by PI3K. These lipid products bind to Akt and induce a conformational change in Akt, thus allowing PDK1 to phosphorylate threonine 308. Moreover, phosphorylation of serine 473 and membrane anchoring are required after threonine 308 phosphorylation for final activation of Akt kinase [19]. As explained above, the mechanism of action of the small peptide inhibitor involved attachment to the Akt kinase, thereby avoiding the phosphorylation of Ser473 [21]. In order to confirm the specific effect of the peptide inhibitor, immunoblotting assays were performed in Caco-2 and MDA-MB-231 cells after treatment with Akt-in nanoparticles for 2 hours at 37°C. As shown from Figure 21, Akt phosphorylation was not altered when cancer cell lines were incubated with control nanoparticles. However, when both cell lines were treated with nanoparticles carrying the inhibitor, phosphorylation of Akt protein at Ser473 was prevented. Consequently, we can conclude that the effect of Akt-in nanoparticles on cell viability is due to the accurate inhibitor delivery and its consequent anti-phosphorylation activity, as expected.

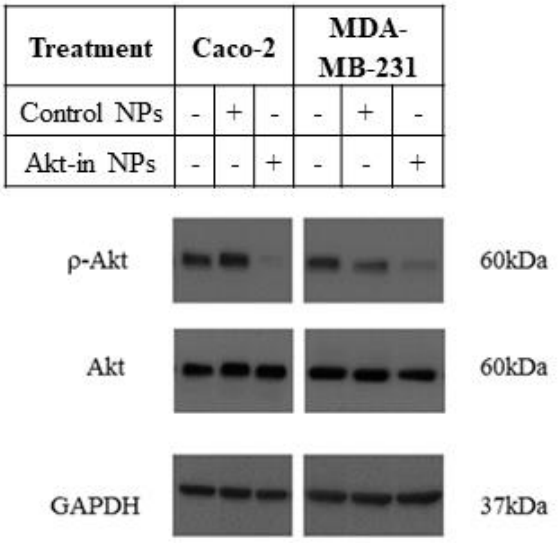

Figure 21. Inhibition of Akt phosphorylation triggered by nanoparticles in MDA-MB-231 and Caco-2 cell lines. Cells were incubated with control and Akt-in nanoparticles, and an immunoblot was performed to measure Akt phosphorylation at Ser473, total Akt and Glyceraldehyde 3-phosphate dehydrogenase (GAPDH) expression, which was used as load control.

5.2.3.7 Apoptotic death triggered by nanoparticles

As shown above, ELR nanoparticles were able to provoke cancer cell death under the conditions tested, therefore the next step was to determine the death pathway provoked (Figure 22). There are two major types of cell death: necrosis and apoptosis. Different diseases, including cancer, deregulate this apoptotic process, thereby resulting in pathological conditions [55]. For this reason, analysis of the signaling pathways that control apoptosis is of great importance for drug discovery and for investigating their therapeutic potential. Akt kinase plays a key role in several multiple signaling pathways involving anti-apoptotic effects [17]. Thus, upon blocking Akt kinase, cells should follow the apoptotic pathway and die. Hiromura *et al.* [21] demonstrated that Akt-in compromised Akt-dependent cellular proliferation and the anti-apoptosis role of Akt. For that reason, apoptotic and necrotic cell percentages were determined in Caco-2 and MDA-MB-231 cells after treatment with nanoparticles carrying Akt-in for 2 hours at 37°C. As Figure 22 shows, apoptosis was the most commonly triggered death pathway for both cancer cell lines. The experiment with Caco-2 cells showed that 95% of cells were in an apoptotic state and only 5% of dead cells in a necrotic state, whereas the experiment with MDA-MB-231 breast cancer cells confirmed that most cells died by apoptosis (93%) instead of necrosis (7%).

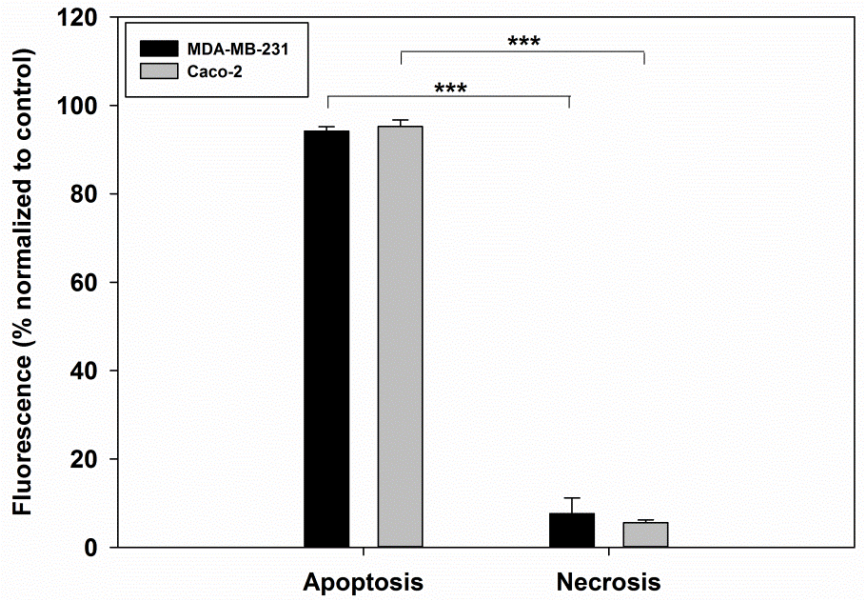

Figure 22. Cell-death pathways triggered by nanoparticles in MDA-MB-231 and Caco-2 cell lines. Cells were incubated with the nanoparticles carrying Akt inhibitor, and an apoptosis/necrosis assay was performed for all samples. H_2O_2 and Triton X-100 treated cells were considered as 100%

apoptosis and necrosis control, respectively. n = 3 independent experiments, mean ± SD. ***p < 0.001

Thus, both cancer cell lines corroborated that the Akt inhibitor unlocked the apoptotic pathway blocked by Akt kinase. This is of particular importance as it shows that our ELR-based nanoparticles enhance the apoptotic pathway instead of being a toxic agent for cells.

5.2.3.8 Endocytic internalization of nanoparticles

Once the specificity of the Akt-in nanoparticles in cancer cell lines had been assessed, their internalization pathway was studied. In general, the internalization pathway for nanoparticles occurs via two mechanisms: phagocytosis and endocytosis [56]. As mentioned above, larger nanoparticles (200 nm) are more likely to undergo phagocytosis whereas smaller ones enter cells by endocytosis. Three different types of endocytosis have been described: macropinocytosis, clathrin-mediated endocytosis (CME) and caveolae-mediated endocytosis (CvME) [34], but only the latter two mechanisms work via receptor-ligand interactions forming vesicles that are invaginated, such as endosomes and lysosomes [34, 57, 58]. In our case, internalization of the NPs via an endocytic mechanism is critical in order to allow the Akt inhibitor to reach the cytoplasm after the participation of lysosomal enzyme Cathepsin D and H5 peptide for endolysosomal escape. Of the six cell lines used above, Caco-2 and MDA-MB-231 were selected to determine the internalization pathway due to their higher levels of Akt expression and the different activity of the Akt-in nanoparticles observed (Figure 18). This selection could give us a better insight into the accuracy and mechanism of action of the nanoparticles when faced with cancer cells in which Akt kinase is overexpressed. As such, this selection could be the most realistic *in vitro* scenario for our study prior to using *in vivo* models in future studies. To determine this, Caco-2 and MDA-MB-231 cells were pre-treated with four different endocytosis inhibitors for 30 min at 37°C and then incubated with Akt-in nanoparticles for 2 hours at 37°C. Maximum viability (positive control) was achieved when cells were treated with PBS for 2 hours, whereas the negative control was achieved with Akt-in NPs instead of PBS. As shown from Figures 23 and 24, the inhibition of macropinocytosis by amiloride (Na^+/H^+ exchange) did not alter the effect of nanoparticles on cell viability, whereas the inhibition of caveolae-mediated endocytosis by filipin only showed a minimum but statistically

significant effect (14% cell viability). However, the inhibition of clathrin-mediated endocytosis by monodansylcadaverine was found to almost completely inhibit the action of nanoparticles and a cell viability of 92% was restored. Additionally, the inhibition of acidification in acidic vesicles by chloroquine also significantly affected (80% cell viability) the action of nanoparticles.

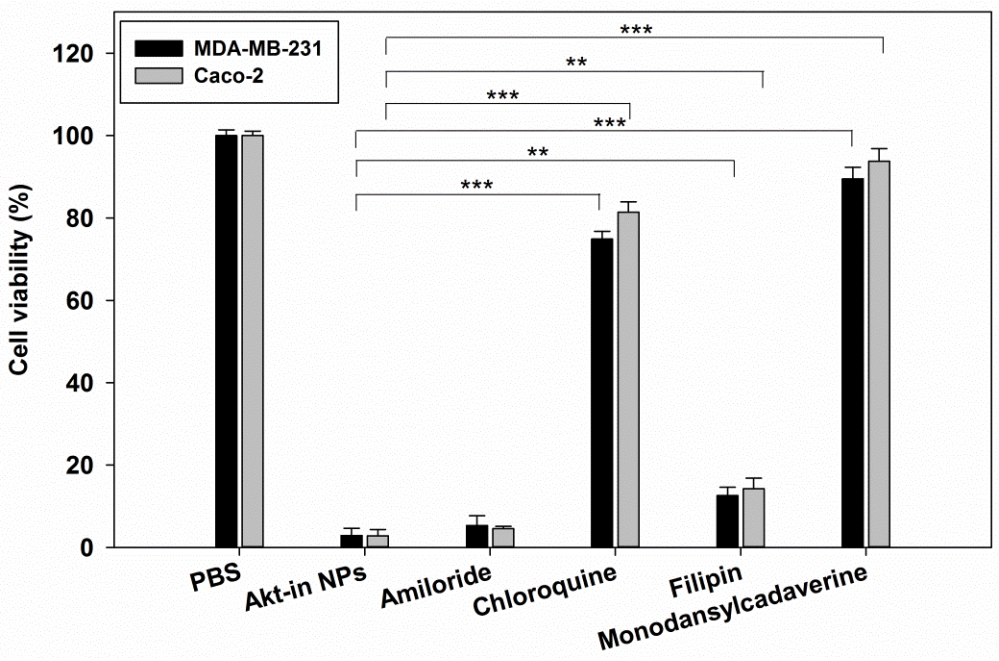

Figure 23. Study of the internalization pathways for nanoparticles carrying Akt inhibitor in MDA-MB-231 and Caco-2 cell lines. Cells were incubated with PBS, 0.5 mg/mL Akt-in nanoparticles or pre-incubated with an internalization inhibitor, such as amiloride, chloroquine, filipin or monodansylcadaverine prior to treatment with 0.5 mg/mL Akt-in nanoparticles. Viability was measured using the LIVE/DEAD assay kit. n = 3 independent experiments, mean ± SD. **p < 0.01 ***p < 0.001

These findings show the primary influence of clathrin-mediated endocytosis for the internalization of nanoparticles, due to the action of the enzyme Cathepsin D on the CatD-sensitive sequence in order to release the Akt inhibitor. We have also demonstrated the importance of endosomal/lysosomal acidification for our nanoparticles as this acidification allows the conformational change and action of H5 peptide in order to escape from acidic vesicles. All these results may also suggest that lysosomes are key actors in the intracellular activation of nanoparticles as, if the nanoparticles underwent a different internalization pathway, they would not be effective.

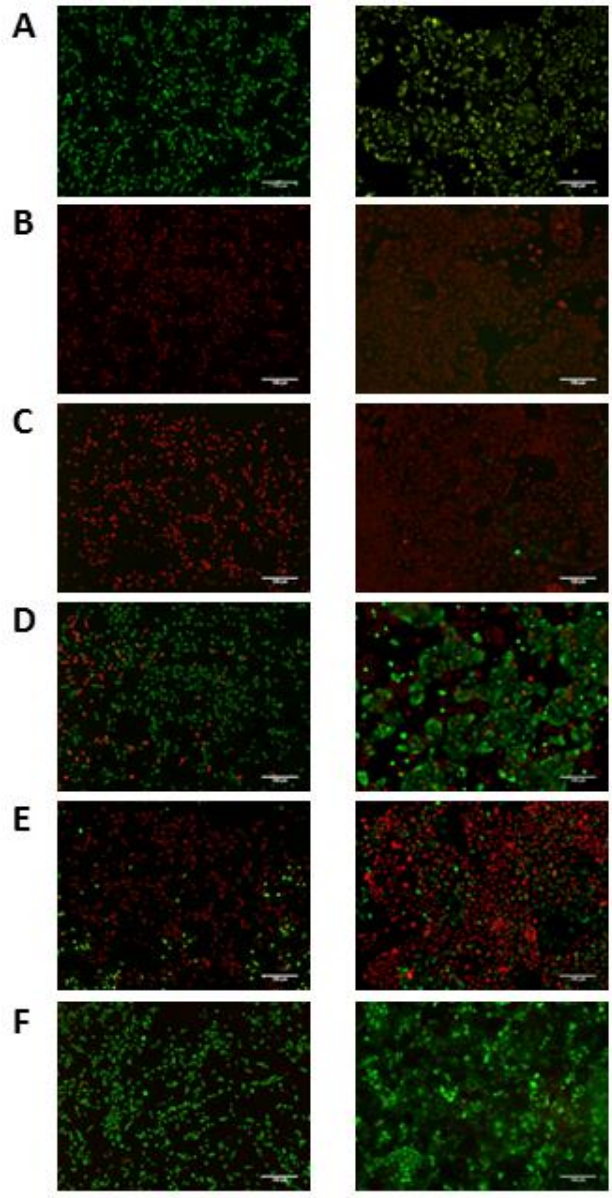

Figure 24. Representative fluorescence microscopy images for Caco-2 (right) and MDA-MB-231 (left) after incubation with A: PBS (100% viability) B: 0.5 mg/mL Akt-in nanoparticles (0% viability) or pre-incubated with an internalization inhibitor, such as: C: amiloride D: chloroquine E: filipin or F: monodansylcadaverine prior to treatment with Akt-in nanoparticles. Cells were incubated with endocytosis inhibitors for 30 min before the treatment with Akt-in nanoparticles 0.5 mg/mL for 120 minutes and viability was measured using the LIVE/DEAD assay kit. Scale bars: 100 µm.

5.2.3.9 Intracellular nanoparticle activation

One of the most promising advantages of genetically engineered ELR-based nanoparticles is the fact that the action on targeted cells and tissues can be modulated by adding different bioactive functionalities. As shown above, endocytic acidification seemed to be a key factor in nanoparticle activation. Endosome acidification upon

fusion with the lysosome also means that multiple degradative enzymes act on the cargo [59]. One of the key lysosomal proteases is the aspartyl endopeptidase Cathepsin D [60], which shows a higher expression in tumors than in normal tissues and is thought to promote tumor invasion and growth [36]. Thus, we included a CatD-sensitive sequence upstream of Akt-in in our polymer in order to allow the inhibitor to be removed from the NP and be released into the cytoplasm after the action of H5 for lysosomal escape, thereby binding to the targeted protein. Thus, as the participation of CatD-directed degradation should be critical for Akt-in activation, we assessed the role of CatD in our system by selectively inhibiting it using Pepstatin A [61].

As such, we hypothesized that when the lysosomal degradative enzyme Cathepsin D is inhibited, the Akt inhibitor peptide cannot be released into the cytoplasm and reach Akt protein in order to block it. The two human cancer cell lines Caco-2 and MDA-MB-231 cells were pre-incubated with 100 μM Pepstatin A for 16 hours at 37°C before treatment with Akt-in nanoparticles for 2 hours at 37°C. The cell viability was then assessed. As shown from Figure 25, incubation of cells with the CatD inhibitor did not produce any effect on cell viability despite blocking an important degradative enzyme. Similarly, when cells were pre-treated with Pepstatin A, the nanoparticles also had no effect and cell viability was not affected, in contrast to the effect of nanoparticles in both these cancer cell lines when the action of CatD is not inhibited. We can therefore conclude that Akt-in nanoparticles lose their effect on cell viability when their intracellular activation is inhibited. This could be due to the fact that the peptide is unable to escape from the lysosome, thus meaning that Akt protein is not reached and continues to enhance cell proliferation and block apoptotic cell death.

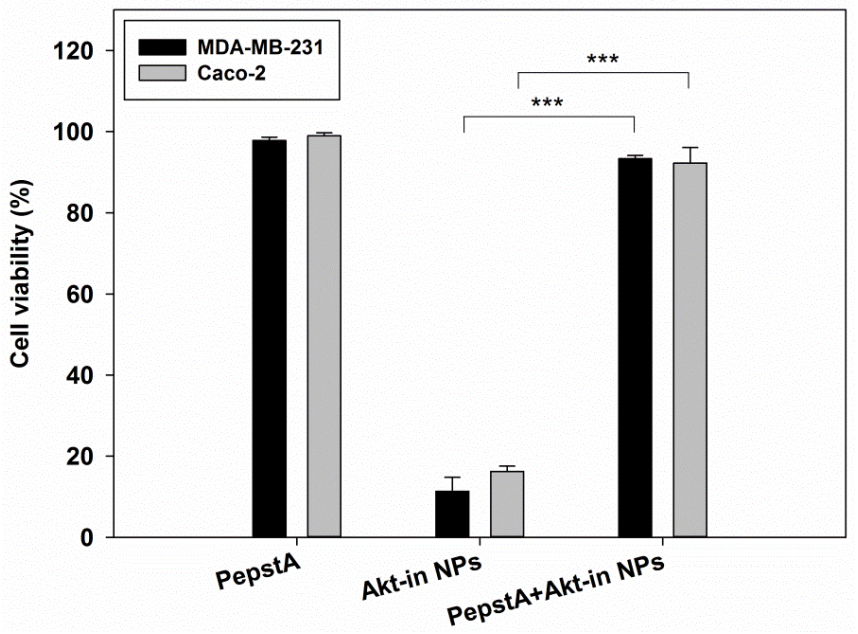

Figure 25. Lysosomal trafficking of nanoparticles carrying Akt inhibitor in MDA-MB-231 and Caco-2 cell lines. Cells were incubated with Pepstatin A (negative control), Akt-in nanoparticles or both, and viability was measured using the LIVE/DEAD assay kit. n = 3 independent experiments, mean ± SD. ***p < 0.001

5.2.4. Final remarks

One of the disadvantages of current chemotherapeutic treatments against cancer is the lack of specificity of the drugs, which therefore results in significant damage to healthy tissues [16]. In order to improve the selectivity of new drugs, nanotechnological approaches with incorporated targeting systems appear to be the best strategy [2]. Furthermore, different types of solid tumor offer multiples obstacles to the drug-delivery systems tested to date. Akt kinase is one of the most interesting of the multiple proteins that can be targeted due to its higher expression in cancerous cells and its role as a key factor controlling multiple signaling pathways and processes, such as cell growth, proliferation and survival [17]. The small peptide inhibitor Akt-in was therefore designed in order to block Akt protein, thereby inhibiting both its essential activity and tumor cell growth [21].

Thus, we have developed a new smart nanodevice specifically designed including different bioactive peptides so as to achieve the proper delivery of therapeutic agents in targeted cells and tissues. Genetic engineering techniques used for the design of these ELR polymers allows us to be able to create different advanced drug delivery systems

with diverse applications as therapeutic approach for multiple diseases, taking advantage of its smart stimuli-responsive behavior. In this chapter, we have developed a new ELR-based nanoparticle carrying a small peptide inhibitor against Akt protein in order to create an advanced approach for application thereof in the therapeutic treatment of cancer. It should be noted that a complex design of the smart nanoparticles, with different actors, was needed in order to successfully release the inhibitor into the cell cytoplasm, thereby avoiding degradative proteases which would not allow the peptide to enter otherwise.

We tested the specificity of this novel ELR nanoparticle in 6 different cell lines. Thus, our drug delivery system showed no effect in three primary non-cancerous cell lines, while the same treatment showed lethal effects in breast and colorectal cancerous cells. Moreover, *in vitro* experiments confirmed that each block included in the polymer was absolutely required for the proper release of the inhibitor in the cellular cytoplasm. Thus, inactivation of lysosomal proteases and inhibition of vesicles acidification resulted in abolished effect of nanoparticles.

Overall, based on our findings, we can conclude that this smart nanodevice could be a novel strategy for the proper release of therapeutic agents at molecular level in targeted cells. This study is the first to report an accurate smart nanodevice against Akt protein after intracellular activation. Interestingly, our system improved the accuracy of the inhibitor in a time- (our system was 12 times faster than the inhibitor alone) and dose-dependent manner (5 times lower amount of inhibitor), compared to previous works with Akt-in [21]. This improved action of Akt-in when carried in nanoparticles could be due to the better internalization of nanoparticles compared to nude peptides and their shielding effect, which protects the inhibitor from cellular proteases.

It is worthy to mention that our new therapeutic system is not limited to one type of cancer, as it is targeted to Akt kinase protein, which is overexpressed in multiple neoplastic diseases, such as colon, pancreatic, breast, ovarian and lung cancer. Further studies are needed to study the accuracy of these nanoparticles in *in vivo* models better resembling the tumor environment and its interactions with nanocarriers. In the future, patients overexpressing Akt may be candidates for therapeutic treatment with

nanoparticles bearing the inhibitor, which could improve the problems caused by current non-specific chemotherapeutic drugs.

5.2.5. References

[1] R. Saxena, M.J. Nanjan. Elastin-like polypeptides and their applications in anticancer drug delivery systems: a review. Drug Deliv, 2015. 22 (2):156-167.
[2] V. Jain, S. Jain, S.C. Mahajan. Nanomedicines based drug delivery systems for anti-cancer targeting and treatment. Curr Drug Deliv, 2015. 12 (2):177-191.
[3] Y. Zhang, H.F. Chan, K.W. Leong. Advanced materials and processing for drug delivery: the past and the future. Adv Drug Deliv Rev, 2013. 65 (1):104-120.
[4] W. Han, A. Chilkoti, G.P. Lopez. Self-assembled hybrid elastin-like polypeptide/silica nanoparticles enable triggered drug release. Nanoscale, 2017. 9 (18):6178-6186.
[5] D. Raucher, I. Massodi, G.L. Bidwell. Thermally targeted delivery of chemotherapeutics and anti-cancer peptides by elastin-like polypeptide. Expert Opin Drug Deliv, 2008. 5 (3):353-369.
[6] J. Shi*, et al.* Cancer nanomedicine: progress, challenges and opportunities. Nat Rev Cancer, 2017. 17 (1):20-37.
[7] D.M. Floss*, et al.* Elastin-like polypeptides revolutionize recombinant protein expression and their biomedical application. Trends Biotechnol, 2010. 28 (1):37-45.
[8] P. Shi, J.A. Gustafson, J.A. MacKay. Genetically engineered nanocarriers for drug delivery. Int J Nanomedicine, 2014. 9 1617-1626.
[9] H. Hillaireau, P. Couvreur. Nanocarriers' entry into the cell: relevance to drug delivery. Cell Mol Life Sci, 2009. 66 (17):2873-2896.
[10] H. Bae*, et al.* Development of functional biomaterials with micro- and nanoscale technologies for tissue engineering and drug delivery applications. J Tissue Eng Regen Med, 2014. 8 (1):1-14.
[11] V.P. Torchilin. Drug targeting. Eur J Pharm Sci, 2000. 11 Suppl 2 S81-91.
[12] Y. Matsumura, H. Maeda. A new concept for macromolecular therapeutics in cancer chemotherapy: mechanism of tumoritropic accumulation of proteins and the antitumor agent smancs. Cancer Res, 1986. 46 (12 Pt 1):6387-6392.
[13] H. Maeda, G.Y. Bharate, J. Daruwalla. Polymeric drugs for efficient tumor-targeted drug delivery based on EPR-effect. Eur J Pharm Biopharm, 2009. 71 (3):409-419.
[14] R.K. Jain. Transport of molecules in the tumor interstitium: a review. Cancer Res, 1987. 47 (12):3039-3051.
[15] M.J. Pina*, et al.* Biocompatible ELR-Based Polyplexes Coated with MUC1 Specific Aptamers and Targeted for Breast Cancer Gene Therapy. Mol Pharm, 2016. 13 (3):795-808.
[16] J.D. Byrne, T. Betancourt, L. Brannon-Peppas. Active targeting schemes for nanoparticle systems in cancer therapeutics. Adv Drug Deliv Rev, 2008. 60 (15):1615-1626.
[17] L.C. Cantley. The phosphoinositide 3-kinase pathway. Science, 2002. 296 (5573):1655-1657.
[18] A. Bellacosa*, et al.* A retroviral oncogene, akt, encoding a serine-threonine kinase containing an SH2-like region. Science, 1991. 254 (5029):274-277.
[19] B. Vanhaesebroeck, D.R. Alessi. The PI3K-PDK1 connection: more than just a road to PKB. Biochem J, 2000. 346 Pt 3 561-576.
[20] J. Luo, B.D. Manning, L.C. Cantley. Targeting the PI3K-Akt pathway in human cancer: rationale and promise. Cancer Cell, 2003. 4 (4):257-262.
[21] M. Hiromura*, et al.* Inhibition of Akt kinase activity by a peptide spanning the betaA strand of the proto-oncogene TCL1. J Biol Chem, 2004. 279 (51):53407-53418.

[22] J.C. Rodriguez-Cabello, *et al.* Synthesis of genetically engineered protein polymers (recombinamers) as an example of advanced self-assembled smart materials. Methods Mol Biol, 2012. 811 17-38.
[23] A. Ribeiro. Functionality development in systems based on Elastin-like recombinamers: From nano-objects to macrogels. PhD Thesis, 2008.
[24] M. Pierna. New strategies to develop bioactive cell-harvesting systems based on elastin like recombinamers. PhD Thesis, 2013.
[25] C.T. Chung, S.L. Niemela, R.H. Miller. One-step preparation of competent Escherichia coli: transformation and storage of bacterial cells in the same solution. Proc Natl Acad Sci U S A, 1989. 86 (7):2172-2175.
[26] C.T. Chung, R.H. Miller. Preparation and storage of competent Escherichia coli cells. Methods Enzymol, 1993. 218 621-627.
[27] U.K. Laemmli. Cleavage of structural proteins during the assembly of the head of bacteriophage T4. Nature, 1970. 227 (5259):680-685.
[28] R.E. Sallach, *et al.* Long-term biostability of self-assembling protein polymers in the absence of covalent crosslinking. Biomaterials, 2010. 31 (4):779-791.
[29] O.S. Fenton, *et al.* Advances in biomaterials for drug delivery. Mol Pharm, 2018. e1705328.
[30] C. Garcia-Arevalo, *et al.* Immunomodulatory nanoparticles from elastin-like recombinamers: single-molecules for tuberculosis vaccine development. Mol Pharm, 2013. 10 (2):586-597.
[31] T. Kowalczyk, *et al.* Elastin-like polypeptides as a promising family of genetically-engineered protein based polymers. World J Microbiol Biotechnol, 2014. 30 (8):2141-2152.
[32] S.R. MacEwan, A. Chilkoti. Applications of elastin-like polypeptides in drug delivery. J Control Release, 2014. 190 314-330.
[33] M. Santos, *et al.* Genetically Engineered Elastin-based Biomaterials for Biomedical Applications. Curr Med Chem, 2018. 26 (40):7117-7146.
[34] G. Sahay, D.Y. Alakhova, A.V. Kabanov. Endocytosis of nanomedicines. J Control Release, 2010. 145 (3):182-195.
[35] N. Ohmori, *et al.* The enhancing effect of anionic alpha-helical peptide on cationic peptide-mediating transfection systems. Biochem Biophys Res Commun, 1997. 235 (3):726-729.
[36] C. Kirana, *et al.* Cathepsin D expression in colorectal cancer: From proteomic discovery through validation using Western Blotting, immunohistochemistry, and tissue microarrays. Int J Proteomics, 2012. 2012 245819.
[37] C. Bure, *et al.* Histidine-rich peptide: evidence for a single zinc-binding site on H5WYG peptide that promotes membrane fusion at neutral pH. J Mass Spectrom, 2009. 44 (1):81-89.
[38] D.T. McPherson, J. Xu, D.W. Urry. Product purification by reversible phase transition following Escherichia coli expression of genes encoding up to 251 repeats of the elastomeric pentapeptide GVGVP. Protein Expr Purif, 1996. 7 (1):51-57.
[39] S. Moktan, *et al.* Thermal targeting of an acid-sensitive doxorubicin conjugate of elastin-like polypeptide enhances the therapeutic efficacy compared with the parent compound in vivo. Mol Cancer Ther, 2012. 11 (7):1547-1556.
[40] C. Bouzin, O. Feron. Targeting tumor stroma and exploiting mature tumor vasculature to improve anti-cancer drug delivery. Drug Resist Updat, 2007. 10 (3):109-120.
[41] D.E. Owens, 3rd, N.A. Peppas. Opsonization, biodistribution, and pharmacokinetics of polymeric nanoparticles. Int J Pharm, 2006. 307 (1):93-102.
[42] O.V. Khullar, *et al.* Nanoparticle migration and delivery of Paclitaxel to regional lymph nodes in a large animal model. J Am Coll Surg, 2012. 214 (3):328-337.
[43] M.E. Davis, Z.G. Chen, D.M. Shin. Nanoparticle therapeutics: an emerging treatment modality for cancer. Nat Rev Drug Discov, 2008. 7 (9):771-782.

[44] L. Martin, *et al.* Temperature-triggered self-assembly of elastin-like block co-recombinamers:the controlled formation of micelles and vesicles in an aqueous medium. Biomacromolecules, 2012. 13 (2):293-298.
[45] J.I. Rodriguez Hernandez, *et al.* Toward 'smart' nano-objects by self-assembly of block copolymers in solution. Progress in Polymer Science (Oxford), 2005. 30 (7):691-724.
[46] I. Grillo, *et al.* Spontaneous formation of nanovesicles in mixtures of nonionic and dialkyl chain cationic surfactants studied by surface tension and SANS. Langmuir, 2009. 25 (7):3932-3943.
[47] S. Bhattacharjee. DLS and zeta potential - What they are and what they are not? J Control Release, 2016. 235 337-351.
[48] S.H. Anastasiadis, I. Gancarz, J.T. Koberstein. Compatibilizing effect of block copolymers added to the polymer/polymer interface. . Macromolecules, 1989. 22 (3):1449-1453.
[49] J. Lin, *et al.* Penetration of lipid membranes by gold nanoparticles: insights into cellular uptake, cytotoxicity, and their relationship. ACS Nano, 2010. 4 (9):5421-5429.
[50] Y. Li, N. Gu. Thermodynamics of charged nanoparticle adsorption on charge-neutral membranes: a simulation study. J Phys Chem B, 2010. 114 (8):2749-2754.
[51] R.R. Arvizo, *et al.* Effect of nanoparticle surface charge at the plasma membrane and beyond. Nano Lett, 2010. 10 (7):2543-2548.
[52] Y. Malam, M. Loizidou, A.M. Seifalian. Liposomes and nanoparticles: nanosized vehicles for drug delivery in cancer. Trends Pharmacol Sci, 2009. 30 (11):592-599.
[53] A. Villanueva, *et al.* The influence of surface functionalization on the enhanced internalization of magnetic nanoparticles in cancer cells. Nanotechnology, 2009. 20 (11):115103.
[54] D.S. Spencer, A.S. Puranik, N.A. Peppas. Intelligent nanoparticles for advanced drug delivery in cancer treatment. Curr Opin Chem Eng, 2015. 7 84-92.
[55] M. van Engeland, *et al.* Annexin V-affinity assay: a review on an apoptosis detection system based on phosphatidylserine exposure. Cytometry, 1998. 31 (1):1-9.
[56] R. Coco, *et al.* Drug delivery to inflamed colon by nanoparticles: comparison of different strategies. Int J Pharm, 2013. 440 (1):3-12.
[57] S.D. Conner, S.L. Schmid. Regulated portals of entry into the cell. Nature, 2003. 422 (6927):37-44.
[58] J.M. Gamboa, K.W. Leong. In vitro and in vivo models for the study of oral delivery of nanoparticles. Adv Drug Deliv Rev, 2013. 65 (6):800-810.
[59] M. Jovic, *et al.* The early endosome: a busy sorting station for proteins at the crossroads. Histol Histopathol, 2010. 25 (1):99-112.
[60] M.Z. Pranjol, *et al.* The potential role of the proteases Cathepsin D and Cathepsin L in the progression and metastasis of epithelial ovarian cancer. Biomolecules, 2015. 5 (4):3260-3279.
[61] A. Amritraj, *et al.* Role of cathepsin D in U18666A-induced neuronal cell death: potential implication in Niemann-Pick type C disease pathogenesis. J Biol Chem, 2013. 288 (5):3136-3152.

Chapter 3

Smart ELR nanoparticles as advanced anti-Akt drug delivery systems for pancreatic cancer therapy

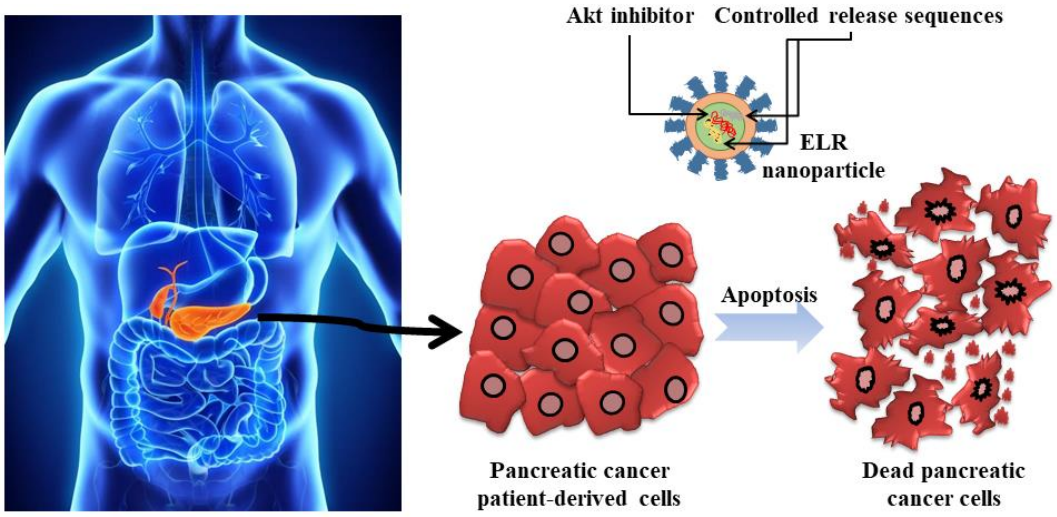

Part of the results of this chapter constitutes the article:

Smart ELR nanoparticles as advanced anti-Akt kinase drug delivery systems for pancreatic cancer therapy. J. Gonzalez-Valdivieso, A. Garcia-Sampedro, A. Hall, A. Girotti, F.J. Arias, S. Pereira and P. Acedo. **2020**. Work in progress.

The author carried out part of this research as a visiting student at the Institute for Liver and Digestive Health (Royal Free Hospital/University College London), for 4 months, supported by the University of Valladolid and the European Union funding. The work was developed under the supervision of Prof. Stephen Pereira.

5.3.1. Introduction

Although different treatments have been discovered during the last years, pancreatic cancer remains as one of the deadliest forms of cancer [1]. In particular, pancreatic ductal adenocarcinoma (PDAC) and cholangiocarcinoma (CCA) are two of the most aggressive types of cancer mainly detected at a late stage. In fact, the 5-year survival rate for PDAC and CCA is less than 5 and 10%, respectively [2]. Different factors are responsible of the poor diagnosis and treatment options available for this disease, such as the difficulty to reach the pancreatic tumor site or the ability of pancreatic cancer cells to rapidly acquire resistance to therapeutic drugs. Side effects on healthy tissues and poor accumulation of drugs in the tumor difficult the effective action of chemotherapeutic agents [3]. Although advances in imaging techniques and early detection tools have been made, novel approaches are needed to yield better sensitivity, specificity and to improve prognosis of patients. The majority of advanced solid malignancies in adults, including pancreatic cancer, are not curable by using conventional therapies [4]. However, the use of targeted agents has resulted in slightly improved survival times [5, 6], as it is known that the use of new targeted therapies in the clinical practice diminishes drug resistance provoked by intratumor heterogeneity [7, 8]. Thus, targeted agents are more effective in tumors in which the targeted pathway is needed for the survival of cancer cells and is effectively inhibited by means of the drug. For these reasons, novel strategies are needed in order to achieve higher rates of successful treatments and avoid undesired effects on healthy tissues [9]. Thus, biomaterials have become one of the most promising therapeutic approaches for drug delivery purposes, aiming at achieving a more specific and controlled action by only affecting targeted cells and overcoming the poor accumulation of current drugs in pancreatic tumors [10].

One of the reasons for the low rates of success in clinical treatments lies on the intratumor heterogeneity of pancreatic tumors, populated by various cell types and lineages within the tumor. *In vitro* cell cultures used by most of researchers highlight one of the biggest problems they face, as established cell lines generally arise from the same single clone and do not reflect the tumor complexity and heterogeneity. Thus, the so-called conventional cell lines are convenient and easy to use, but have important limitations in terms of preclinical drug discovery and development. Therefore, a relevant disadvantage resides in their lack of predictive value for clinical trials. Established cell lines used in *in*

vitro assays do not represent the characteristic genetic heterogeneity of a tumor. Oncology is quickly evolving from a general approach to a new era in which patients' tumors are greatly detailed and profiled in order to select the most appropriate treatment: the personalized medicine [11]. Thus, the use of preclinical models is a core component in translational cancer research, from the biologic understanding of the disease to the development of new therapeutic treatments [12]. Xenograft models are more biologically representative of patient tumors and valuable models in order to predict clinical outcome of drugs. Xenografts derived directly from patient biopsies with minimal *in vitro* manipulation better contain morphological and molecular markers of the source tumors [13, 14] However, some of the supporting elements in these tumors indeed have mouse origin rather than human. Different groups have established disease-specific panels of xenografts directly from patient tumors and have shown this approach as a feasible tool, with a high rate of engraftment for some tumors, such as pancreatic, lung, and colon cancer [13-15]. Thus, patient-derived models help researchers to study novel therapeutic drugs in more physiological conditions including cancer cells from different origins [16, 17]. For all these reasons, we used in this chapter two different clinically relevant pancreatic cancer patient-derived cells [14, 18, 19]: PDX185 and PDX354.

Photodynamic therapy (PDT) is a novel therapeutic strategy and involves the exposure of localized tumor tissue containing a photosensitizer (PS) to light of a determined wavelength [20]. PDT has been considered as a promising method for cancer treatment, in comparison with chemotherapy or radiotherapy, due to its low invasiveness and limited side effects [21]. The cytotoxic effect of PDT is based on the combination of photosensitizer, light and molecular oxygen. The light energy, which is provided by laser irradiation, induces PS excitation within the tumor cells and, as a consequence, leads to photo-oxidative reactions between the photosensitizer and oxygen [22]. The therapeutic success of PDT relies on the generation of reactive oxygen species (ROS), which is related to the PS concentration in tumor tissue and tumor oxygenation [23]. Moreover, the ROS generation can be controlled by selecting the photosensitizer localization and the confinement of light to a targeted tumor microenvironment [24].

In this chapter, we studied the effect of a novel therapeutic treatment based on smart self-assembling nanoparticles for controlled drug delivery purposes on pancreatic cancer

patient-derived cells in combination with PDT. We determined the effect of nanoparticles on cellular metabolic activity and viability, cellular uptake and subcellular accumulation and their molecular mechanism of action. Although these ELR nanoparticles were previously characterized and studied in breast and colorectal cancer cell cultures *in vitro* [25], patient-derived cells are presented as a head step to advance towards the development and validation of the novel therapeutic strategy proposed. Therefore, we took advantage of a complex *in vitro* model based on patient-derived models and closer to real pancreatic cancer.

5.3.2. Methods

5.3.2.1 Fluorescent ELR labeling

ELR polymers were covalently modified with NHS-Fluorescein or NHS-Cy5, when indicated, by conjugation to free amines following the protocol described in Chapter 2 section 2.13.

5.3.2.2 Cell culture

PANC-1 cells were maintained in DMEM supplemented with 10% FBS, 100 U/mL penicillin and 0.1 mg/mL streptomycin at 5% CO2 and 37°C. PDX185 and PDX354 cells were cultured in RPMI medium supplemented with 10% FBS, 100 U/mL penicillin and 0.1 mg/mL streptomycin at 5% CO2 and 37°C. When required, cells were collected using a solution of 0.05% Trypsin-EDTA.

5.3.2.3 Flow cytometry

PANC-1, PDX185 and PDX354 cells ($5x10^5$ cells/well in 6-well plates) were incubated with complete media containing fluorescein-labelled ELR nanoparticles at 0.5 mg/mL for 3 or 24 hours. Cells were washed with PBS, harvested and resuspended in PBS. Flow cytometry analysis were performed to assess the fluorescein internalized in cells with a BD LSR II flow cytometer with a laser line at 640 nm (red) and complemented with appropriate filters. 10000 events per sample were recorded and single cells were discriminated from doublets by pulse-processing. Finally, FlowJo v10 software (Tree Star, Inc) was used to analyze and plot the acquired data.

5.3.2.4 Confocal microscopy

Cells were seeded onto FluoroDish glass bottom dishes in a quantity of 8×10^3 and 1.6×10^4 cells for PANC-1 and PDX cells respectively, and incubated overnight prior to the treatment. PANC-1 cells were treated with fluorescein-labeled ELR nanoparticles at 0.5 mg/mL for 3 or 24 hours. After washing with PBS, cells were incubated with 75 nM LysoTracker Red DND-99 (1 mM working solution in DMSO) for 1 hour at 37°C. Fluorescence images were taken with an Olympus TIRF confocal microscope equipped with SIM scanner and an incubator to maintain the conditions constant at 37°C, 95% humidity and 5% CO_2.

5.3.2.5 Metabolic activity

5×10^3 (PANC-1) and 1×10^4 (PDXs) cells/well, were seeded onto 96-well plates in order to obtain similar confluence level for all the lines 16 hours prior to treatment. PANC-1, PDX185 and PDX354 cells were treated independently with three different concentrations (0.25 mg/mL, 0.5 mg/mL and 1 mg/mL) of ELR nanoparticles for 3 and 24 hours. Following treatment, MTT assay was performed according to manufacturer's instructions. Briefly, stock solution of MTT reagent (0.5 mg/mL for PANC-1 and 1 mg/mL for patient-derived cells) was diluted in complete media and sterilized by filtration (0.45 µm). 100 µL/well of MTT solution were added and samples were incubated for 1 hour in the dark. After that, media was removed and 100 µL/well of DMSO were added to solve MTT crystals. Absorbance was measured at 562 nm using an Infinite M200 PRO microplate reader (Tecan Group Ltd.). Additionally, images of cultures were taken with an EVOS Digital Color fluorescence microscope. Three independent experiments, each in triplicate, were performed.

5.3.2.6 Cell viability

PANC-1, PDX185 and PDX354 cells were seeded and treated as described in section 2.5. LIVE/DEAD Viability/Cytoxicity Assay Kit was used according to the manufacturer's instructions, as described in Chapter 1 section 2.13, using an Infinite M200 PRO microplate reader. Additionally, images of cultures were taken with an EVOS Digital Color fluorescence microscope.

5.3.2.7 Cell morphology

PANC-1, PDX185 and PDX354 cells were seeded on glass coverslips ($5x10^4$ for PANC-1 cells and $1x10^5$ for PDXs) and incubated in complete media. After 48 hours, media was replaced with complete media containing ELR nanoparticles at 0.5 mg/mL. After 3 and 24 hours, when indicated, samples were fixed using cold methanol for 5 minutes and, once dried, stained for 2 minutes with Neutral Red dye prepared at 0.5% in distilled water. Samples were washed carefully with distilled water, dried and mounted with DePeX mounting medium. Pictures were taken with an Olympus BX63 microscope.

5.3.2.8 Western Blot

PANC-1, PDX185 and PDX354 cells ($5x10^5$ cells/well in 6-well plates) were incubated with complete media containing 0.5 mg/mL nanoparticles for 3 or 24 hours. After washing with PBS, cells were lysed with RIPA buffer supplemented with PhosSTOP® phosphatase inhibitor cocktail and COMPLETE® protease inhibitor cocktail, and protein concentrations were measured by the Bradford assay. 50 μg of total protein were separated by standard SDS-PAGE (10% acrylamide) and transferred to PVDF membranes. Blocking was performed with 5% BSA in PBS for 1 hour at room temperature. Primary antibodies against total Akt, ρ-Akt, ρ-JNK, NF-κB (p65), Cleaved caspase-3, β-actin and GAPDH were used according to manufacturer's instructions. Briefly, membranes were incubated with the primary antibody diluted 1:1000 in PBS with 0.5% BSA and 0.1% Tween-20, at 4°C overnight. After extensive washes, secondary antibodies, goat anti-mouse or goat anti-rabbit HRP-linked, were used at 1:10000 dilutions for 1 hour at room temperature, according to manufacturer's instructions. After extensive washes, the specific proteins were detected using ECL chemoluminiscent substrate.

5.3.2.9 Photodynamic therapy

Cells were seeded onto 96-well plates in a quantity of $5×10^3$ and $1×10^4$ cells/well for PANC-1 and PDXs, respectively, in order to maintain similar confluence levels for all the cell lines overnight prior to the treatment. PANC-1, PDX185 and PDX354 cells were co-incubated with TPP2Sa photosensitizer for 24 hours and Akt-in nanoparticles at two different concentrations (0.25 mg/mL, 0.5 mg/mL), during 3 or 24 hours. Then, culture media was removed, fresh media was added and the 96-well plates were illuminated in

an UV lamp, for 5 or 7 minutes (PANC-1 and patient-derived cells, respectively). The cell metabolic activity was then determined as described in section 2.5. Three independent experiments, each in triplicate, were performed.

5.3.2.10 *In vivo* pharmacokinetic analysis

All animal experiments were conducted in accordance with the institutional guidelines for the care and use of experimental animals of the University of Valladolid (Spain) in accordance with Directive 2010/63/EU (Resolution Number 2010/2/23) under the supervision of the Animal Research and Welfare Committee.

BALB/c mice aged 14-16 weeks were injected intravenously with 50 µL of 15 µM fluorescein-labelled ELR nanoparticles (n=5). For the time course analysis, 20 µL of blood was collected from the submandibular vein at 1, 2, 3, 4, 5, 6 and 24 hours after injection and immediately diluted into 80 µL of heparinized PBS. The blood was centrifuged at 21100 xg for 10 minutes at 4°C and the supernatant was loaded onto a black clear bottom 96-well plate for fluorescence reading using a SpectraMax M5e Molecular Devices microplate reader with excitation and emission wavelengths of 494 nm and 518 nm, respectively. Plasma auto fluorescence was determined in negative control (non-injected) mice and subtracted to the samples values. Fluorescence intensity values were converted to concentration by extrapolation from a linear standard curve.

To obtain the pharmacokinetic parameters for the compartmental analysis, the data set of each individual mouse was fit to a one-compartment pharmacokinetic model using SAAM II software (University of Washington, WA).

5.3.2.11 *In vivo* biodistribution

All animal experiments were conducted in accordance with the institutional guidelines for the care and use of experimental animals of the University of Valladolid (Spain) in accordance with Directive 2010/63/EU (Resolution Number 2010/2/23).

BALB/c mice aged 14-16 weeks were injected intravenously via the tail vein with 15 µM Cy5-labeled ELR nanoparticles. Animals were anaesthetized with isoflurane in oxygen (4% for induction and 1.5% for maintenance) and transferred immediately to the IVIS

imaging system with continuous anaesthesia during measurement. Fluorescence of an untreated mouse was simultaneously measured as basal fluorescence control. Animals were scanned for fluorescence by the IVIS *In Vivo* Imaging System (Perkin Elmer, Waltham, MA). Excitation and emission wavelengths were 650 and 670 nm, respectively. Moreover, heart, liver, spleen and kidneys were collected and scanned. Fluorescence of the animals was plotted by subtracting background from an untreated mouse.

5.3.2.12 Histopathological analysis

Collected liver, spleen, heart and kidneys from BALB/c mice used for the *in vivo* studies (as described in section 2.11) were processed with an automatic tissue processor (Leica TP1020, UK) and embedded in paraffin blocks. Tissue sections of 4 µm of each organ were subsequently de-paraffinized and re-hydrated for hematoxylin-eosin (H&E) staining following manufacturer's instructions. Assessment on key parameters of organ microstructure and physiology were performed by the Histopathology Department of the Royal Free Hospital (London, UK). fixed with PFA 4% and embedded in paraffin.

5.3.2.13 Statistical analysis

Data are reported as mean ± SD (n = 3). Statistical analysis was analyzed by variance analysis in combination with a subsequent analysis using the Bonferroni method. A p-value of less than 0.05 was considered to be statistically significant. *p < 0.05, **p < 0.01, ***p < 0.001. Data were handled using the SPSS Statistics software version 20 (IBM).

5.3.3. Results and Discussion

5.3.3.1 Internalization kinetics and subcellular localization of ELR nanoparticles

The nanoparticle cellular uptake by pancreatic cancer cells was determined by flow cytometry. PANC-1 cell line and pancreatic cancer patient-derived cells were incubated with fluorescein-labeled control or Akt-in nanoparticles at 0.5 mg/mL for 3 or 24 hours. Surface charge is one of the most important features of a nanodevice, as this parameter affects the internalization rate through the cellular membrane. The cellular membrane possesses negative charge, so neutral and negatively charged nanoparticles are thought to enter into the cells via endocytic pathways [26]. Conversely, cationic carriers tend to cause membrane depolarization and disruption [27], which leads to a reduction of

viability of normal cells. Moreover, cationic nanoparticles are more likely to form aggregates with interacting proteins in the biological fluids such as blood, increasing their size due to protein corona formation before they reach the targeted tumor [28, 29]. ELR nanoparticles were previously characterized (Chapter 2 section 3.3) [25], where surface charge was measured by Dynamic Light Scattering. As previously described, both types of nanoparticles clearly showed negative ζ-potential: -27.8 and -26.2 mV for control and Akt-in nanoparticles, respectively. The negative surface charge was due to the presence of glutamic acid residues contained in the hydrophilic block forming the nanoparticles.

Flow cytometry results (Figure 1) show overlapping histograms of cells treated with control and Akt-in nanoparticles. This suggests that the uptake of both nanocarriers occurred at the same rate, showing no significant differences when they carry the inhibitor compared to when they do not. The fluorescence intensity observed from cells treated for 3 hours was almost identical to 24 hours treatment, indicating that the internalization of the nanoparticles occurred in a rather short time (3 hours) after which time no further uptake occurs. Similar trends were observed in PANC-1, PDX354 and PDX185 cells. Therefore, we could conclude that both control and Akt-in nanoparticles were internalized at the same rate and the difference regarding cell viability and metabolic activity was only due to the presence of Akt kinase inhibitor.

In Figure 1C-D, cellular uptake of control and Akt-in nanoparticles over time was depicted. Interestingly, the same amount of ELR nanoparticles was internalized after 3 or 24 hours. Moreover, PANC-1 cells showed lower internalization rates than pancreatic cancer patient-derived cells, which could be explained because primary tumor cells have enhanced metabolic activity and internalization ability than established cell lines.

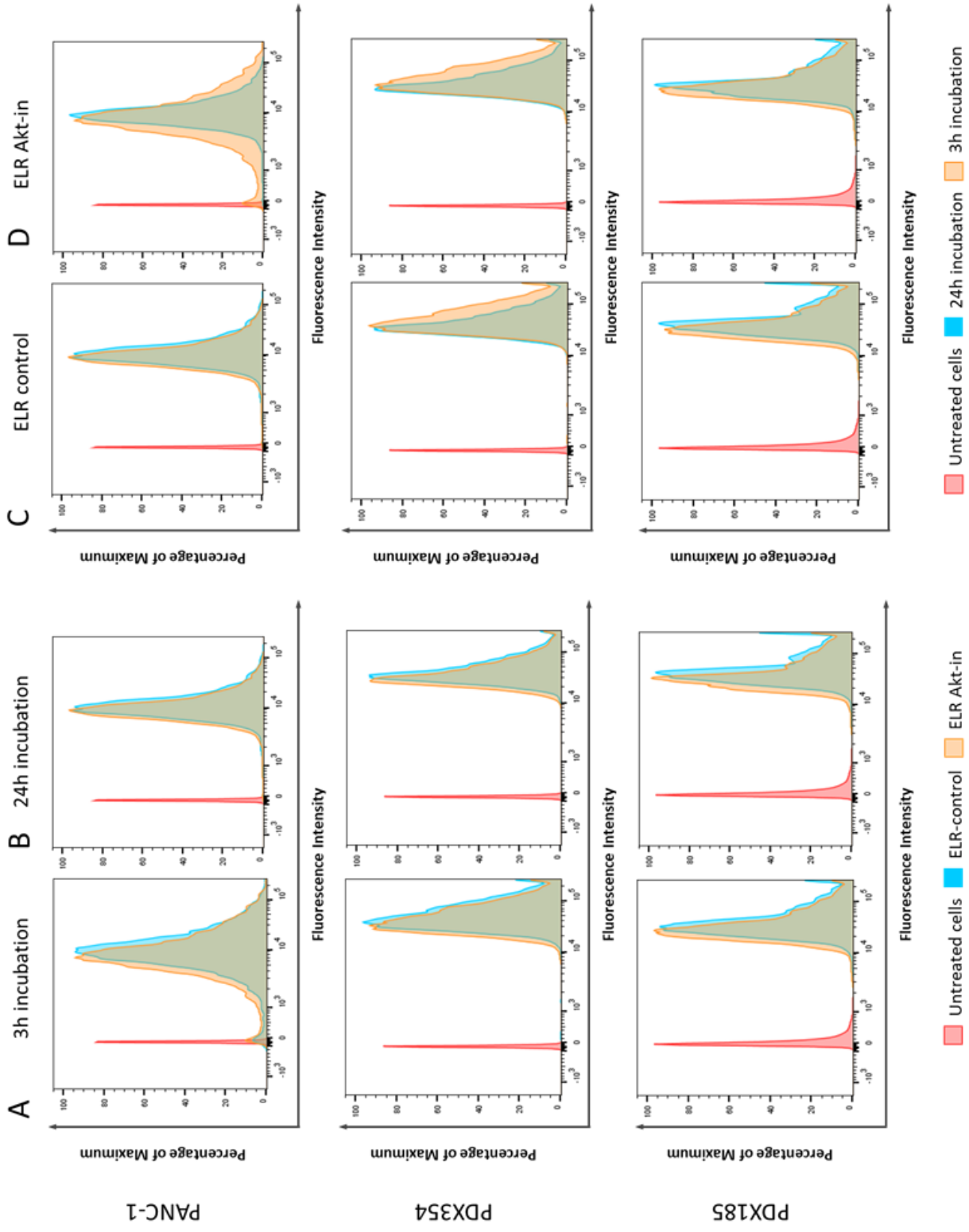
A
3h incubation
B
24h incubation
C
ELR control
D
ELR Akt-in
PANC-1
PDX354
PDX185
Percentage of Maximum
Fluorescence Intensity
Untreated cells
ELR-control
ELR Akt-in
24h incubation
3h incubation

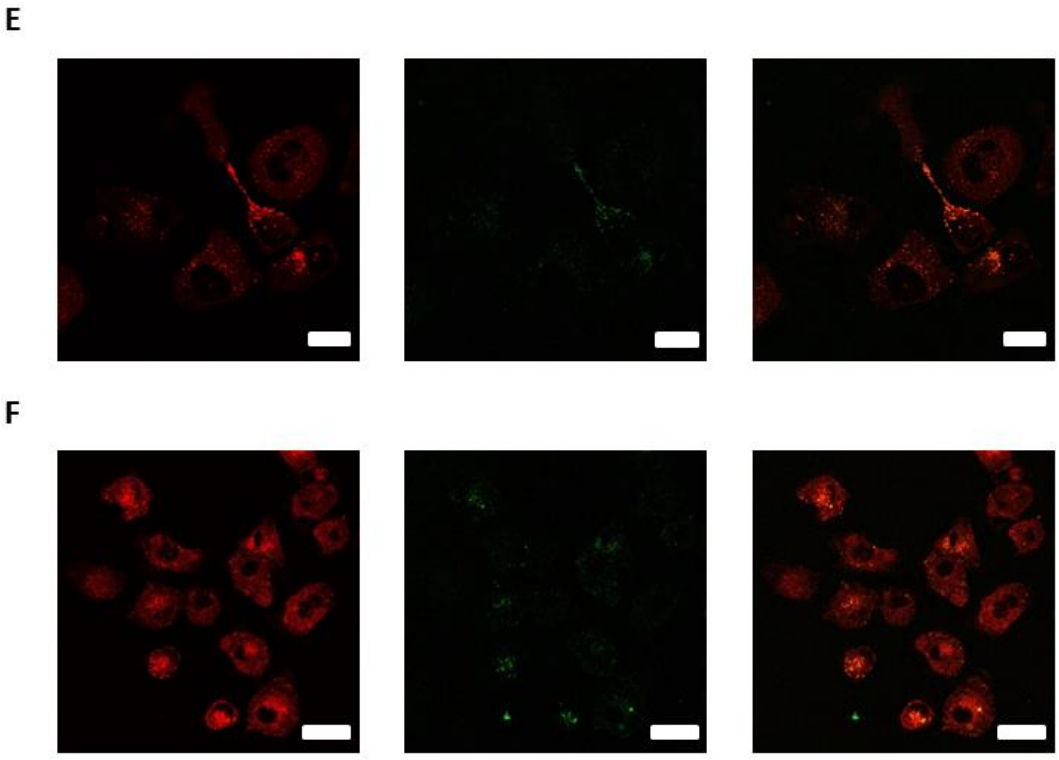

Figure 1. Cellular uptake of ELR-based nanoparticles in PANC-1 and patient-derived PDX354 and PDX185. A-B: Flow cytometry analysis of PANC-1, PDX354 and PDX185 cells incubated with control (Blue) and Akt-in (Orange) fluorescein-labelled nanoparticles at 0.5 mg/mL for (A) 3 hours or (B) 24 hours. C-D: Flow cytometry time-course analysis of PANC-1, PDX354 and PDX185 cells incubated with (C) control and (D) Akt-in fluorescein-labelled nanoparticles at 0.5 mg/mL for 3 hours (Orange) or 24 hours (Blue). Untreated cells are plotted in red. E-F: Confocal microscopy images of PANC-1 cells containing fluorescein-labeled nanoparticles (green channel) after 3 hours (E) or 24 hours (F). Lysosomes were stained with Lysotracker Red (red channel). The overlapping of the green and red channels resulted in orange stain (right panel). Scale bars: 15 µm (E) and 25 µm (F).

Confocal microscopy was also carried out in order to study the subcellular localization of nanoparticles in pancreatic cancer cells (Figure 1E-F). PANC-1, PDX354 and PDX185 cells were incubated with fluorescein-labeled ELR nanoparticles and Lysotracker Red, a selective dye for labeling acidic organelles. As shown in Figure 1E-F, ELR nanoparticles were localized inside the cells and co-localized with lysosomes. Intracellular lysosomal localization in fact was essential for the accurate action of nanoparticles, as the Cathepsin D-sensitive sequence included in the ELR molecule is recognized by lysosomal protease Cathepsin D. Moreover, at acidic lysosome pH, H5 peptide triggers the formation of pores in the lysosomal membrane and the small Akt-in inhibitor is released to the cytoplasm. All of these concatenated steps are necessary for effective ELR nanoparticle anti-tumor action. If nanoparticles were not internalized into lysosomes, the Akt-in inhibitor would not be released to the cytoplasm and could never reach the target protein.

5.3.3.2 Effect of nanoparticles on cellular metabolic activity

Once the uptake and localization of nanoparticles was determined, their cytotoxic effect was analyzed. Previous work (Chapter 2 section 3.5) demonstrated that control nanoparticles did not affect cell viability. Moreover, ELR nanoparticles showed to be innocuous for human primary non-cancer cells, such as fibroblasts, endothelial and mesenchymal stem cells, whereas an enhanced effect was appreciated on cancer cell viability [25]. One of the main purposes of drug screening consists on the achievement of predictive models. Although *in vitro* cell culture of established cell lines is a useful tool, the disadvantage of the lack of cellular heterogeneity limits the reliability of results. Thus, xenograft models from patient-derived samples better mirror the tumor heterogeneity and could improve therapeutic outcomes of novel therapeutic agents. Moreover, these models retain most morphological and molecular features of the original tumor. For these reasons, we present the testing of a previously described drug delivery system in pancreatic cancer patient-derived cells. In our opinion, this approach is more accurate and potentially improve the predictability of therapeutic treatments for pancreatic cancer. The biological effect of our nanoparticles on the pancreatic cancer cell line PANC-1 and patient-derived cells PDX354 and PDX185 was determined by MTT assay (Figure 2). Cancer cells were incubated with three different concentrations of ELR nanoparticles, ranging from the critical micellar concentration (CMC) 0.25 mg/mL to 1 mg/mL, for 3 or 24 hours. As shown in Figure 2, control nanoparticles did not significantly affect the metabolic activity of any cell line compared to untreated cells. Thus, results showed no difference either between the three different concentrations, or between time points. In this light, we can conclude that the basic ELR structure of our nanocarriers did not show an effect in the overall metabolic activity of the models, linking any reduction of it to the presence of the Akt-in inhibitor.

Interestingly, when pancreatic cancer cells were incubated with Akt-in ELR nanoparticles for 3 hours, cellular metabolism was affected (Figure 2A). Metabolic activity was decreased to 58%, 74% and 63% when PANC-1, PDX354 and PDX185 were incubated with the lower dose (0.25 mg/mL). When nanoparticle concentration was increased to 0.5 mg/mL, the three different cell line cultures decreased their metabolic activity to 34-38%. Treatment with higher concentration (1 mg/mL) decreased the metabolic activity to 13-18%. These results not only showed a dose-dependent trend, but also a time-dependent

mode of action. As expected, when the incubation time was increased from 3 hours to 24 hours, Akt-in nanoparticles showed an increased effect (Figure 2B). Indeed, the high concentration strongly decreased metabolic activity of cell culture to 4%, 6% and 7% in PANC-1, PDX354 and PDX185, respectively. Regarding the intermediate concentration (0.5 mg/mL), the three cell lines showed only 12-14% of metabolic activity. Lastly, when PANC-1, PDX354 and PDX185 cells were treated with the low concentration of Akt-in nanoparticles (0.25 mg/mL), cellular metabolism was decreased to 27%, 31% and 28%, respectively.

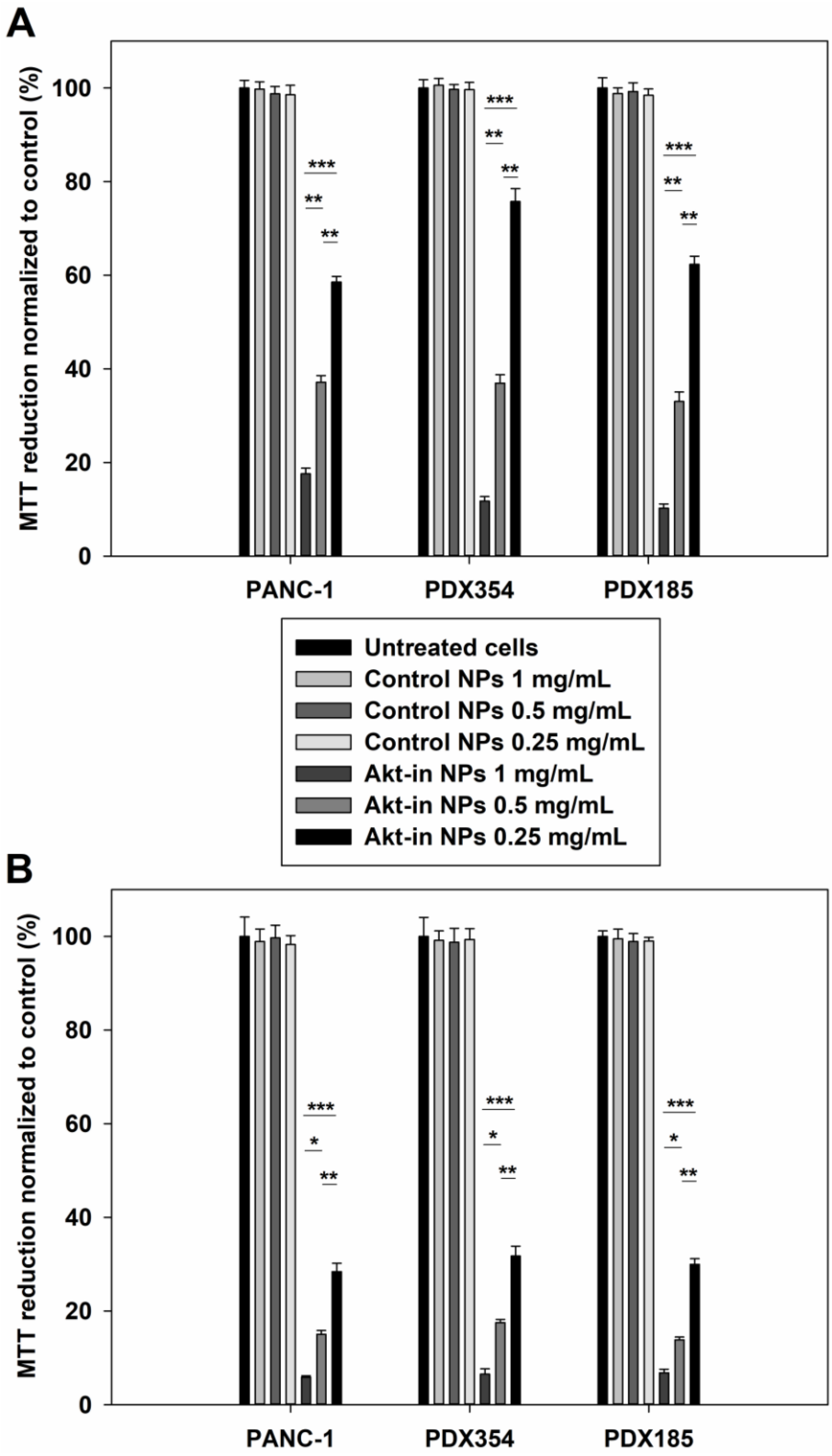

Figure 2. Metabolic activity of PANC-1, patient-derived PDX354 and PDX185 cells after treatment with ELR-based nanoparticles. Cells were incubated with control and Akt-in nanoparticles at three concentrations 3 hours (A) or 24 hours (B), and metabolic activity was measured using the MTT assay. n = 3 independent experiments, mean ± SD. *p < 0.05; **p < 0.01; ***p < 0.001

Once the effect of ELR nanoparticles was determined, the percentage of viable cells with active metabolism was measured after allowing cells to recover for 96 hours after treatment (Figure 3). Once again, control nanoparticles showed no detectable effect on cellular metabolism.

However, recovery time slightly decreased the effect of Akt-in nanoparticles on metabolic activity. When the high concentration of Akt-in nanoparticles was used (1 mg/mL), cellular metabolism decreased to 22%, 23% and 18% in PANC-1, PDX354 and PDX185, respectively. Thus, when cells were allowed to recover for 96 hours after the treatment with Akt-in nanoparticles, the metabolic activity was slightly increased. When cells were incubated with the intermediate and the low concentration, pancreatic cancer cells showed cellular metabolism rates of 46-52% and 70-83%, respectively. These results suggest that by allowing cells to recover for 4 days after treatment, only a small population of surviving cells were able to remain metabolically active.

However, the effect of recovery time on pancreatic cancer cells treated with Akt-in nanoparticles for 24 hours was very similar compared to cells treated for 3 hours. When the low and intermediate concentrations were used, the number of metabolically active cells was recovered by 15%. Thus, pancreatic cancer cells showed metabolic activity 45%, 50% and 43% for PANC-1, PDX185 and PDX354, respectively. Moreover, cells treated with 0.5 mg/mL showed 30% of metabolic activity. As expected, patient-derived cells showed less recovery percentages when treated with 1 mg/mL nanoparticles compared to PANC-1, due to the higher nanoparticle internalization observed.

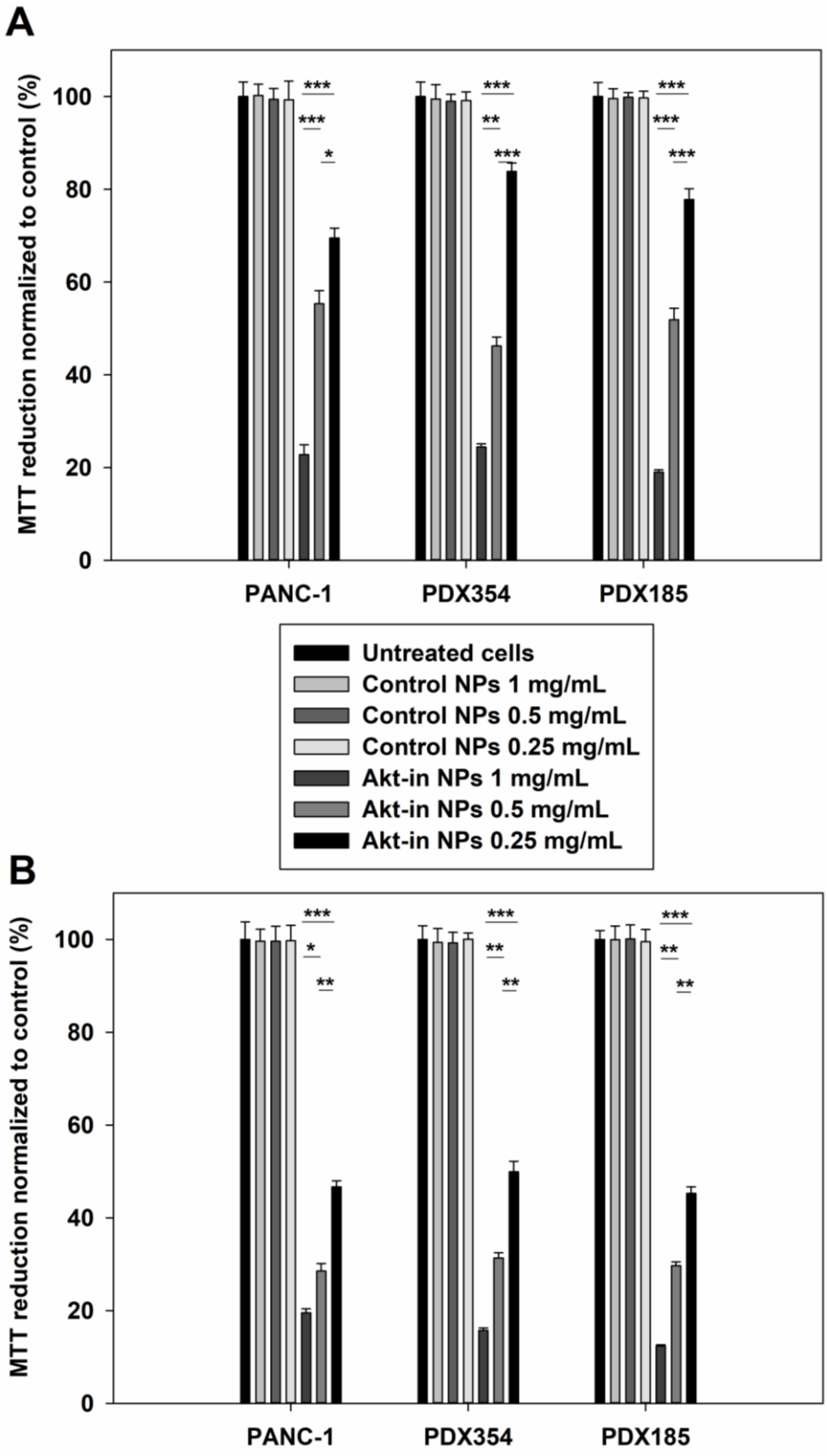

Figure 3. Metabolic activity of PANC-1, patient-derived PDX354 and PDX185 cells after treatment with ELR-based nanoparticles. Cells were incubated with control and Akt-in nanoparticles at three concentrations for 3 (A) or 24 hours (B), media was replaced and metabolic activity was measured after 96 hours. n = 3 independent experiments, mean ± SD. *p < 0.05; **p < 0.01; ***p < 0.001

5.3.3.3 Effect of nanoparticles on cell viability

Once the effect of ELR nanoparticles on the metabolic activity of the models was determined, cellular viability was analyzed by the differential staining of live and dead cells with fluorescent dyes. For this purpose, pancreatic cancer cells were incubated under the same conditions of previous experiments and treated with three concentrations of nanoparticles for two incubation times. First, the cytotoxic effect of control nanoparticles was determined. Control nanoparticles did not significantly affect the viability of any of the three pancreatic cancer cells lines. Indeed, results showed no difference between the three different concentrations at any time point. We can conclude that control nanoparticles did not provoke a viability decrease on both established cell line PANC-1 and patient-derived cells PDX185 and PDX354.

Conversely, when pancreatic cancer cells were incubated with Akt-in nanoparticles, cellular viability was affected (Figure 4). Thus, when the low dose was used (0.25 mg/mL), cellular viability was higher than 60% after treating for 3 hours, while using the intermediate concentration the three cell lines showed 43-47% viability. Interestingly, patient-derived cells were more resistant when incubated with the low dose of nanoparticles, which could be due to the fact that patient-derived cells are more aggressive than established cell lines. When the nanoparticle dose was increased to 1 mg/mL, PAN-1 cells and PDX354 showed 25% viability, whereas PDX185 cells were more affected and only 17% survived (Figure 4A).

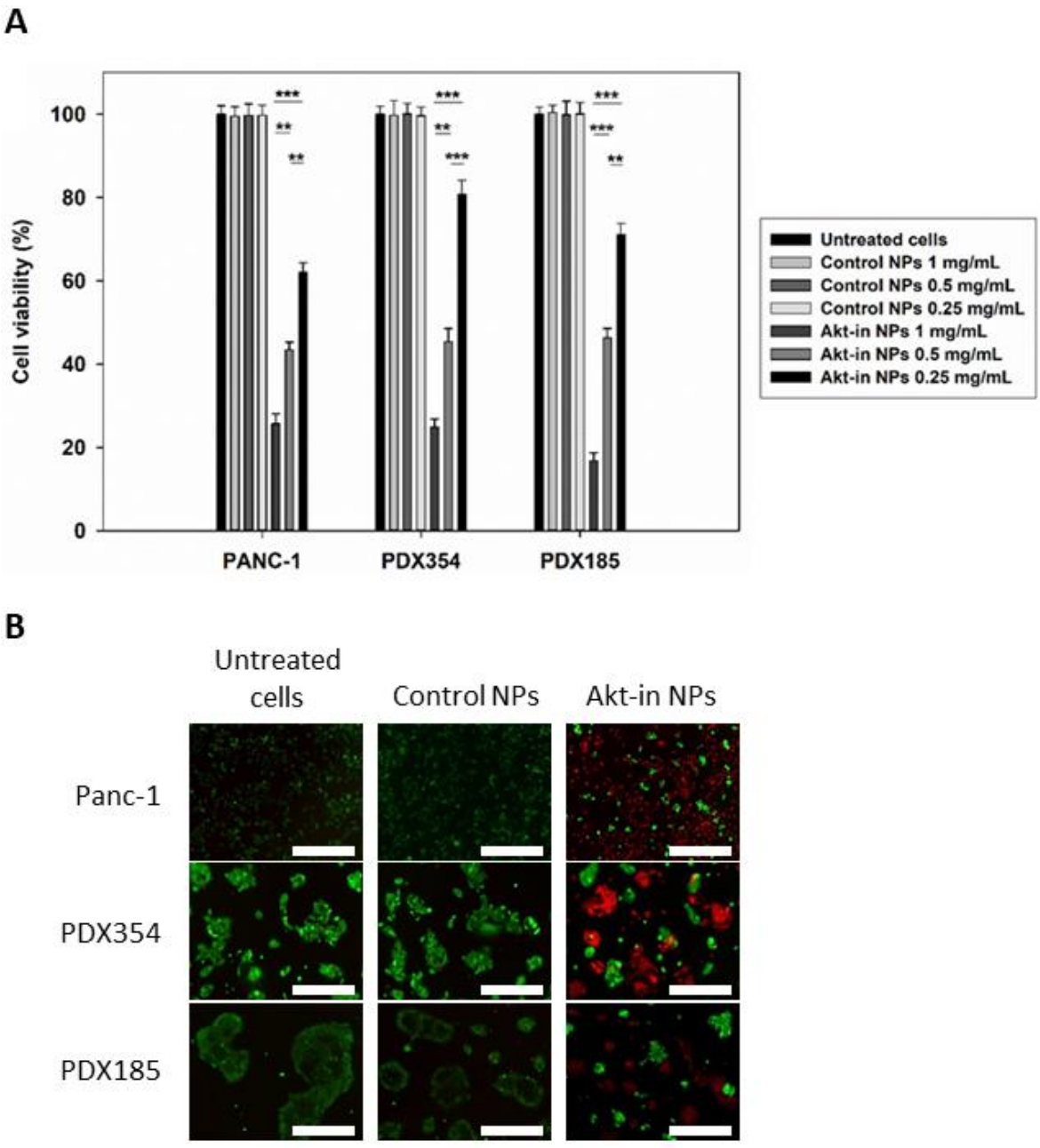

Figure 4. A: Percentage of viability of PANC-1 and patient-derived PDX354 and PDX185 cells compared to untreated cells. Cells were incubated with three concentrations of control and Akt-in nanoparticles for 3 hours and cell viability was measured using the LIVE/DEAD assay kit. B: Representative fluorescence microscopy images. Scale bars: 100 µm. Alive cells are stained in green while dead cells are red. n = 3 independent experiments, mean ± SD. **p < 0.01; ***p < 0.001

Furthermore, we observed that cell viability was dependent on the exposition time with therapeutic ELR nanoparticles. When increasing from 3 to 24 hours incubation, results showed that Akt-in nanoparticles were more effective (Figure 5). Thus, at lower concentration, PANC-1, PDX354 and PDX 185 showed 38%, 42% and 34% cell viability, respectively. PANC-1 cells treated with the intermediate concentration (0.5 mg/mL) were

more affected and showed 18% of cell viability after treatment. Patient-derived cells PDX354 and PDX185 appeared to be more resistant to Akt-in nanoparticles and showed 26% and 22% cell viability, respectively. When cells were incubated with the high concentration of Akt-in nanoparticles (1 mg/mL), the three pancreatic cancer cell lines showed similar values and only 4-7% of cancer cells survived to treatment. Representative fluorescence microscopy pictures corroborated the quantitative data obtained (Figure 5B).

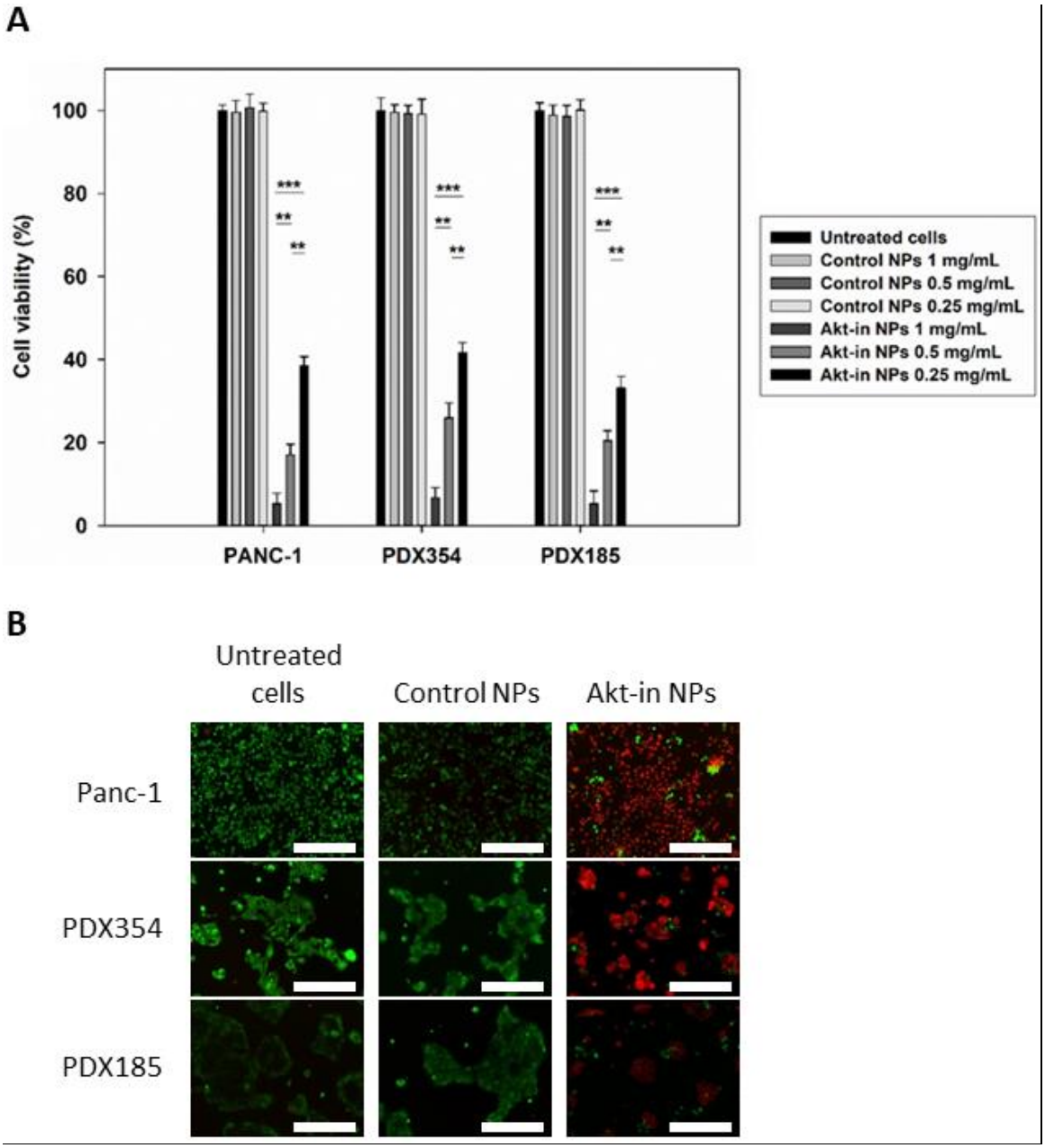

Figure 5. A: Percentage of viability of PANC-1 and patient-derived PDX354 and PDX185 cells compared to untreated cells. Cells were incubated with three concentrations of control and Akt-in nanoparticles for 24 hours and cell viability was measured using the LIVE/DEAD assay kit. B:

Representative fluorescence microscopy images. Scale bars: 100 µm. Alive cells are stained in green while dead cells are red. n = 3 independent experiments, mean ± SD. **p < 0.01; ***p < 0.001

The effect of ELR nanoparticles on cell viability was also studied 96 hours after treatment for recovery (Figures 6 and 7). First, results confirmed that control nanoparticles were completely innocuous and did not affect cell viability. Interestingly, cell viability percentages were higher compared to results when pancreatic cancer cells were treated for 3 hours (Figure 4). Thus, the higher effect was observed when cells were treated with Akt-in nanoparticles at 0.25 mg/mL for 3 hours and then added fresh media for 96 hours (Figure 6). Under this experimental condition, the three pancreatic cancer cell lines showed cell viability above 80%. When the intermediate dose was used, the recovery effect was lower, except for PANC-1 cells, which showed 67% of cell viability. However, when cancer cells were treated with Akt-in nanoparticles at 1mg/mL, the difference with non-recovered cells was only 10%, which corroborated this concentration as a very lethal dose (Figure 6A).

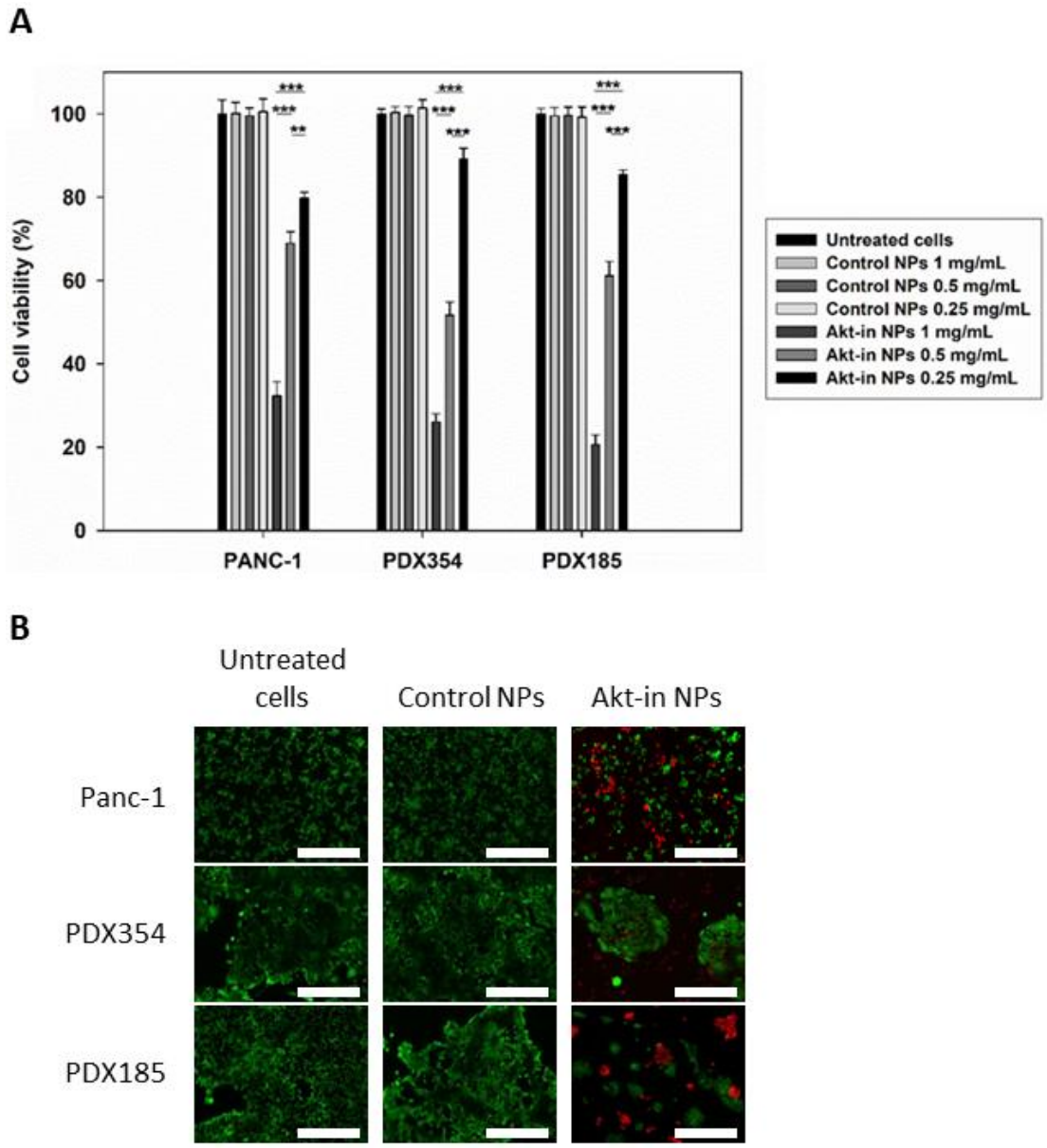

Figure 6. A: Percentage viability of PANC-1 and patient-derived PDX354 and PDX185 cells compared to untreated cells. Cells were incubated with three concentrations of control and Akt-in nanoparticles for 3 hours. Media was refreshed and cell viability 96 hours after treatment was measured using the LIVE/DEAD assay kit. B: Representative fluorescence microscopy images. Scale bars: 100 µm. Alive cells are stained in green while dead cells are red. n = 3 independent experiments, mean ± SD. **p < 0.01; ***p < 0.001

As expected, the effect of recovery time was much lower when cells were treated with nanoparticles for 24 hours (Figure 7). Thus, cell viability of PANC-1, PDX354 and PDX185 did not reach 60% when treated with a lower dose of ELR nanoparticles, 0.25 mg/mL (Figure 7A). When cells were treated with the intermediate concentration, pancreatic cancer cells only recovered 10% cell viability. PDX354 cells treated with the

higher dose showed slightly increased cell viability, whereas PDX185 cells seemed to be more affected by Akt-in nanoparticles and the difference to non-recovered cells was minimal. Contrary, PANC-1 cells showed an enhanced recovery. The recovery of cell viability after 96 hours could be due to the fact that, according to MTT results, some cells remained metabolically inactive but still alive and the addition of fresh media allowed them to recover from treatment and gain their normal activity. Moreover, these results could explain that cells not affected by nanoparticles carrying the inhibitor were able to grow and proliferate.

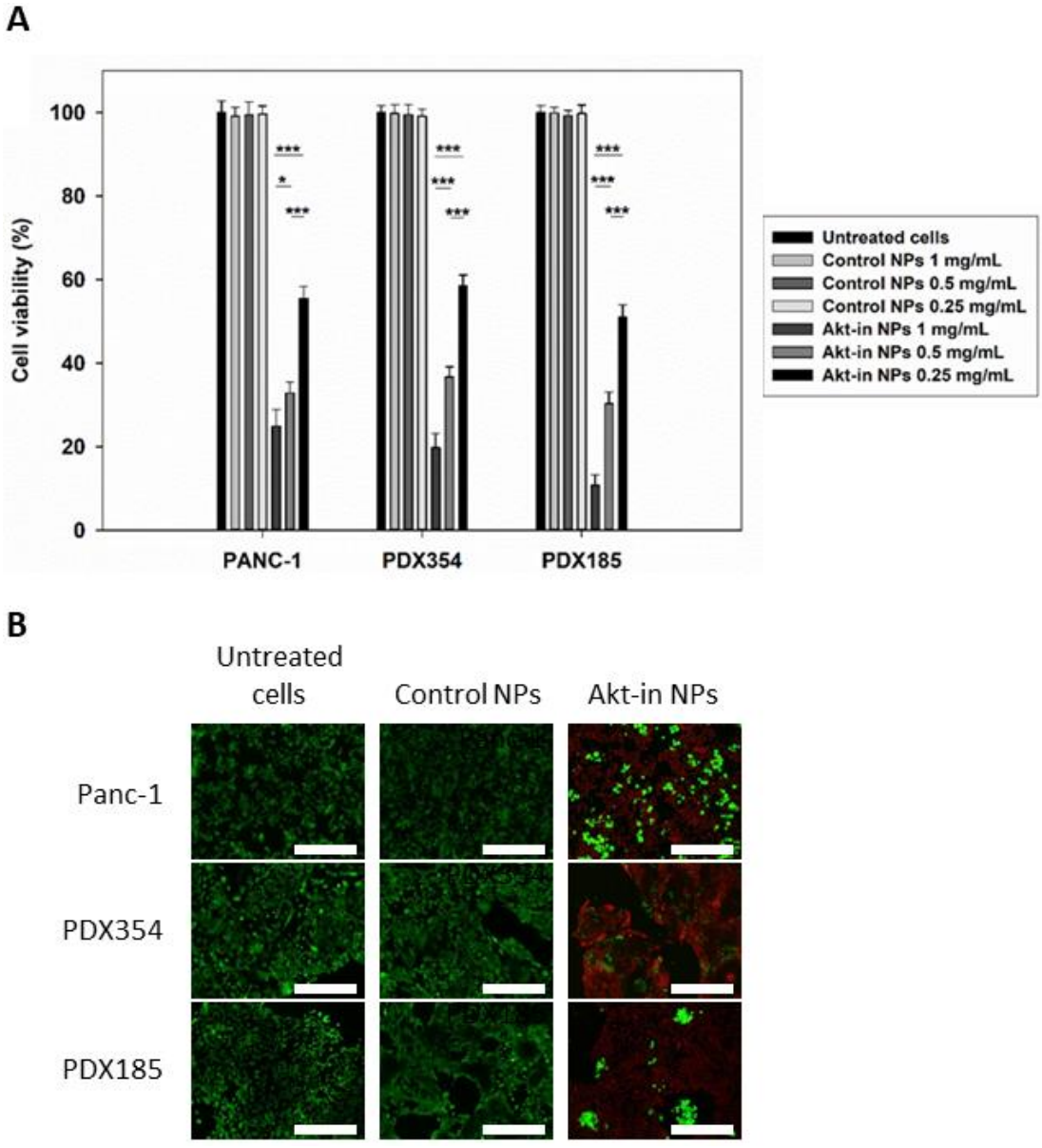

Figure 7. A: Percentage of viability of PANC-1 and patient-derived PDX354 and PDX185 cells compared to untreated cells. Cells were incubated with three concentrations of control and Akt-in nanoparticles for 24 hours. Media was refreshed and cell viability 96 hours after treatment was

measured using the LIVE/DEAD assay kit. B: Representative fluorescence microscopy images. Scale bars: 100 µm. Alive cells are stained in green while dead cells are red. n = 3 independent experiments, mean ± SD. **p < 0.01; ***p < 0.001

At light of the results, the intermediate concentration of ELR-based nanoparticles was selected for further experiments, as this dose affected metabolic activity and cell viability in patient-derived pancreatic cancer cells. Moreover, previous experiments (Chapter 2) determined that a dose of 0.5 mg/mL markedly affected breast and colorectal cancer cells viability without significant effects in primary non-cancerous cells, such as fibroblasts, endothelial and mesenchymal stem cells [25].

5.3.3.4 Effect of nanoparticles on cell morphology

After determining the effect of ELR nanoparticles on cell viability and metabolic activity, cellular morphology was also studied to corroborate how pancreatic cancer cells were affected by the treatment with the smart nanocarriers. PANC-1, PDX185 and PDX354 cells were incubated with ELR nanoparticles at 0.5 mg/mL for 3 and 24 hours and (Figure 8).

Thus, PANC-1 cells could be appreciated as individualized cells (Figure 8A) whereas both pancreatic cancer patient-derived cultures PDX354 and PDX185 typically grew in cell clusters (Figure 8B-C). Well-known morphological criteria were used for the analysis of general morphology [30]. When incubated with control nanoparticles (Figure 8 middle column), pancreatic cancer cells showed normal morphology, similar to untreated cells (Figure 8 left column). Contrary, when cells were incubated with Akt-in nanoparticles, cell morphology dramatically changed (Figure 8 right column). In fact, cells treated with nanoparticles carrying Akt inhibitor were unable to spread properly and most of them showed aberrant shape, compared to untreated cells.

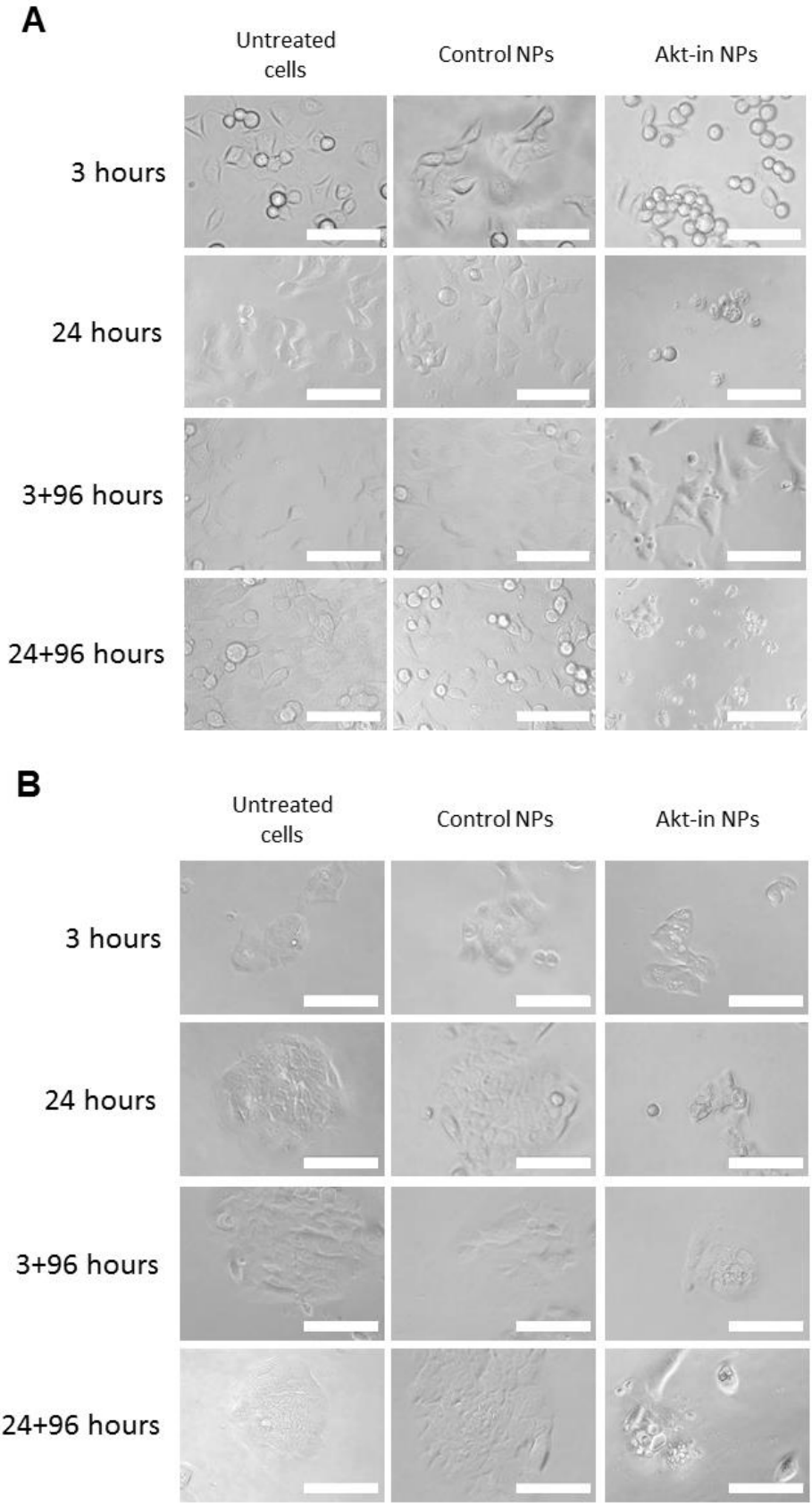
A
Untreated cells
Control NPs
Akt-in NPs
3 hours
24 hours
3+96 hours
24+96 hours
B
Untreated cells
Control NPs
Akt-in NPs
3 hours
24 hours
3+96 hours
24+96 hours

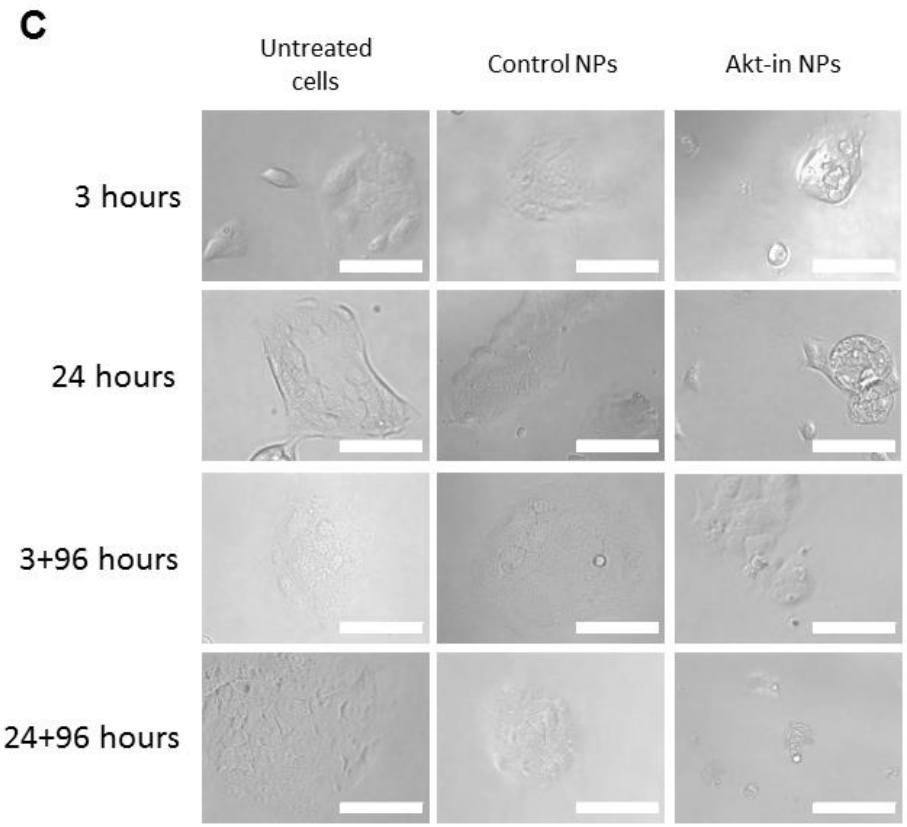

Figure 8. Representative images of PANC-1 (A) and patient-derived PDX354 (B) and PDX185 (C) cells incubated with ELR nanoparticles at 0.5 mg/mL in culture media for indicated times. From top to bottom: 3 and 24 hours incubation with nanoparticles, 3 hours and 24 hours incubation with nanoparticles + 96 hours in culture medium without nanoparticles. Left column: untreated cells; Middle column: cells treated with control nanoparticles. Right column: cells treated with Akt-in nanoparticles. Pictures were taken by optical microscopy at phase contrast. Scale bars: 100 μm.

Moreover, Neutral Red staining was used for the analysis morphological changes induced after treatment with the nanodevices (Figure 9).

Regarding treatment with control nanoparticles, no major differences in cellular morphology and density were found in any of the three lines compared to untreated controls, at any of the selected incubation times. However, when pancreatic cancer cells were incubated with Akt-in nanoparticles, a great number of cells showed significant morphological changes and underwent apoptosis-mediated cell death, as can be deduced from typical apoptotic features such as cell shrinkage, chromatin condensation and nuclear fragmentation (Figure 9 Left columns). PANC-1 cells (Figure 9A) showed a higher sensitivity to the treatment with nanoparticles containing the inhibitor than PDXs, corroborating the data obtained by MTT and Live/Death assays. Treatments for 24 hours

with Akt-in nanoparticles showed a complete disruption of the normal pattern of growth and colony formation of the three lines. The few surviving cells after 24 hours of treatment displayed a rounded morphology typical of cells undergoing cell death, which strongly supports the higher effect in cell viability observed before.

In experimental conditions where cells were treated for 3 or 24 hours and then media was refreshed to allow for any possible recovery during the next 96 hours, PANC-1 cells showed a strong decrease in cell density suggesting that no major cell recovery happened after the treatment. On the contrary, PDX354 and PDX185 cells did show detectable recovery after treatment with Akt-in containing nanoparticles, indicating that cells surviving the therapy are able to regain normal activity and ability to duplicate.

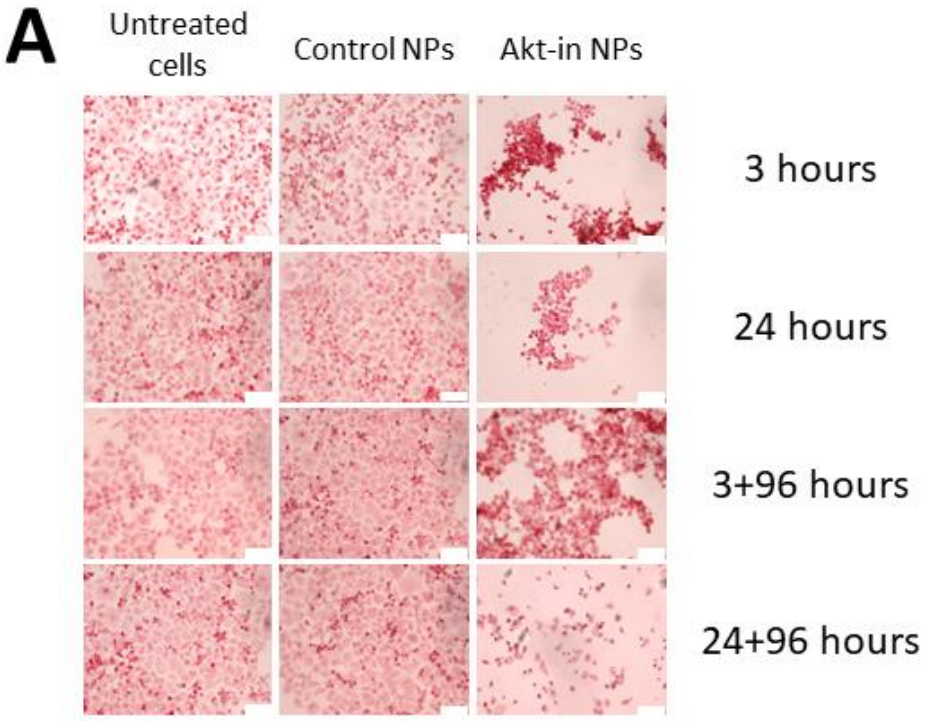

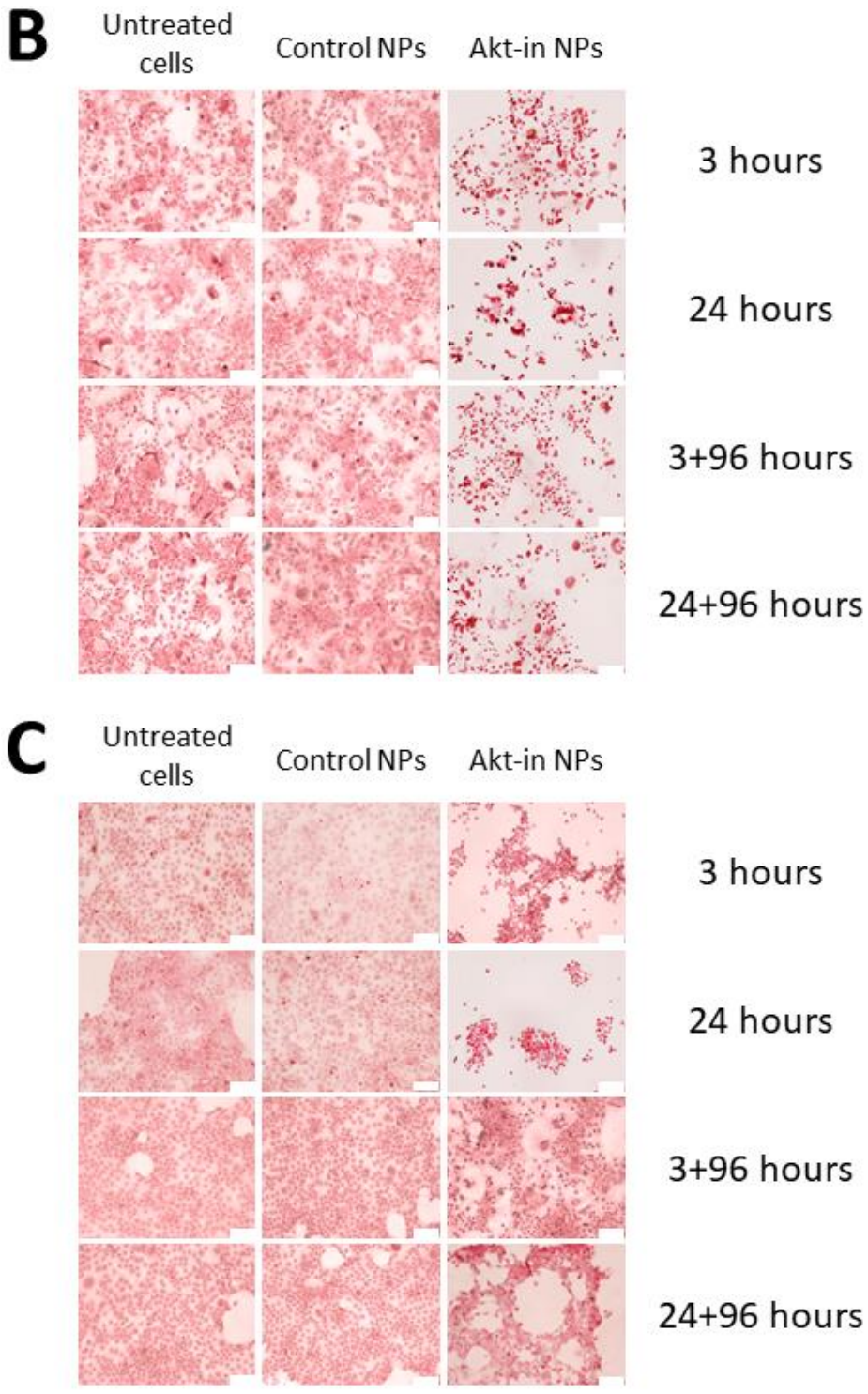

Figure 9. Cell morphology of PANC-1 (A) and patient-derived PDX354 (B) and PDX185 (C) cells treated with ELR-based nanoparticles. Cells were incubated with control and Akt-in nanoparticles at 0.5 mg/mL and then stained with Neutral Red reagent. Scale bars: 100 μm.

5.3.3.5 Action of Akt inhibitor on cell signaling pathways

As described above, the primary aim of this work consists on the controlled delivery of the small peptide inhibitor of the phosphorylation of Akt to the cellular cytoplasm. In this

regard, the expression of certain protein involved in cell signaling pathways controlled by Akt was studied in order to confirm the nanoparticles mechanism of action and their accurate effect in Akt phosphorylation.

Akt protein is activated after being phosphorylated at a threonine and serine residues as it is shown in Figure 11. Thus, Akt kinase is involved in the regulation of various signaling downstream pathways which control cell growth, proliferation and survival [31, 32]. This makes Akt a promising target for cancer therapy.

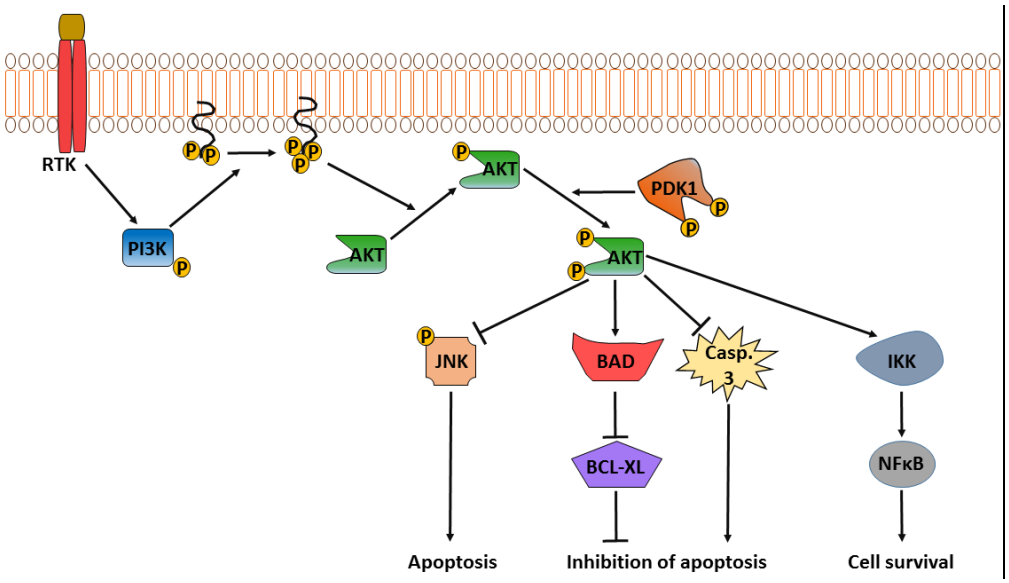

Figure 11. Cell signaling pathways involving Akt kinase. Akt is phosphorylated at a threonine and a serine sites by PI3K and PDK1. Then, Akt kinase is active and plays important roles in multiple signaling pathways of different cellular processes.

As our advanced drug delivery system carried a small inhibitor of Akt phosphorylation and consequent activation, immunoblots were performed to check the mechanism of action of the inhibitor released from nanoparticles and measure the expression levels of several proteins involved in multiple cell signaling pathways (Figure 11). The pancreatic tumor cells showed serine 473 phosphorylated Akt kinase, which corroborated the fact that cancer cells have this signaling pathway constitutively activated. As expected, when cancer cells were treated with control nanoparticles, the phosphorylation of Akt protein was not altered after 3 (Figure 12A) or 24 hours (Figure 12B). However, Akt phosphorylation was markedly inhibited when cells were incubated with Akt-in nanoparticles after both incubation times. Furthermore, expression levels of total Akt

protein did not change after treatment with control nanoparticles or Akt-in nanoparticles in PANC-1, PDX 354 and PDX185.

Even though the blockade of Akt phosphorylation and consequent activation was demonstrated, we measured the downstream effect of ELR-based nanoparticles in the Akt pathway in order to corroborate the action of Akt-in nanoparticles over cell signaling. Nuclear factor kappa-B, NFκB transcription factor, is located downstream in the Akt signaling pathway and is activated by phosphorylated Akt kinase (Figure 11) [33]. Moreover, NFκB protein controls over cell survival, which is one of the characteristic features of cancer cells [34]. For these reasons, NFκB, expression levels were measured. Figure 12 shows untreated pancreatic cancer cells displaying a high expression of NFκB. This expression levels were not altered when PANC-1 and patient-derived pancreatic cancer cells were treated with control nanoparticles. By contrast, when pancreatic cancer cells were incubated with ELR nanoparticles carrying the Akt inhibitor, expression levels of NFκB decreased. The effect of Akt-in nanoparticles on decreasing NFκB expression was again observed after treating pancreatic cancer cells for 3 (Figure 12A) or 24 hours (Figure 12B). This result corroborated the fact that Akt phosphorylation, and consequent activation and signaling, was properly inhibited and cell survival controlled by NFκB was also blocked by treating cells with nanoparticles carrying the small inhibitor.

In the previous chapter, we demonstrated that cancer cell death triggered by treatment with Akt-in nanoparticles occurred via apoptosis [25]. Also, we hypothesized that when nanoparticles were able to inhibit the anti-apoptotic effect of Akt activation, cancer cells would undergo in apoptosis-mediated death. For this reason, cleaved caspase 3 expression levels were determined, as this protein is essential for apoptotic death [35, 36]. Some apoptotic markers were undetectable after 3 hours, so cleaved caspase 3 expression levels were determined after 24 hours treatment. Results proved that untreated cells, which possessed aberrant growth, showed no cleaved caspase 3 expression. When pancreatic cancer cells were incubated with control nanoparticles, caspase 3 expression was not increased. This result suggests that control nanoparticles did not induce apoptosis. This result was in accordance with results shown in section 3.3, where it is demonstrated that control nanoparticles were innocuous for cell viability. As shown in Figure 12B, caspase 3 was only cleaved when pancreatic cancer cells were incubated with

nanoparticles carrying Akt inhibitor. Thus, we could conclude that effective inhibition of Akt phosphorylation and activation, allowed pancreatic cancer cells to undergo apoptosis-mediated death.

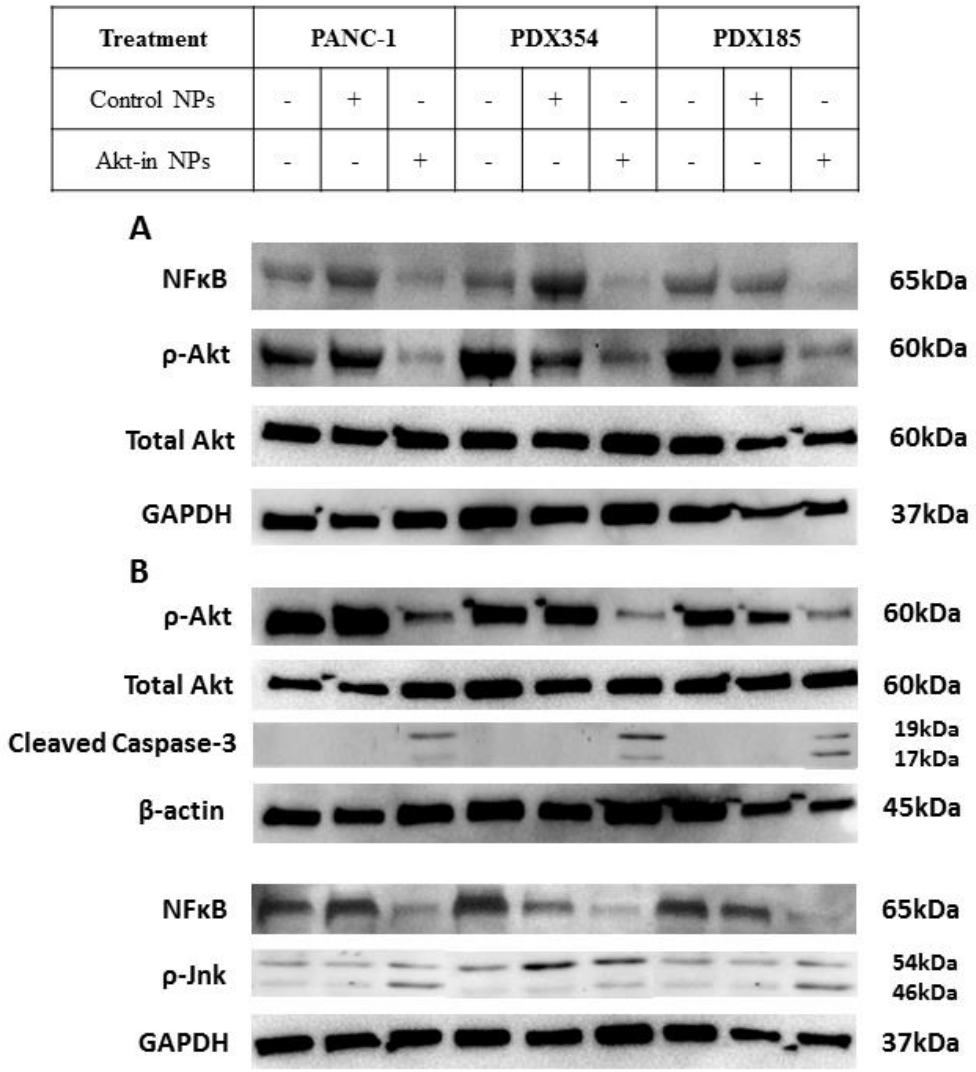

Figure 12. Effect of ELR nanoparticles on cell signaling pathways involving Akt kinase. PANC-1, PDX354 and PDX185 pancreatic cancer cells were incubated with 0.5 mg/mL control and Akt-in nanoparticles for 3 (A) or 24 hours (B). Immunoblots were performed to measure NFκB, Akt phosphorylation at Ser473, total Akt, cleaved casapase-3 and ρ-Jnk expression. Glyceraldehyde 3-phosphate dehydrogenase (GAPDH) and β-actin were used as loading control.

Moreover, phosphorylation levels of Jnk protein were determined after 24 hours incubation with ELR-based nanoparticles (Figure 12B), as this pro-apoptotic protein is inhibited by phosphorylated Akt kinase in cancer cells (Figure 11) [37, 38]. Western Blot results showed that phosphorylation and consequent activation of Jnk protein was not

altered by the incubation with control nanoparticles. Furthermore, enhanced phosphorylation levels of Jnk protein were detected when the activation of Akt kinase was inhibited by ELR nanoparticles carrying the small inhibitor. These results demonstrated that the accurate mode of action of nanoparticles over Akt protein was not only due to the inhibition of its phosphorylation, but also due to the blockade of the cell survival signaling controlled by NFκB pathway and the subsequent activation of the ρ-Jnk pathway leading to caspase 3-mediated cell apoptosis. Moreover, apoptotic death of pancreatic cancer cells treated with Akt-in nanoparticles was corroborated by measuring cleaved caspase-3 expression.

5.3.3.6 Synergic action of Akt phosphorylation inhibition and photodynamic therapy

Photodynamic therapy (PDT) is the local treatment of tumor tissue containing a photosensitizer (PS) and its exposure to light of the appropriate wavelength [39, 40]. PDT is becoming a promising strategy for cancer treatment and offers multiple advantages compared to chemotherapy or radiotherapy, such as low invasiveness and limited side effects [21, 41]. Thus, PDT combines a photosensitizer, light and molecular oxygen [20]. The light energy produced by laser irradiation induces PS excitation inside tumor cells, leading to photo-oxidative reactions between the PS and oxygen [22]. The therapeutic accuracy of the PDT is based on ROS generation, which is related to the PS concentration in tumor tissue. Interestingly, the ROS generation can be controlled with dual selectivity by localization of the photosensitizer and confinement of light to a targeted tumor microenvironment [22, 42].

Once the toxic effect of Akt-in nanoparticles was determined in pancreatic cancer cells, we hypothesized that the combination of drug delivery systems with photodynamic therapy could be a good strategy for cancer treatment. Thus, we used TPP2Sa photosensitizer, a reagent which disrupts lysosome membrane. In our opinion this combination could allow us to increase the cytotoxic effect of nanoparticles carrying Akt-in inhibitor, due to the effect of TPP2Sa photosensitizer by disrupting lysosome membrane and therefore enhancing the release of Akt inhibitor to cellular cytoplasm, where the inhibitor is able to reach targeted Akt protein and block it.

For this purpose, pancreatic cancer established and patient-derived cells were co-incubated with TPP2Sa photosensitizer for 24 hours and Akt-in nanoparticles, at 0.25 and 0.5 mg/mL, for 3 or 24 hours. Then, culture medium was removed, fresh medium was added and cells were illuminated in an UV lamp, for 5 or 7 minutes for PANC-1 and patient-derived cells, respectively. The cellular metabolic activity was then determined by MTT assays.

Interestingly, combination of photodynamic therapy and Akt-in nanoparticles showed statistically significant differences, compared to cells treated with ELR-based nanoparticles only (Figure 13). Indeed, results demonstrated that pancreatic cancer cell line PANC-1 treated with Akt-in nanoparticles showed 53.7% and 26.4% of metabolic activity when treated with 0.5 mg/mL Akt-in nanoparticles for 3 and 24 hours, respectively. However, when nanoparticles were combined with photodynamic therapy, PANC-1 cells showed 33.4% and 17.5% metabolic activity. On the other hand, when pancreatic cancer patient-derived cells PDX354 and PDX185 were incubated with 0.5 mg/mL ELR-based nanoparticles, cells showed 46.6% and 54.6% of metabolic activity after 3 hours treatment and 27.3% and 26.8% after 24 hours treatment. Interestingly, we did not appreciate significant differences between the two concentrations of TPP2Sa photosensitizer.

Although combined therapy showed to have a synergic effect in cancer cells, we then studied how effective this combination of Akt-in nanoparticles, at the lowest dose of nanoparticles, and photodynamic therapy was (Figure 13). Thus, PANC-1 cells treated with 0.25 mg/mL Akt-in nanoparticles showed 68.3% and 42.7% of metabolic activity after 3 and 24 hours treatment respectively, whereas cells treated with combination of photodynamic therapy and Akt-in nanoparticles showed 34.3% and 18% metabolic activity. The same synergic effect was appreciated in patient-derived cells. Thus, when pancreatic cancer patient-derived cells PDX354 and PDX185 were only incubated with 0.25 mg/mL ELR-based nanoparticles, cells showed 85.2% and 80.6% of metabolically active cells after 3 hours treatment and 50.2% and 44.9% after 24 hours treatment. Finally, when PDX354 and PDX185 cells were treated with combined therapy, results showed 33.9% and 28.6% of cells were metabolically active after 3 hours treatment and 27.2% and 17.9% after 24 hours treatment.

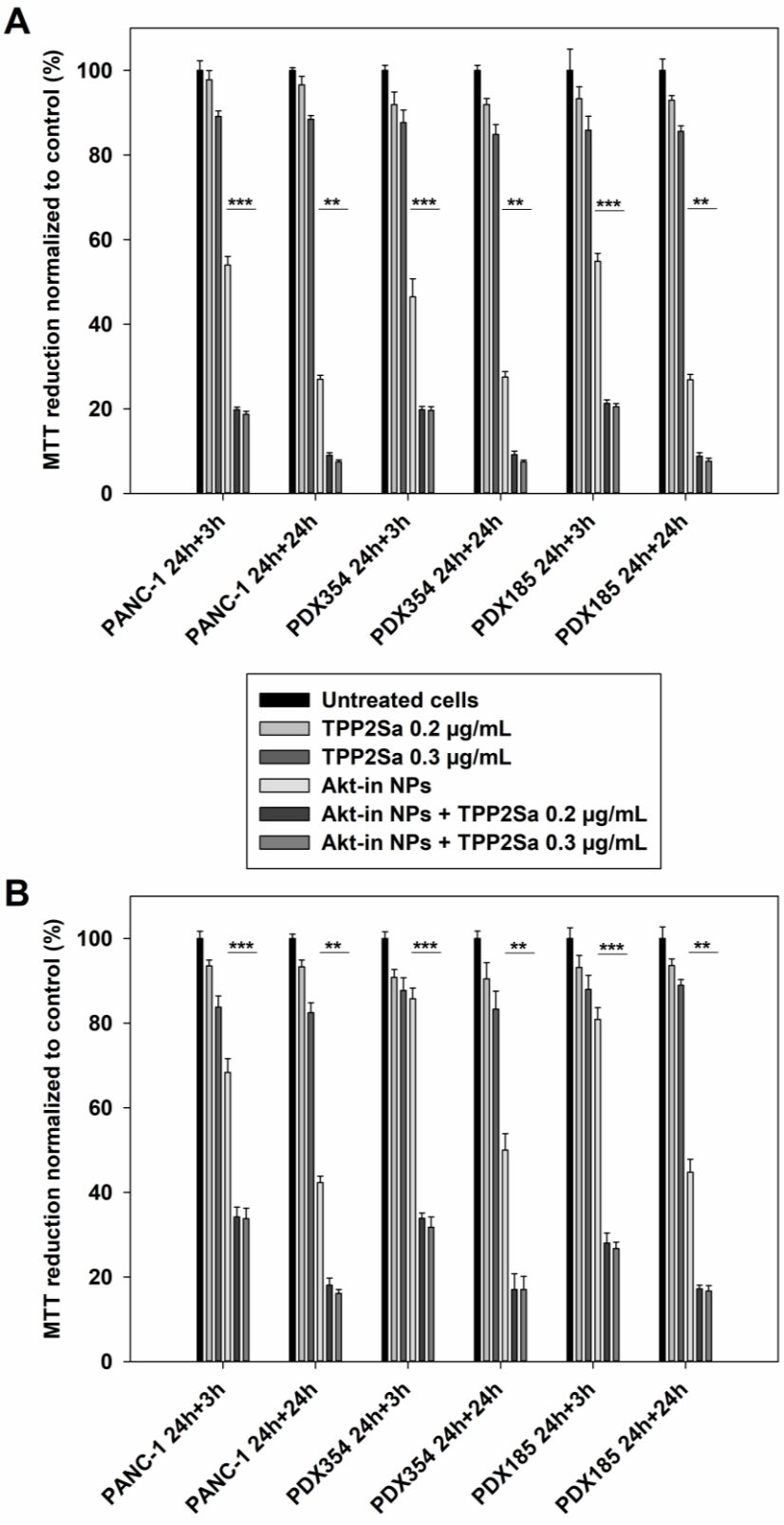

Figure 13. Metabolic activity of PANC-1 and patient-derived PDX354 and PDX185 cells after combined treatment with ELR-based nanoparticles and photodynamic therapy. Cells were co-incubated with TPP2Sa photosensitizer and Akt-in nanoparticles at 0.5 mg/mL (A) or 0.25 mg/mL (B) for two different times, as indicated, and then metabolic activity was measured by using the MTT reagent. n = 3 independent experiments, mean ± SD. **p < 0.01; ***p < 0.001.

We could conclude that combination of photodynamic therapy and ELR-based nanoparticles significantly enhanced the effect of small Akt inhibitor in pancreatic cancer cells. Therefore, this combination triggered a synergic effect, which could be a promising therapeutic approach with improved results and, also avoid side effects of high doses currently used in cancer treatment, by allowing us to use lower drug doses.

5.3.3.7 *In vivo* pharmacokinetic analysis of ELR-based nanoparticles

Short circulating half-life is the main disadvantage of therapeutic agents, such as drugs or peptides, so frequent administration and high concentrations are required to obtain therapeutically effective levels which usually result in high toxicity and off-target effects in healthy tissues [43, 44]. Therapeutic molecules have to pass through several biological barriers to reach the targeted tissue and ensure an effective dose. ELR-based carriers play an interesting role as regards overcoming all these limitations as they are able to extend the circulating half-life of therapeutic peptides or drugs and also improve their targeting and pharmacokinetics [45].

The pharmacokinetic profiles of control and Akt-in nanoparticles were compared after intravenous administration of fluorescein-labelled ELRs in BALB/c mice and the collection of blood samples at various time points. Figure 14 shows the plasma concentration versus time curve for both ELR polymers, in which one-phase decay behavior was observed. Therefore, the one-compartmental model was used to fit the plasma concentration-time curve by SAAM II software. This model assumes that the whole body acts like a single uniform compartment, the drug is distributed instantaneously throughout the entire body and drug elimination occurs immediately after the intravenous bolus injection [46, 47].

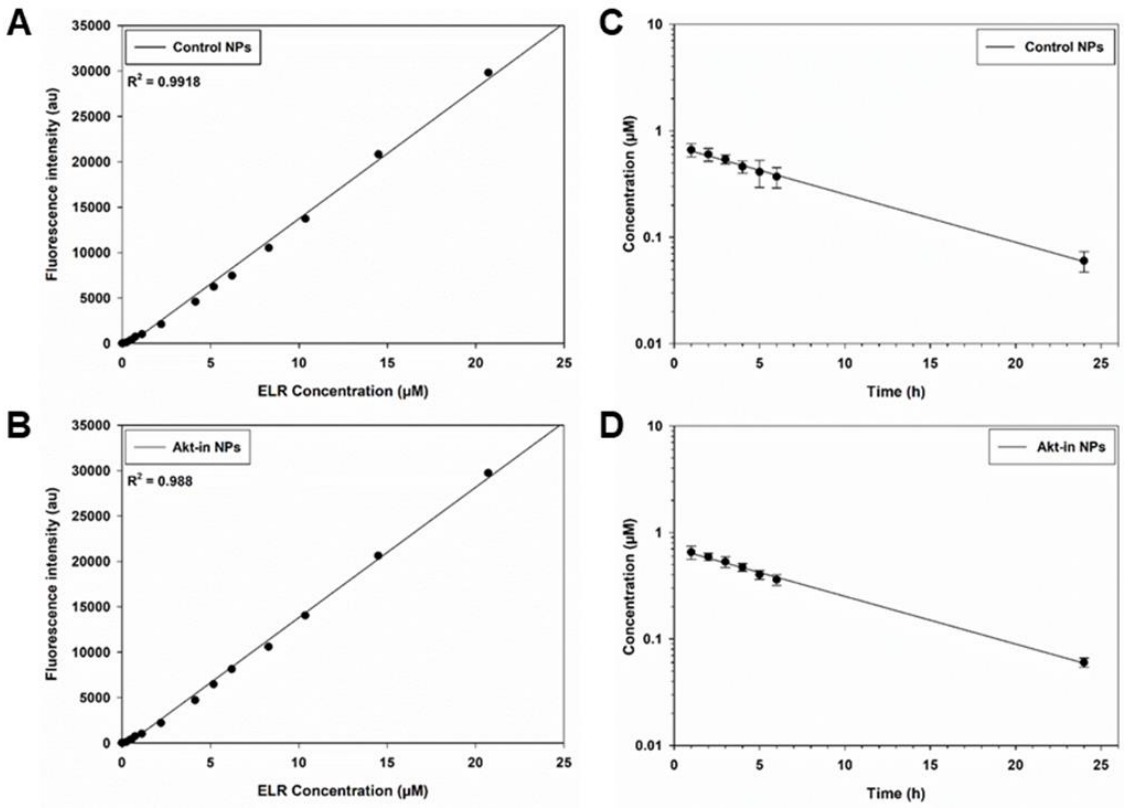

Figure 14. Control and Akt-in nanoparticles pharmacokinetic profiles after systemic administration in BALB/c mice. A linear standard curve was achieved by depicting the background-subtracted fluorescence versus the control (A) and Akt-in (B) ELR concentration. Briefly, increasing concentrations of fluorescence-labeled ELR nanoparticles were added to mice plasma and fluorescence intensity was determined. Plasma concentration versus time curve of control (C) and Akt-in (D) nanoparticles after systemic administration to 14-16 week old BALB/c mice (n=5 mice per treatment). Mean ± SD.

Pharmacokinetic parameters were determined (Table 1). The distribution volume of control and Akt-in nanoparticles was almost the same than plasma volume of a mouse. These values indicate that ELR nanoparticles were not rapidly accumulated in organs and tissues after administration. As presented in Table 1, ELR-based nanoparticles showed long half-life (5.8 and 5.3 hours for control and Akt-in nanoparticles, respectively), similar to previous ELRs developed for drug delivery purposes [48-50]. Moreover, no statistical difference was observed in any parameter when comparing control and Akt-in nanoparticles, which indicates that both nanoparticles have similar *in vivo* distribution and elimination. These pharmacokinetic parameters are considered suitable features in terms of delivery of therapeutic agents and drugs [46, 48]. These results indicate that our novel advanced nanoparticles are suitable biomaterials for drug delivery purposes.

Table 1. Pharmacokinetic parameters of intravenously administered control and Akt-in nanoparticles. One compartment analysis. Mean ± SD. Abbreviations: AUC: Area under the curve, F: Bioavailability, CL: Clearance, Vd: Volume of distribution, $T_{1/2\ elimination}$: Terminal half-life, $K_{elimination}$: elimination rate constant.

	Control NPs	**Akt-in NPs**
AUC (μm·h)	148 ± 8	129 ± 12
F (%)	100	100
CL (mL·h)	0.22 ± 0.08	0.25 ± 0.04
Vd (mL)	1.8 ± 0.3	1.9 ±0.5
$T_{1/2\ elimination}$ (h)	5.8 ± 0.4	5.3 ± 0.6
$K_{elimination}$ (h^{-1})	0.12 ± 0.02	0.13 ± 0.02

5.3.3.8 *In vivo* biodistribution

Once *in vivo* pharmacokinetics were determined, *in vivo* biodistribution was analyzed in mice (Figure 15). The pharmacokinetic profile of ELR-based nanoparticles showed that this nanocarrier could be a suitable device for drug delivery purposes presentingappropriate distribution volume (Vd) and half-life. For this reason, the biodistribution of the carriers was studied in order to determine whether the nanoparticles get preferentially accumulated in any specific organ upon intravenous administration. Briefly, ELR polymers were labeled with Cy5 as described above. Due to their characteristic thermoresponsiveness, ELRs self-assemble above the Tt into nanoparticles with the fluorescent label attached to the corona. Cy5-labeled nanoparticles were injected intravenously into BALB/c mice and the biodistribution was monitored using the IVIS *In Vivo* Imaging System after subtracting background from an untreated mouse. Moreover, heart, liver, spleen and kidneys were collected and scanned.

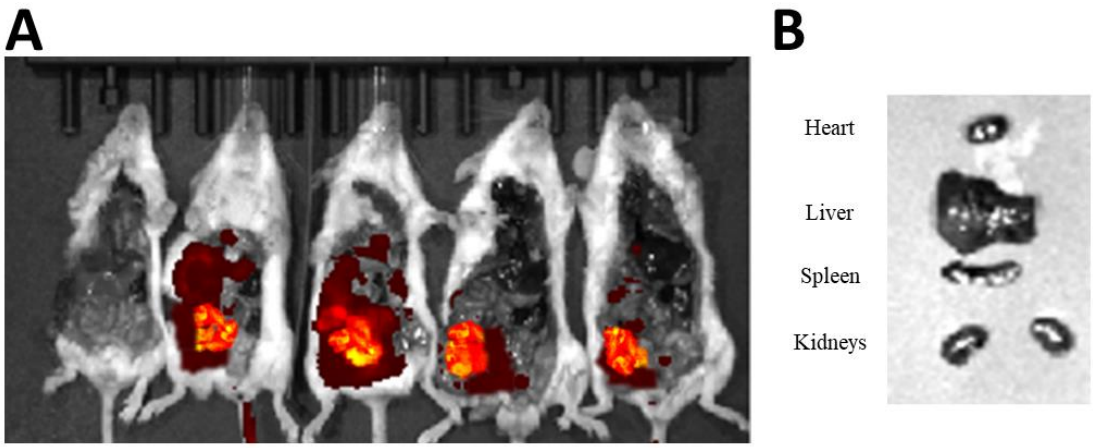

Figure 15. *In vivo* imaging of the biodistribution of Cy5-labeled nanoparticles into BALB/c mice. Cy-5 labeled ELR nanoparticles were systemically injected via tail vein. After 2 hours, animals were sacrificed and transferred immediately to the IVIS imaging system. A: Untreated animal (first from left) was measured as control. The other four animals were injected intravenously with Cy5-labeled nanoparticles via tail vein. B: Heart, liver, spleen and kidneys from treated animal 4 were collected and fluorescence was measured.

Figure 15A shows an increased accumulation of nanoparticles in the gastrointestinal tract (GIT) 2 hours post injection. GIT has been proposed as one of the major agents for nanomaterials interaction and uptake [51-54]. Thus, several GIT features have been described as key factors for nanoparticles uptake, such as the presence of enterocytes or the mucus layer [55-57]. Moreover, intestinal mucus secretion enhances nanomedicine transportation and uptake by endocytosis-mediated pathways [58]. One of the main problems of nanoparticles for drug delivery purposes is the accumulation in critical organs, such as heart, liver or kidneys. Thus, nanoparticles bigger than 100 nm are able to escape from liver capture [59]. Also, particles smaller than 10 nm suffered from renal clearance [60]. Therefore, nanoparticles with sizes ranging from 10 to 100 nm are preferred [61, 62]. In this work, ELR-based nanoparticles showed sizes of 66 and 72 nm for control and Akt-in nanodevices, respectively (Chapter 2 section 3.3). As expected, there was no signal detected in liver or kidneys (Figure 15B). Furthermore, there was no heart accumulation (Figure 15B). This is important, as some of the side effects of current chemotherapeutic drugs are due to heart toxicity [9]. At light of these results, we could conclude that the developed ELR-based nanoparticles were suitable as drug delivery nanodevices because no accumulation was appreciated in critical organs.

5.3.3.9 Histopathology examination of vital organs

The pharmacokinetic profile and organ biodistribution of our ELR-based nanocarriers confirmed their potential safety as no critical accumulation was observed in key organs. However, an in-depth analysis of the organ microstructure was also performed to check for any internal damage that may have arisen upon injection of control and Akt-in nanoparticles into the mice. In this regard, sections from key organs including liver, kidney, spleen and heart were stained with H&E (Figure 16) and assessed (Figure 17) by members of the Histopathology Department of the Royal Free Hospital (London, UK).

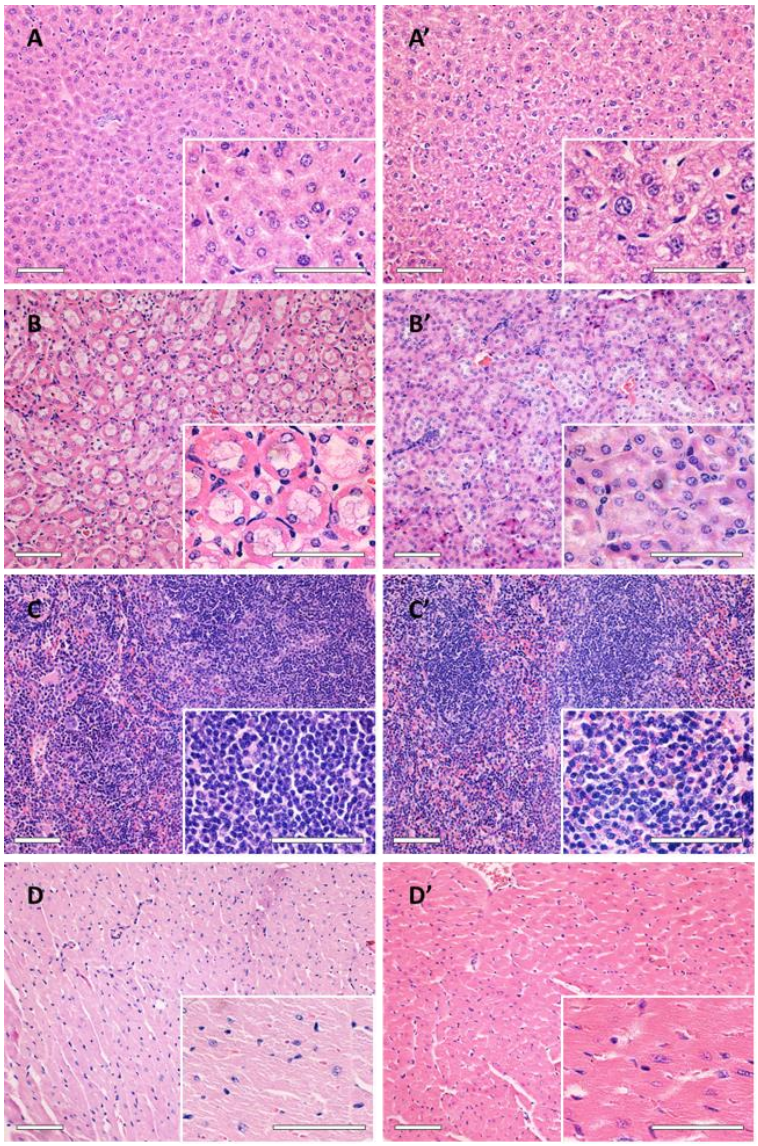

Figure 16. Effect of the treatment on organ histology. Selected organs from BALB/c mice treated with control (A-D) or Akt-in nanoparticles (A'-D'). A: Liver; B: Kidney; C: Spleen; D: Heart. Scale bars: 50 µm.

The results obtained from the examination are depicted in Figure 17. It must be stressed that only minor abnormalities were observed in organs of mice treated with control or Akt-in nanoparticles and in no case these abnormalities scored more than 2 out of 4 in the scoring system for each organ. Liver sections of mice treated with nanoparticles with or without the inhibitor did not show any effect (0/4) on lobular inflammation, ballooning, fibrosis or portal inflammation. Mild effects on steatosis (1/4) were observed in the liver of mice treated with Akt-in nanoparticles and were absent in samples of control nanoparticles (0/4). In terms of effects on the spleen, any of the treatments showed detectable alterations in neutrophils or signs of necrosis (0/4) and only mild thrombosis (1/4) was detected in upon nanoparticle administration. No myocardial damage was observed on heart sections after any of the treatments (0/4). Lastly, sections of the kidney showed no altered tubular vacuolation (0/4) or interstitial fibrosis (0/4) and no damaged vessels (0/4). Mild interstitial inflammation (1/4) was detected in kidneys from both treatment groups and also some glomerular cellularity was observed in the control group (1/4) which was moderate (2/4) in the Akt-in group of treatment. Altogether, these results corroborate previous findings on the safety of the nanocarriers which did not generate major deterioration on organs typically affected by free or encapsulated drugs. In addition, it was confirmed that the incorporation of the inhibitor Akt-in to the nanodevice did not change the mode of action of the nanomedicine compared to its analogous control nanoparticles.

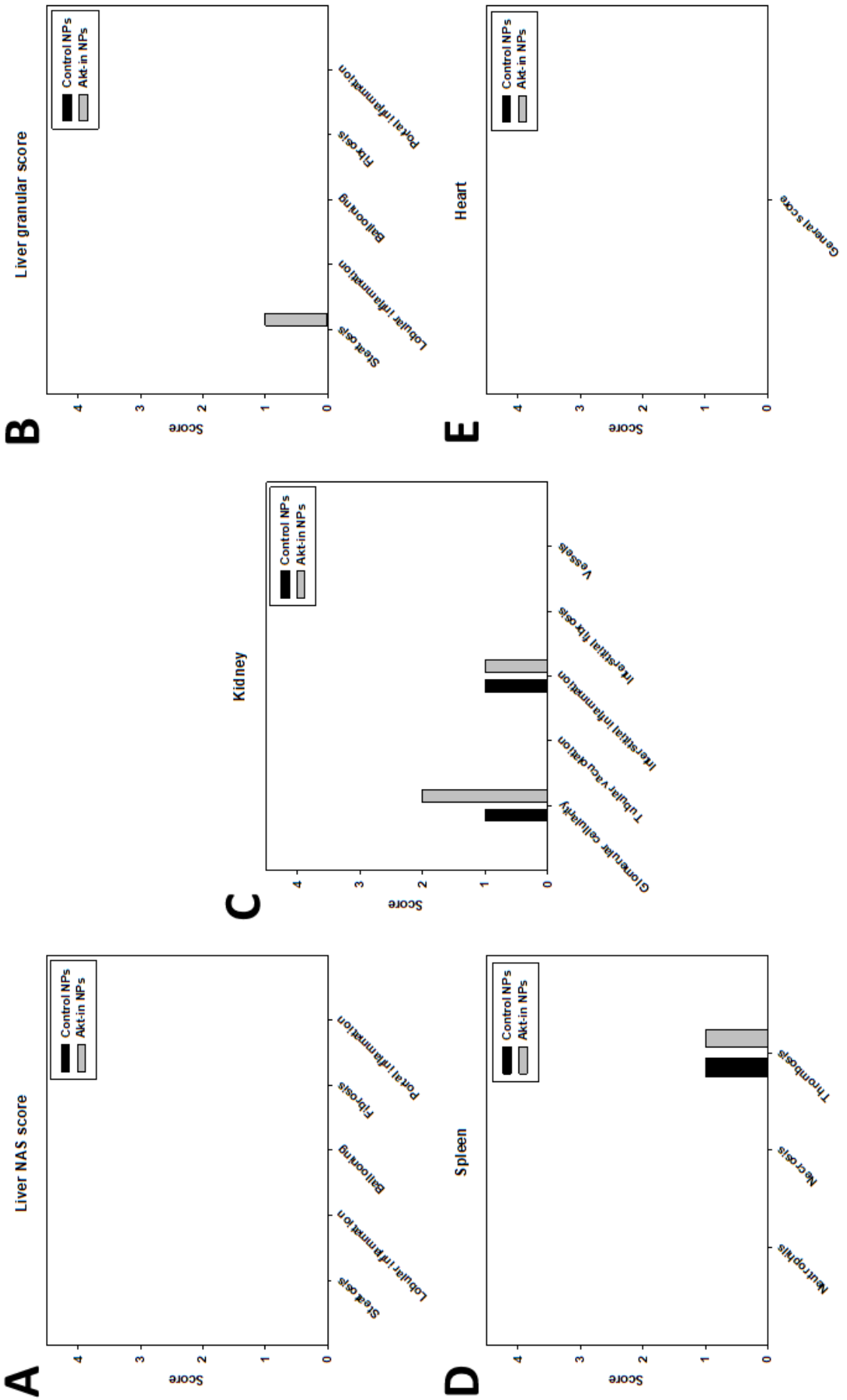
A
Liver NAS score
Control NPs
Akt-in NPs
Score
Steatosis
Lobular inflammation
Ballooning
Fibrosis
Portal inflammation
B
Liver granular score
Control NPs
Akt-in NPs
Score
Steatosis
Lobular inflammation
Ballooning
Fibrosis
Portal inflammation
C
Kidney
Control NPs
Akt-in NPs
Score
Glomerular cellularity
Tubular vacuolation
Interstitial inflammation
Interstitial fibrosis
Vessels
D
Spleen
Control NPs
Akt-in NPs
Score
Neutrophils
Necrosis
Thrombosis
E
Heart
Control NPs
Akt-in NPs
Score
General score

Figure 17. Histopathology score of liver, kidney, spleen and heart of mice treated with control or Akt-in nanoparticles. Liver assessment is based on NAS type scoring [63]; spleen is based on methodology described by Gibson-Corley *et al.* [64] and heart score is based on a system developed by Sachdeva *et al.* [65]. All score systems range from 0 to a maximum of 4.

5.3.4. Final remarks

Low specificity and side effects in healthy tissues are two of the main disadvantages of current drugs used for pancreatic cancer therapy. Nanotechnology appears as a promising approach for controlled drug delivery and optimal-dose reduction of therapeutic drugs. Moreover, poor drug accumulation and difficult access to the tumor-site are major hurdles in pancreatic cancer therapy leading to limited success of current drugs.

In this chapter, we took advantage of ELRs, which are obtained by using recombinant DNA technologies that allow us the complete control of the sequence, thus providing us the ability to include different bioactive sequences and create advanced polymers with conformational complexity for controlled drug delivery. We used two previously characterized (Chapter 2) ELR-based polymers which were able to self-assemble into nanoparticles of 66 and 72 nm of diameter when the temperature was increased above 15°C. The nanoparticles carried a small fifteen amino acid peptide which binds to the cytoplasmic Akt protein and inhibits its activation. Furthermore, the nanoparticles included different bioactive sequences in order to facilitate the internalization, enzymatic release of the inhibitor and escape from the lysosomes to the cellular cytoplasm, where the inhibitor reaches its target.

We determined the internalization of nanoparticles in three different pancreatic cancer cells: stablished PANC-1 cell line and two clinically relevant pancreatic cancer patient-derived cells [14], PDX185 and PDX354. Flow cytometry showed that both control and Akt-in nanoparticles were internalized at the same rate. Moreover, confocal microscopy determined that ELR nanoparticles were localized within the lysosomes, where the escape sequences were designed to act in order to properly release the inhibitor to the cytoplasm. Results also demonstrated that Akt-in nanoparticles not only reduced cellular metabolic activity, but also pancreatic cancer cell viability. In fact, cancer cells underwent apoptosis and died. Contrary, control nanoparticles did not impact cell metabolism nor viability. Based on our results, we can conclude that nanoparticles properly inhibited Akt signaling

pathway and consequently, blocked cell survival controlled by NFκB pathway. Interestingly, this toxic effect of nanoparticles in pancreatic cancer cells was enhanced by combination with a photosensitizer agent used for photodynamic therapy. This approach has a synergic effect as cancer treatment and, to the best of our knowledge, this is the first time that smart nanoparticles and photodynamic therapy are combined. Thus, this advanced nanoparticle based on different blocks of high conformational complexity showed to be an accurate drug delivery system for controlled release in pancreatic cancer cells.

In vivo pharmacokinetic profiles showed that both control and Akt-in nanoparticles present long half-life and distribution volume, which suggested that our nanoparticles are suitable drug delivery devices for systemic administration. Furthermore, *in vivo* assays showed that the developed ELR-based nanoparticles did not accumulate in critical organs, damage their microstructure or alter their normal physiology, some of the most common disadvantages leading to low accuracy and undesired side effects.

As Akt protein is not only overexpressed in pancreatic, but also in other types of cancer, different studies could be potentially accomplished in order to test the efficacy of this nanodevice in other cancers. Even though we studied the accuracy of these nanoparticles in a patient-derived cancer model, which is one of the closest research models to real disease [16, 19], further studies will be needed to determine the effectiveness of these nanoparticles in human patients. In the future, cancer patients overexpressing Akt protein may be candidates for clinical studies with nanoparticles carrying the inhibitor, which could improve the problems caused by current unspecific chemotherapeutic drugs.

5.3.5. References

[1] A. Vincent*, et al.* Pancreatic cancer. Lancet, 2011. 378 (9791):607-620.
[2] J.E. Everhart, C.E. Ruhl. Burden of digestive diseases in the United States Part III: Liver, biliary tract, and pancreas. Gastroenterology, 2009. 136 (4):1134-1144.
[3] P.L. Labib, G. Goodchild, S.P. Pereira. Molecular pathogenesis of cholangiocarcinoma. BMC Cancer, 2019. 19 (1):185.
[4] T.P. Yeo*, et al.* Pancreatic cancer. Curr Probl Cancer, 2002. 26 (4):176-275.
[5] H. Hurwitz*, et al.* Bevacizumab plus irinotecan, fluorouracil, and leucovorin for metastatic colorectal cancer. N Engl J Med, 2004. 350 (23):2335-2342.
[6] F.A. Shepherd*, et al.* Erlotinib in previously treated non-small-cell lung cancer. N Engl J Med, 2005. 353 (2):123-132.

[7] C. Swanton. Intratumor heterogeneity: evolution through space and time. Cancer Res, 2012. 72 (19):4875-4882.
[8] P.L. Bedard*, et al.* Tumour heterogeneity in the clinic. Nature, 2013. 501 (7467):355-364.
[9] M.L. Rossi, A.A. Rehman, C.S. Gondi. Therapeutic options for the management of pancreatic cancer. World J Gastroenterol, 2014. 20 (32):11142-11159.
[10] W. Han, A. Chilkoti, G.P. Lopez. Self-assembled hybrid elastin-like polypeptide/silica nanoparticles enable triggered drug release. Nanoscale, 2017. 9 (18):6178-6186.
[11] L.A. Garraway. Genomics-driven oncology: framework for an emerging paradigm. Journal of Clinical Oncology, 2013. 31 (15):1806-1814.
[12] J.M. Venditti, R.A. Wesley, J. Plowman. Current NCI preclinical antitumor screening in vivo: results of tumor panel screening, 1976-1982, and future directions. Adv Pharmacol Chemother, 1984. 20 1-20.
[13] R. Perez-Soler*, et al.* Response and determinants of sensitivity to paclitaxel in human non-small cell lung cancer tumors heterotransplanted in nude mice. Clinical Cancer Research, 2000. 6 (12):4932-4938.
[14] B. Rubio-Viqueira*, et al.* An in vivo platform for translational drug development in pancreatic cancer. Clinical Cancer Research, 2006. 12 (15):4652-4661.
[15] I. Fichtner*, et al.* Anticancer drug response and expression of molecular markers in early-passage xenotransplanted colon carcinomas. European Journal of Cancer, 2004. 40 (2):298-307.
[16] D. Sia*, et al.* The future of patient-derived tumor xenografts in cancer treatment. Pharmacogenomics, 2015. 16 (14):1671-1683.
[17] S. Aparicio, M. Hidalgo, A.L. Kung. Examining the utility of patient-derived xenograft mouse models. Nature Reviews Cancer, 2015. 15 (5):311-316.
[18] B. Rubio-Viqueira, M. Hidalgo. Direct in vivo xenograft tumor model for predicting chemotherapeutic drug response in cancer patients. Clin Pharmacol Ther, 2009. 85 (2):217-221.
[19] M. Hidalgo*, et al.* Patient-derived xenograft models: an emerging platform for translational cancer research. Cancer Discov, 2014. 4 (9):998-1013.
[20] D. Bechet*, et al.* Photodynamic therapy of malignant brain tumours: a complementary approach to conventional therapies. Cancer Treat Rev, 2014. 40 (2):229-241.
[21] J.F. Lovell*, et al.* Activatable photosensitizers for imaging and therapy. Chem Rev, 2010. 110 (5):2839-2857.
[22] S. Mallidi*, et al.* Beyond the barriers of light penetration: Strategies, perspectives and possibilities for photodynamic therapy. Theranostics, 2016. 6 (13):2458-2487.
[23] P. Agostinis*, et al.* Photodynamic therapy of cancer: an update. Cancer Journal for Clinicians, 2011. 61 (4):250-281.
[24] K. Cengel. Adapting preclinical concepts for use in clinical trials of serosal and interstitial photodynamic therapy. Journal of the National Comprehensive Cancer Network, 2012. 10 Suppl 2 S18-22.
[25] J. Gonzalez-Valdivieso*, et al.* Self-assembling ELR-based nanoparticles as smart drug-delivery systems modulating cellular growth via Akt. Biomacromolecules, 2019. 20 (5):1996-2007.
[26] Y. Li, N. Gu. Thermodynamics of charged nanoparticle adsorption on charge-neutral membranes: a simulation study. The Journal of Physical Chemistry B, 2010. 114 (8):2749-2754.
[27] J. Lin*, et al.* Penetration of lipid membranes by gold nanoparticles: insights into cellular uptake, cytotoxicity, and their relationship. ACS Nano, 2010. 4 (9):5421-5429.
[28] Y. Malam, M. Loizidou, A.M. Seifalian. Liposomes and nanoparticles: nanosized vehicles for drug delivery in cancer. Trends Pharmacol Sci, 2009. 30 (11):592-599.
[29] R.R. Arvizo*, et al.* Effect of nanoparticle surface charge at the plasma membrane and beyond. Nano Lett, 2010. 10 (7):2543-2548.
[30] S. Rello*, et al.* Morphological criteria to distinguish cell death induced by apoptotic and necrotic treatments. Apoptosis, 2005. 10 (1):201-208.

[31] L.C. Cantley. The phosphoinositide 3-kinase pathway. Science, 2002. 296 (5573):1655-1657.
[32] J. Luo, B.D. Manning, L.C. Cantley. Targeting the PI3K-Akt pathway in human cancer: rationale and promise. Cancer Cell, 2003. 4 (4):257-262.
[33] A. Mantovani. Molecular pathways linking inflammation and cancer. Curr Mol Med, 2010. 10 (4):369-373.
[34] Q. Huang, *et al.* Increased mitochondrial fission promotes autophagy and hepatocellular carcinoma cell survival through the ROS-modulated coordinated regulation of the NFKB and TP53 pathways. Autophagy, 2016. 12 (6):999-1014.
[35] A.G. Porter, R.U. Janicke. Emerging roles of caspase-3 in apoptosis. Cell Death Differ, 1999. 6 (2):99-104.
[36] M.A. Savitskaya, G.E. Onishchenko. Mechanisms of apoptosis. Biochemistry 2015. 80 (11):1393-1405.
[37] H.F. Zhao, J. Wang, S.S. Tony To. The phosphatidylinositol 3-kinase/Akt and c-Jun N-terminal kinase signaling in cancer: Alliance or contradiction? (Review). Int J Oncol, 2015. 47 (2):429-436.
[38] Y. Choi, *et al.* HER2-induced metastasis is mediated by AKT/JNK/EMT signaling pathway in gastric cancer. World J Gastroenterol, 2016. 22 (41):9141-9153.
[39] P.J. Muller, B.C. Wilson. Photodynamic therapy of malignant brain tumours. The Canadian Journal of Neurological Sciences, 1990. 17 (2):193-198.
[40] J.H. Kang, Y.T. Ko. Dual-selective photodynamic therapy with a mitochondria-targeted photosensitizer and fiber optic cannula for malignant brain tumors. Biomaterials Scicience, 2019.
[41] A. Garcia-Sampedro, *et al.* Multimodal use of the porphyrin TMPyP: From cancer therapy to antimicrobial applications. Journal of Porphyrins and Phthalocyanines, 2019. 23 11-27.
[42] L. Ayaru, S.G. Bown, S.P. Pereira. Photodynamic therapy for pancreatic and biliary tract carcinoma. Int J Gastrointest Cancer, 2005. 35 (1):1-13.
[43] D. Raucher, I. Massodi, G.L. Bidwell. Thermally targeted delivery of chemotherapeutics and anti-cancer peptides by elastin-like polypeptide. Expert Opinion in Drug Delivery, 2008. 5 (3):353-369.
[44] M. Santos, *et al.* Genetically Engineered Elastin-based Biomaterials for Biomedical Applications. Curr Med Chem, 2018.
[45] S.R. MacEwan, A. Chilkoti. Applications of elastin-like polypeptides in drug delivery. Journal of Controlled Release, 2014. 190 314-330.
[46] J.A. MacKay, *et al.* Self-assembling chimeric polypeptide-doxorubicin conjugate nanoparticles that abolish tumours after a single injection. Nat Mater, 2009. 8 (12):993-999.
[47] C. Lee, *et al.* Berunda polypeptides: biheaded Rapamycin carriers for subcutaneous treatment of autoimmune dry eye disease. Mol Pharm, 2019.
[48] P. Shi, *et al.* Elastin-based protein polymer nanoparticles carrying drug at both corona and core suppress tumor growth in vivo. Journal of Controlled Release, 2013. 171 (3):330-338.
[49] S.M. Janib, *et al.* Kinetic quantification of protein polymer nanoparticles using non-invasive imaging. Integrative Biology 2013. 5 (1):183-194.
[50] J. Hu, *et al.* Enhancing pharmacokinetics, tumor accumulation, and antitumor efficacy by Elastin-Like polypeptide fusion of Interferon Alpha. Advanced Materials, 2015. 27 (45):7320-7324.
[51] P. Jani, *et al.* Nanoparticle uptake by the rat gastrointestinal mucosa: quantitation and particle size dependency. J Pharm Pharmacol, 1990. 42 (12):821-826.
[52] E. Frohlich, E. Roblegg. Models for oral uptake of nanoparticles in consumer products. Toxicology, 2012. 291 (1-3):10-17.
[53] I.L. Bergin, F.A. Witzmann. Nanoparticle toxicity by the gastrointestinal route: evidence and knowledge gaps. Int J Biomed Nanosci Nanotechnol, 2013. 3 (1-2):

[54] A.P. Walczak, *et al.* In vitro gastrointestinal digestion increases the translocation of polystyrene nanoparticles in an in vitro intestinal co-culture model. Nanotoxicology, 2015. 9 (7):886-894.
[55] M.A. Clark, M.A. Jepson, B.H. Hirst. Exploiting M cells for drug and vaccine delivery. Adv Drug Deliv Rev, 2001. 50 (1-2):81-106.
[56] A. des Rieux, *et al.* Transport of nanoparticles across an in vitro model of the human intestinal follicle associated epithelium. European Journal of Pharmaceutical Sciences, 2005. 25 (4-5):455-465.
[57] J.S. Crater, R.L. Carrier. Barrier properties of gastrointestinal mucus to nanoparticle transport. Macromol Biosci, 2010. 10 (12):1473-1483.
[58] D. Yang, *et al.* Intestinal mucin induces more endocytosis but less transcytosis of nanoparticles across enterocytes by triggering nanoclustering and strengthening the retrograde pathway. ACS Applied Materials & Interfaces, 2018. 10 (14):11443-11456.
[59] J. Shi, *et al.* Cancer nanomedicine: progress, challenges and opportunities. Nature Reviews Cancer, 2017. 17 (1):20-37.
[60] D.S. Spencer, A.S. Puranik, N.A. Peppas. Intelligent nanoparticles for advanced drug delivery in cancer treatment. Curr Opin Chem Eng, 2015. 7 84-92.
[61] R.K. Jain. Transport of molecules in the tumor interstitium: a review. Cancer Res, 1987. 47 (12):3039-3051.
[62] S. Behzadi, *et al.* Cellular uptake of nanoparticles: journey inside the cell. Chem Soc Rev, 2017. 46 (14):4218-4244.
[63] D.E. Kleiner, *et al.* Design and validation of a histological scoring system for nonalcoholic fatty liver disease. Hepatology, 2005. 41 (6):1313-1321.
[64] K.N. Gibson-Corley, A.K. Olivier, D.K. Meyerholz. Principles for valid histopathologic scoring in research. Vet Pathol, 2013. 50 (6):1007-1015.
[65] J. Sachdeva, W. Dai, R.A. Kloner. Functional and histological assessment of an experimental model of Takotsubo's cardiomyopathy. J Am Heart Assoc, 2014. 3 (3):e000921.

Chapter 4

ELR-based smart nanohybrids as dual-approach drug delivery system against colorectal cancer

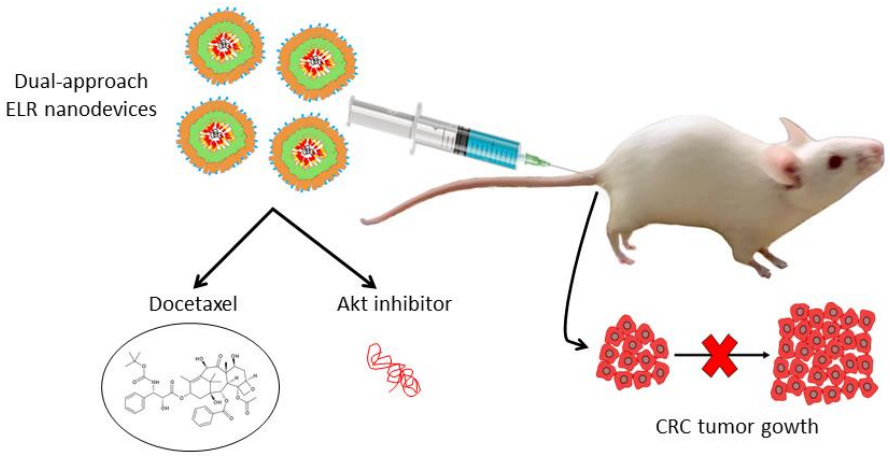

Part of the results of this chapter constitutes the articles:

Elastin-like based nanoparticles for docetaxel encapsulation by Supercritical Anti-Solvent process as smart drug delivery systems. R. Vallejo, J. Gonzalez-Valdivieso, M. Santos, S. Rodriguez-Rojo, F. J. Arias. Work in progress.

ELR-based smart nanohybrids as dual-approach drug delivery system against colorectal cancer. J. Gonzalez-Valdivieso, R. Vallejo, A. Girotti, M. Santos, S. Rodriguez-Rojo, F. J. Arias. Work in progress.

5.4.1. Introduction

Colorectal cancer (CRC) is one of the most commonly diagnosed cancers worldwide [1]. Indeed, CRC ranked in 2018 third in prevalence in men and second in women, with over 1.8 million new cases all over the world [2]. CRC provoked 242.000 deaths, 130.000 deaths in men and 112.000 deaths in women, in Europe in 2018 and was the second cause of death from cancer in Europe. Moreover, the World Health Organization expects an increase of 77% and 80% in terms of new cases and deaths from CRC by 2030, respectively. There are several reasons that can explain both high incidence and mortality of colorectal cancer, such as genetic predisposition, environmental factors, coexistence of other diseases, or late detection of cancer [3]. Therefore, novel approaches exploring new drugs are needed due to the lack of current accurate therapies.

Current strategies against CRC are based on two different approaches: first, early diagnosis and prevention of the disease in populations with increased risk factors, such as age, hereditary colorectal cancer syndromes, or other related diseases, as inflammatory bowel [4, 5]. Secondly, the therapy that combines both surgery and chemotherapeutic drugs. However, the most used drugs nowadays, such as oxaliplatin and 5-FU, present several problems in terms of lack of selectivity and undesired side effects in healthy tissues within the organism [6]. For this reason, more accurate drugs and promising targets are needed in order to specifically attack cancer cells [7]. Among these novel strategies, smart biomaterials are one of the most promising therapeutic approaches, as they are able to overcome the limitations of current drugs [8-10].

The ideal nanocarrier should transport the proper amount of therapeutic agent to the target cell even when simultaneous treatment of different organs is required, as in metastatic cancers. Even though nanoparticles present important advantages compared to free drugs, some problems need to be overcome, in terms of biodistribution and tumor accumulation [11]. Nanoparticles have already been demonstrated to reduce side effects in critical organs, such as kidney, heart, liver or brain [12]. In fact, nanotechnology takes advantage of the enhanced permeability and retention effect (EPR effect), which was purposed by Matsumura and Maeda, and consists on the fact that tumors have poor lymphatic drain system, aberrant multi-branched vasculature and abnormal vascular endothelium [13, 14]. However, EPR effect alone is not enough for ensure an improved drug accumulation

within the tumors. Therefore, targeting systems are needed in order to selectively drive the nanoparticles to the tumor cells and avoid any unspecific action in non-cancer cells [15, 16].

In this chapter, we developed advanced nanohybrids as dual-approach drug delivery systems with two different therapeutic agents. First, nanohybrids included a small peptide inhibitor (Akt-in) of Akt phosphorylation. Akt is an intracellular kinase involved in many cellular processes, such as cell proliferation, growth and survival, and is overexpressed in colorectal cancer cells [17, 18].

Moreover, chemotherapeutic agent Docetaxel (DTX) was encapsulated within ELR-based nanohybrids. DTX is a well-known antimitotic agent (by means of enhanced microtubule polymerization) clinically used for the treatment breast, ovarian, colorectal, lung and head and neck cancer [19-22]. However, DTX is highly hydrophobic as most chemotherapeutic drugs, so drug encapsulation is a promising approach in order to achieve increase drug solubility, availability and sustained and continuous drug delivery in targeted cancer cells [23-27]. Furthermore, DTX provokes undesired side effects and shows low efficacy, so DTX encapsulation could become an encouraging strategy for selective delivery and successful overcome rates in tumor treatments. In this chapter, we took advantage of the supercritical anti-solvent (SAS) process [28] in order to successfully encapsulate DTX inside ELR-based nanoparticles.

The use of accurate targeting systems could play a crucial role in terms of the effective action of therapeutic nanoparticles. Thus, the so-called cancer markers, such as overexpressed membrane receptors, are used in order to get selective internalization of nanodevices and achieve higher success rates [15, 29]. Although many cell receptors have been used for targeting systems, CD44 has been selected as one of the most common tumor markers, as it is overexpressed in many solid tumors, such as colon, pancreatic, breast and head and neck cancer [30-32]. CD44 is a transmembrane protein located in the cell surface and is the main receptor of hyaluronic acid (HA) [33, 34]. The receptor is composed by the cytoplasmic domain, the transmembrane domain, and the ectodomain, which contains an N-terminal globular domain that provides the binding site for hyaluronic acid [35]. Furthermore, CD44 is involved in multiple interactions with other

cellular proteins in order to regulate different cell processes, such as cell proliferation, migration, motility, growth, survival, and angiogenesis, among others [35, 36]. For this reason, CD44 has been widely used for specific targeting of therapeutic molecules against cancer [36]. Different targeting agents can be used, as proteins (antibodies and their fragments), nucleic acids (aptamers) or other receptor ligands (peptides, vitamins, carbohydrates) [37-41] Aptamers are chemically synthesized short single strand DNA or RNA oligonucleotides [42, 43]. They show high affinity and are synthesized from random oligonucleotides pools by the so-called process Systematic Evolution of Ligands by Exponential Enrichment (SELEX), whose aim resides in the ability of aptamers to fold in 3D structures showing high specificity and affinity for their ligands [44, 45]. Aptamers also present several advantages, as they can be chemically modified and have low toxicity and immunogenicity [46, 47].

The objectives of this study were to synthesize and characterize an advanced dual-approach therapeutic system for its application in colorectal cancer. Recombinant technology and SAS process allowed us to develop targeted nanohybrids carrying Akt inhibitor and DTX and specifically release both anti-tumor drugs inside colorectal cancer cells. In light of the above, we determined *in vitro* the therapeutic efficacy of ELR-based nanohybrids in Caco-2 and HUVEC cells. Moreover, we studied *in vivo* the anti-tumor activity in a colorectal cancer animal model.

5.4.2. Methods

5.4.2.1 ELRs design, bioproduction and purification

The ELRs used in this chapter were obtained as previously described by the group [48] and Chapter 2 sections 2.2-2.5 and were bioproduced in a 15-L bioreactor (Applikon Biotechnology, Netherlands) as described in Chapter 2 sections 2.3 and 2.4. The ELRs were purified by several cooling and heating purification cycles (Inverse Transition Cycling-ITC) as described in Chapter 2 section 2.5. SDS-PAGE was performed in order to determine the purity of the recombinamers, as previously described in Chapter 2 section 2.4. MALDI-TOF/MS was performed by Laboratory of Instrumental Technics from University of Valladolid, following the protocol described in Chapter 2 section 2.6, to determine their molecular weight. NMR and HPLC were realized by Laboratory of

Instrumental Technics from University of Valladolid to verify the amino acid composition following the protocols described in Chapter 2 sections 2.7 and 2.8.

5.4.2.2 Chemical modification and DNA aptamer functionalization by click chemistry

1 equivalent of ELRs was mixed with 0.33 equivalents of NHS-PEG-Cyclooctine ((2,5-Dioxopyrrolidin-1-yl1 ((1R,8S,9s)-bicycle (6.1.0) non-4-yn-9-yl) - 3,14-dioxo-2,7,10-trioxa-4-13diazaoctadecan-18-oate) (3 mg/mL) both in DMF under nitrogen atmosphere at room temperature. The mixture was stirred overnight at 4 °C, dialyzed against cold ultrapure water type I and lyophilized. The incorporation of PEG as ELR-PEG-Cyclooctine to the ELR was evaluated by ^{1}H-NMR (Chapter 2 section 2.7).

The sequence of the azide-modified DNA aptamer for specific binding to CD44 [41] is the following:

5′-C3-azide-GAGATTCATCACGCGCATAGTCCCAAGGCCTGCAAGGGAACCAAGGACACAGCGACTATGCGATGATGTCTT-3’.

For the aptamer functionalization by click chemistry, 1 equivalent of CD44-Azide was mixed with 1 equivalent of ELR-PEG-Cyclooctine previously dissolved in ultrapure water type I (pH 7.4) and the mixture was left at 4 °C for 24 hours. After this time, the product was dialyzed against cold ultrapure water type I and lyophilized. The incorporation of CD44 aptamer by cycloadition of azide and activated cyclooctine was corroborated by spectrophotometry measuring the absorbance at 260 nm with a Nanodrop 2000 (Thermo Scientific).

5.4.2.3 Supercritical antisolvent process

Nanohybrids were developed in collaboration with the High Pressure Process Group from BioEcoUVa Research Institute on Bioeconomy at University of Valladolid [49]. Briefly, the supercritical antisolvent technique was used in order to co-precipitate ELR hybrid polymers and DTX. The use of supercritical fluids (SCFs) is a viable option to take into account when producing micro- or nano-particulate systems for controlled drug release. Thus, the solute of interest was first dissolved in a conventional solvent and this solution

was then continuously sprayed through a nozzle into a reactor where CO_2 is present in a supercritical state. This $scCO_2$ acted as an anti-solvent decreasing the solubility of the solutes in the mixture, which resulted in a rapid supersaturation and the nucleation and formation of nano- or microparticles. The desired particle size and morphology can be controlled by adjusting the process parameters, including SCF density, solution concentration, nozzle geometry and flow rate.

Composition and proportions of ELR hybrid nanosystems were calculated by comparing the integral of the signal for the methyl groups from the ELR with those for the protons in the aryl moieties of DTX in the ^{1}H-NMR spectra [49]. Nuclear magnetic resonance spectroscopic data were acquired using an Agilent 400 NMR spectrometer (Laboratory of Instrumental Techniques, University of Valladolid). Analysis of the spectra with MestReNova v 9.0.1 allowed us to calculate the ELR and DTX ratio in each nanohybrid.

5.4.2.4 Particle size and ζ-potential

The size and ζ-potential of the ELR-based nanoparticles were determined by DLS at 37°C as described in Chapter 2 section 2.10. Solutions of ELRs were prepared by dissolving the ELRs at 37°C in PBS (pH 7.4) or ultrapure water type I (pH 7.4), when indicated. The solutions were dissolved and filtered using a 0.45 μm poly(vinylidene difluoride) (PVDF) syringe filter. The samples were then introduced into polystyrene cuvettes and stabilized for 2 min at the desired temperature. Autocorrelation functions were used to obtain the size distribution and polydispersity index (PDI). Z-average mean (nm) and ζ-potential (mV) were used for data analysis. Three different samples of each type of particle were analyzed.

For BSA interaction experiments, ELR nanoparticles were incubated in 5% BSA-containing PBS at 37°C for 1 hour and then filtered, introduced into polystyrene cuvettes and stabilized for 2 min at the desired temperature. Autocorrelation functions were used to obtain the size distribution and polydispersity index. Z-average mean (nm) were used for data analysis. Three different samples of each type of particle were analyzed.

5.4.2.5 Transmission Electron Microscopy (TEM)

Solutions were prepared by dissolving the ELRs in ultrapure water type I (pH 7.4) and later incubation for 30 minutes at 37°C to allow supramolecular assembly to occur. Then, the samples were stained with uranyl acetate solution (1,0 wt %) to enhance the contrast of the nanohybrids on a carbon-coated copper grid, followed by solvent evaporation. Samples were observed using a JEM-2200 electron microscope operating at 200 kV at Laboratory of Instrumental Techniques, University of Valladolid.

5.4.2.6 Cell culture

Endothelial HUVEC cells were grown in Medium 200 supplemented with 1% gentamicin/amphotericin and with low serum growth supplement (LSGS) at 5% CO_2 and 37°C. MDA-MB-231 breast cancer cells were cultured in L-15 medium supplemented with 10% FBS, 100 U/mL penicillin and 0.1 mg/mL streptomycin at 0% CO_2 and 37°C. Caco-2 colorectal cancer cells were maintained in MEM supplemented with 10% FBS, 2 mM glutamine, 1% NEAA, 100 U/mL penicillin and 0.1 mg/mL streptomycin at 5% CO_2 and 37°C. When required, cells were detached using a solution of 0.05% Trypsin-EDTA. Cells were seeded onto 96-well plates in a density of 2×10^4 cells per cm^2 for tumor cells and 1×10^4 cells per cm^2 for primary endothelial cells overnight before treatments, in order to maintain similar levels of confluence for all cell lines.

5.4.2.7 Confocal microscopy

Caco-2 cells were seeded and, after 24 hours, incubated with rhodamine-loaded ELR nanohybrids for 1 hour. Then, cells were washed with PBS 1X, fixed with PFA 4% and permeabilized with Triton 0.1%. Cellular nuclei were stained with DAPI. Images were taken with a Leica TCS SP8 X confocal microscope at Laboratory of Instrumental Techniques, University of Valladolid.

5.4.2.8 Cell viability

HUVEC and MDA-MB-231 cells were treated for 24 hours with free DTX at three concentrations (0.1, 1 and 10 µM) or the equivalent amount of encapsulated drug within ELR nanoparticles (lacking or containing DTX).

Caco-2 cells were treated with 1 µM free DTX or ELRs at equivalent normalized concentrations for 30 min or 24 hours.

Cell viability was measured by Live and Dead staining following the manufacturer's instructions, as described in Chapter 1 section 2.13. Three independent experiments, each in triplicate, were performed.

5.4.2.9 Cell proliferation

For the preliminary assays, MDA-MB-231 cells were treated with free 1 µM DTX or different ELRs at equivalent normalized concentrations for 72 hours.

For the determination of the effectiveness of the DNA aptamer conjugation, Caco-2 and HUVEC cells were treated with ELRs at three different concentrations (0.25, 0.5 and 1 mg/mL) for 72 hours.

For the assays involving ELR nanohybrids, Caco-2 and HUVEC cells were treated with 1 µM free DTX or ELRs at equivalent normalized concentrations for 72 hours.

Confluence percentages were determined each 4 hours by using the Cytosmart OMNI software (Cyotsmart, Netherlands). Additional confluence percentages were determined each hour during the first 6 hours. Three independent experiments, each in triplicate, were performed.

5.4.2.10 Apoptosis/Necrosis assay

Caco-2 cells were incubated with 1 µM free DTX or ELRs at equivalent normalized concentrations for 30 min or 24 hours. FITC-conjugated annexin V and propidium iodide staining was used according to the manufacturer's instructions, as described in Chapter 2 section 2.20. Three independent experiments, each in triplicate, were performed.

5.4.2.11 *In vivo* pharmacokinetic analysis

All animal experiments were conducted in accordance with the institutional guidelines for the care and use of experimental animals of the University of Valladolid (Spain) in accordance with Directive 2010/63/EU (Resolution Number 2010/2/23) under the supervision of the Animal Research and Welfare Committee.

BALB/c mice aged 14-16 weeks (n=5) were injected intravenously via tail vein with 100 µL of rhodamine-loaded ELR nanohybrids (tNPs-Ai-DTX-Rho) previously dissolved in PBS at 3 mg/mL. For the time course analysis, 20 µL of blood were collected at 1, 2, 3, 4, 5, 6 and 24 hours after injection and immediately diluted into 80 µL of heparinized PBS. The blood was centrifuged at 21100 xg for 10 minutes at 4°C and the supernatant was loaded onto a black clear bottom 96-well plate. Fluorescence intensity was read using a SpectraMax M5e Molecular Devices microplate reader with excitation and emission wavelengths of 553 nm and 627 nm, respectively. Plasma auto fluorescence was determined from negative control (non-injected) mice and subtracted to the samples values. The fluorescence intensity values were converted to concentration by extrapolation from a linear standard curve.

To obtain pharmacokinetic parameters for the compartmental analysis, the data set of each individual mouse was fit to a one-compartment pharmacokinetic model using SAAM II software (University of Washington).

5.4.2.12 *In vivo* tumor induction

Tumor induction was performed as previously described by Neufert *et al.* [50]. Briefly, BALB/c mice aged 6-8 weeks (n=82) were intraperitoneally injected with 7.5 mg/Kg Azoxymethane (AOM). 5 days later mice were treated with 3% dextran sodium sulphate (DSS) in drinking water for 5 days, followed by 15 days of regular drinking water. DSS treatment was repeated twice (total of 3 cycles of DSS were provided). The experimental course for tumor induction is depicted in Figure 1. Body weight and animal welfare were monitored each three days during the whole experiment.

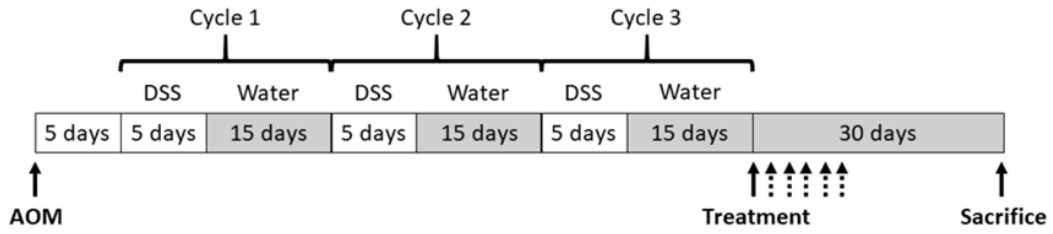

Figure 1. Scheme for the experimental course of AOM-induced colon carcinogenesis with inflammation-driven tumor progression. Dashed lines indicate the alternative additional doses of treatment AOM: Azoxymethane; DSS: Dextran sodium sulphate; Adapted from Neufert *et al.* [50].

5.4.2.13 *In vivo* Magnetic Resonance Imaging (MRI)

Magnetic Resonance Imaging was performed at Laboratory of Instrumental Techniques, University of Valladolid, using a 9.4T 160 mm Bore Actively Screened MRI system (Agilent Technologies, Santa Clara, USA) equipped with 400 mT/m gradient inserts and a 15 mm volume resonator RF coil (RAPID Biomedical, Rimpar, Germany). For the preliminary tumor induction assay, MRI was performed after animal sacrifice. For the assessment of anti-tumor efficacy of ELR nanohybrids, MRI was performed at day 25 post-treatment. Animals were anaesthetized with isoflurane in oxygen (4% for induction and 1.5% for maintenance).

5.4.2.14 *In vivo* anti-tumor efficacy

After the last DSS cycle for tumor induction, BALB/c mice were randomly divided into twelve groups with 6 mice in each one and the treatment started, which is considered as day 0. The experimental groups are the following: Placebo group (mice treated with PBS), control empty ELR nanohybrids (tNPs [2 mg/Kg]), free DTX 5 mg/Kg, free DTX 2 mg/Kg, nanohybrids only containing DTX 2 mg/Kg (tNPs-DTX 2 mg/Kg), nanohybrids only containing Akt inhibitor (tNPs-Ai [2 mg/Kg]), high dose group (tNPs-Ai-DTX 5 mg/Kg), medium dose group (tNPs-Ai-DTX 2 mg/Kg) and low dose group (tNPs-Ai-DTX 1 mg/Kg). Furthermore, three multidose groups were also established: low dose in two injections (tNPs-Ai-DTX 0.5 mg/Kg x 2), medium dose in 4 injections (tNPs-Ai-DTX 0.5 mg/Kg x 4) and medium dose in 6 injections (0.5 mg/Kg x 6). The use of brackets in tNPs [2 mg/Kg] and tNPs-Ai [2 mg/Kg] group names means that these groups were administered with the same amount of ELR than tNPs-DTX 2 mg/Kg group. Thus, animals were intravenously injected with PBS, free DTX or ELR nanohybrids at indicated concentrations via tail vein. Dosage were adjusted to the group average weight. One month later, which corresponded to 95 days from the beginning of the protocol, mice were sacrificed and colons were extracted after necropsy. Also, tumor polyps were counted and measured. Representative images of tumor polyps were taken with Leica DMS 1000 microscope.

5.4.2.15 Tissue processing and histological staining

Colons were fixed with PFA 4% and subsequently dehydrated by immersion in ethanol solutions from 70% to 100%, finishing with two changes in xylene solution. Samples

were embedded in paraffin and then serially sliced into sections with a thickness of 5 µm with a microtome. Histological sections were transferred onto glass microscopy slides and deparaffinized and rehydrated with subsequent immersion in xylene, ethanol solutions of decreasing concentration and, finally, distilled water. Samples were stained with hematoxylin-eosin (H&E).

5.4.2.16 Statistical analysis

Data are reported as mean ± SD (n = 3). Statistical analysis involved a variance analysis in combination with a subsequent analysis using the Bonferroni method. A p value of less than 0.05 was considered to be statistically significant. *p < 0.05, **p < 0.01, ***p < 0.001. Data were handled using the SPSS Statistics software version 20 (IBM).

5.4.3. Results and Discussion

5.4.3.1 DTX-loaded ELR nanoparticles directed by RGD peptide

5.4.3.1.1 ELRs design for DTX encapsulation

In this chapter, we will study the anti-tumor activity of novel targeted ELR nanodevices involving encapsulation of therapeutic agents in order to be used as multi-treatment against cancer.

First, we developed smart nanocarriers to study the encapsulation and therapeutic release of antimitotic drug Docetaxel (DTX), in collaboration with High Pressure Process Group from BioEcoUVa Research Institute on Bioeconomy at the University of Valladolid by supercritical antisolvent process (SAS) [49]. Thus, we used a previously described ELR polymer based on an amphiphilic tetrablock consisting on the alternation of hydrophilic glutamic acid-containing and hydrophobic isoleucine-rich blocks [51, 52]. Moreover, we used a second ELR [53] consisting on the same backbone and an additional block including the RGD peptide (Arg–Gly-Asp), a tripeptide motif present in several structural extracellular matrix proteins that binds preferentially to $\alpha_v\beta_3$ and $\alpha_v\beta_5$ integrin heterodimers. RGD is an excellent model to test novel targeted carriers for drug delivery as it increases cell internalization and has been widely studied for active cancer targeting [54]. These two ELR-based constructs were used in order to study the encapsulation of highly hydrophobic DTX into monodisperse nanoparticles. These nanodevices would

also avoid adverse side effects from systemic administration and improve the cytotoxic activity of the chemotherapeutic drug (Figure 2).

The amino acid sequences of (EI)x2 and (EI)x2RGD are the following:

- MESLLP-[[(VPGVG)$_2$**VPGEG**(VPGVG)$_2$]$_{10}$-(**VGIPG**)$_{60}$]$_2$-V
- MESLLP-[[(VPGVG)$_2$**VPGEG**(VPGVG)$_2$]$_{10}$-(**VGIPG**)$_{60}$]$_2$-VG-[(VPGIG)$_{10}$-AVTG**RGD**SPASS-(VPGIG)$_{10}$]$_2$-V

Both polymers contain two different functional blocks in order to achieve an adequate balance between biocompatibility and mechanical and thermal responses. The hydrophilic block contains polar glutamic acid (E), responsible for the pH-responsiveness, whereas the second block, which contains Isoleucine (I), is thermo-responsive in physiological conditions. In the case of (EI)x2RGD, the latter block contains a peptide loop found in the human fibronectin protein with the well-known RGD sequence for cancer cell targeting.

Figure 2. Scheme of (EI)x2RGD and (EI)x2 polymers designed for DTX encapsulation (top and bottom scheme, respectively). Non-scaled scheme.

The results from this first therapeutic approach based on DTX encapsulation are depicted in section 3.1.2.

In a second strategy, ELRs described in Chapter 2 were used as the second therapeutic approach comprised in the multi-treatment strategy. As previously described (Chapter 2 section 3.5), results showed that these biopolymers were able to self-assemble into nanoparticles able to release a pro-apoptotic peptide (Akt-in) within cells, whose effect was enhanced in cancer cell lines compared to non-cancer cells. However, these biopolymers were improved by attaching a targeting system in order to specifically drive the nanoparticles to CRC cancer cells and avoid side effects in healthy tissues. Thus, a

DNA aptamer was covalently conjugated to specifically interact with CD44 membrane receptor, which is overexpressed in CRC cells and has been stablished as CRC marker [30-32]. The results from this second therapeutic approach are depicted in section 3.3.

5.4.3.1.2 Effect of DTX-loaded ELR nanoparticles directed by RGD peptide on cell viability

The efficiency of DTX encapsulation and delivery was determined *in vitro* using two different human cell lines, namely breast cancer MDA-MB-231 cells and human endothelial HUVEC cells. These cell lines were chosen due to the fact that both are well-known for their high expression of surface integrin receptors [55]. Moreover these integrins are overexpressed in a wide range of cancers [56] and recognize the RGD sequence included in polymer molecules [57-60]. Moreover, endothelial cells could allow us to study the cytotoxic effect of ELR nanoparticles after intravenous systemic administration.

Three different concentrations (0.1, 1 and 10 µM) of free and encapsulated DTX in both types of ELR nanoparticles, NPs+DTX and NPs-RGD+DTX depending on the presence of the RGD sequence, were tested (Figure 3). These DTX concentrations were selected on the basis of the solubility of the drug and the standard concentrations used in the literature, thus allowing us to study the therapeutic window of the drug. For example, Saw *et al*. demonstrated that 1 µM DTX-loaded liposomes and micelles decreased the viability of SCC-7 cells by 40% and 20%, respectively [23]. Furthermore, 1 µM DTX-loaded albumin nanoparticles showed *in vitro* effects on murine melanoma B16F10 (20% cell viability) and breast cancer MCF-7 cells (10% cell viability) [61]. Due to cytocompatibility of ELR backbone and the presence of RGD targeting system, our smart nanocarriers were therefore expected to behave as accurate drug-delivery devices by improving the effectiveness of the chemotherapeutic drug DTX on cancer cells and decreasing undesired effects in healthy cells.

Empty ELR nanoparticles, NPs and NPs-RGD were used as a control in order to determine both the effect of carriers and the internalization process in cell viability. The cytotoxic effect of control nanoparticles was determined initially as, although this type of nanoparticle does not carry any drug, its internalization could affect cell viability.

Incubation with both type of control nanoparticles, NPs or NPs-RGD, did not significantly affect the viability of either of the cell lines. Indeed, our results showed no differences between three different concentrations, thereby corroborating previous studies from this group, where ELR polymers with and without the RGD peptide were characterized and showed no cytotoxicity [53]. As such, we can conclude that, under our experimental conditions, control nanocarriers did not result in a decrease in the viability of either cancer or non-cancer cells.

Concerning the effect of free DTX, incubation of cells with the highest drug concentration (10 µM) for 24 hours induced a markedly toxic effect, with cell viability diminishing to 3-5%. In contrast, when the lowest concentration was used for the same time, cell viability was only slightly affected (92-93% cell viability), whereas an intermediate concentration (1 µM) decreased cell viability to 23-29%. Interestingly, there were no noticeable differences between the two types of cells (MDA-MB-231 and HUVEC) at any concentration, thus meaning that DTX acts on cells undergoing division (Figure 3A-B) and is not selective for cancer cells. This result is in accordance with previous reports by Liu *et al*. and Wang *et al*., who demonstrated that the viability of HUVEC cells was also dramatically affected after treatment with DTX [62, 63].

Furthermore, different effects could be appreciated when DTX-loaded nanoparticles were used. Thus, NPs+DTX did not improve free DTX action at any drug concentration and cytotoxicity on both cancer and non-cancer cells was reduced. This could be explained by slower delivery of encapsulated DTX, and therefore longer incubation times are needed for therapeutic action. However, when MDA-MB-231 cells were treated with NPs-RGD+DTX, the cytotoxic effect of encapsulated DTX was improved compared to both free drug and NPs+DTX (Figure 3B). Indeed, targeted NPs-RGD+DTX significantly decreased cancer cell viability (10% and 78%) when compared to free DTX (25% and 93%) and NPs+DTX (42% and 96%) for 1 and 0.1 µM, respectively. As can be seen in Figure 3C, cell lines showed different behavior when treated with different drug presentations as 1 µM free DTX or the equivalent amount encapsulated within ELR nanoparticles. Interestingly, the same dose of NPs-RGD+DTX differently affected cancer and HUVEC cells. A decrease in viable MDA-MB-231 cells was found with respect to cells treated with free DTX. Moreover, this effect was not seen in HUVEC cells, which

showed increased cell viability levels compared to free DTX. This different behavior in both HUVEC and MDA-MB-231 cells could be due to the presence of RGD motive for active targeting.

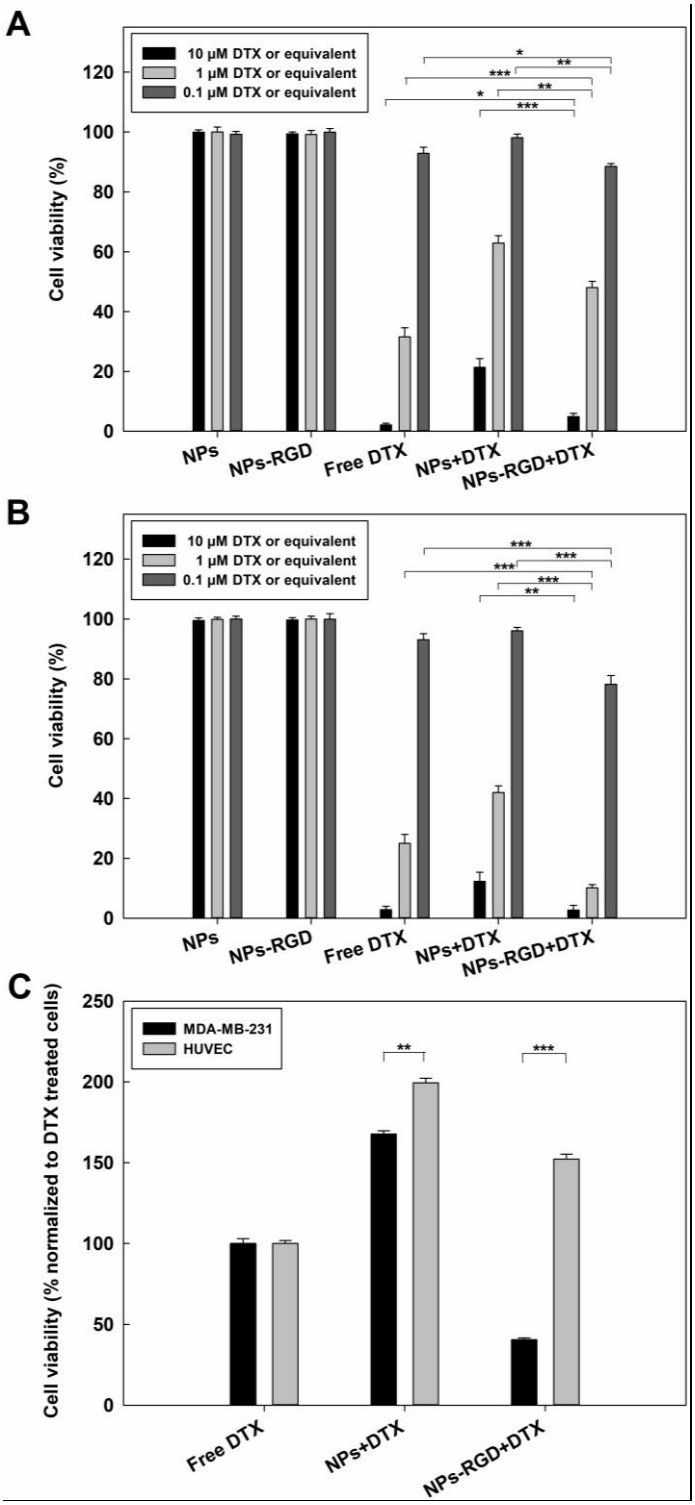

Figure 3. Effect of ELR nanoparticles in cell viability of HUVEC (A) and MDA-MB-231 cells (B). Cells were incubated with free DTX at three concentrations (0.1, 1 and 10 µM) or ELR nanoparticles

at the corresponding concentrations for 24 hours and viability was measured using the LIVE/DEAD Assay kit. C: The percentage viability of both cell lines treated with 1 µM DTX-loaded ELR nanoparticles compared to free DTX treated cells. n = 3 independent experiments, mean ± SD. *p < 0.05, **p < 0.01, ***p < 0.001

The enhanced internalization of MDA-MB-231 cells was demonstrated when treated with nanoparticles lacking RGD, as this cell line was more affected than endothelial cells. In addition, DTX-loaded nanoparticles containing the RGD sequence (NPs-RGD+DTX) were found to be more toxic in breast cancer cells compared to HUVEC, thereby highlighting the specific effect due to the overexpression of integrins binding RGD motif.

5.4.3.1.3 Effect of DTX-loaded nanoparticles directed by RGD peptide on cell proliferation

After determining the lineage-specific effect on cell viability, the potential use of ELR nanoparticles was next tested by measuring *in vitro* cell proliferation for 72 hours in MDA-MB-231 breast cancer cells incubated with 1 µM DTX or the corresponding amounts of ELR nanoparticles. Thus, cell proliferation rate was measured every 4 hours by performing a cell confluence analysis, which allowed us to determine a real-time trend, rather than other studies every 24 hours, which are unable to determine the accurate time of a change. Drug concentration was chosen in light of the results shown in Figure 3, where it can be seen that 1 µM DTX-loaded NPs-RGD+DTX were more effective after 24 hours treatment than free DTX in breast cancer cells and not in HUVEC cells. As such, cell proliferation assays were carried out over 72 hours in order to determine the effect of DTX-loaded nanoparticles during several cell divisions.

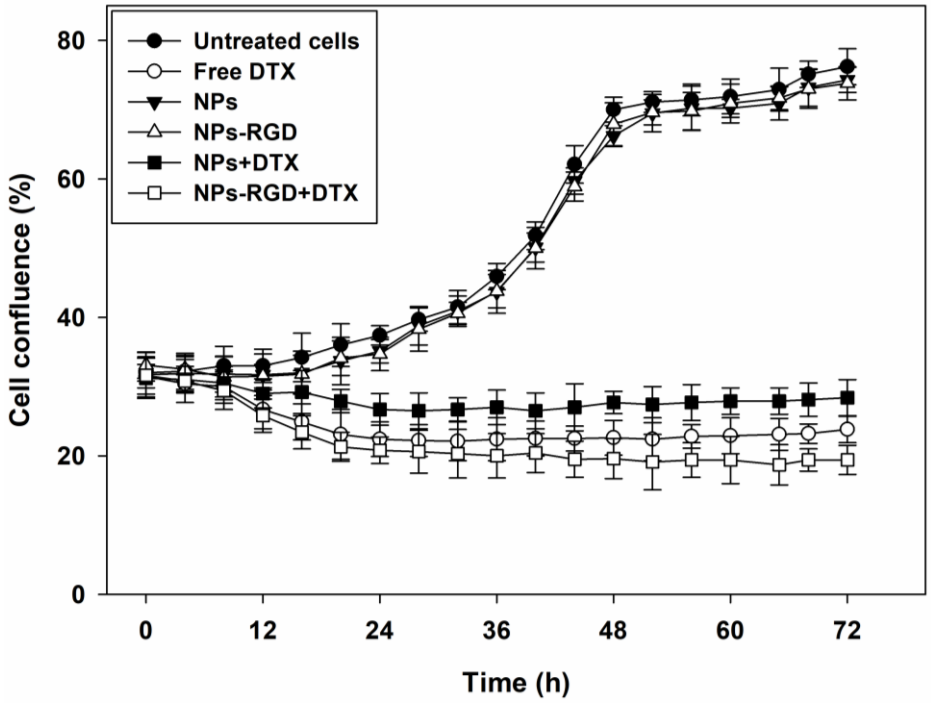

Figure 4. Effect of ELR nanoparticles in cell proliferation of MDA-MB-231 analyzed by cell confluence measurements. Cells were incubated with free 1 µM DTX, empty ELR nanoparticles or 1 µM DTX-loaded ELR nanoparticles for 72 hours and confluence was measured using OMNI software. Values are given as mean ± SD. Three independent experiments, each in triplicate, were performed.

As can be seen from Figure 4, empty ELR nanoparticles, either with or without the RGD sequence NPs-RGD and NPs, respectively), lacked any effect on cell proliferation and exhibited similar values to those from untreated cells. With regard to the trend in cell proliferation, breast cancer cells seemed to start growing in an exponential mode after 12 hours, with cell proliferation ceasing after 48 hours and remaining stable up to 72 hours. This final stabilized period with no proliferation could be due to a limitation of the nutrients available in the culture medium after 3 days of highly proliferative growth.

However, when cancer cells were treated with 1 µM free DTX, cell proliferation stopped after 12 hours of treatment and remained so up to 72 hours. As explained above (Figure 3), when MDA-MB-231 cancer cells were treated with 1 µM free DTX, the cell viability after 24 hours was only 25%. As cell proliferation was not enhanced at any time point, this could be due to the fact that the cancer cells were dead and that the very low percentage of living cells present were unable to proliferate. Interestingly, the same effect on proliferation was observed when cancer cells were treated with 1 µM DTX-loaded nanoparticles lacking the RGD sequence (NPs+DTX). It should be noted that these

nanoparticles not only improved the effect of DTX but also this cell proliferation was higher when compared with cells treated with free DTX. This result corroborated the finding whereby encapsulation of the drug in ELR nanoparticles lacking the RGD (NPs+DTX) sequence diminishes the effect of the chemotherapeutic agent on cells, as was also seen in terms of cell viability (Figure 3). Furthermore, when breast cancer cells were treated with 1 µM DTX-loaded nanoparticles containing the RGD sequence (NPs-RGD+DTX), cell proliferation was completely halted and exhibited even lower values compared to cells treated with free DTX. This result is in agreement with the results in Figure 3, which shows that DTX-loaded nanoparticles containing the RGD sequence (NPs-RGD+DTX) enhance the cytotoxic effect of free DTX on cells. Thus, we can conclude that DTX provokes cell death and that surviving cells are unable to proliferate, probably as a result of entering into a senescent state.

5.4.3.2 Akt-in nanoparticles directed by CD44 aptamer

5.4.3.2.1 DNA aptamer conjugation to ELR polymers

Although DTX encapsulation within ELR nanoparticles had shown promising results and RGD peptide has been widely used for active targeting in order to specifically drive therapeutic systems to cancer cells, there is some controversy about using RGD as targeting system for cancer treatment. Even if recognized by the majority of tumor cells, up to eight human integrin dimers (αvβ1, αvβ3, αvβ5, αvβ6, αvβ8, α5β1, α8β1, and αIIbβ3) recognize the tripeptide RGD motif within ECM proteins [64]. Multiple molecules are used as targeting systems in order to improve the specific entry of nanoparticles in cancer cells and avoid undesired effects in non-cancer cells. We selected CD44, which is a membrane receptor overexpressed by colorectal cancer cells and is established as a tumor marker [30-32], as targeting molecule. For this reason, we covalently conjugated a DNA aptamer, specifically designed to interact with CD44 membrane receptor [41], to the ELR polymers.

Thus, we took advantage of previously described click chemistry [60, 65] and covalently linked the DNA aptamer to the ELR previously modified with PEG, which act as spacer between the aptamer and the polymer and thereby facilitate the interaction of the aptamer and the targeted receptor. Both control and Akt-in polymers were functionalized with NHS-PEG-Cyclooctine by amidation reaction between the ε-amine group from lysines

present in both ELR polymers and the activated carboxylic group as N-succinimidyl ester of NHS-PEG-Cyclooctine.

The proper binding of NHS-PEG-Cyclooctine was corroborated by ^{1}H-NMR (Figure 5), as new signals from PEG-Cyclooctyne appeared at 3.0 ppm (assigned to the methylene groups adjacent to the nitrogen of lysine thereby forming the new amide bond), 4.0 ppm (methylene group adjacent to carbamate and cyclopropyl group) and 7.0 ppm (H-N from carbamate). These three signals allowed us to appreciate the presence of NHS-PEG-Cyclooctine along the peptide chain.

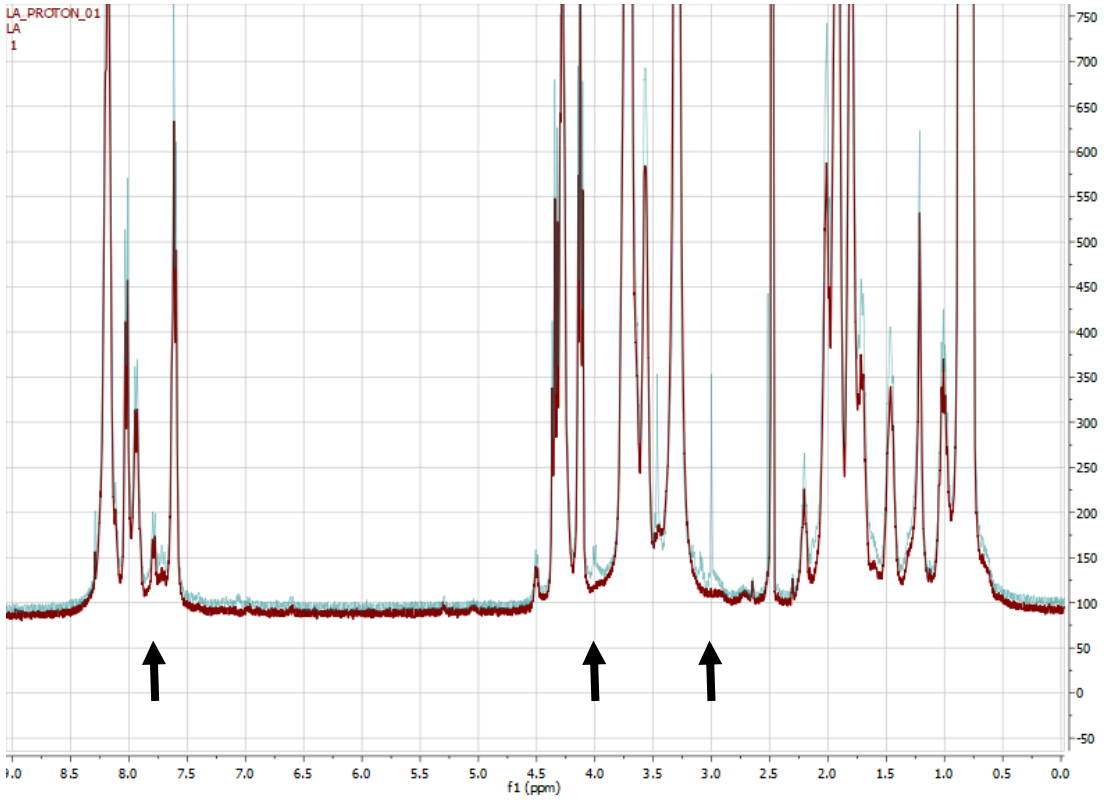

Figure 5. Chemical binding of NHS-PEG-Cyclooctine to Control polymer. Comparative of spectra of Control polymer (red spectrum) and Cyclooctine-PEG-Control polymer (blue spectrum). Black arrows indicate the three characteristic signals from PEG-Cyclooctine at 3.0, 4.0 and 7.0 ppm, which are only present in the Cyclooctine-PEG-Control polymer (blue spectrum).

Even though previous experience with click chemistry showed high levels of substitution [60], the presence of the DNA aptamer was estimated by measuring the absorbance at 260 nm. As can be seen in Figure 6, the absorbance of non-targeted ELR polymers (Control and Akt-in) was almost 0, whereas targeted polymers (tControl and tAkt-in)

showed almost 0.6 absorbance values. Thus, these results confirmed that the DNA aptamer was successfully conjugated to ELR polymers.

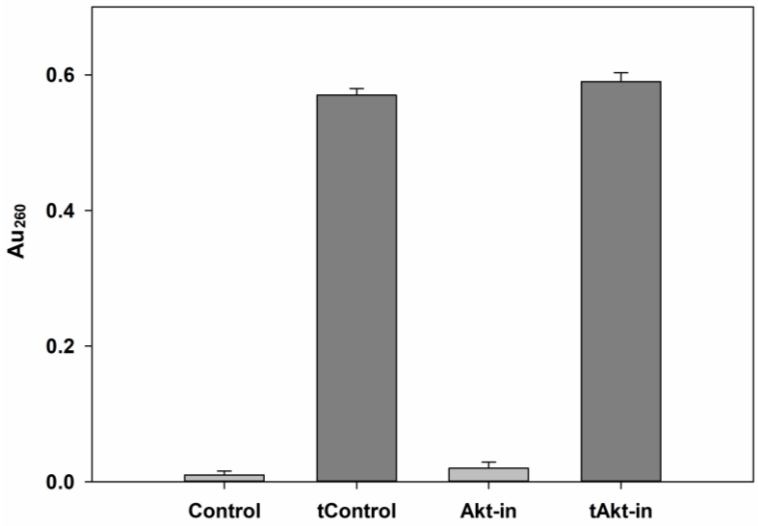

Figure 6. Analysis of aptamer conjugation to Cyclooctine-PEG-polymers. The ELR polymers with (dark bars) and without (light bars) DNA aptamer against CD44 were dissolved at 1 mg/mL in ultrapure water and UV absorption of DNA at 260 nm was measured. n = 3 independent experiments, mean ± SD.

5.4.3.2.2 Internalization effect of DNA aptamer

The proper bioactivity of attached DNA aptamer was determined by cell proliferation assays (Figures 7 and 8). Thus, human colorectal cancer (Caco-2) and endothelial cells (HUVEC) were incubated with previously described ELR-based nanoparticles carrying Akt inhibitor [66], with the DNA aptamers anchored to the corona (Control and Akt-in tNPs) and without that targeting system (Control and Akt-in NPs). These smart nanoparticles provoked apoptosis-mediated cell death, so we hypothesized that targeted nanoparticles would enter into the cells faster and, as a consequence, the cytotoxic effect of Akt inhibitor would be observed at earlier times. CD44 receptor is overexpressed in the membrane of colorectal cancer cells and, in fact, it is considered a cancer marker [30-32]. The different expression of the targeted receptor in cancer cells, when compared to non-cancer cells, could be a promising approach in order to achieve selective internalization and consequent cytotoxicity only in such targeted cells.

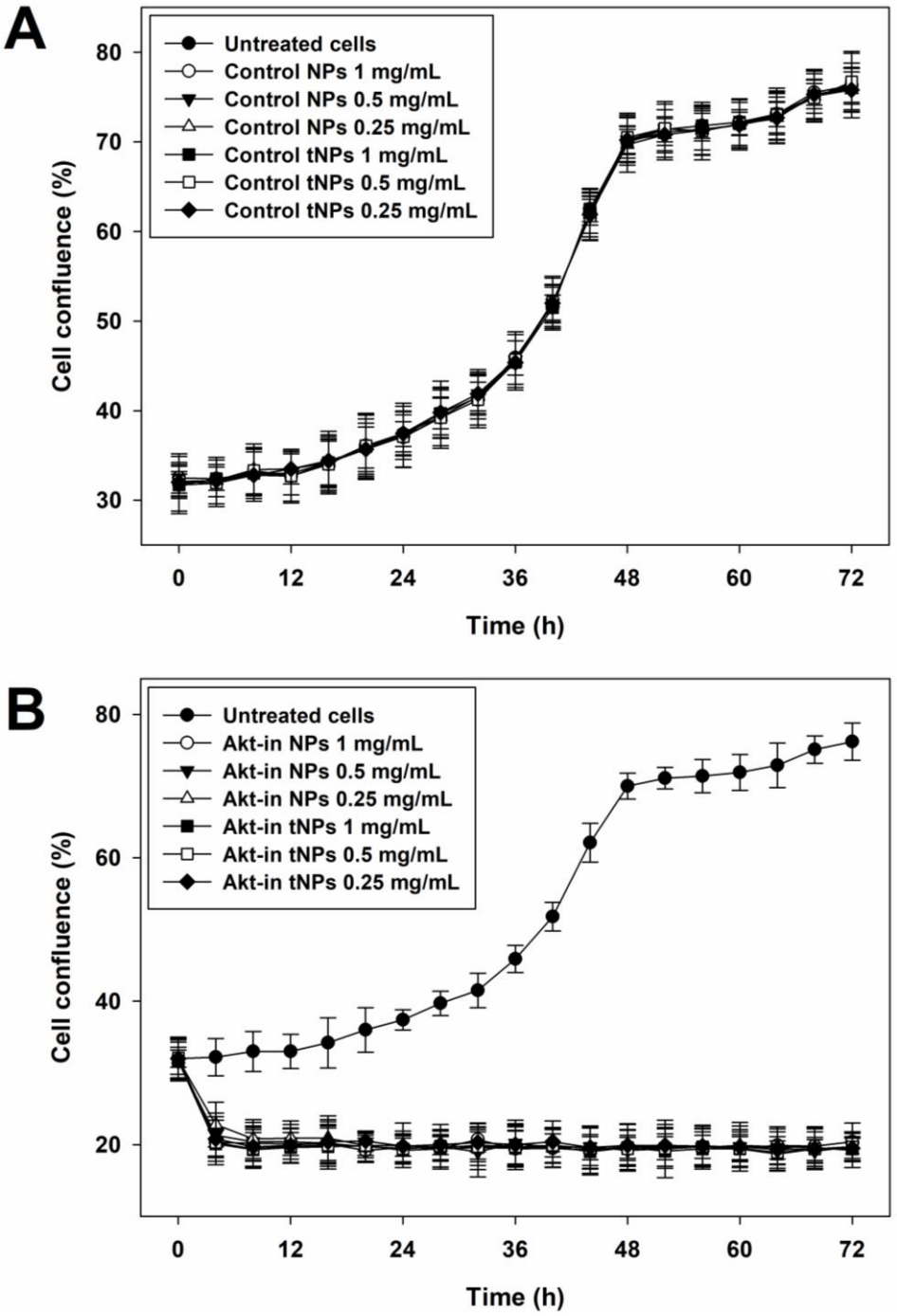

Figure 7. Effect of targeted ELR nanoparticles in Caco-2 cells proliferation analyzed by cell confluence measurements. Cells were incubated with control (A) or Akt-in (B) nanoparticles for 72 hours and confluence was measured by using OMNI software. Both untargeted (Control NPs and Akt-in NPs) and targeted (Control tNPs and Akt-in tNPs) nanodevices were used. Confluence percentages were determined each 4 hours. Values are given as mean ± SD. Three independent experiments, each in triplicate, were performed.

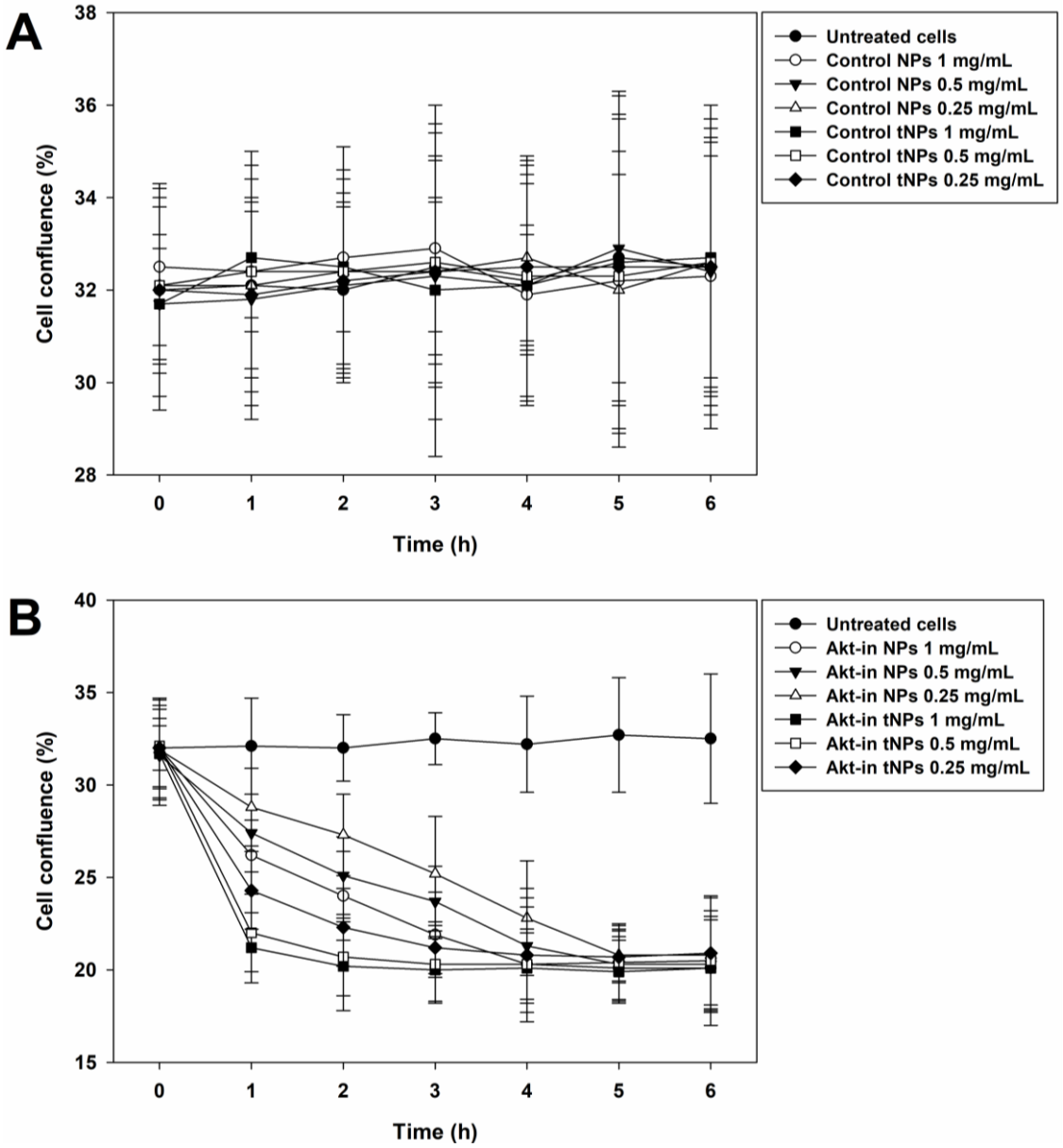

Figure 8. Effect of targeted ELR nanoparticles in Caco-2 cells proliferation analyzed by cell confluence measurements. Cells were incubated with control (A) or Akt-in (B) nanoparticles and confluence was measured by using OMNI software. Both untargeted (Control NPs and Akt-in NPs) and targeted (Control tNPs and Akt-in tNPs) nanodevices were used. Confluence percentages determined each hour during the first 6 hours. Values are given as mean ± SD. Three independent experiments, each in triplicate, were performed.

Control nanoparticles, with (Control tNPs) or without targeting system (Control NPs), were completely innocuous for both Caco-2 and HUVEC cells, as their proliferation was similar to untreated cells (Figures 7 and 8). These results demonstrated that the ELR structure did not have any cytotoxic effect and also that the internalization of the

nanoparticles neither affect cell viability even after the chemical reaction performed to attach the aptamer.

As expected, cell proliferation of Caco-2 colorectal cancer cells was dramatically affected when treated with nanoparticles carrying the Akt inhibitor (Akt-in NPs) (Figure 7). Furthermore, when incubated with ELR nanoparticles including the DNA aptamer attached to the corona (Akt-in tNPs), Caco-2 cell proliferation was affected earlier than those cells incubated with the same nanoparticles only lacking the targeting system against CD44 (Akt-in NPs). In fact, lower concentration (0.25 mg/mL) of targeted nanoparticles (Akt-in tNPs), was more effective than the highest concentration (1 mg/mL) of untargeted nanoparticles (Akt-in NPs) in terms of cell proliferation inhibition. This result confirmed the fact that DNA aptamer against CD44 was properly effective in terms of nanoparticles internalization in colorectal cancer cells. On the other hand, although HUVEC cells seemed to be slightly affected by nanoparticles with the Akt inhibitor at very early time points independently of the presence of the targeting system, most of cells were able to keep proliferating in a similar manner than untreated cells (Figures 9 and 10). This observed effect could be due to the fact that few cells internalized ELR-based nanoparticles and then the rest of the cell culture was able to properly proliferate.

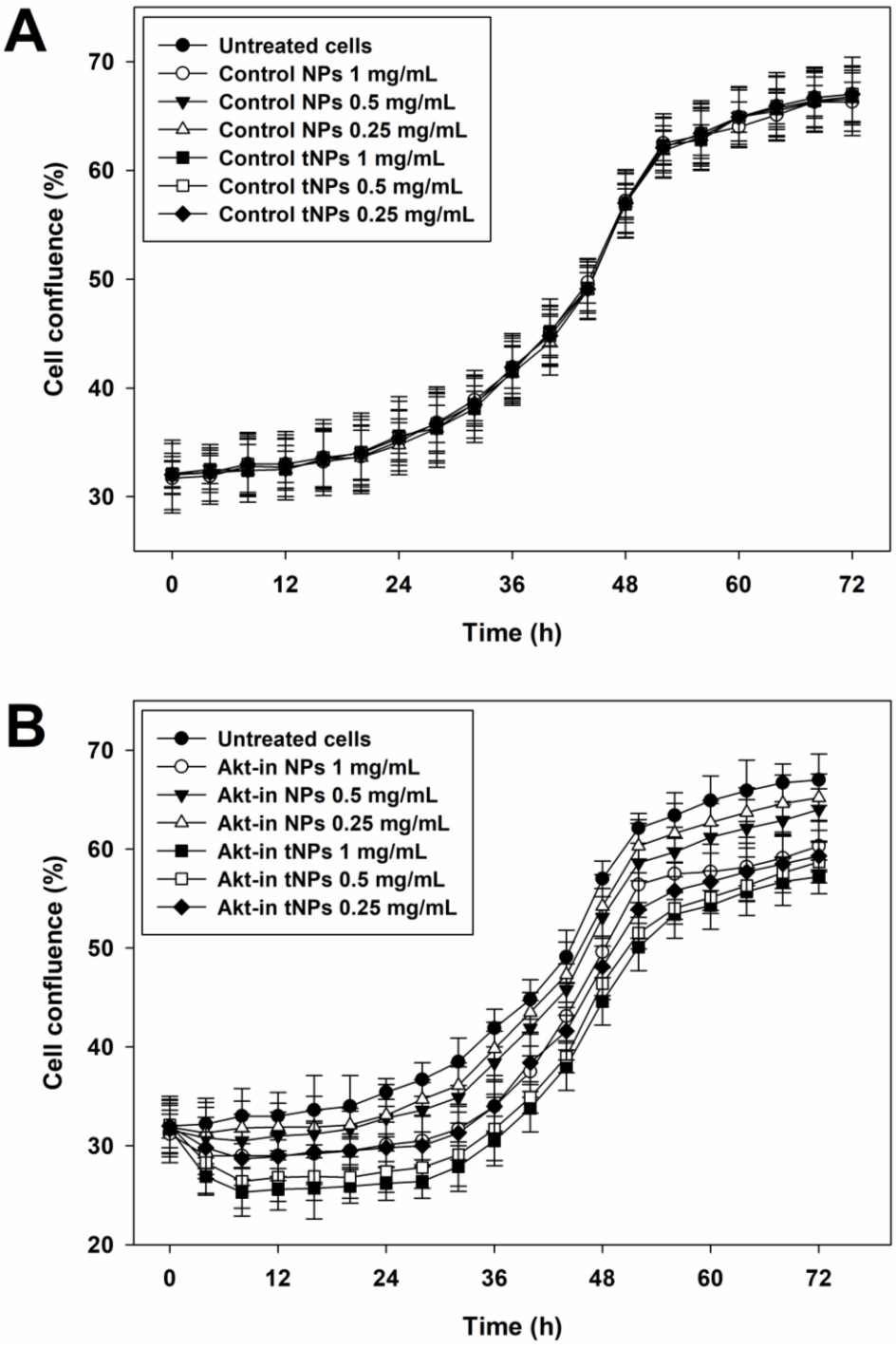

Figure 9. Effect of targeted ELR nanoparticles in HUVEC cells proliferation analyzed by cell confluence measurements. Cells were incubated with control (A) or Akt-in (B) nanoparticles at three different concentrations for 72 hours and confluence was measured by using OMNI software. Both untargeted (Control NPs and Akt-in NPs) and targeted (Control tNPs and Akt-in tNPs) nanodevices were used. Confluence percentages were determined each 4 hours. Values are given as mean ± SD. Three independent experiments, each in triplicate, were performed.

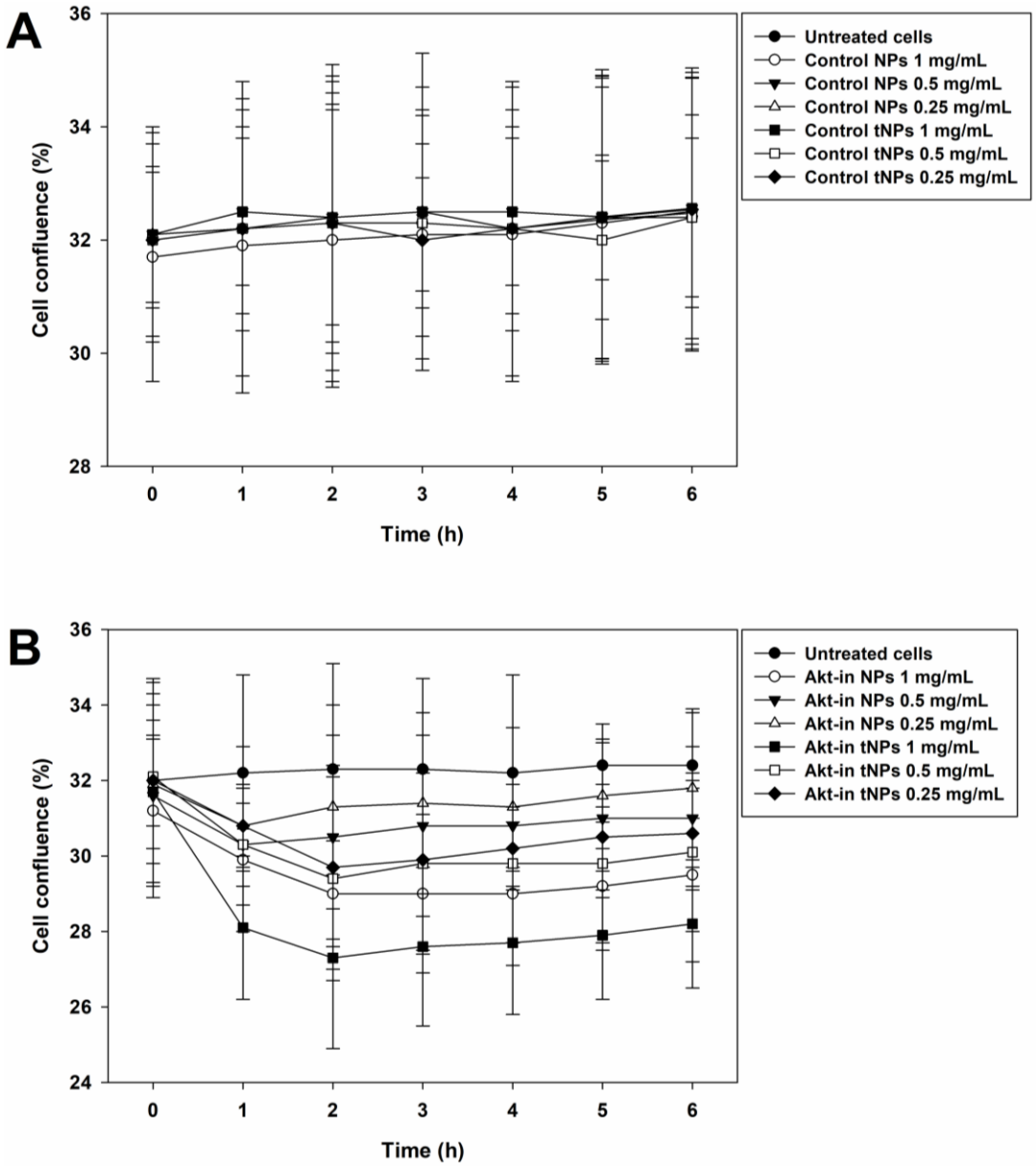

Figure 10. Effect of targeted ELR nanoparticles in HUVEC cells proliferation analyzed by cell confluence measurements. Cells were incubated with control (A) or Akt-in (B) nanoparticles and confluence was measured by using OMNI software. Both untargeted (Control and Akt-in NPs) and targeted nanoparticles (Control and Akt-in tNPs) were used. Confluence percentages determined each hour during the first 6 hours. Values are given as mean ± SD. Three independent experiments, each in triplicate, were performed.

Therefore, we could conclude that the chemical linking of the DNA aptamer targeted against CD44 to the nanoparticles corona not only improved the cytotoxic action of the therapeutic nanodevices in targeted cancer cells, but also helped to specifically affect to colorectal cancer cells and therefore avoid further undesired effects in non-cancer cells.

5.4.3.3 Dual approach ELR nanohybrids

5.4.3.3.1 Design of ELR hybrid nanosystems

In Chapter 2 and previous sections 3.1 and 3.2 we developed two different therapeutic nanodevices in order to specifically tackle cancer cells by unlocking apoptotic pathway blocked by Akt kinase and, on the other hand, by properly releasing antimitotic drug in cancer cells. Thus, we demonstrated that both types of nanoparticles had reduced cytotoxic effect in non-cancer cells, which is one of the most important requirements when working with novel target therapeutic agents, and therefore a therapeutic window was determined.

However, cancer is a complex disease with high variability between cell populations within a tumor. For this reason, accurate therapies are based on combination of multiple strategies in order to attack cancer cells by different ways, such as surgery, radiotherapy, chemotherapy or immunotherapy. Due to drug encapsulation is an encouraging strategy aimed to develop new therapeutic treatments, we designed novel hybrid ELR nanodevices in order to develop a dual approach drug delivery system (Figure 11). The nomenclature depicted in Figure 11 will be used hereafter. Thus, this strategy would combine two different therapeutic agents in the same vehicle to tackle tumor growth by two ways: inhibition of Akt phosphorylation (apoptosis trigger) and DTX encapsulation (antimitotic effect). For this purpose, we used the previously described (Chapter 2) recombinamers consisting on an amphiphilic ELR backbone including several bioactive sequences in order to properly deliver a small peptide Akt inhibitor [66]. As previously described, this ELR polymer was able to self-assemble into highly monodisperse nanoparticles able to internalize by clathrin-mediated endocytosis into cancer cells and properly deliver the Akt inhibitor in the cell cytoplasm. There, the inhibitor blocked Akt phosphorylation and consequent activation, thereby triggering apoptosis-mediated cell death [66]. Secondly, we used the ELR polymer based on an amphiphilic tetrablock previously described in section 3.1 and prior works from the group [51, 52]. This ELR-based construct was able to encapsulate DTX and diminish cancer cell viability (Section 3.1). The block composition of the designed hybrid ELR polymers is depicted in Figure 11 and Table 1.

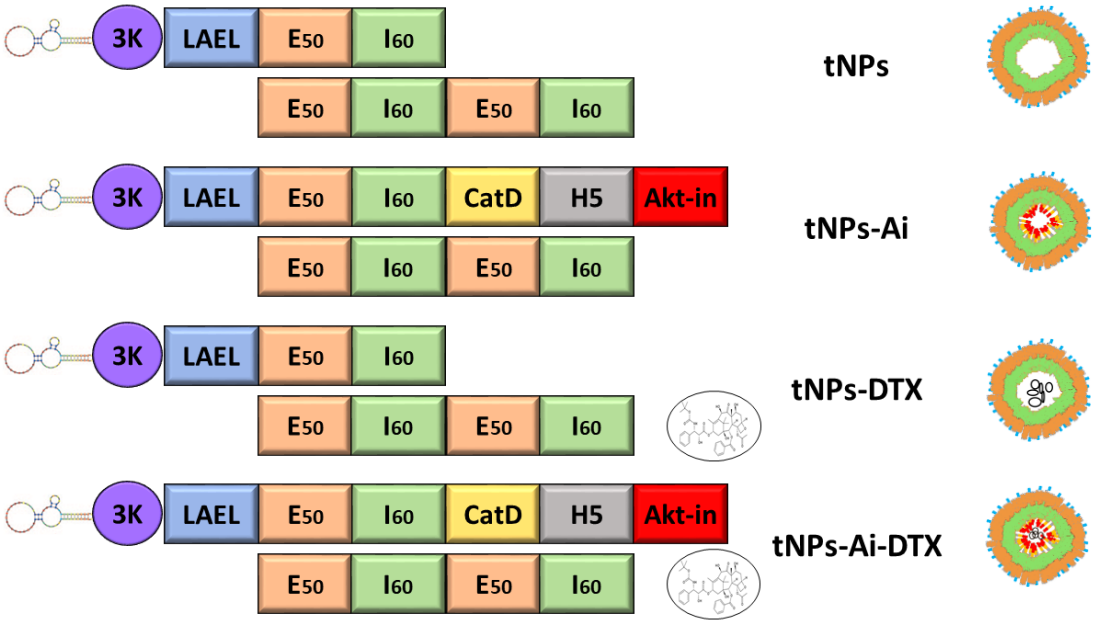

Figure 11. Composition of hybrid ELR-based targeted nanoparticles (tNPs) (i.e. including the anti-CD44 aptamer): **tNPs**: targeted nanoparticles tNPs without therapeutic molecules as negative control; **tNPs-Ai**: nanodevices containing the Akt inhibitor able to induce apoptosis in cancer cells; **tNPs-DTX**: antimitotic drug DTX encapsulated within nanodevices; **tNPs-Ai-DTX**: nanodevices involving both therapeutic agents Akt inhibitor and DTX. Non scaled scheme.

In this new approach, ELR hybrid polymers were specifically targeted to CD44 membrane receptor. Thus, taking advantage of this cancer marker could be an accurate strategy in order to specifically release both Akt inhibitor and DTX within cancer cells.

Therefore, we hypothesized that, taking advantage of SAS process, we could develop novel hybrid ELR-based devices in order to treat colorectal cancer cells by two different therapeutic approaches: the Akt inhibitor and encapsulated DTX.

Table 1. Amino acid sequences of the different blocks forming hybrid ELR polymers.

3K	LAEL	E_{50}	I_{60}	CatD	H5	Akt-in
MGKK KPV	$(LAEL)_3$	$[(VPGVG)_2 (VPGEG) (VPGVG)_2]_{10}$	$[VGIPG]_{60}$	VQEY VYD	LFHAIA HFHIHG GWHGL IHGWY	AVTDH PDRLW AWERF

5.4.3.3.2 Physicochemical characterization of ELR nanohybrids

The hybrid polymers were developed in collaboration with the High Pressure Process Group from BioEcoUVa Research Institute on Bioeconomy at the University of

Valladolid by supercritical antisolvent process (SAS) [49]. Thus, this technique allowed us to encapsulate highly hydrophobic DTX within ELR-based nanohybrids.

ELRs are characterized by their thermosensitivity [67, 68], which allows them to be a promising alternative for the development of biomedical applications, such as drug delivery devices. Thus, the self-assembling availability of ELR-based polymers with lower Tt than the physiological temperature is extremely important for the formation of drug delivery devices within the human body.

The thermal behavior of the hybrid ELR polymers was determined by means of turbidimetric spectrometry in PBS [49]. All the polymers showed a Tt between 15 and 16°C and there were no significant differences between them. As previously demonstrated [66], the presence of bioactive sequences, such as the CatD recognition sequence, H5 peptide and Akt inhibitor, did not alter the Tt of the polymers. Furthermore, encapsulated DTX neither affected the thermal properties of ELR polymers and the Tt was similar to polymers without DTX. The observed transition corresponds to the hydrophobic blocks forming the inner core, as glutamic acid blocks are not able to self-assemble. Due to the fact that Tt were lower than body temperature, results pointed these ELR constructs as suitable devices for biomedical applications.

As explained in Chapter 2 section 3.3, the application of nanotechnology for cancer treatment explores the characteristic abnormalities of tumors, such as hypervascularization, aberrant vascular architecture, high production of vascular permeability factors, and deficient lymphatic drainage [13]. For these reasons, nanodevices are able to enter into tumors without proper removal and, as a consequence, they remain retained within the tumors. Due to the enhanced permeability and retention effect (EPR), nanodrugs are accumulated within the tumors and thereby show higher accumulation and concentration compared to other organs with normal vasculature [13]. ELR polymers were able to form nanodevices of size between 52 (tNPs-Ai and tNPs-Ai-DTX) and 67 nm (tNPs-DTX), as described by Vallejo [49]. Moreover, DLS assays showed that the nanohybrids size did not change after longer times [49], so we can conclude that our nanodevices remained stable over time. Size and morphology of ELR-

based nanohybrids were corroborated by TEM images (Figure 12). Thus, developed hybrid ELR-based polymers met all the requirements in terms of size, as explained above.

After systematically administration, interaction with plasmatic proteins affect nanoparticles fate in the blood torrent. Thus, ELR-based nanohybrids were incubated with BSA for 1 hour, as albumin is the major plasmatic protein. Results showed no differences when incubated with BSA (Table 2), so we can conclude that ELR nanohybrids seemed to remain stable under physiologic conditions.

Table 2. Characterization of ELR nanohybrids. Size and polydispersity index (PdI) of nanohybrids dissolved in PBS or PBS + 5% BSA measured by dynamic light scattering (DLS). Surface charge of self-assembled polymers dissolved in ultrapure water type I measured by dynamic light scattering (DLS). Mean ± SD.

Nanohybrid	**PBS**		**PBS + 5% BSA**		**ζ-potential (mV)**
	Size (nm)	**PdI**	**Size (nm)**	**PdI**	
tNPs	61.50 ± 2.26	0.201	62.30 ± 3.56	0.254	-31.3 ± 1.3
tNPs-Ai	52.10 ± 3.10	0.134	51.90 ± 1.90	0.168	-28.2 ± 2.2
tNPs-DTX	67.50 ± 1.30	0.178	68.60 ± 1.82	0.224	-28.6 ± 0.4
tNPs-Ai-DTX	52.14 ± 3.30	0.176	53.40 ± 2.79	0.212	-26.7 ± 0.4

As explained in Chapter 2 section 3.3, the surface charge of nanoparticles has great importance in terms of nanodevice stability and electrostatic interactions between nanoparticles and the cellular membrane [69-72]. Thus, ζ-potential was measured and all the constructs showed clearly negative surface charge (-28 mV in average), due to the presence of glutamic acid residues and attached DNA molecules at the nanohybrid corona (Table 2).

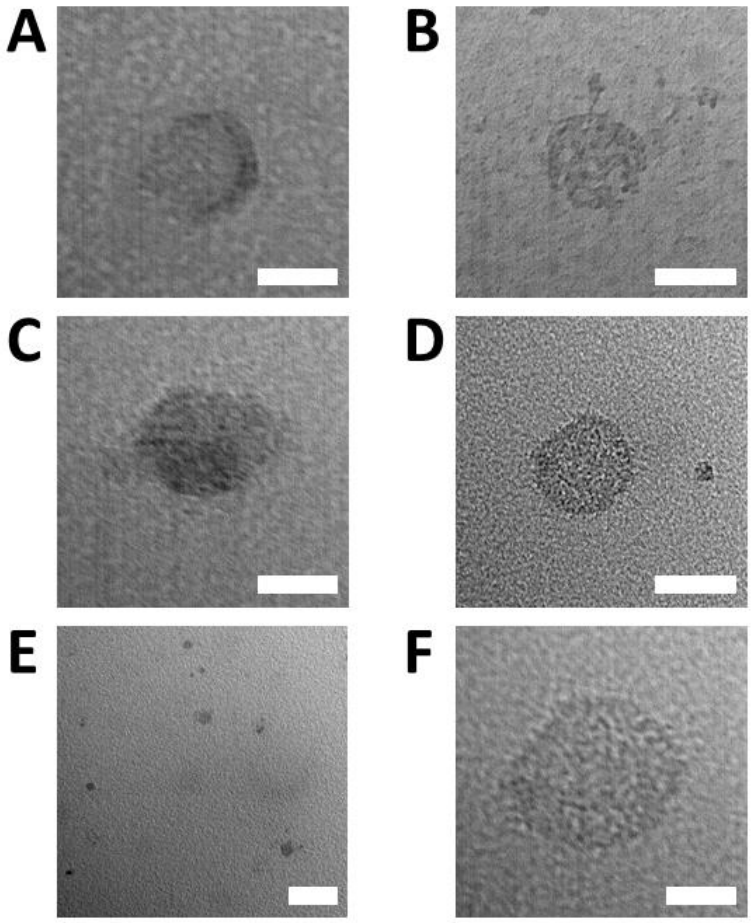

Figure 12. Representative TEM images of tNPs (A), tNPs-Ai (B), tNPs-DTX (C), tNPs-Ai-DTX (D). General view (E) and zoom (F) of tNPs-Ai-DTX nanohybrids. Scale bars are 50 nm (A-D), 200 nm (E) and 20 nm (F).

The proportion of each component within the nanohybrids was previously determined in the group by ^{1}H-NMR [49]. Thus, comparison of integrals of the signal for methyl groups from the ELR and protons in the aryl moieties from DTX allowed us to calculate the ELR and DTX ratio in each nanohybrid (Table 3).

Table 3. Characterization of ELR nanohybrids. Proportion of components within the nanohybrids measured by ^{1}H-NMR.

Nanohybrid	Proportion (%)	
	ELR	DTX
tNPs	98.1	-
tNPs-Ai	98.1	-
tNPs-DTX	53.3	44.17
tNPs-Ai-DTX	50.0	49.08

5.4.3.3.3 Effect of ELR nanohybrids in cell proliferation

The effect of ELR nanohybrids in cell proliferation was determined *in vitro* (Figures 13 and 14). Thus, colorectal cancer Caco-2 cells and endothelial HUVEC cells were incubated with 1 µM free DTX or the corresponding amounts of ELR-based nanohybrids for 72 hours. Real-time proliferation was analyzed by determining the cell confluence every 4 hours. The DTX concentration was chosen in light of the results from previous studies.

As in the previous experiments, ELR nanohybrids (tNPs) only composed by the amphiphilic ELR backbone with no therapeutic agents were absolutely innocuous for either colorectal cancer either non-cancer cells.

Contrary, results showed that cell proliferation of colorectal cancer cells treated with 1 µM free DTX stopped after 12 hours (Figure 13). This effect was also observed after incubation with the same concentration of encapsulated DTX (tNPs-DTX). On the other hand, ELR nanohybrid only carrying Akt inhibitor (tNPs-Ai) affected cell proliferation at earlier points. Moreover, this fast effect in cell proliferation was also observed when cancer cells were incubated with ELR-based nanohybrids carrying both Akt inhibitor and DTX (tNPs-Ai-DTX). Thus, results showed that the effect of Akt inhibitor was faster than chemotherapeutic agent DTX, which was in accordance to previous data.

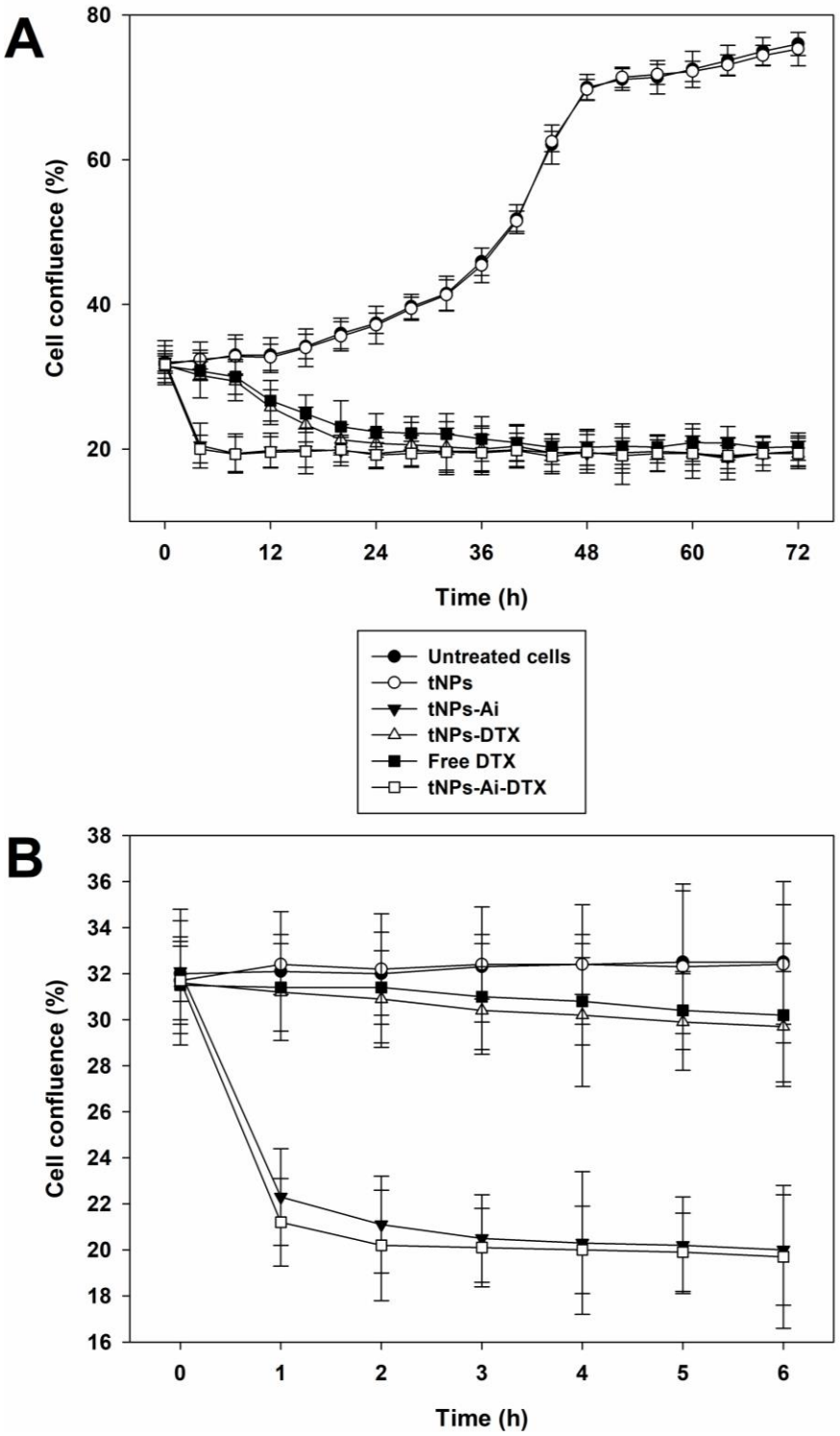

Figure 13. Effect of ELR nanohybrids in Caco-2 cells proliferation analyzed by cell confluence measurements. Cells were incubated with free DTX or ELR nanohybrids for 72 hours and confluence was measured by using OMNI software. A: Confluence percentages were determined each 4 hours. B: Additional confluence percentages were determined each hour during the first 6 hours. Values are given as mean ± SD. Three independent experiments, each in triplicate, were performed.

Cell proliferation of endothelial HUVEC cells was also determined (Figure 14). When cells were treated with tNPs, cell proliferation was not affected and results showed similar values to untreated cells. Also, ELR-based nanohybrids only carrying Akt inhibitor (tNPs-Ai) slightly affected cell proliferation. This result could be explained by the fact that a reduced number of nanohybrids was able to enter into endothelial cells compared to cancer cells (Figure 13), which overexpress CD44 and better internalize ELR nanohybrids. This result also demonstrated the proper action of the cancer-specific targeting system. Contrary, free DTX dramatically affected cell proliferation of non-cancer cells. This result confirmed the main problem inherent to most chemotherapeutic agents currently used: their effect is not selective for cancer cells. Docetaxel is an antimitotic drug, so it has enhanced effect in cancer cells as they possess aberrantly enhanced cell division, but its effect also affects non-cancer cells. Moreover, encapsulated DTX within ELR nanohybrids (tNPs-DTX) affected cell proliferation of endothelial cells. Although targeted nanohybrids were not able to enter into non-cancer cells, DTX was released to the culture medium and, as a consequence, the antimitotic drug acted. Furthermore, the proper action of DNA aptamer against CD44 could be appreciated when compared the effect of ELR nanohybrids in cell proliferation of Caco-2 (Figure 13) and HUVEC cells (Figure 14). Thus, when incubated with either tNPs-DTX either tNPs-Ai-DTX, cell proliferation was altered at earlier time points in colorectal cancer cells compared to endothelial ones. Finally, when HUVEC cells were incubated with combined therapy within hybrid nanodevices (tNPs-Ai-DTX), the effect in cell proliferation was similar to those cells treated with tNPs-DTX due to the presence of DTX in the culture medium. Together, these results confirmed that the incorporation of DNA aptamer, specifically targeted to CD44 receptor, enhanced the nanohybrids internalization by colorectal cancer cells, which overexpress CD44 receptor in their plasmatic membrane.

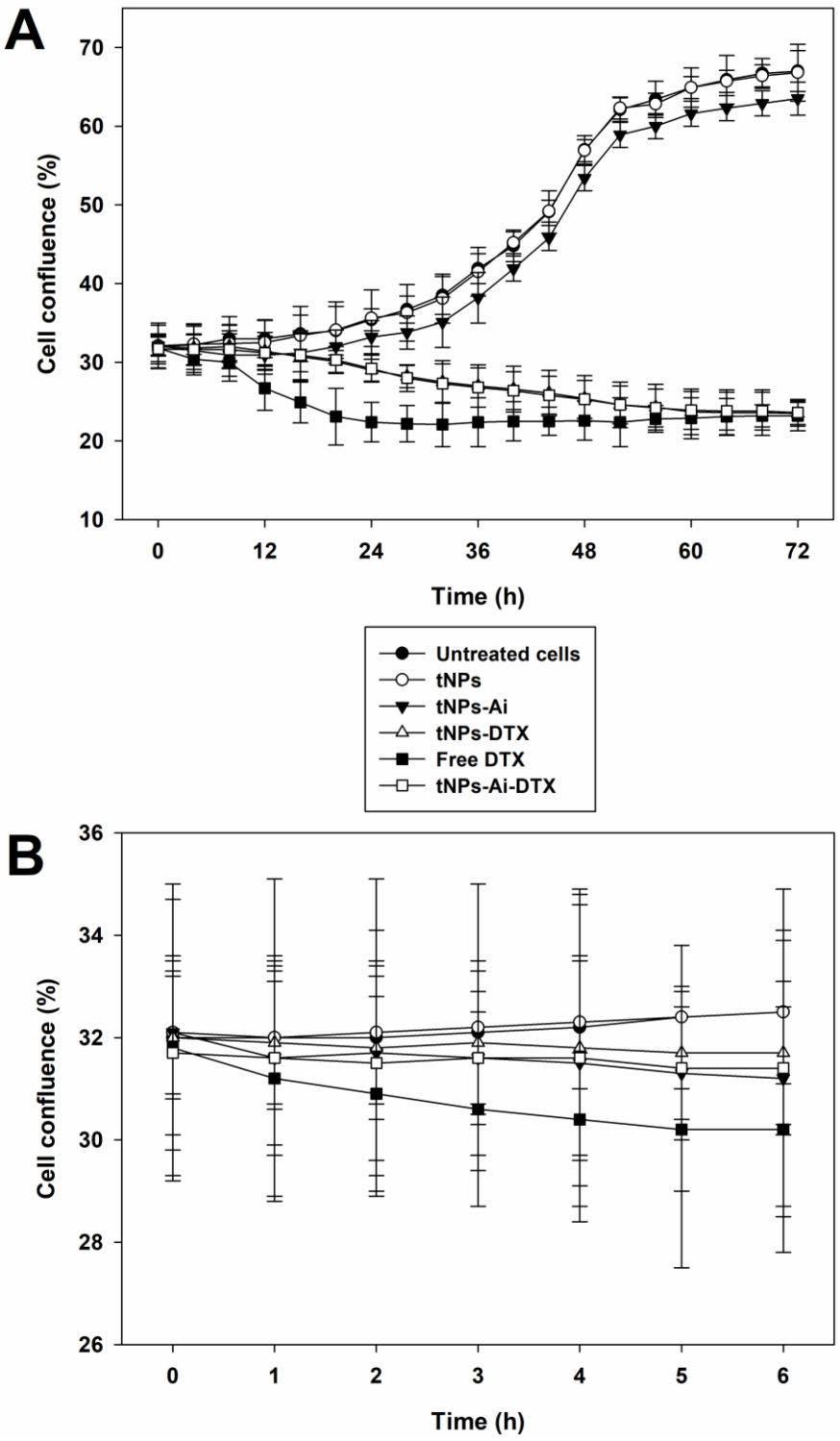

Figure 14. Effect of ELR nanohybrids in endothelial HUVEC cells proliferation analyzed by cell confluence measurements. Cells were incubated with free DTX or ELR nanohybrids for 72 hours and confluence was measured by using OMNI software. A: Confluence percentages were determined each 4 hours. B: Additional confluence percentages were determined each hour during the first 6 hours. Values are given as mean ± SD. Three independent experiments, each in triplicate, were performed.

We can therefore conclude that colorectal cells are unable to proliferate after treatment with ELR nanohybrids combining both Akt inhibitor and DTX. Moreover, the therapeutic action of the dual approach nanodevice seemed to be faster than encapsulated DTX alone.

5.4.3.3.4 Specific cytotoxicity of ELR nanohybrids

Once determined the effect of ELR nanohybrids in cell proliferation, we studied the specific cytotoxicity of nanodevices in Caco-2 colorectal cancer cells (Figure 15). We studied two different incubation times, 30 minutes and 24 hours, based on proliferation assays described above and previous works regarding the time-related drug's efficacy, as the effect of Akt inhibitor was much faster than chemotherapeutic DTX drug. First of all, we determined the cytotoxic effect of control empty nanohybrids (tNPs). Results showed that incubation with control nanohybrids did not affect Caco-2 viability after either short or prolonged incubation time.

Contrary, when Caco-2 cells were incubated with nanohybrids only carrying Akt inhibitor (tNPs-Ai), cell viability was decreased to 35% and 2.5% after incubation for 30 minutes and 24 hours, respectively (Figure 15). These results corroborated the fast internalization of ELR-based nanodevices due to the presence of the targeting DNA aptamer. Furthermore, cell viability only decreased to 90% after incubation with DTX-loaded nanohybrids (tNPs-DTX) for 30 min. However, when the incubation time was longer (24 hours), encapsulated DTX decreased cell viability to 8.5%. Encapsulation of DTX within ELR nanodevices seemed to improve the cytotoxic effect in colorectal cancer cells, as free DTX only decreased cell viability to 94.5% and 32% after 30 minutes and 24 hours, respectively. These results also corroborated the proper internalization of DTX due to the CD44 targeting system. Interestingly, the combination of Akt inhibitor and DTX within ELR nanohybrids (tNPs-Ai-DTX) seemed to have a strong effect and cell viability of Caco-2 decreased to 29.8% and 2.7% after 30 minutes and 24 hours treatment, respectively. Moreover, the effect of hybrid ELR nanodevices combining both therapeutic agents was statistically significant compared to nanohybrids only carrying Akt-in (30 min) or encapsulated DTX (30 min and 24 h). Thus, results demonstrated that combination of Akt inhibitor and DTX has a synergic effect in cell viability in Caco-2 cells. Furthermore, both therapeutic agents seemed to act by different pathways as they needed very different incubation times.

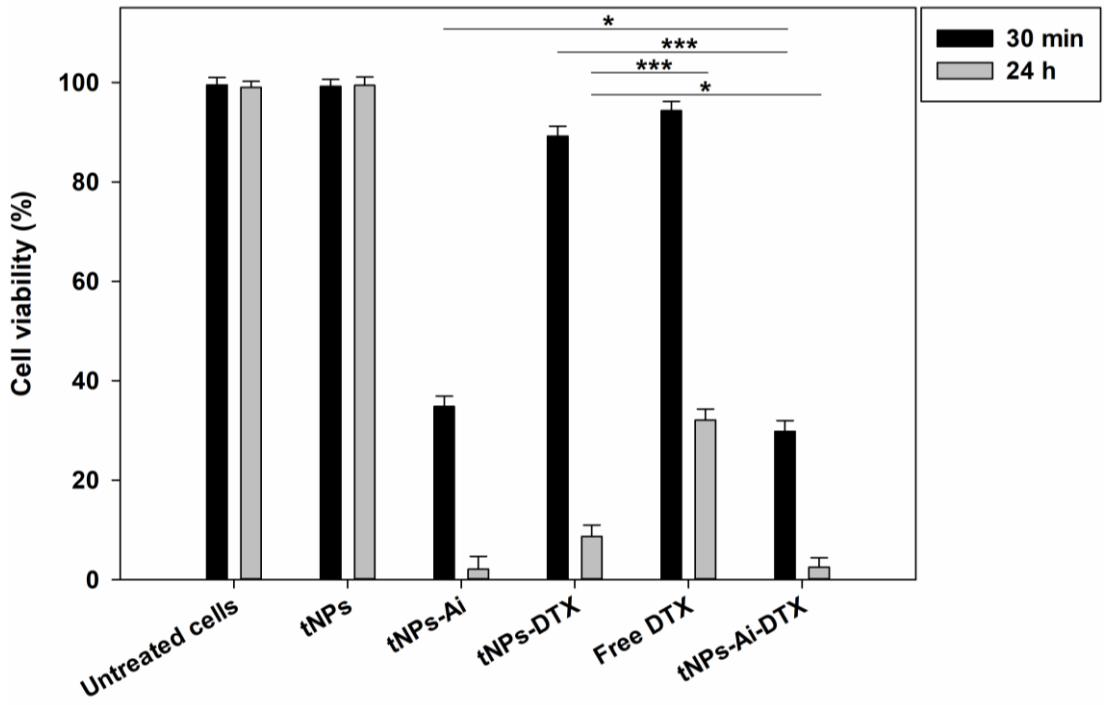

Figure 15. Effect of ELR nanohybrids in Caco-2 colorectal cancer cells viability. Cells were incubated with 1 μM free DTX or ELR nanohybrids at the corresponding normalized concentrations for 30 min (black bars) or 24 hours (grey bars) and viability was measured using the LIVE/DEAD Assay kit. Three independent experiments, each in triplicate, were performed. *p < 0.05, **p < 0.01, ***p < 0.001

5.4.3.3.5 Death pathway triggered by ELR nanohybrids

As both *in vitro* cell proliferation and viability assays showed that Akt-in and DTX had different temporal therapeutic trends, we hypothesized that it could be explained by the fact that the two therapeutic agents triggered different death pathways. We had previously demonstrated that ELR-based nanoparticles carrying Akt inhibitor triggered apoptosis-mediated cell death as the peptide inhibitor unlocked the apoptotic pathway blocked by Akt kinase [66]. Contrary, bibliography showed that DTX provokes not only apoptosis but also necrotic cell death [73-76]. For this reason, Caco-2 cells were incubated with therapeutic ELR nanohybrids and apoptotic and necrotic cell percentages were measured (Figure 16). When nanohybrids carrying Akt-in (tNPs-Ai) were used for early time points, 95% of cells died by apoptosis. However, cells incubated for 30 minutes with either free DTX either encapsulated DTX (tNPs-DTX) showed both types of cell death (60% apoptosis and 40% necrosis). Moreover, short incubation of Caco-2 cells with hybrid nanodevices carrying both Akt-in and DTX (tNPs-Ai-DTX) triggered 81% apoptosis and 19% necrosis. On the other hand, 93% of dead colorectal cancer cells corresponded to

necrotic cells, when incubated with nanohybrids only carrying Akt-in (tNPs-Ai) for 24 hours. This change from apoptosis to necrosis after longer treatments could be explained by the evolution of apoptotic cells to necrotic ones at longer times. Again, long incubation with free DTX or encapsulated DTX (tNPs-DTX) showed both apoptotic and necrotic cells, 57-59% and 43-41% respectively. Moreover, incubation with combined Akt inhibitor and DTX (tNPs-Ai-DTX) showed 97% of necrotic cells. This change between 30 minutes and 24 hours incubation could have two different explanations: First, early apoptosis state evolved to necrosis and, secondly, those cells surviving to Akt-in underwent necrosis triggered by DTX. Therefore, we could conclude that, as assumed, our ELR nanohybrids tNPs-Ai-DTX may lead two different therapeutic strategies, thereby involving two different approaches in order to treat colorectal cancer cells: apoptotic Akt inhibitor and DTX, which also triggered cell necrosis.

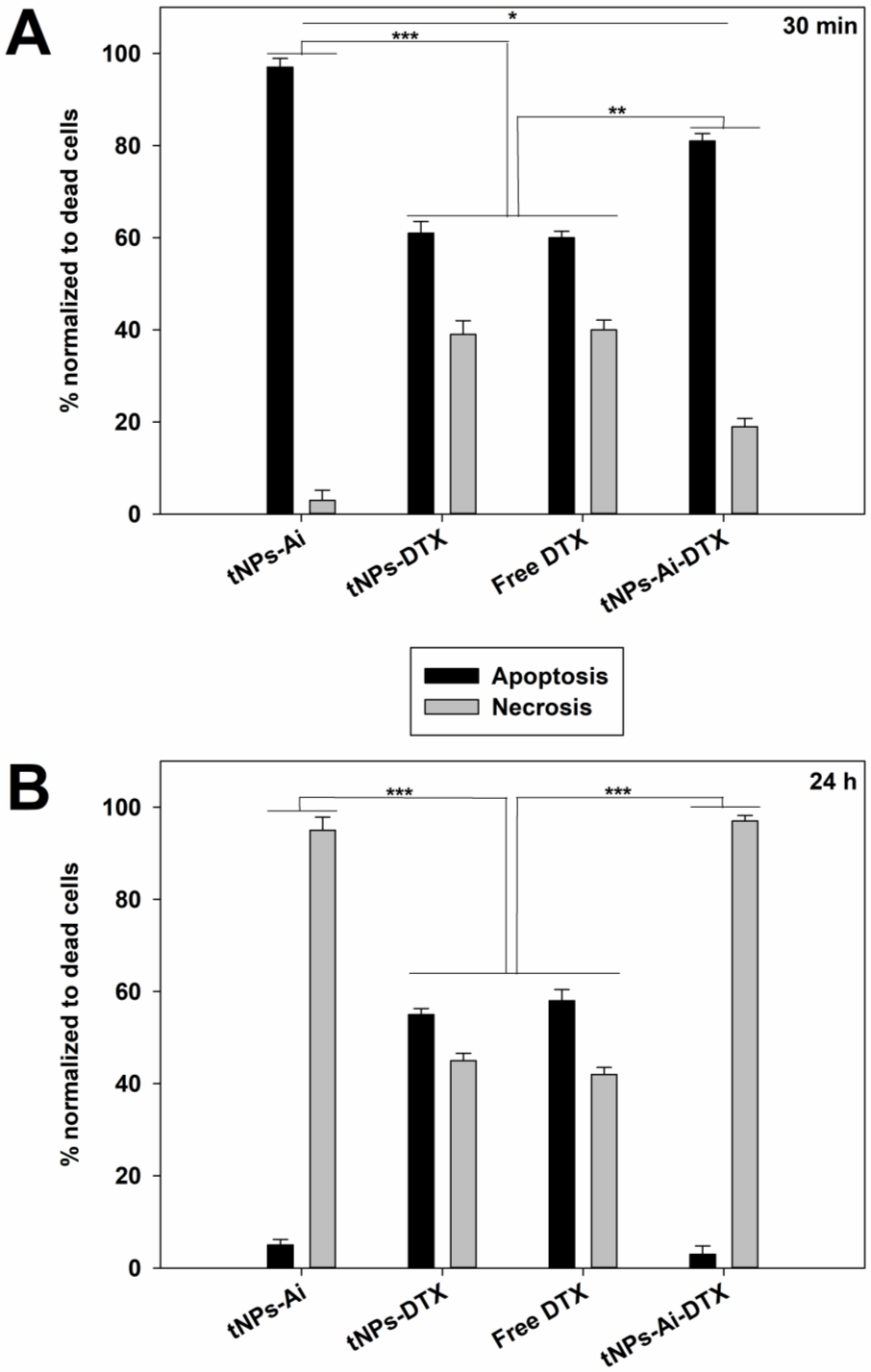

Figure 16. Cell-death pathways triggered by ELR nanohybrids in Caco-2 cells. Cells were incubated with 1 µM free DTX or nanohybrids at the corresponding normalized concentrations for 30 min (A) or 24 hours (B) and an apoptosis/necrosis assay was performed. Three independent experiments, each in triplicate, were performed. mean ± SD. *p < 0.05, **p < 0.01, ***p < 0.001

5.4.3.3.6 Effect of ELR nanohybrids in cell morphology

As explained in sections 3.3.4 and 3.3.5, ELR-based nanohybrids had specific cytotoxic effect in Caco-2 colorectal cancer cells. By taking advantage of confocal microscopy, we could determine changes in cell morphology when cancer cells were incubated with ELR

nanohybrid systems. For this reason, a novel ELR nanodevice was developed by SAS technique in collaboration with the High Pressure Process Group from BioEcoUVa Research Institute on Bioeconomy at the University of Valladolid, and included encapsulation of rhodamine within the nanohybrid core (tNPs-Ai-DTX-Rho). As shown in Figures 17 and 18, rhodamine-loaded ELR nanohybrids showed perinuclear localization and typical morphological changes from cell death could be appreciated, such as chromatin fragmentation or appearance of apoptotic vesicles.

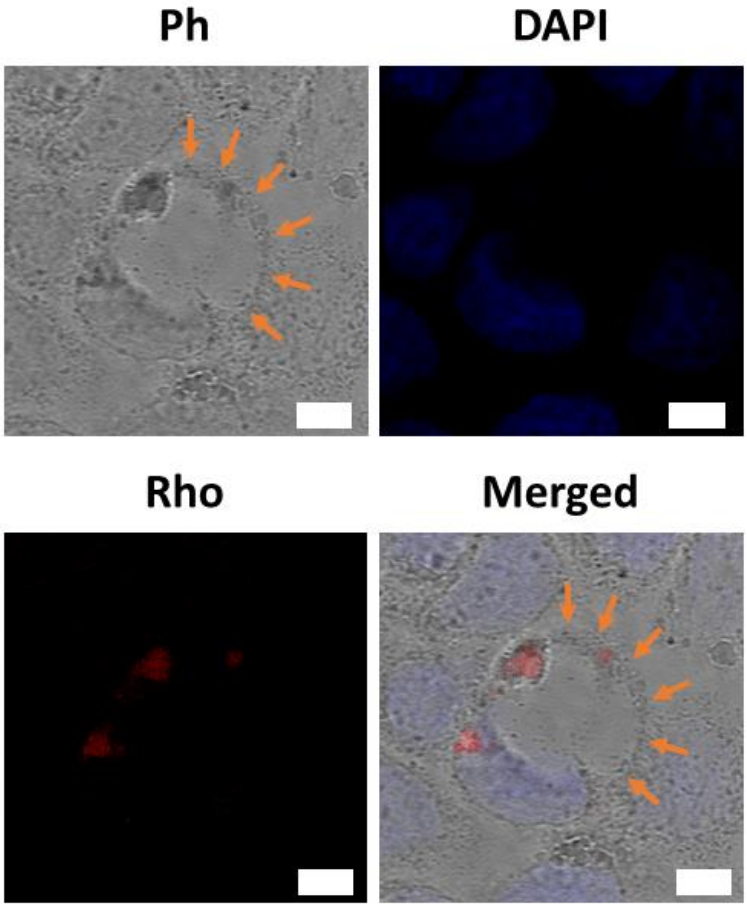

Figure 17. Representative confocal microscopy images of Caco-2 cells incubated with rhodamine-loaded nanohybrids. Cells were incubated with tNPs-Ai-DTX-Rho ELR nanohybrids for 1 hour. Fluorescence-field (DAPI and Rho), phase contrast (Ph) and merged images. Cell nuclei were stained with DAPI. Orange arrows indicate apoptotic vesicle. Scale bars: 10 µm.

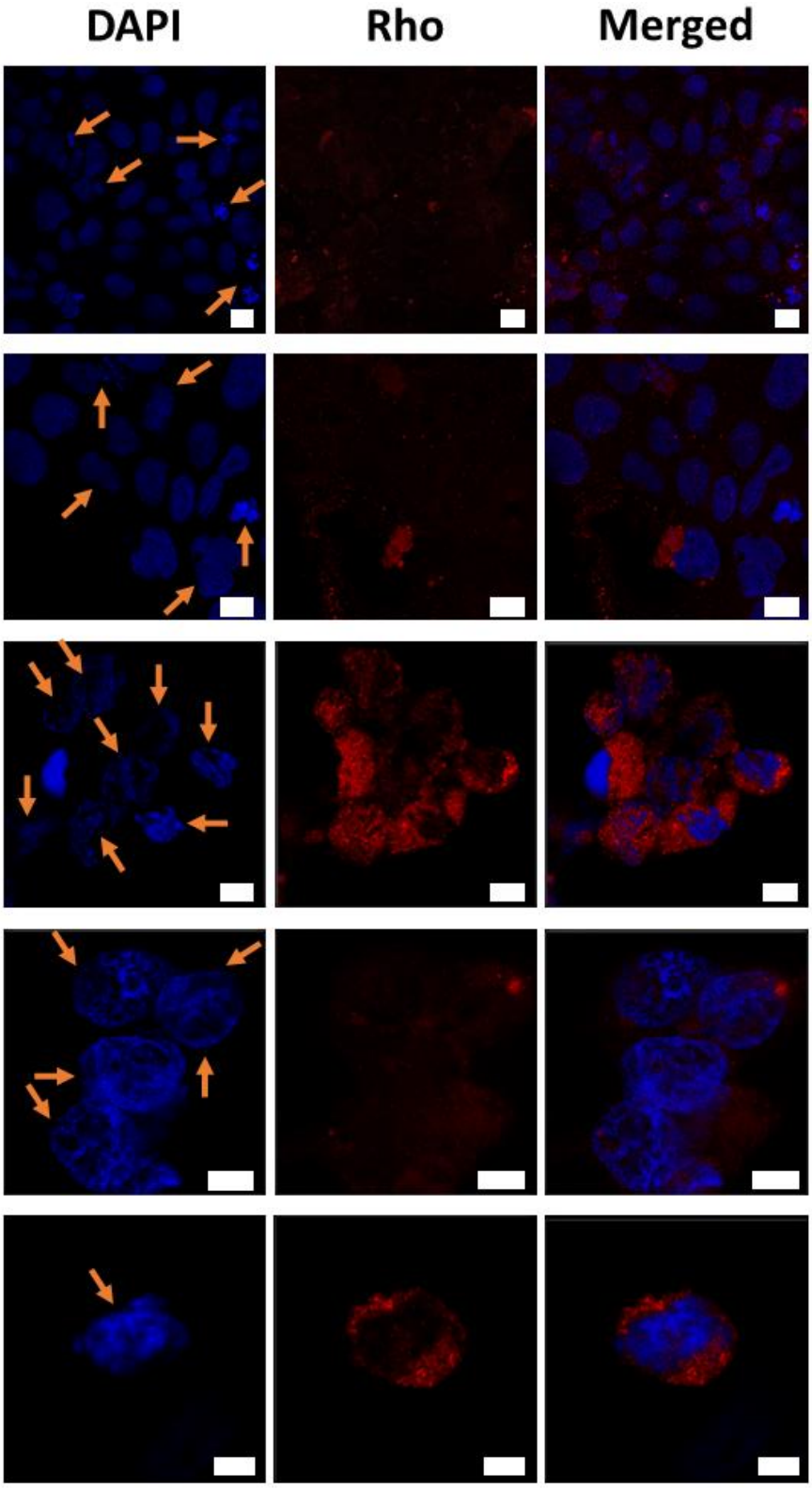

Figure 18. Representative confocal microscopy images of Caco-2 cells incubated with rhodamine-loaded nanohybrids. Cells were incubated with tNPs-Ai-DTX-Rho ELR nanohybrids for 1 hour. Fluorescence-field (DAPI and Rho) and merged images. Cell nuclei were stained with DAPI. Orange arrows indicate chromatin fragmentation. Scale bars: 20 µm (rows 1-3) and 10 µm (rows 4-5).

5.4.3.3.7 *In vivo* pharmacokinetic profile

When designing a novel therapeutic drug with potential *in vivo* applications, circulating half-life is the one of the main features to take into account. Thus, until reaching the damaged tissue, drugs pass through different biological barriers. Although often administrations and higher concentrations are frequently used to get effective doses, higher undesired cytotoxicity in healthy tissues is provoked. ELRs have been previously shown as an accurate tool to extend the *in vivo* circulating half-life of drugs [77-80].

In vivo pharmacokinetic profile was determined by systemic injection of 100 µL of rhodamine-loaded nanohybrids (tNPs-Ai-DTX-Rho) previously dissolved at 3 mg/mL in BALB/c mice via tail vein. Blood fluorescence was assessed at different time points and results showed one-phase decay behavior of fluorescent nanohybrids in the plasma, so the one-compartmental model was used and the plasma concentration-time curve was fit by means of SAAM II software (Figure 19C). In this model, the whole body is thought to act as one uniform compartment and the drug is immediately spread [81].

Results showed that the distribution volume of ELR-based nanohybrids was similar to the theoretical plasma volume in mice (Table 4). This result meant that the nanohybrids were not quickly gathered in organs after systemic administration. Moreover, ELR nanohybrids showed long circulating half-life (5.5 hours). This value was in accordance to previous works involving ELR nanoparticles developed as drug delivery systems [78, 79]. Therefore, both pharmacokinetic parameters are considered appropriate properties for drug delivery devices [81]. Regarding the results, we could conclude that our nanocarriers have proper *in vivo* behavior for controlled release of therapeutic agents.

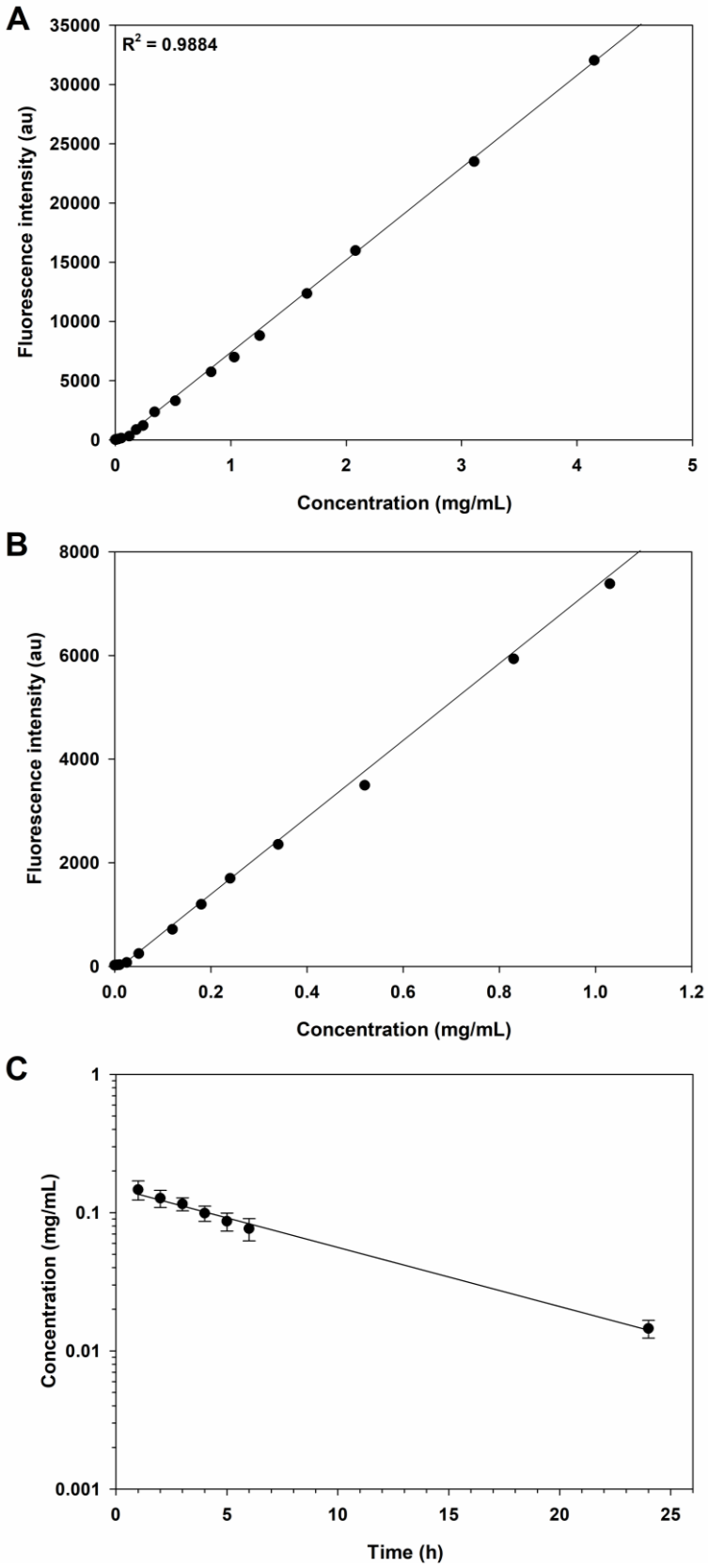

Figure 19. Pharmacokinetic profile of ELR nanohybrids after systemic administration in BALB/c mice. A: A linear standard curve was achieved by depicting the background-subtracted fluorescence versus the nanohybrid concentration. Briefly, increasing concentrations of rhodamine-loaded ELR

nanohybrids were added to mice plasma and fluorescence intensity was determined. B: Zoom of linear standard curve between 0 and 1 mg/mL. C: Plasma concentration versus time curve of ELR nanohybrids after systemic administration to 14-16 week old BALB/c mice (n=5). Mean ± SD.

Table 4. *In vivo* pharmacokinetic parameters of systemically administered rhodamine-loaded nanohybrids (tNPs-Ai-DTX-Rho) into BALB/c mice via tail vein. One compartment analysis. Mean ± SD. Abbreviations: AUC: Area under the curve; F: Bioavailability; CL: Clearance; Vd: Volume of distribution; $T_{1/2\ elimination}$: Terminal half-life; $K_{elimination}$: elimination rate constant.

AUC (µm·h)	137 ± 9
F (%)	100
CL (mL·h)	0.23 ± 0.07
Vd (mL)	1.8 ± 0.6
$T_{1/2\ elimination}$ (h)	5.5 ± 0.7
$K_{elimination}$ (h^{-1})	0.15 ± 0.03

5.4.3.3.8 *In vivo* anti-cancer accuracy of ELR nanohybrids

In order to determine the efficacy of hybrid ELR nanodevices in colorectal cancer, we used the well-known azoxymethane/dextran sodium sulfate (AOM/DSS) murine model, previously described by Neufert *et al*. [50]. It is important to highlight that this animal model was developed in non-immunosuppressed mice, which allowed us to test our ELR-based nanohybrids in physiologic conditions in order to better determine the activity of the nanodevices in the whole system. Furthermore, AOM-induced tumors exhibit molecular and histopathological features similar to human CRC [50]. Contrary to other models of CRC, tumors induced by AOM are usually present in the distal part of the colon, thereby resembling the predominant localization of spontaneous CRC in humans. Moreover, the AOM/DSS mouse CRC model is a stable and reliable model which possesses interesting advantages, such as high potency and reproducibility. The scheme used for the tumor induction protocol of CRC in mice is depicted in Figure 1. Briefly, we intraperitoneally injected the tumorigenic agent azoxymethane (AOM) and, after 5 days, we provided proinflammatory dextrane sodium sulfate (DSS) in drinking water for 5 days followed by 15 days of regular drinking water. DSS treatment was repeated twice (total of 3 cycles).

This animal model has been described as a reliable tool showing predictable tumor development characterized by a high incidence in a short-term period [82]. Furthermore, this model has a great ability for mimicking many aspects of human CRC, as well as the possibility to study the disease from inflammation to dysplasia and later carcinogenesis. CRC is usually diagnosed by clinical characteristics and endoscopic mucosal features. Although colonoscopy allows us to directly visualize the colonic mucosa and the achievement of biopsies, this technic is invasive and can cause complications, such as bleeding and perforation. Thus, the use of noninvasive imaging techniques, including MRI, allows the monitoring of the disease at early stages and the characterization of the disease at advanced stages [83].

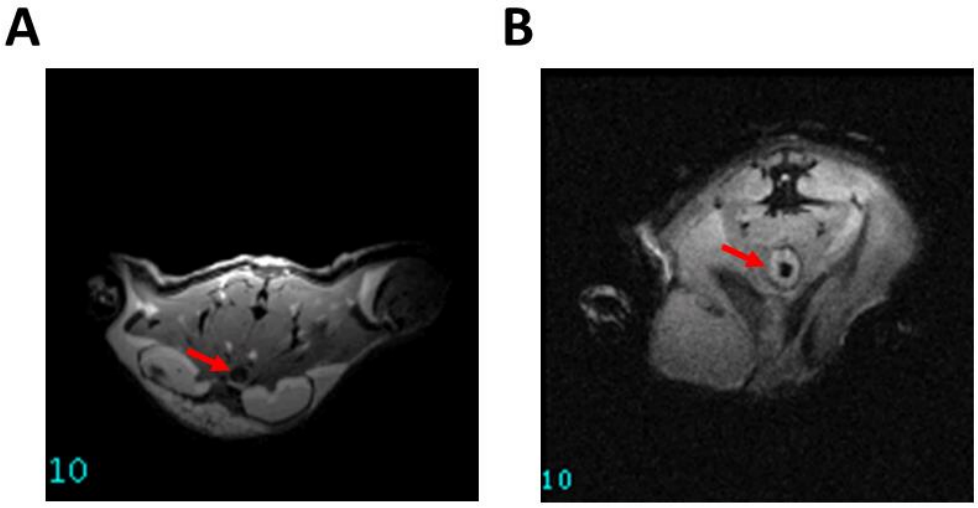

Figure 20. MRI images from control mouse (A) or CRC-induced mouse (B). Tumors were induced with AOM/DSS method as described in Figure 1. At the end of the tumor induction, animals were sacrificed and MRI were performed. Red arrows point colon. The light halo surrounding colon appreciated in B image indicates inflammation.

Moreover, as the inflammation and tumor development could not be appreciated by palpation during the tumor induction protocol, we used MRI imaging in order to evaluate the proper inflammation-driven tumorigenesis within the colorectal tract. The lack of water in the colon of healthy mouse resulted in a dark image (Figure 20A). Contrary, the colonic inflammation triggered by DSS treatment was appreciated as brighter halo around the lumen, indicated by red arrows (Figure 20B). Therefore, we were able to corroborate by MRI technic the characteristic inflammation in the AOM/DSS mouse model.

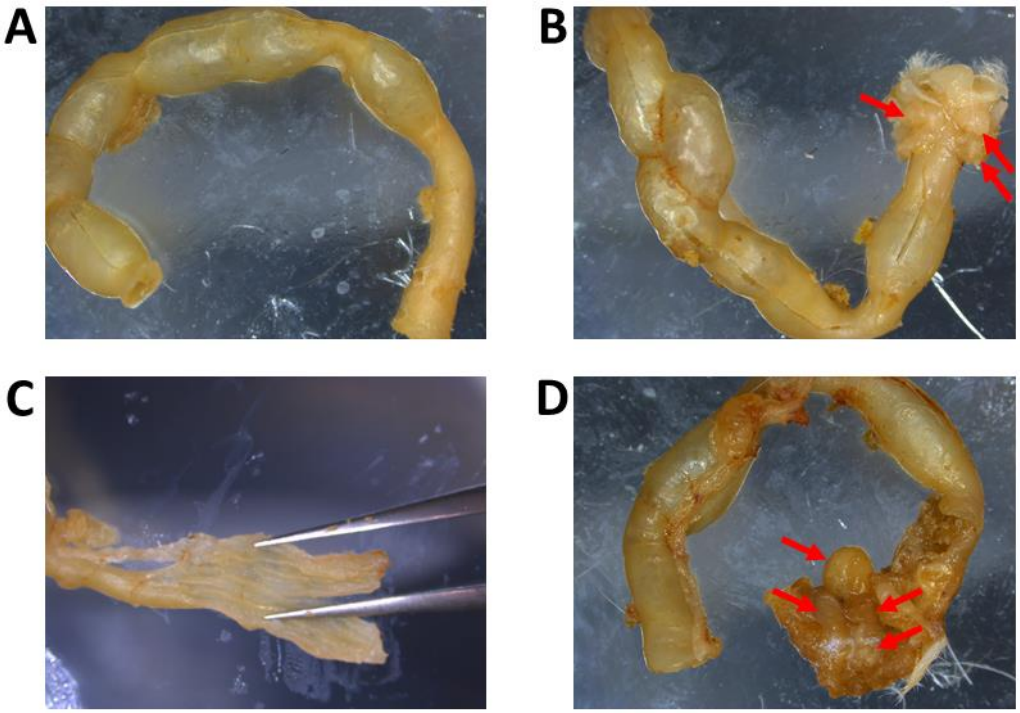

Figure 21. Tumor induction by AOM/DSS treatment. A-B: Representative images of colons from control (A and C) and treated (B and D) animals. C-D: Images of representative distal open colons after tumor induction by AOM/DSS from control (A) and treated (B) mice. Arrows indicate tumor polyps.

As can be seen in Figure 21A and C, the *ex vivo* examination of murine colons shown as the control mice did not show visible tumor polyps, whereas AOM/DSS treatment provoked tumorigenesis at murine distal colon where multiple tumors were detected (Figure 21B and D). Therefore, results showed that the AOM/DSS treatment could be used as a reliable tool to mimic CRC and thereby study its treatment by systemic administration of ELR-based nanohybrids.

Table 5. Experimental groups for the *in vivo* assay. The encapsulated therapeutic agent within ELR nanohybrids, the amount of DTX and the number of intravenous administrations are indicated. The use of brackets in tNPs [2 mg/Kg] and tNPs-Ai [2 mg/Kg] group names means that these control groups were administrated with the same amount of ELR used in the tNPs-DTX 2 mg/Kg group.

Animal group name	Therapeutic agent	Total amount of DTX injected (mg/Kg)	Number of injections	Amount of DTX per injection (mg/Kg)
PBS	-	-	1	-
tNPs [2mg/Kg]	-	-	1	-
Free DTX 5 mg/Kg	DTX	5	1	5
Free DTX 2 mg/Kg	DTX	2	1	2
tNPs-DTX 2 mg/Kg	DTX	2	1	1
tNPs-Ai [2mg/Kg]	Ai	-	1	-
tNPs-Ai-DTX 5 mg/Kg	Ai+DTX	5	1	5
tNPs-Ai-DTX 2 mg/Kg	Ai+DTX	2	1	2
tNPs-Ai-DTX 1 mg/Kg	Ai+DTX	1	1	1
tNPs-Ai-DTX 0.5 mg/Kg x 2	Ai+DTX	1	2	0.5
tNPs-Ai-DTX 0.5 mg/Kg x 4	Ai+DTX	2	4	0.5
tNPs-Ai-DTX 0.33 mg/Kg x 6	Ai+DTX	2	6	0.33

Once the protocol for tumor induction had been demonstrated as an accurate approach for CRC tumorigenesis, 72 mice (n=6 for each treatment) were used for tumor induction. At the end of the protocol, mice were randomly divided in 12 experimental groups (Table 5). Placebo group (mice treated with PBS), control empty ELR nanohybrids (tNPs [2 mg]) were included as negative controls. Furthermore, another two groups were included as control: nanohybrids only containing DTX 2 mg/Kg (tNPs-DTX 2 mg) and nanohybrids only containing Akt inhibitor (tNPs-Ai [2 mg]). The use of brackets in tNPs [2 mg/Kg] and tNPs-Ai [2 mg/Kg] group names means that these groups were administrated with the same amount of ELR than tNPs-DTX 2 mg/Kg group. There is no standard dose of

DTX for *in vivo* assays in the literature, where DTX amount possesses high variability, from 2 to 13 mg/Kg [23-26, 84]. For this reason, we administrated different amounts of DTX: 2 and 5 mg/Kg. Thus, we established two experimental groups involving free DTX: free DTX 5 mg/Kg and free DTX 2 mg/Kg. The same amounts of encapsulated chemotherapeutic drug DTX were used for groups involving dual approach ELRs (tNPs-Ai-DTX 5 mg/Kg and tNPs-Ai-DTX 2 mg/Kg). Moreover, we used a third dose of 1 mg DTX/Kg (tNPs-Ai-DTX 1 mg/Kg). Apart from the accuracy of ELR-based nanohybrids as anti-cancer treatment, we also studied the effect of multiple administrations instead of one single injection with the same amount of drug in order to improve the therapeutic activity of our nanodevices. Moreover, the multidose strategy could be an encouraging approach in order to avoid side effects of chemotherapeutic agent DTX. For these reasons, three multidose (administrations each 3 days) groups were included in the *in vivo* assay: tNPs-Ai-DTX 0.5 mg/Kg x 2 (2 injections, 1 mg/Kg in total), tNPs-Ai-DTX 0.5 mg/Kg x 4 (4 injections, 2 mg/Kg in total) and tNPs-Ai-DTX 0.33 mg/Kg x 6 (6 injections, 2 mg/Kg in total). A summary of experimental groups is indicated in Table 5.

Body weight and animal welfare were measured during the whole assay and mice did not show toxicity signals in terms of the normal weight gain during the experiment (Figure 22). Untreated animals (PBS group) did not gain body weight after treatment. Moreover, those animals treated with control empty ELR nanohybrids (tNPs [2 mg/Kg]) showed similar values compared to untreated mice. In fact, groups treated with PBS and tNPs [2 mg/Kg] lost 0.64% and 1.89% of body weight respectively, whereas the other experimental groups gained between 0.6% and 2.54% body weight.

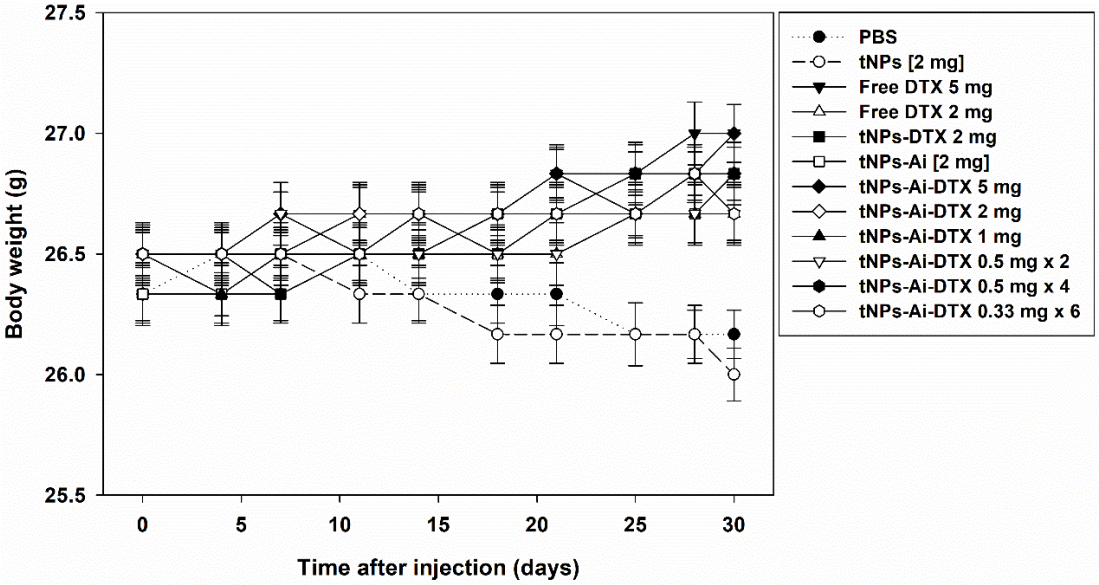

Figure 22. Body weight evolution after treatment. Tumors were induced with AOM/DSS as described in Figure 1. Then, animals were systemically injected with indicated treatments and finally sacrificed. Body weight was measured each 3 days during the whole experiment.

As explained in sections 3.7 and 3.11, ELR-based nanohybrids were suitable as drug delivery systems *in vivo* for systemic administration. In fact, as shown in Table 2, the nanohybrids size was not affected by interaction with BSA protein, which is the most abundant plasma protein. Thus, ELR nanohybrids were systemically administrated by injection via tail vein in mice. As no macroscopic examination was possible without animal sacrifice, MRI was performed 25 days post injection, in order to obtain preliminary results in terms of the efficacy of ELR-based nanohybrids to resolve the inflammation-driven carcinogenesis (Figure 23). Thus, MRI images were taken from some treated animals randomly chosen. When mice were treated with tNPs-DTX-Ai 2 mg/Kg (Figure 23E), MRI showed less inflammation than untreated mice (PBS group). It is worthy to notice that image resolution is lower, compared to Figure 20, due to the fact that animals were alive and background was higher because of breathing. Moreover, both tNPs-DTX 2 mg/Kg and tNPs-Ai [2 mg/Kg] (Figure 23C and D) seemed to better resolve inflammation than free DTX (Figure 23B), in which the bright halo indicating inflammation was better appreciated by MRI.

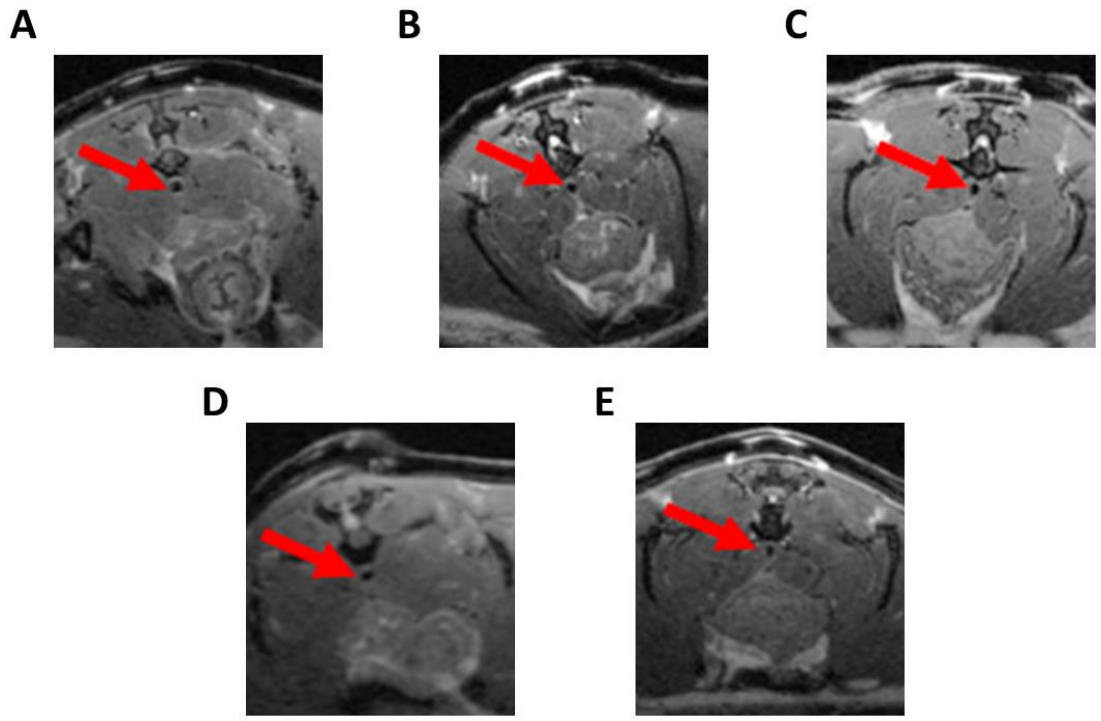

Figure 23. Representative MRI images from treated mice. Tumors were induced with AOM/DSS as described in Figure 1 and then mice were systemically injected with different treatments. MRI was performed at day 25 post injection. A: PBS; B: Free DTX 5 mg/Kg; C: tNPs-Ai [2 mg/Kg]; D: tNPs-DTX 2 mg/Kg; (E): tNPs-Ai-DTX 2 mg/Kg. Arrows point colon. The light halo surrounding colon indicates inflammation. The image resolution is lower compared to Figure 20, due to the fact that animals were alive and background was higher because of breathing.

Ex vivo examination of murine colons at the end of the protocol revealed differences regarding the number of tumor polyps per animal in the groups (Figures 24 and 25). Thus, untreated animals (PBS group) had 8.83 tumor polyps in average. Similar values were found in the negative control group, which corresponded to mice treated with empty ELR nanohybrids (tNPs [2 mg/Kg]). The examination of colons from animals treated with antitumor devices showed a significant decrease in terms of the number of tumors per animal. Results showed that groups treated with 5 mg/Kg or 2 mg/Kg free DTX had 3.17 and 5.5 tumors per animal in average, respectively. Thus, results showed that administration of free DTX had a dose-dependent effect in the number of polyps. Moreover, when DTX was encapsulated within targeted ELR nanohybrids (tNPs-DTX 2 mg/Kg), the number of tumor polyps diminished to 4.33. Therefore, the encapsulation of the chemotherapeutic drug enhanced its anti-cancer effect. This result could be explained by the higher bioavailability of the drug due to the encapsulation and also by the fact that encapsulated DTX (tNPs-DTX 2 mg/Kg) was driven to the colorectal cancer cells by the

targeting system against CD44, instead of being distributed within the whole body. On the other hand, ELR nanohybrids only carrying Akt inhibitor (tNPs-Ai [2 mg/Kg]) also diminished the number of tumor polyps in a similar level than free DTX, despite that they triggered a more complex therapeutic mechanism. Although results from Chapters 2 and 3 indicated an encouraging therapeutic activity of ELR-based nanoparticles involving Akt kinase, this is the first time that controlled release of Akt inhibitor leads to tumor reduction *in vivo*. Nevertheless, the anti-tumor effect of targeted nanohybrids only carrying DTX (tNPs-DTX 2 mg/Kg) was even better than free DTX or nanohybrids only carrying Aky inhibitor (tNPs-Ai [2 mg/Kg]).

Regarding the combination of Akt inhibition and DTX within the same ELR-based nanohybrids (tNPs-Ai-DTX), animals only had 2.83, 3.83 and 4.83 polyps in average when treated with dual-approach nanohybrids (5, 2 and 1 mg/Kg of DTX, respectively). Again, a dose-dependent effect was appreciated. Moreover, the combined therapy improved not only the therapeutic action of free DTX, but also nanohybrids with only one therapeutic agent, either DTX either Akt inhibitor. Therefore, results showed synergic effect of Akt inhibitor and DTX when included within the same nanohybrid.

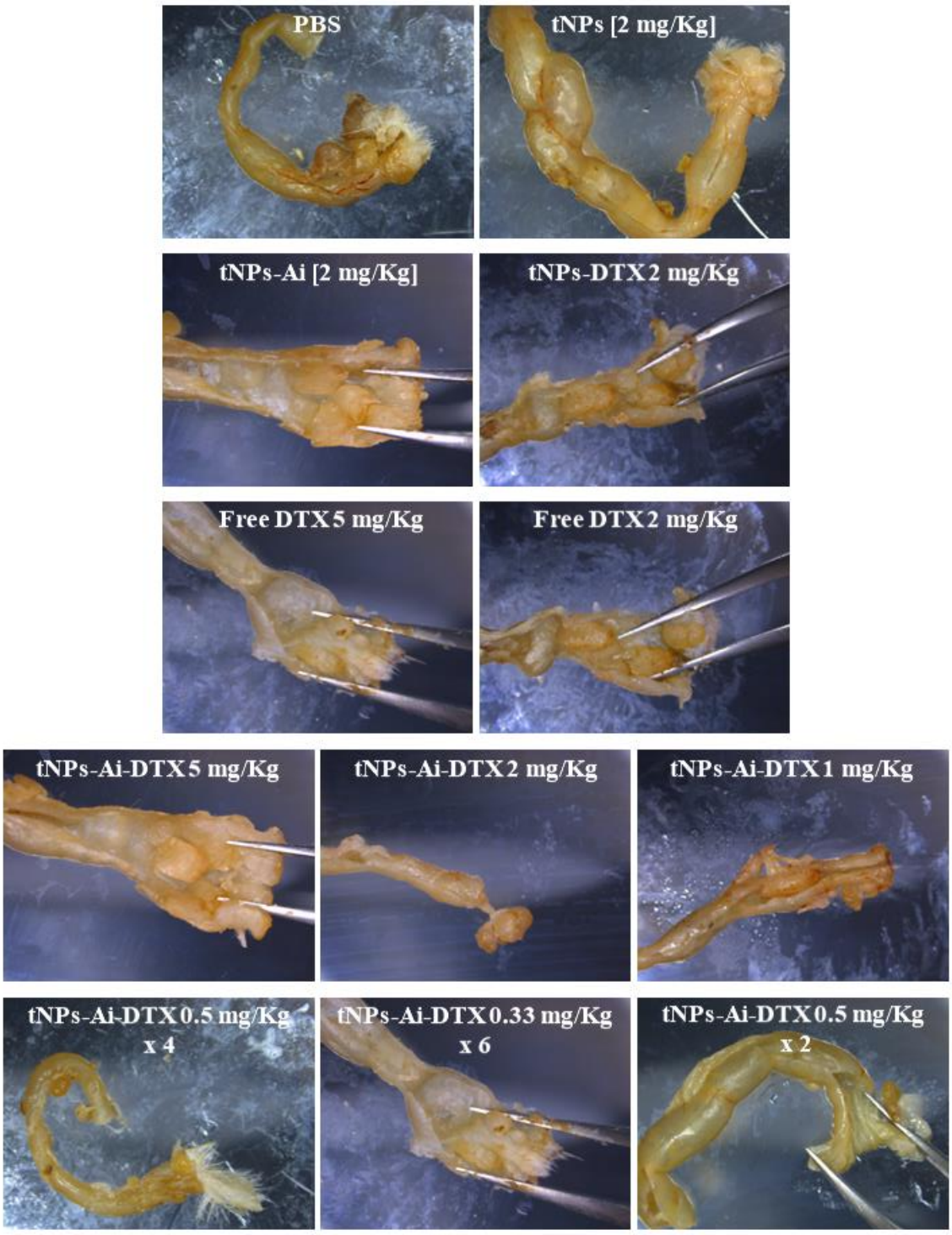

Figure 24. Effect of ELR nanohybrids in tumorigenesis in a murine model of colorectal cancer. Tumors were induced with AOM/DSS as described in Figure 1. Then, animals were systemically injected with indicated treatments. Animals were sacrificed, colons were collected and polyps were counted and measured.

The effect of multiple administrations (each 3 days) of dual-approach nanohybrids (tNPs-Ai-DTX) in the number of tumor polyps was also studied (Figures 24 and 25). This

strategy could be a promising approach as it could reduce problems related to the administration of DTX and the consequent adverse side effects. Thus, when treated with tNPs-Ai-DTX 1 mg/Kg, animals had less tumor polyps (3.83 in average) compared to animals treated with the same amount of ELR nanohybrids in one single injection (4.83 polyps). Moreover, the same enhanced effect by multi dose treatments was appreciated in animals treated with tNPs-Ai-DTX 2 mg/Kg dosed in 4 injections compared to treated mice with tNPs-Ai-DTX 2 mg/Kg in one systemic injection (3 and 3.83 polyps, respectively). However, this effect was not seen when tNPs-Ai-DTX 2 mg/Kg was administrated in 6 injections, as this group had 4.33 tumor polyps. Even though this group significantly reduced the number of tumor polyps when compared to PBS group, its worse anti-tumor activity observed could be explained by the fact that a minimum amount required in each administration was not achieved in order to improve the results appreciated in animals treated with only one administration. At light of these results, the best anti-tumor activity in terms of number of tumor polyps were found when treating with free DTX 5 mg/Kg, tNPs-Ai-DTX 5 mg/Kg or tNPs-Ai-DTX 2 mg/Kg dosed in 4 injections. Thus, multiple administrations improve the effect of the chemotherapeutic drugs with a minimal dose of 0.5 mg/Kg per injection.

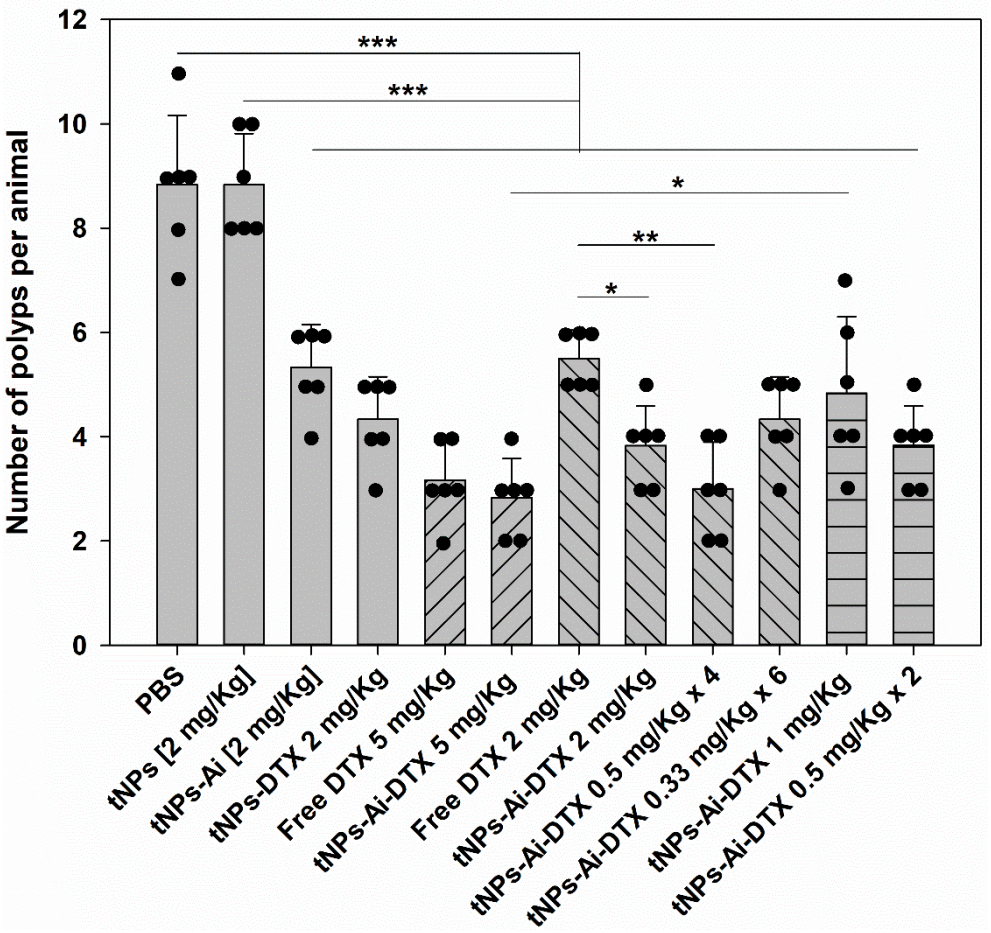

Figure 25. Effect of ELR nanohybrids in CRC tumorigenesis in mice. Tumors were induced with AOM/DSS as described in Figure 1. Then, animals were systemically injected with indicated treatments. Animals were sacrificed, colons were collected and polyps were counted. Number of polyps per animal. Each dot depicts an animal. Bars pattern: Left coarse: 5 mg/Kg DTX treatments; Right coarse: 2 mg/Kg DTX treatments; Horizontal coarse: 1 mg/Kg DTX treatments. Data represent the mean ± SD. *p < 0.05, **p < 0.01, ***p < 0.001

Moreover, *ex vivo* examination of murine colons involved the measurement of tumor polyps size (Figure 26 and Table 6). Most tumors from untreated animals (PBS group) had a size between 2 and 4 mm (45%), whereas small polyps (>2 mm) and big polyps (>4 mm) represented 32% and 21%, respectively. Systemic administration of control empty ELR nanohybrids (tNPs [2 mg/Kg]) did not cause changes in the tumor size distribution. This result, together with the no variation in terms of tumor number, shows that the ELRs backbone does not influence the development of the disease. When animals were treated with 5 mg/Kg free DTX the tumor sizes were 37%, 47% and 16% for small, medium and big polyps, respectively. Even though the amount of DTX had a dose-dependent effect in terms of number of tumor polyps (Figure 25), their size was not affected, as animals treated with 2 mg/Kg free DTX had 35%, 46% and 19% of small, medium and big polyps.

The encapsulation of DTX within ELR nanohybrids did not significantly changed the size distribution, as treatment with tNPs-DTX 2 mg/Kg showed 37%, 43% and 20% of small, medium and big polyps, respectively. Furthermore, the treatment of CRC with ELR nanohybrids only carrying Akt inhibitor (tNPs-Ai [2 mg/Kg]) neither significantly changed the size distribution of tumors (36%, 45% and 19%). However, dual-approach ELR nanohybrids showed a different trend in terms of size distribution, as there were less big tumors (>4 mm) and more small polyps (<2 mm). Thus, when animals were treated with tNPs-Ai-DTX 5 mg/Kg, the size distribution changed to 40%, 46% and 14% for small, medium and big tumors. Moreover, when the amount of DTX was reduced to 2 mg/Kg (tNPs-Ai-DTX 2 mg/Kg), the percentages were 34%, 50% and 16%. Finally, animals treated with tNPs-Ai-DTX 1 mg/Kg had 31% small, 52% medium and 17% big polyps. Therefore, results showed that combined therapy of Akt inhibitor and DTX reduced the amount of big tumors (>4 mm) and increased the number of small (>2 mm) and medium (2-4 mm) polyps.

Furthermore, we studied the effect of multiple administrations (each 3 days) of dual-approach nanohybrids (tNPs-Ai-DTX) in the size distribution of tumor polyps (Figure 26 and Table 6). Thus, when animals were treated with tNPs-Ai-DTX 1 mg/Kg in two administrations, results showed more small polyps and less amount of big tumors (39%, 48% and 13%) compared to animals treated with the same amount of ELR nanohybrids in one single injection (31%, 52% and 17%). Also, when animals were treated with tNPs-Ai-DTX 2 mg/Kg in 4 injections, the size distribution changed to 44% small, 44% medium and 12% big polyps. This result was much different in comparison with animals treated with the same amount of therapeutic nanohybrids administrated in one injection (34%, 50% and 16%). Moreover, when animals were injected with tNPs-Ai-DTX 2 mg/Kg distributed in 6 injections, results showed 40%, 46% and 14% of small, medium and big polyps, respectively. Thus, results showed a trend in which the use of multiple doses of ELR nanohybrids reduced the tumor volume compared to the same amount of drug in one single dose.

Together, results showed that animals treated with 0.5x4 had the same number of tumor polyps tan those animals treated with free DTX 5 mg/Kg or tNPs-Ai-DTX 5 mg/Kg and, interestingly, size distribution determined that tumor polyps were smaller in animals from

tNPs-Ai-DTX 0.5 mg/Kg x4 group. Therefore, tNPs-Ai-DTX 2 mg/Kg administrated in four injections is the more effective dosage. Moreover, this dose would be less toxic for the potential patient due to the lower amount of drug administrated in each injection.

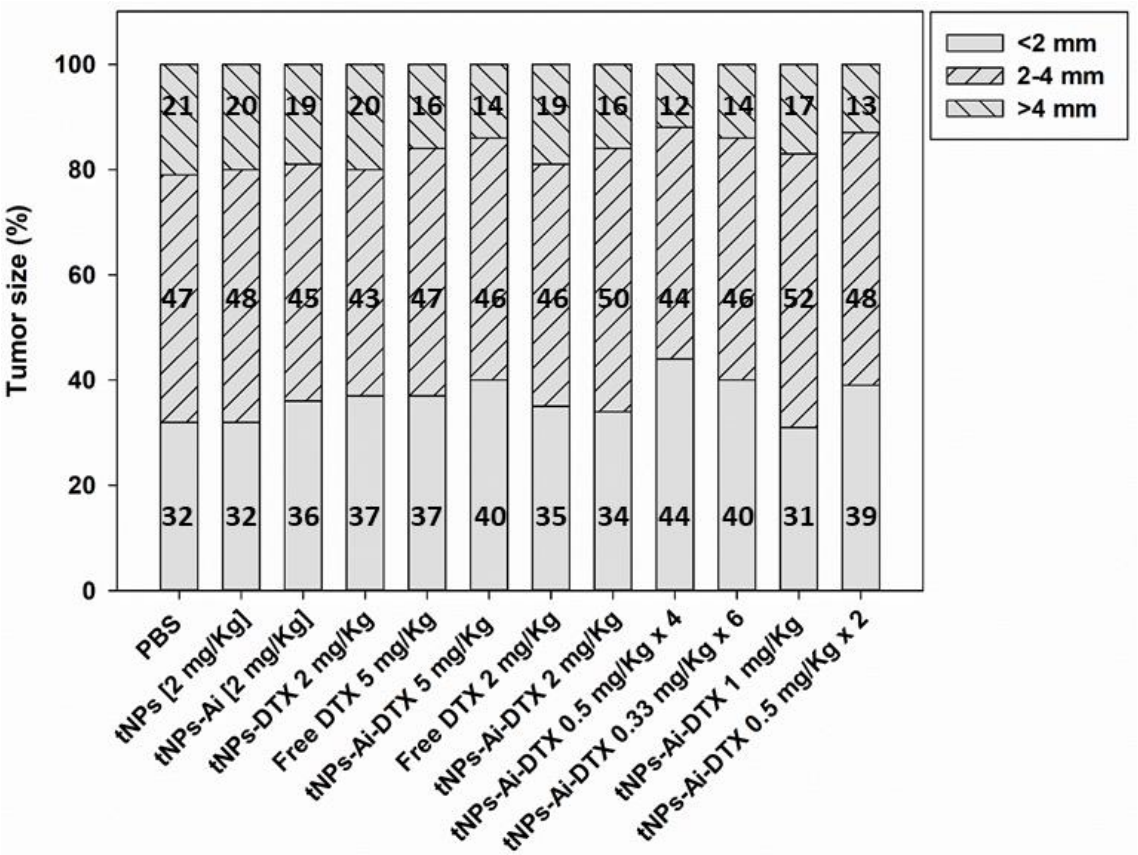

Figure 26. Effect of ELR nanohybrids in CRC tumorigenesis in mice. Tumors were induced with AOM/DSS in mice as described in Figure 1. Then, animals were systemically injected with indicated treatments. Animals were sacrificed, colons were collected and polyps were measured. Tumor size distribution is depicted.

Table 6. Tumor diameter distribution in mice. Tumors were induced with AOM/DSS as described in Figure 1. Then, animals were systemically injected with indicated treatments. Animals were sacrificed, colons were collected and polyps were measured. Colors indicate the tumor size distribution compared to PBS group: Green: decrease; Orange: identical; Red: increase.

Treatment	Tumor size distribution (%)		
	<2 mm	2-4 mm	>4 mm
PBS	32	47	21
tNPs [2 mg/Kg]	32	48	20
tNPs-Ai [2 mg/Kg]	36	45	19
tNPs-DTX 2 mg/Kg	37	43	20
Free DTX 5 mg/Kg	37	47	16
tNPs-Ai-DTX 5 mg/Kg	40	46	14
Free DTX 2 mg/Kg	35	46	19
tNPs-Ai-DTX 2 mg/Kg	34	50	16
tNPs-Ai-DTX 0.5 mg/Kg x 4	44	44	12
tNPs-Ai-DTX 0.33 mg/Kg x 6	40	46	14
tNPs-Ai-DTX 1 mg/Kg	31	52	17
tNPs-Ai-DTX 0.5 mg/Kg x 2	39	48	13

Furthermore, histological analysis of murine colons was performed (Figure 27). Tumor polyps (red arrows) were found as abnormal solid masses composed by a tumor core surrounded by connective tissue and blood vessels. These areas showed a high cell density, which was demonstrated by the more intense hematoxylin staining compared to the rest of the tissue, and were compatible with invasive carcinoma. Histological assessment of both PBS and tNPs [2 mg/Kg] groups showed severe crypt damage and high architectural distortion. Cell infiltration can be also perceived, as AOM-induced tumors are frequently infiltrated by T lymphocytes and other immune cells [85]. The morphological and pathological features were concordant with high-grade dysplasia, which is the previous stage before malignant degeneration and invasion of the bowel wall [86]. Histological sections from animals treated with tNPs-Ai [2 mg/Kg] or tNPs-DTX showed unstructured tissue, in which crypts with aberrant shapes could be observed.

However, infiltrating cells were better appreciated in sections from animals treated with tNPs-DTX [2 mg/Kg]. Regarding to animals treated with tNPs-Ai-DTX 2 mg/Kg in one single dose, tissue sections seemed to have mild disruption and higher structuration and organization. Even though some abnormal crypts can be seen, most crypts possessed small and round shapes. Furthermore, there were no differences compared to murine colons from animals treated with the same amount of ELR nanohybrids split in 4 administrations (tNPs-Ai-DTX 0.5 mg/Kg x 4). Thus, structured tissue with majority of normal crypts and less infiltrating cells could be observed.

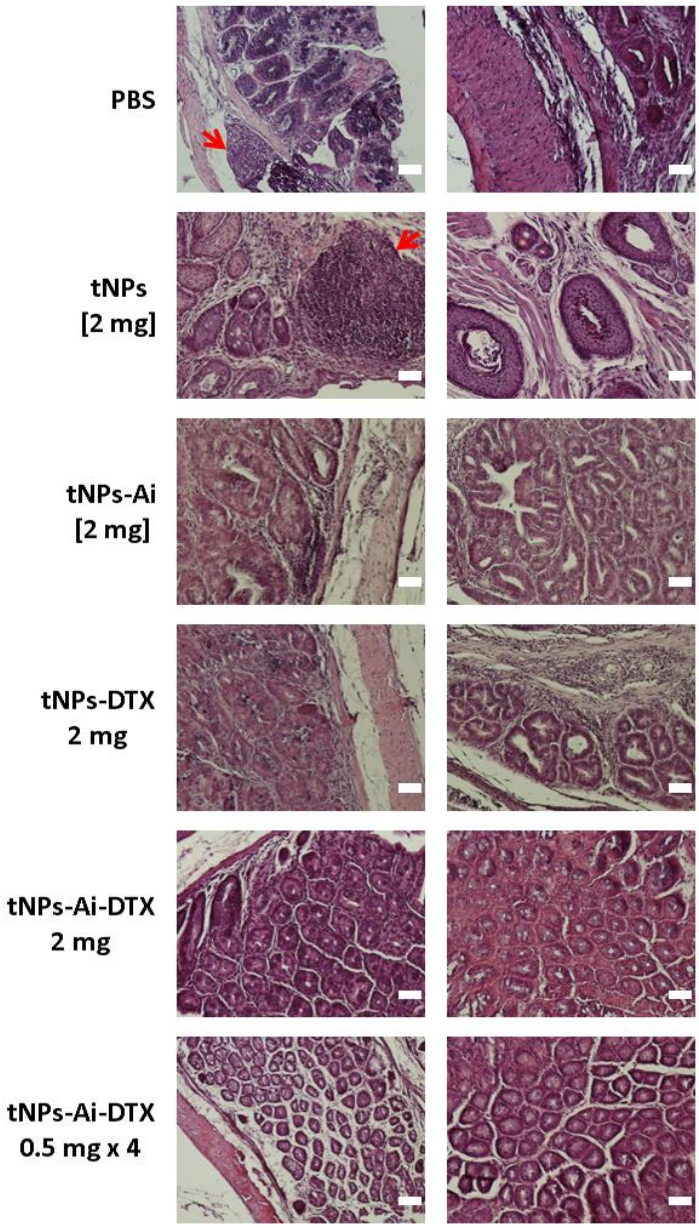

Figure 27. Effect of ELR nanohybrids in CRC tumorigenesis in mice. After animal sacrifice, colons were collected and processed for histology. Histopathological analysis of murine colons after

hematoxylin-eosin (H&E) staining. Representative images of H&E stained sections. Magnification: 10x and 20x. Scale bars: 200 μm.

5.4.4. Final remarks

Even though cancer treatments are becoming more and more successful due to improved therapies, novel strategies are needed. Cancer is a complex disease and involves multiple processes which difficult the accurate action of one single therapy. As a consequence, current therapeutic strategies are based on combination of different approaches, such as surgery, chemotherapy, radiotherapy or immunotherapy. At light of this tendency, we hypothesized that ELRs could be a smart system in order to combine several therapeutic agents. Thus, in this chapter, the development of a hybrid nanodevice involving Akt inhibition and release of anti-mitotic agent Docetaxel as a dual-approach drug delivery system was achieved.

By taking advantage of amphiphilic ELR biopolymers, we were able to successfully encapsulate antimitotic agent DTX into targeted nanoparticles, which were able to improve the cytotoxic effect of the drug in cancer cells. Furthermore, the encapsulation of DTX within ELR-based nanoparticles reduced the impact of DTX in non-cancer cells.

Thus, according to results from Chapter 2, in which ELR nanoparticles were able to avoid Akt phosphorylation and trigger apoptosis-mediated cell death in cancer cells, and accurate effect of DTX-loaded nanocarriers, we designed a dual-approach nanosystem based on the combination of both therapeutic strategies: inhibition of Akt phosphorylation and release of antimitotic drug Docetaxel.

Chemical conjugation of DNA aptamer by means of click chemistry to ELR biopolymers allowed us to develop a tailor-made nanodevice specifically targeted to CD44, a membrane receptor which is also a cancer marker. Physicochemical characterization demonstrated that we obtained stable monodisperse nanohybrids with suitable size and zeta-potential for cell internalization and controlled drug delivery purposes. Moreover, ELR nanohybrids were stable after incubation with BSA protein in order to mimic physiologic conditions after systemic administration. As expected, enhanced effect of

therapeutic ELR-based nanodevices was achieved, when compared to non-targeted systems, in terms of cancer cell viability and proliferation.

Thus, *in vitro* assays showed that dual-approach ELR nanohybrids were able to avoid Caco-2 cells proliferation. Moreover, Akt inhibitor seemed to act at early time points while the therapeutic effect of DTX occurs at longer times. Viability assays also showed that ELR nanohybrids not only dramatically affected colorectal cancer cell viability, but also avoided undesired cytotoxicity in endothelial HUVEC cells. As hypothesized, the impact of dual-approach ELR nanohybrids in terms of cell viability improved the effect of nanodevices only carrying either Akt inhibitor either DTX drug. This result pointed the synergic effect of both therapeutic agents included within the ELR-based nanohybrids. Therefore, in concordance to the main objective of this chapter in terms of a dual-approach strategy, our system allowed us to tackle cancer cells by two different ways: Akt inhibitor involved apoptosis, whereas DTX triggered both apoptosis- and necrosis-mediated cell death.

In vivo pharmacokinetic profile was also determined. The results showed that the tailor-made therapeutic nanodevices met the parameters required for drug delivery systems. Pharmacologic assays revealed that ELR nanohybrids possessed a proper distribution volume and long half-life in systemic circulation.

Finally, the *in vivo* anti-tumor efficacy was determined in a colorectal cancer mouse model. Although most chemotherapeutic drugs are tested in immunosuppressed animals, the use of the AOM/DSS model allowed us to study the therapeutic potential of our nanodevices *in vivo* in a more significant and realistic way respect to athymic mice, as natural immunosurveillance influences cancer progression. The *in vivo* assay showed the expected anti-tumor effect of ELR-based nanohybrids. Thus, a significant reduction in terms of the number of tumor polyps in the distal colon was observed after systemic administration of targeted nanodevices. Furthermore, results showed that encapsulation of DTX within ELR nanohybrids improved the effect of the antimitotic agent. Similar to the effect in cell viability, the use of the dual-approach strategy was more accurate than the administration involving only Akt inhibitor or DTX. Moreover, results showed that multiple administrations of ELR nanohybrids reduced the number of tumor polyps

compared to one single injection with the same amount of therapeutic agent. The use of multiple administrations not only diminished the number of tumor polyps, but also showed a trend in which the size distribution changed. Thus, the amount of big polyps (>4 mm) was reduced and small polyps (>2 mm) were more abundant. At light of the results, the more effective dose consisted on multiple administrations of an intermediate amount of doubly loaded nanoparticles (DTX and Akt inhibitor). This treatment not only reduced the number of tumor polyps to similar values than the higher drug amount, but also their size was smaller.

Histological analysis of murine colons showed that systemic administration of dual-approach ELR nanohybrids improved the tissue organization and crypts morphology, compared to non-treated mice. Nonetheless, further immunohistochemistry analysis may be done in the future in order to better characterize the tumor tissue composition and malignancy.

5.4.5. References

[1] https://seer.cancer.gov.
[2] https://www.wcrf.org/dietandcancer/cancer-trends/colorectal-cancer-statistics.
[3] R.L. Siegel, *et al.* Colorectal cancer statistics, 2017. CA Cancer J Clin, 2017. 67 (3):177-193.
[4] L. Roncucci, F. Mariani. Prevention of colorectal cancer: How many tools do we have in our basket? Eur J Intern Med, 2015. 26 (10):752-756.
[5] M. Navarro, *et al.* Colorectal cancer population screening programs worldwide in 2016: An update. World J Gastroenterol, 2017. 23 (20):3632-3642.
[6] C.J. Punt, M. Koopman, L. Vermeulen. From tumour heterogeneity to advances in precision treatment of colorectal cancer. Nat Rev Clin Oncol, 2017. 14 (4):235-246.
[7] A. Tiwari, *et al.* Basics to advances in nanotherapy of colorectal cancer. Drug Deliv Transl Res, 2019.
[8] Y. Zhang, H.F. Chan, K.W. Leong. Advanced materials and processing for drug delivery: the past and the future. Adv Drug Deliv Rev, 2013. 65 (1):104-120.
[9] J. Shi, *et al.* Cancer nanomedicine: progress, challenges and opportunities. Nat Rev Cancer, 2017. 17 (1):20-37.
[10] M.J. Pina, *et al.* A double safety lock tumor-specific device for suicide gene therapy in breast cancer. Cancer Lett, 2020. 470 43-53.
[11] H. Hillaireau, P. Couvreur. Nanocarriers' entry into the cell: relevance to drug delivery. Cell Mol Life Sci, 2009. 66 (17):2873-2896.
[12] H. Bae, *et al.* Development of functional biomaterials with micro- and nanoscale technologies for tissue engineering and drug delivery applications. J Tissue Eng Regen Med, 2014. 8 (1):1-14.
[13] Y. Matsumura, H. Maeda. A new concept for macromolecular therapeutics in cancer chemotherapy: mechanism of tumoritropic accumulation of proteins and the antitumor agent smancs. Cancer Res, 1986. 46 (12 Pt 1):6387-6392.

[14] H. Maeda, G.Y. Bharate, J. Daruwalla. Polymeric drugs for efficient tumor-targeted drug delivery based on EPR-effect. Eur J Pharm Biopharm, 2009. 71 (3):409-419.
[15] J.D. Byrne, T. Betancourt, L. Brannon-Peppas. Active targeting schemes for nanoparticle systems in cancer therapeutics. Adv Drug Deliv Rev, 2008. 60 (15):1615-1626.
[16] M.J. Pina*, et al.* Biocompatible ELR-based polyplexes coated with MUC1 specific aptamers and targeted for breast cancer gene therapy. Mol Pharm, 2016. 13 (3):795-808.
[17] L.C. Cantley. The phosphoinositide 3-kinase pathway. Science, 2002. 296 (5573):1655-1657.
[18] J. Luo, B.D. Manning, L.C. Cantley. Targeting the PI3K-Akt pathway in human cancer: rationale and promise. Cancer Cell, 2003. 4 (4):257-262.
[19] M.L. Hensley*, et al.* Gemcitabine and docetaxel in patients with unresectable leiomyosarcoma: results of a phase II trial. J Clin Oncol, 2002. 20 (12):2824-2831.
[20] Q. Tan*, et al.* Current development in nanoformulations of docetaxel. Expert Opin Drug Deliv, 2012. 9 (8):975-990.
[21] R. Fan*, et al.* Docetaxel load biodegradable porous microspheres for the treatment of colorectal peritoneal carcinomatosis. Int J Biol Macromol, 2014. 69 100-107.
[22] J.M. Lee*, et al.* pH-Responsive hyaluronated liposomes for docetaxel delivery. Int J Pharm, 2018. 547 (1-2):377-384.
[23] P.E. Saw*, et al.* Hyper-cell-permeable micelles as a drug delivery carrier for effective cancer therapy. Biomaterials, 2017. 123 118-126.
[24] M.M. Badran*, et al.* Novel docetaxel chitosan-coated PLGA/PCL nanoparticles with magnified cytotoxicity and bioavailability. Biomed Pharmacother, 2018. 106 1461-1468.
[25] V. Kushwah*, et al.* Co-delivery of docetaxel and gemcitabine using PEGylated self-assembled stealth nanoparticles for improved breast cancer therapy. Nanomedicine, 2018. 14 (5):1629-1641.
[26] A. Kadari*, et al.* Design of multifunctional peptide collaborated and docetaxel loaded lipid nanoparticles for antiglioma therapy. Eur J Pharm Biopharm, 2018. 132 168-179.
[27] J. Wan*, et al.* Docetaxel-decorated anticancer drug and gold nanoparticles encapsulated apatite carrier for the treatment of liver cancer. J Photochem Photobiol B, 2018. 185 73-79.
[28] P. Girotra, S.K. Singh, K. Nagpal. Supercritical fluid technology: a promising approach in pharmaceutical research. Pharm Dev Technol, 2013. 18 (1):22-38.
[29] A.J. Yiu, C.Y. Yiu. Biomarkers in colorectal cancer. Anticancer Res, 2016. 36 (3):1093-1102.
[30] P. Herrlich, S. Pals, H. Ponta. CD44 in colon cancer. Eur J Cancer, 1995. 31a (7-8):1110-1112.
[31] M. Zoller. CD44: can a cancer-initiating cell profit from an abundantly expressed molecule? Nat Rev Cancer, 2011. 11 (4):254-267.
[32] L. Ma, L. Dong, P. Chang. CD44v6 engages in colorectal cancer progression. Cell Death Dis, 2019. 10 (1):30.
[33] V.J. Wielenga*, et al.* CD44 glycoproteins in colorectal cancer: expression, function, and prognostic value. Adv Cancer Res, 2000. 77 169-187.
[34] C. Chen*, et al.* The biology and role of CD44 in cancer progression: therapeutic implications. J Hematol Oncol, 2018. 11 (1):64.
[35] V. Orian-Rousseau, J. Sleeman. CD44 is a multidomain signaling platform that integrates extracellular matrix cues with growth factor and cytokine signals. Adv Cancer Res, 2014. 123 231-254.
[36] V. Orian-Rousseau, H. Ponta. Perspectives of CD44 targeting therapies. Arch Toxicol, 2015. 89 (1):3-14.
[37] A.D. Ellington, J.W. Szostak. In vitro selection of RNA molecules that bind specific ligands. Nature, 1990. 346 (6287):818-822.
[38] G.L. Bidwell, 3rd, D. Raucher. Therapeutic peptides for cancer therapy. Part I - peptide inhibitors of signal transduction cascades. Expert Opin Drug Deliv, 2009. 6 (10):1033-1047.

[39] N. Ababneh, *et al.* In vitro selection of modified RNA aptamers against CD44 cancer stem cell marker. Nucleic Acid Ther, 2013. 23 (6):401-407.
[40] W. Alshaer, *et al.* Functionalizing liposomes with anti-CD44 aptamer for selective targeting of cancer cells. Bioconjug Chem, 2015. 26 (7):1307-1313.
[41] H.Y. Jeong, *et al.* Robust fluorescence sensing platform for detection of CD44 cells based on graphene oxide/gold nanoparticles. Colloids Surf B Biointerfaces, 2015. 135 309-315.
[42] F. Li, *et al.* Adenosine detection by using gold nanoparticles and designed aptamer sequences. Analyst, 2009. 134 (7):1355-1360.
[43] B. Soontornworajit, Y. Wang. Nucleic acid aptamers for clinical diagnosis: cell detection and molecular imaging. Anal Bioanal Chem, 2011. 399 (4):1591-1599.
[44] C. Tuerk, L. Gold. Systematic evolution of ligands by exponential enrichment: RNA ligands to bacteriophage T4 DNA polymerase. Science, 1990. 249 (4968):505-510.
[45] R. Stoltenburg, C. Reinemann, B. Strehlitz. SELEX--a (r)evolutionary method to generate high-affinity nucleic acid ligands. Biomol Eng, 2007. 24 (4):381-403.
[46] S.D. Jayasena. Aptamers: an emerging class of molecules that rival antibodies in diagnostics. Clin Chem, 1999. 45 (9):1628-1650.
[47] A.D. Keefe, S. Pai, A. Ellington. Aptamers as therapeutics. Nat Rev Drug Discov, 2010. 9 (7):537-550.
[48] J.C. Rodriguez-Cabello, *et al.* Synthesis of genetically engineered protein polymers (recombinamers) as an example of advanced self-assembled smart materials. Methods Mol Biol, 2012. 811 17-38.
[49] R. Vallejo. Encapsulación de fármacos hidrofóbicos con recombinámeros tipo elastina para aplicaciones avanzadas en biomedicina. PhD Thesis, 2020.
[50] C. Neufert, C. Becker, M.F. Neurath. An inducible mouse model of colon carcinogenesis for the analysis of sporadic and inflammation-driven tumor progression. Nat Protoc, 2007. 2 (8):1998-2004.
[51] L. Martin, *et al.* Rapid micropatterning by temperature-triggered reversible gelation of a recombinant smart elastin-like tetrablock-copolymer. Soft Matter, 2010. 6 1121-1124.
[52] A. Fernandez-Colino, *et al.* Development of a mechanism and an accurate and simple mathematical model for the description of drug release: Application to a relevant example of acetazolamide-controlled release from a bio-inspired elastin-based hydrogel. Mater Sci Eng C Mater Biol Appl, 2016. 61 286-292.
[53] D. Pescador, *et al.* Regeneration of hyaline cartilage promoted by xenogeneic mesenchymal stromal cells embedded within elastin-like recombinamer-based bioactive hydrogels. Journal of Materials Science: Materials in Medicine, 2017. 28 (8):115.
[54] F.F. Lang, *et al.* Phase I study of DNX-2401 (Delta-24-RGD) oncolytic adenovirus: replication and immunotherapeutic effects in recurrent malignant glioma. Journal of Clinical Oncology, 2018. 36 (14):1419-1427.
[55] T. Meyer, J.F. Marshall, I.R. Hart. Expression of alphav integrins and vitronectin receptor identity in breast cancer cells. British journal of cancer, 1998. 77 (4):530-536.
[56] S.L. Goodman, H.J. Grote, C. Wilm. Matched rabbit monoclonal antibodies against alphav-series integrins reveal a novel alphavbeta3-LIBS epitope, and permit routine staining of archival paraffin samples of human tumors. Biol Open, 2012. 1 (4):329-340.
[57] E. Ruoslahti. RGD and other recognition sequences for integrins. Annu Rev Cell Dev Biol, 1996. 12 697-715.
[58] J.C. Liu, S.C. Heilshorn, D.A. Tirrell. Comparative cell response to artificial extracellular matrix proteins containing the RGD and CS5 cell-binding domains. Biomacromolecules, 2004. 5 (2):497-504.
[59] C. Chollet, *et al.* The effect of RGD density on osteoblast and endothelial cell behavior on RGD-grafted polyethylene terephthalate surfaces. Biomaterials, 2009. 30 (5):711-720.

[60] I. Gonzalez de Torre, *et al.* Elastin-like recombinamer catalyst-free click gels: characterization of poroelastic and intrinsic viscoelastic properties. Acta Biomater, 2014. 10 (6):2495-2505.
[61] G. Battogtokh, *et al.* Triphenylphosphine-docetaxel conjugate-incorporated albumin nanoparticles for cancer treatment. Nanomedicine (Lond), 2018. 13 (3):325-338.
[62] X. Wang, *et al.* NGR-modified micelles enhance their interaction with CD13-overexpressing tumor and endothelial cells. J Control Release, 2009. 139 (1):56-62.
[63] F. Liu, *et al.* Tumor-specific delivery and therapy by double-targeted DTX-CMCS-PEG-NGR conjugates. Pharm Res, 2014. 31 (2):475-488.
[64] M. Nieberler, *et al.* Exploring the role of RGD-recognizing integrins in cancer. Cancers (Basel), 2017. 9 (9):
[65] I. Gonzalez de Torre, *et al.* Nanogel formation from dilute solutions of clickable elastin-like recombinamers and its dependence on temperature: two fractal gelation modes. ACS Appl Mater Interfaces, 2014. 6 (16):14509-14515.
[66] J. Gonzalez-Valdivieso, *et al.* Self-assembling ELR-based nanoparticles as smart drug-delivery systems modulating cellular growth via Akt. Biomacromolecules, 2019. 20 (5):1996-2007.
[67] D.W. Urry, *et al.* Temperature-correlated force and structure development in elastomeric polypeptides: the Ile1 analog of the polypentapeptide of elastin. Biopolymers, 1986. 25 (10):1939-1953.
[68] D.W. Urry. Molecular machines: How motion and other functions of living organisms can result from reversible chemical changes. Angewandte Chemie International Edition, 1993. 32 (6):819-841.
[69] J. Lin, *et al.* Penetration of lipid membranes by gold nanoparticles: insights into cellular uptake, cytotoxicity, and their relationship. ACS Nano, 2010. 4 (9):5421-5429.
[70] R.R. Arvizo, *et al.* Effect of nanoparticle surface charge at the plasma membrane and beyond. Nano Lett, 2010. 10 (7):2543-2548.
[71] Y. Malam, M. Loizidou, A.M. Seifalian. Liposomes and nanoparticles: nanosized vehicles for drug delivery in cancer. Trends Pharmacol Sci, 2009. 30 (11):592-599.
[72] Y. Li, N. Gu. Thermodynamics of charged nanoparticle adsorption on charge-neutral membranes: a simulation study. J Phys Chem B, 2010. 114 (8):2749-2754.
[73] D.L. Morse, *et al.* Docetaxel induces cell death through mitotic catastrophe in human breast cancer cells. Mol Cancer Ther, 2005. 4 (10):1495-1504.
[74] H. Hernandez-Vargas, J. Palacios, G. Moreno-Bueno. Molecular profiling of docetaxel cytotoxicity in breast cancer cells: uncoupling of aberrant mitosis and apoptosis. Oncogene, 2007. 26 (20):2902-2913.
[75] F. Impens, *et al.* Mechanistic insight into taxol-induced cell death. Oncogene, 2008. 27 (33):4580-4591.
[76] M. Mediavilla-Varela, *et al.* Docetaxel-induced prostate cancer cell death involves concomitant activation of caspase and lysosomal pathways and is attenuated by LEDGF/p75. Mol Cancer, 2009. 8 68.
[77] M.F. Shamji, *et al.* An injectable and in situ-gelling biopolymer for sustained drug release following perineural administration. Spine (Phila Pa 1976), 2008. 33 (7):748-754.
[78] P. Shi, *et al.* Elastin-based protein polymer nanoparticles carrying drug at both corona and core suppress tumor growth in vivo. J Control Release, 2013. 171 (3):330-338.
[79] J. Hu, *et al.* Enhancing pharmacokinetics, tumor accumulation, and antitumor efficacy by Elastin-Like polypeptide fusion of Interferon Alpha. Adv Mater, 2015. 27 (45):7320-7324.
[80] A.R. Chade, *et al.* Renal therapeutic angiogenesis using a bioengineered polymer-stabilized Vascular Endothelial Growth Factor construct. J Am Soc Nephrol, 2016. 27 (6):1741-1752.
[81] J.A. MacKay, *et al.* Self-assembling chimeric polypeptide-doxorubicin conjugate nanoparticles that abolish tumours after a single injection. Nat Mater, 2009. 8 (12):993-999.

[82] M. De Robertis, *et al.* The AOM/DSS murine model for the study of colon carcinogenesis: From pathways to diagnosis and therapy studies. J Carcinog, 2011. 10 9.
[83] D. Mustafi, *et al.* High-resolution magnetic resonance colonography and dynamic contrast-enhanced magnetic resonance imaging in a murine model of colitis. Magn Reson Med, 2010. 63 (4):922-929.
[84] P. Zahedi, *et al.* Chitosan-phospholipid blend for sustained and localized delivery of docetaxel to the peritoneal cavity. Int J Pharm, 2009. 377 (1-2):76-84.
[85] C. Becker, *et al.* TGF-beta suppresses tumor progression in colon cancer by inhibition of IL-6 trans-signaling. Immunity, 2004. 21 (4):491-501.
[86] G.P. Boivin, *et al.* Pathology of mouse models of intestinal cancer: consensus report and recommendations. Gastroenterology, 2003. 124 (3):762-777.

Conclusions

6. Conclusions

6.1 A novel DNA vaccine delivery platform based on ELR nanosystems

- ✓ Six different fusion genes, consisting on multiple ELR blocks involving different amino acids as guest residue and a viral antigen from Rift Valley fever virus, were successfully engineered by recombinant techniques under the control of a constitutive viral promoter.

- ✓ Cell viability assays showed that the constructs were completely safe, one of the main requirements when working with DNA vaccination systems. Furthermore, fusion proteins Gn-E75 and Gn-V84, based on glutamic acid and valine respectively, increased 40% and 29% respectively the expression of Gn viral glycoprotein in eukaryotic cells. Gn-E75 construct remained soluble in the cellular cytoplasm, contrary to the other fusion proteins which showed aggregates-like appearance in the cellular cytoplasm.

- ✓ *In vivo* biodistribution assays revealed that the fusion constructs accumulated in the spleen after systemic administration, where the constructs are recognized by APC cells and trigger immune responses. *In vivo* immune-challenge experiments determined the immunogenicity and efficacy after challenge of the construct Gn-V168, which induced the best response in terms of reduction of viral load. Furthermore, Gn-V168 construct induced a high expression of IL1β, IL-4, IL-5, IL-6, IL12p70 and IL-13, which indicated a strong Th2 polarization and stronger levels of cell-mediated soluble effectors.

- ✓ Therefore, this system could be a promising approach in order to achieve high yield productions of natural antigens, which could have great importance when huge amounts of vaccines are needed in pandemic situations. Even though peptide antigens are not enough immunogenic to initiate adaptive immune responses, adjuvants are responsible of the long-term efficacy of vaccines but also of undesired side effects. For all these reasons, ELR-based nanosystems, which possess most of features from an ideal adjuvant factor, such as biodegradability, stability, low cost, easy manufacture, minimal adverse effects and wide

applicability, could be promising tools in order to act as accurate adjuvants and improve immunogenic responses triggered by nude antigens.

6.2 Self-assembling ELR-based nanoparticles as smart drug-delivery systems modulating cellular growth via Akt

- ✓ A new ELR and its control have been designed and developed to constitute a new device for drug delivery purposes. The final recombinamer included several functional blocks and a small peptide inhibitor Akt-in, which has been tested to be able to avoid phosphorylation and consequent activation of protein kinase Akt, which controls aberrant proliferation and growth in cancer cells.

- ✓ Both ELRs were able to self-assemble above 15ºC into highly monodisperse nanoparticles of 70 nm size and negative surface charge (-27 mV), thereby indicating that the presence of the functional motifs did not significantly disturb the ELRs self-assembling. The physicochemical properties met the requirements for enhanced internalization of therapeutic nanodevices within tumor tissue, which also remained stable in physiologic conditions that nanoparticles would face after systemic administrations. Moreover, nanoparticle showed negligible interactions with representative plasmatic proteins, thereby showing to be good candidates for vascular administration.

- ✓ *In vitro* assays demonstrated that control nanoparticles were innocuous for six different cell lines, comprising breast and colorectal cancer cells and, conversely, healthy endothelial, fibroblasts and mesenchymal stem cells. However, therapeutic nanoparticles carrying Akt-in peptide significantly affected cell viability of breast and colorectal cancer cells (97%) in a time- and dose-dependent manner. Even though Akt-in nanoparticles seemed to have slight cytotoxic effect (29%) on HUVEC endothelial cells at high concentrations, long-term cell proliferation was not affected.

- ✓ Moreover, ELR nanoparticles were internalized by clathrin-mediated endocytosis and then, CatD-sensitive sequence was recognized by lysosomal proteases and H5

peptide allowed the release of the therapeutic inhibitor from endolysosomes to the cytoplasm, where proper inhibition of Akt phosphorylation was achieved.

- ✓ Therefore, a complex design of smart nanoparticles with different actors was needed in order to successfully release a therapeutic inhibitor into the cell cytoplasm, thereby avoiding degradative proteases that would not allow the peptide to enter otherwise. This advanced nanodevice has shown encouraging potential for modulating cell processes.

6.3 Smart ELR nanoparticles as advanced anti-Akt drug delivery systems for pancreatic cancer therapy

- ✓ *In vitro* assays in stablished PANC-1 cell line and two different types of clinically relevant pancreatic cancer patient-derived cells demonstrated that therapeutic nanoparticles reduced both cellular metabolic activity and viability. While control nanoparticles did not impact cells, the cytotoxic effect of Akt-in nanoparticles was time- and dose-dependent.

- ✓ Flow cytometry demonstrated that both control and Akt-in nanoparticles were internalized at the same rate, which pointed that effects of therapeutic nanoparticles in pancreatic cancer cells were only due to the release of peptide inhibitor. ELR-based nanoparticles were localized within the lysosomes, which demonstrated that the smart nanodevices undergo the accurate and controlled intracellular trafficking in order to successfully deliver the therapeutic peptide within cell cytoplasm and perform its anti-tumor action.

- ✓ Cell morphology dramatically changed after treatment with therapeutic nanoparticles and pancreatic cancer cells were unable to properly spread and showed aberrant shape, cell shrinkage, chromatin condensation and nuclear fragmentation. Therapeutic nanoparticles properly inhibited Akt signaling pathway and, as a consequence, cell survival controlled by NFκB pathway was blocked. Moreover, pancreatic cancer cells incubated with Akt-in nanoparticles triggered apoptosis-mediated cell death.

- ✓ The cytotoxic effect of therapeutic nanoparticles in pancreatic cancer cells was enhanced by combination with a photosensitizer agent used for photodynamic therapy. This approach had a synergic effect and combined treatment decreased 20%-40% of cellular metabolic activity compared to nanoparticles monotherapy.

- ✓ The pharmacokinetic profiles were determined that both control and Akt-in nanoparticles possess long half-life (5.8 and 5.3 hours, respectively) and distribution volume was almost 2 mL, which suggested the nanoparticles as suitable drug delivery devices for systemic administration. Furthermore, *in vivo* biodistribution showed that the smart ELR nanodevices did not damage vital organs and accumulated in the gastrointestinal tract, one of the major agents for nanomaterials interaction and uptake.

- ✓ Thus, this smart nanoparticle composed by different blocks of high conformational complexity showed to be an accurate drug delivery system for controlled release in patient-derived pancreatic cancer cells, one of the closest research models to real disease. As Akt protein is not only overexpressed in pancreatic, but also in other multiple types of cancer, further studies could be done in other cancer models.

6.4 ELR-based smart nanohybrids as dual-approach drug delivery system against colorectal cancer

- ✓ A dual-approach drug delivery system consisting on a hybrid nanodevice based on the combination of two different therapeutic strategies was set up: inhibition of Akt phosphorylation and release of anti-mitotic agent Docetaxel. By means of amphiphilic ELR biopolymers, a drug delivery nanosystem able to successfully encapsulate antimitotic agent DTX into targeted nanoparticles was obtained, which enhanced the cytotoxic effect of the drug in cancer cells and reduced its non-selective impact in non-cancer cells.

- ✓ Chemical conjugation of a DNA aptamer against CD44 as targeting system triggered the selective action of ELR nanoparticles in colorectal cancer cells and minimum toxicity in endothelial cells.

- ✓ Physicochemical characterization demonstrated that obtained stable monodisperse nanodevices with suitable size and ζ-potential for controlled release in a physiologic environment after systemic administration were obtained.

- ✓ *In vitro* assays showed that targeted ELR nanodevices dramatically affected both proliferation and viability of colorectal cancer cells and avoided undesired cytotoxicity in endothelial cells. As hypothesized, the impact of dual-approach nanodevices was improved compared to encapsulated Akt inhibitor or DTX and pointed the synergic effect of both therapeutic agents included within the same ELR nanodevice. In concordance to the main objective of this chapter, the nanosystem allowed us to tackle cancer cells by two different ways: Akt inhibitor involved apoptosis at early time points, whereas DTX triggered both apoptosis- and necrosis-mediated cell death at longer times.

- ✓ The *in vivo* anti-tumor efficacy showed a significant reduction (up to 67%) in terms of the number of tumor polyps in the distal colon after systemic administration. While DTX encapsulation improved the effect of the anti-mitotic drug, the dual-approach strategy was more accurate than monotherapy with Akt inhibitor or DTX. Moreover, results showed that multiple administrations of ELR nanodevices not only diminished the number of tumor polyps compared to one single injection with the same drug amount, but also showed a trend in which the size distribution changed. At light of the results, the more effective dose consisted on multiple administrations of an intermediate amount (2 mg/Kg) of doubly loaded nanoparticles, which reduced the number of tumor polyps to similar values than the higher drug amount (2.5 fold higher) and their size was smaller. Furthermore, histological analysis of murine colons showed that dual-approach ELR nanodevices improved the tissue reorganization towards a normal morphology.

- ✓ Therefore, a dual-approach drug delivery system was set up and demonstrated as an effective therapeutic treatment for colorectal cancer. The developed ELR nanosystem exerted an accurate anti-tumor activity and demonstrated a promising therapeutic potential for future perspectives.

Appendix

7.1 Abbreviations

^{1}H-NMR: Proton nuclear magnetic resonance

A: Absorbance

ANOVA: Analysis of variance

AOM: Azoxymethane

APC: Antigen-presenting cells

APS: Ammonium persulphate

Au: Arbitrary units

AUC: Area under the curve

AIM-TB: Autoinduction medium Terrific-Broth

bp: Base pair

BSA: Bovine serum albumine

CatD: Cathepsin D

CCA: Cholangiocarcinoma

CL: Clearance

CMC: Carboxy-methylcellulose

CMC: Critical micellar concentration

CME: Clathrin-mediated endocytosis

CMT: Critical micelle temperature

CMV: Cytomegalovirus

CPE: Cytopathic effect

C-terminal: Carboxile terminal

CvME: Caveolae-mediated endocytosis

Da: Daltons

DAPI: Diamino-2-phenylindole-dyhydrochloride

DLS: Dynamic light scattering

DMEM: Dulbecco's modified Eagle medium

DMF: Dimethylformamide

DMSO: Dimethyl sulfoxide

DNA: Deoxyribonucleic acid

DPBS: Dulbecco's phosphate buffered saline

DSC: Differential scanning calorimetry

DSS: Dextrane sodium sulfate

DTX: Docetaxel

EBP: Elastin binding protein

***E. coli*:** *Escherichia coli*

ECM: Extracellular matrix

EDTA: Ethylendiamine tetraacetic acid

ELbcR: Elastin-like block co-recombinamer

ELR: Elastin-like recombinamer

ELP: Elastin-like Polymer

EMEM: Eagle's minimum essential medium

EPR: Enhanced permeability and retention

EU: Endotoxin units

FBS: Fetal bovine serum

FDA: Food and drug administration

FITC: Fluorescein isothiocyanate

GAPDH: Glyceraldehyde 3-phosphate dehydrogenase

GIT: Gastrointestinal tract

HEPES: 4-(2-hydroxyethyl)-1-piperazineethanesulfonic acid

HFF: Human foreskin fibroblasts

hMSCs: Human mesenchymal stem cells

HPLC: High-performance liquid cromatography

HUVEC: Human umbilical vein endothelial cells

H&E: Hematoxylin and Eosin

IL: Interleukin

i.m.: Intramuscular

i.p.: Intraperitoneal

ITC: Inverse transition cycling

ITT: Inverse temperature transition

i.v.: Intravenous

$K_{elimination}$: Elimination rate constant

LCST: Lower critical solution temperature

LDL: Low density lipoprotein

LSGS: Low serum growth supplement

KDa: KiloDalton

LB: Luria Broth

MALDI-TOF: Matrix-Assisted Laser Desorption/Ionization-Time-Of-Flight

MEM: Minimum essential medium

MHC: Major histocompatibility complex

MPS: Mononuclear phagocyte system

MTT: Thiazolyl Blue tetrazolium bromide

MVB: Multivesicular bodies

MW: Molecular weight

NF-κB: Nuclear factor kappa-light-chain-enhancer of activated B cells

Nm: Nanometers

NMR: Nuclear magnetic resonance

NPs: Nanoparticles

N-terminal: Amine terminal

PBP: Protein-based polymer

PBS: Phosphate buffered saline

PDAC: Pancreatic ductal adenocarcinoma

PDI: Polydispersity index

PDT: Photodynamic therapy

PEG: Polyethyleneglycol

pET: Expression vector

PFA: Paraformaldehyde

PFU: Plaque-forming units

PGA: Polyglycolic acid

PH: Pleckstrin homology

p.i.: post injection

PLGA: Poly-dl-lactic-co-glycolic acid

PLLA: Poly-l-lactic acid

PMSF: Phenylmethylsulfonyl fluoride

PRNT: plaque reduction neutralization test

PS: Photosensitizer

PVDF: poly(vinylidene difluoride)

P/S: Penicillin/Streptomycin

RDL: Recursive directional ligation

RdRp: RNA-dependent RNA polymerase

RES: Reticuloendothelial system

ROS: Reactive oxygen species

RPMI: Roswell Park Memorial Institute

RVF: Rift Valley fever

RVFV: Rift Valley fever virus

SAP: Shrimp alkaline phosphatase

SAPE: Streptavidin-Phycoerythrin

SD: Standard deviation

SDS: Sodium dodecyl sulfate

SDS-PAGE: Sodium Dodecyl Sulfate-Polyacrylamide Gel Electrophoresis

SELEX: Systematic Evolution of Ligands by Exponential Enrichment

$T_{1/2\ elimination}$: Terminal half-life

TAE: Tris-Acetate-EDTA

TBS: Tris buffered saline

TCID: Tissue culture infectivity dose

TE: Tris-EDTA

TEM: Transmission electron microscopy

TEMED: Tetramethylenediamine

TNFα: Tumor fecrosis factor α

Tris: Tris(hydroximethyl)aminomethane

TSS: Transformation and storage solution

Tt: Transition temperature

UV: Ultra Violet

Vd: Volume of distribution

VLP: Virus-like particle

w/v: weight/volume

7.2 Additional

Publications:

2020

- **J. Gonzalez-Valdivieso**, B. Borrego, A. Girotti, S. Moreno, A. Brun, J.F. Bermejo-Martin, F.J. Arias. A DNA vaccine delivery platform based on Elastin-Like Recombinamer nanosystems for Rift Valley fever virus. *Molecular Pharmaceutics*. 2020. 17(5): 1608-1620.
  DOI: 10.1021/acs.molpharmaceut.0c00054

- A. Girotti, **J. Gonzalez-Valdivieso**, F.J. Arias, M. Santos, L. Martin. Functional characterization of an enzymatically degradable multi-bioactive Elastin-Like Recombinamer. *International Journal of Biological Macromolecules*. Under revision.

- R. Vallejo, **J. Gonzalez-Valdivieso**, M. Santos, S. Rodriguez-Rojo, F.J. Arias. Elastin–like based nanoparticles for docetaxel encapsulation by Supercritical Anti-solvent process as smart drug delivery systems. *Chemical Engineering Journal*. Under revision.

- **J. Gonzalez-Valdivieso**, A. Garcia-Sampedro, A. Girotti, F.J. Arias, S. Pereira, P. Acedo. Smart ELR nanoparticles as advanced anti-Akt drug delivery systems for pancreatic cancer therapy. Journal of Controlled Release. In progress.

- **J. Gonzalez-Valdivieso,** R. Vallejo, A. Girotti, M. Santos, S. Rodriguez-Rojo, F.J. Arias. ELR-based smart nanohybrids as dual-approach drug delivery system against colorectal cancer. In progress.

2019

- **J. Gonzalez-Valdivieso**, A. Girotti, R. Muñoz, JC. Rodríguez-Cabello, F.J. Arias. Self-assembling ELR-based nanoparticles as smart drug-delivery systems

modulating cellular growth via Akt. *Biomacromolecules*. 2019. 20(5): 1996-2007. DOI: 10.1021/acs.biomac.9b00206

- M. Santos, S. Serrano-Ducar, **J. Gonzalez-Valdivieso**, R. Vallejo, A. Girotti, P. Cuadrado, F.J. Arias. Genetically engineered biopolymers for pharmaceutical and biomedical applications. *Current Medicinal Chemistry*. 2019. 26(40): 7117-7146. DOI: 10.2174/0929867325666180508094637

Congresses and conferences:

2020

- AACR Virtual Annual Meeting I.

2019

- 3rd Young Researchers Workshop on Biomaterials and Applications bioMAPP19 (Bilbao, Spain). ORAL COMMUNICATION. Smart self-assembling nanoparticles as dual-approach drug delivery system against colorectal cancer.

- I Conference of Scientific Divulgation "Café con Ciencia" (Valladolid, Spain). ORAL COMMUNICATION. Self-assembling nanoparticles as smart drug delivery systems for cancer treatment.

- United European Gastroenterology Week (Barcelona, Spain). FLASH TALK & POSTER COMMUNICATION. Smart drug-delivery systems for pancreatic cancer treatment.

- 12th European Congress of Chemical Engineering. 5th European Congress of Applied Biotechnology (Florence, Italy). ORAL COMMUNICATION. Encapsulation of docetaxel with elastin like recombinamers by supercritical CO2 for advanced anticancer applications.

- EACR Congress. Nanotechnology in Cancer: Engineering for Oncology (Cambridge, United Kingdom). POSTER COMMUNICATION. Elastin-like

Recombinamers-based nanoparticles: a new smart system for effective drug delivery on cancer cells.

- IX Workshop Early Researchers in Nanosciences (Madrid, Spain). ORAL COMMUNICATION. Self-assembling ELR nanoparticles: smart drug delivery systems for cancer therapy.

- Frontiers in Biomedical Polymers (Puerto de la Cruz, Spain). ORAL COMMUNICATION. Self-assembling nanoparticles as smart drug delivery systems for cancer therapy.

- Division of Medicine Research Retreat (London, United Kingdom). POSTER COMMUNICATION. Self-assembling nanoparticles as smart drug delivery systems for pancreatic cancer therapy.

2018

- British Society for Nanomedicine: Annual Early Career Researcher's Meeting (Londres, 2018). ORAL COMMUNICATION. Elastin-like Recombinamers-based nanoparticles: an accurate drug delivery system on cancer cells.

- 25th Congress of the European Association for Cancer Research: From Fundamental Insight to Rational Cancer Treatment (Amsterdam, 2018). POSTER COMMUNICATION. Elastin-like Recombinamers nanoparticles: an effective drug delivery system on colorectal cancer cells.

- I Conference in Bioengineering and Medicine (Valladolid, Spain). POSTER COMMUNICATION. ELR nanoparticles as drug delivery systems against colorectal cancer.

2017

- II National Congress of Early Researchers in Biomedicine (Valencia, Spain). ORAL COMMUNICATION. Elastin-Like Recombinamer-based nanoparticles as carriers for drug delivery against colorectal cancer.

- III Conference in Early Researchers in Polymers (Madrid, 2017). ORAL COMMUNICATION. New elastin-based nanoparticles as polymeric carriers for drug delivery against colorectal cancer.

- Workshop "From 2D to 3D scaffolding for regenerative medicine: 3D printing" (Sedano, 2017). ORAL COMMUNICATION. Development of nanoparticles for gene delivery and as immunomodulatory agents.

Courses and accreditations:

2020

- ***Ex Vivo* Modelling.** Manchester Cancer Research Centre. 2020

- **Light & biology, light & energy, light & computing, light & health.** Iberian Nanotechnology Laboratory. 2020

- **How to peer review a review article.** Elsevier. 2020

2019

- **XII Course in biomedical research management.** ICICOR and Junta of Castile and León. 2019

- **Certification "*In vivo* experimentation for the design and realization of animal trials".** University of Salamanca. 2019

- **Certified peer review course.** Elsevier. 2019

2018

- **Nanoscience conference. UCL Seminar on Translational Nanomedicine.** University College London. 2018

- **Traslational medicine conference. Apollo London: The Launch.** University College London. 2018

- **Conference "Organs on-a-chip to model human diseases".** University College London. 2018

- **Introduction to data analysis through SPSS statistics software. Advanced level.** University of Valladolid. 2018

- **Nano-Bioengineering for medicine.** Life and Health Sciences Research Institute and University of Minho. 2018

2017

- **How to review a manuscript.** Elsevier. 2017

- **III International conference IMFAHE-Universitat de Valencia: "Connecting emigrated talent to universities, businesses and governments: a new socio-economic model based on education".** IMFAHE-University of Valencia. 2017

- **Data base "Scifinder".** University of Valladolid. 2017

- **Introduction to Biomaterials Science.** Polytechnic University of Madrid. 2017

- **Update in Clinical Microbiology and Infections.** University Hospital Río Hortega of Valladolid. 2017

- **Introduction to data analysis through SPSS statistics software. Intermediate level.** University of Valladolid. 2017

- **Care and management of laboratory animals.** University of Valladolid. 2017

- **How genomes evolved.** University of Navarra. 2017

2016

- **Basic principles of scientific dissemination.** University of Cantabria. 2016

- **Ethics in university research.** University of the Basque Country. 2016

Honors and awards:

- **Poster of Excellence. United European Gastroenterology Week (Barcelona, Spain).** United European Gastroenterology.

- **Article of the Month Award, October 2019.** Spanish Society of Biochemistry and Molecular Biology. Self-Assembling ELR-Based Nanoparticles as Smart Drug-Delivery Systems Modulating Cellular Growth via Akt. Juan Gonzalez-Valdivieso, Alessandra Girotti, Raquel Muñoz, J. Carlos Rodriguez-Cabello, and F. Javier Arias. Biomacromolecules 2019 20 (5), 1996-2007.
  DOI: 10.1021/acs.biomac.9b00206

- **First prize. I Competition of Scientific Photography for Young Researchers. PHOTOPOL2019.** Institute of Polymer Science and Technology (ICTP). Spanish National Research Council (CSIC). 2019.

- **Honorary Collaborator at Department of Biochemistry, Molecular Biology and Physiology.** University of Valladolid. Academic courses 2016-2017, 2017-2018, 2018-2019 and 2019-2020.

- **Academic Award.** Foundation Dr. Antoni Esteve. 2017.

- **Mentee in the International Mentor Program.** International Mentoring Foundation for the Advancement of Higher Education. Supervisor: Dr. Itsaso García-Arcos. 2016-2017.

Other contributions:

- Teaching activities for undergraduate students at School of Medicine (University of Valladolid). Co-supervision of master students from the Master in Biomedical Research and undergraduate students from summer internships.